Hydrothermal Habitats:

Measurements of Bulk Microbial Elemental Composition,

and Models of Hydrothermal Influences on the Evolution of Dwarf Planets

by

Marc François Laurent Neveu

A Dissertation Presented in Partial Fulfillment
of the Requirements for the Degree
Doctor of Philosophy

Approved October 2015 by the
Graduate Supervisory Committee:

Steven J. Desch, Co-Chair
Ariel D. Anbar, Co-Chair
Everett L. Shock
James J. Elser
Allen K. McNamara

ARIZONA STATE UNIVERSITY

December 2015

©2015 Marc François Laurent Neveu

All Rights Reserved

ABSTRACT

Finding habitable worlds is a key driver of solar system exploration. Many solar system missions seek environments providing liquid water, energy, and nutrients, the three ingredients necessary to sustain life.

Such environments include hydrothermal systems, spatially-confined systems where hot aqueous fluid circulates through rock by convection. I sought to characterize hydrothermal microbial communities, collected in hot spring sediments and mats at Yellowstone National Park, USA, by measuring their bulk elemental composition. To do so, one must minimize the contribution of non-biological material to the samples analyzed. I demonstrate that this can be achieved using a separation method that takes advantage of the density contrast between cells and sediment and preserves cellular elemental contents. Using this method, I show that in spite of the tremendous physical, chemical, and taxonomic diversity of Yellowstone hot springs, the composition of microorganisms there is surprisingly ordinary. This suggests the existence of a stoichiometric envelope common to all life as we know it. Thus, future planetary investigations could use elemental fingerprints to assess the astrobiological potential of hydrothermal settings beyond Earth.

Indeed, hydrothermal activity may be widespread in the solar system. Most solar system worlds larger than 200 km in radius are dwarf planets, likely composed of an icy, cometary mantle surrounding a rocky, chondritic core. I enhance a dwarf planet evolution code, including the effects of core fracturing and hydrothermal circulation, to demonstrate that dwarf planets likely have undergone extensive water-rock interaction. This supports observations of aqueous products on their surfaces. I simulate the alteration of chondritic rock by pure water or cometary fluid to show that aqueous alteration feeds back on geophysical evolution: it modifies the fluid antifreeze content,

affecting its persistence over geological timescales; and the distribution of radionuclides, whose decay is a chief heat source on dwarf planets. Interaction products can be observed if transported to the surface. I simulate numerically how cryovolcanic transport is enabled by primordial and hydrothermal volatile exsolution. Cryovolcanism seems plausible on dwarf planets in light of images recently returned by spacecrafts. Thus, these coupled geophysical-geochemical models provide a comprehensive picture of dwarf planet evolution, processes, and habitability.

DEDICATION

I dedicate this dissertation to my wife, Svet, for making these PhD years some of the best in my life. I also dedicate this work to my parents, Marie-Christine and Luc, who encouraged me to push my studies as far as I could long before I was convinced of undertaking doctoral studies; and to my sister Anne, wishing her to complete her own dissertation soon.

My gratitude also goes to the mentors without whom I would not have begun this work: Emily Wilson, Delphine Faye, John Mather, and Steven Benner.

ACKNOWLEDGEMENTS

This work is the collective product of many people over the past four years. The research ideas behind this dissertation were first formulated by Ariel Anbar (Chapters 2 and 3) and Steve Desch (Chapters 4 through 7), together with Jim Elser (Chapters 2 and 3), Julie Castillo-Rogez (Chapters 4 through 7), and Everett Shock (all chapters, really). Steve and Ariel's skillful advising and mentorship have been central to the success of this research. I also thank my committee, including Allen McNamara, for their continued encouragements. I am grateful to Amisha Poret-Peterson, Natasha Zolotova, Gwyn Gordon, and the Group Exploring Organic Processes in Geochemistry (GEOPIG) for teaching me lab and fieldwork skills which, beyond the research of Chapters 2 and 3, will surely prove essential in the future. Finally, I thank Zarraz Lee and Chris Glein for co-authoring Chapters 2 and 6, respectively. Acknowledgements specific to each chapter are detailed below.

Chapter 2 and 3: Many thanks to Laura Steger for her advice on the cell separation protocol, to Mayra Buenrostro, Nina Popovic, Tristyn Bercel, and Grace Chang for carrying out most of the complex and time-consuming cell separations, to Marcia Kyle for performing the bulk sediment elemental analyses, and to the GEOPIG for sample collection and field measurements. Tristyn also helped with DNA sequencing; all the content regarding taxonomic analyses in Chapter 3 is from her and Amisha, not me. Elemental analyses were carried out in the W. M. Keck Foundation Laboratory for Environmental Biogeochemistry at ASU. DNA sequencing was performed in the DNASU Genomics Core Facility at ASU. The Research Office at Yellowstone National Park granted the permit (YELL-2009-SCI-5434) that allowed collection of these samples. This research was supported by the NASA Astrobiology Institute grant NAI5-0018 and by the National Science Foundation grant DEB-0950175.

Chapter 5: Jeff Dick helped modify the *CHNOSZ R* geochemistry package to work at subzero temperatures, and Denise Napolitano and Angela Edwards helped with preliminary *CHNOSZ* calculations.

Chapter 7: A significant fraction of the text from this chapter was contributed by Steve Desch. This work benefited from helpful conversations with Hilairy Hartnett, Kelin Whipple, David Williams, and Mikhail Zolotov. Sue Selkirk created Figure 43.

Chapters 4 through 7: These studies were funded by the NASA Astrobiology Institute team at Arizona State University (NAI5-0018), and by the NASA Outer Planets Research (NNX14AR25G) and Earth & Space Science Fellowship (PLANET14F-0032) programs. Part of this work was carried out at the Keck Institute for Space Studies, and at the Jet Propulsion Laboratory, California Institute of Technology, in the summer of 2013. The thermal evolution and geochemistry codes, thermodynamic data with original references, and input files used for these chapters are freely available at https://github.com/MarcNeveu/IcyDwarf.

TABLE OF CONTENTS

Page

LIST OF TABLES xiv

LIST OF FIGURES xvi

CHAPTER

1 OVERVIEW AND SIGNIFICANCE OF HYDROTHERMAL SYSTEMS 1

1.1 Relevant Hydrothermal Processes and Settings 2

1.2 Occurrence of Hydrothermal Systems in the Solar System 3

1.3 Astrobiological Significance of Hydrothermal Systems 6

1.3.1 Hydrothermal Sources of Energy and Nutrients 8

1.3.2 Emergence and Early Evolution of Life 8

1.3.3 Biosignature Preservation 9

1.4 Scope of This Dissertation 10

1.4.1 Biological Demand in Hydrothermal Systems 10

1.4.2 Occurrence of Hydrothermal Systems on Dwarf Planets 11

2 PROKARYOTIC CELLS SEPARATED FROM SEDIMENTS ARE SUITABLE FOR ELEMENTAL COMPOSITION ANALYSIS 13

2.1 Introduction 14

2.2 Materials and Procedures 17

2.2.1 Cell-Sediment Separation Procedure 18

2.2.2 Cell Counting 21

2.2.3 Elemental Analysis 22

2.2.3.1 Carbon and Nitrogen 22

2.2.3.2 Phosphorus and Trace Elements 22

2.3 Assessment 24

CHAPTER Page

2.3.1 Cell Recovery Yields 24
2.3.2 Preservation of Elemental Content 24
2.3.2.1 Gain of Elements (Contamination) 26
2.3.2.2 Loss of Elements 27
2.3.3 Application to Field Samples 29
2.3.3.1 Cell-Sediment Separation 29
2.3.3.2 Cell Recovery Yields 30
2.3.3.3 Elemental Composition of Cells Separated from Sediment 31
2.4 Discussion 35
2.5 Comments and Recommendations 38
3 ORDINARY STOICHIOMETRY OF EXTRAORDINARY MICROORGANISMS 40
3.1 Introduction 41
3.2 Methods 45
3.2.1 Sample Collection 45
3.2.2 Cell-Sediment Separation 48
3.2.3 Elemental Analysis 51
3.2.4 Quantification of Sediment Contamination 55
3.2.5 Statistical Analyses of Elemental Stoichiometries 60
3.2.6 16S rRNA Gene V4 Region Sequencing 61
3.3 Results 69
3.3.1 C:N:P Stoichiometries 69
3.3.2 Trace Element Stoichiometries 71

CHAPTER Page

3.3.3 Elemental Abundances and Microbial Community Composition . . . 77
3.4 Discussion . . . 79
3.4.1 What Causes High Biomass C:P and N:P Ratios? . . . 79
3.4.2 Patterns in Trace Element Abundances . . . 81
3.4.3 Ordinary Major and Trace Element Stoichiometries . . . 83
3.5 Conclusion . . . 87
4 CORE CRACKING AND HYDROTHERMAL CIRCULATION CAN PROFOUNDLY AFFECT CERES' GEOPHYSICAL EVOLUTION . . . 91
4.1 Introduction . . . 92
4.2 Thermal Evolution Code . . . 96
4.3 Geophysical-Geochemical Model of Core Fracturing . . . 100
4.3.1 Brittle-Ductile Transition in Hydrated Rock . . . 101
4.3.2 Micro-Cracking by Thermal Expansion Mismatch . . . 105
4.3.3 Expansion of Pore Water upon Heating . . . 108
4.3.4 Hydration Swelling and Dehydration Shrinking . . . 111
4.3.5 Dissolution and Precipitation of Mineral Species . . . 114
4.3.6 Neglected Effects . . . 118
4.3.6.1 Thermal Expansion of the Rock Matrix . . . 118
4.3.6.2 Fluid Pressure Changes Linked to Conduit Size . . . 119
4.3.6.3 Anisotropy in Rock Permeability . . . 119
4.3.6.4 Gas Processes and Multi-Phase Flows . . . 119
4.3.6.5 Species Transport . . . 120
4.3.6.6 Anisotropy in Serpentine Properties . . . 122

CHAPTER Page

4.4 Inclusion in Thermal Evolution Code 123

4.4.1 Rock Hydration and Dehydration 123

4.4.2 Hydrothermal Circulation in the Cracked Layer 126

4.5 Results 130

4.5.1 Thermal and Geophysical Evolution of Ceres 130

4.5.1.1 Simulations with Negligible NH_3 Amounts 131

4.5.1.2 Simulations with $NH_3/H_2O = 0.01$ by Mass 135

4.5.2 Cracking Model Sensitivity to Free Parameters 139

4.5.3 Timescales of Cracking Processes 142

4.5.3.1 Fracture Healing 142

4.5.3.2 Thermal Mismatch 143

4.5.3.3 Pore Water Pressurization 143

4.5.3.4 Core Hydration and Dehydration 143

4.5.3.5 Dissolution and Precipitation 144

4.5.4 Material Compressibility 145

4.5.5 Heat Sources 146

4.6 Discussion 147

4.6.1 Comparison with Results of Previous Studies 147

4.6.1.1 Core Cracking Models of Vance et al. (2007) 147

4.6.1.2 Models of McCord and Sotin (2005) 148

4.6.1.3 Models of Castillo-Rogez and McCord (2010) 149

4.6.1.4 Models of Malamud and Prialnik (2015) 150

4.6.2 Geophysical and Geochemical Feedbacks 151

4.6.3 Testing Predictions with *Dawn* Observations 153

CHAPTER Page

4.6.3.1 Gravity Measurements . . . 153

4.6.3.2 Compositional Mapping . . . 155

4.6.3.3 Possible Cryovolcanic Activity . . . 157

4.7 Conclusions . . . 157

5 AQUEOUS GEOCHEMISTRY IN ICY WORLD INTERIORS: FATE OF ANTIFREEZES AND RADIONUCLIDES . . . 160

5.1 Introduction . . . 162

5.2 Geochemical Models and Simulations . . . 166

5.2.1 Geochemical Model, Code, and Starting Conditions . . . 166

5.2.2 Initial Rock and Fluid Compositions . . . 169

5.2.3 Thermodynamic Data . . . 173

5.2.4 Limitations of our Equilibrium Simulations . . . 176

5.3 Modeling Results . . . 177

5.3.1 Dependency on Initial Conditions . . . 178

5.3.2 Equilibrium Assemblages . . . 180

5.3.2.1 Simulation Products . . . 180

5.3.2.2 Comparison with Carbonaceous Chondrite Mineralogies 184

5.3.2.3 Comparison with Icy World Ocean Chemistries . . . 186

5.3.3 Fate of Antifreezes . . . 188

5.3.4 Fate of Radionuclides . . . 192

5.4 Effects on Geophysical Evolution . . . 195

5.4.1 Suggestions for Geophysical Models . . . 195

5.4.2 Implications for Exsolution-Driven Cryovolcanism . . . 196

5.4.3 Application to Ceres . . . 197

CHAPTER Page

5.5 Conclusions 201

6 PREREQUISITES FOR EXPLOSIVE CRYOVOLCANISM ON DWARF PLANET-CLASS KUIPER BELT OBJECTS 202

6.1 Introduction 203

6.1.1 Explosive Volcanism and Outgassing 205

6.1.2 Evidence for Cryovolcanism in the Outer Solar System 206

6.2 Ingredients for Explosive Cryovolcanism 208

6.2.1 Liquid Persistence 208

6.2.2 Bringing Cryolavas to the Surface 210

6.2.2.1 Pressurization and Crack Opening 210

6.2.2.2 Crack Propagation 212

6.2.3 Volatile Inventory of KBOs 213

6.2.3.1 Carbon Species 216

6.2.3.2 Nitrogen Species 217

6.2.3.3 Sulfur Species, Hydrogen, and Noble Gases 219

6.3 Geochemical Model 220

6.3.1 Modeling Geochemical Equilibrium 220

6.3.2 Implementation of the Geochemical Model 222

6.3.3 Modeling at Low Temperature and High Pressure 224

6.3.4 Condition for Crack Propagation 227

6.4 Results 228

6.4.1 Application to Charon 228

6.4.2 Uncertainty on Gas Solubilities 232

6.5 Discussion 233

CHAPTER Page

6.5.1 Comparing the Explosiveness of Gases 233

6.5.2 Fate of CO in a Subsurface Ocean 235

6.5.3 Effect of Internal Structure 239

6.5.4 Freezing During Ascent 242

6.5.5 Other Model Considerations 246

6.5.6 Predictions for Pluto and Charon 250

6.6 Conclusions 253

7 GEOCHEMISTRY, THERMAL EVOLUTION, AND CRYOVOLCANISM ON CERES WITH A MUDDY ICE MANTLE 255

7.1 Introduction 256

7.2 Differentiation and Origin of a Muddy Ice Mantle 259

7.3 Thermal Evolution 263

7.4 Geochemistry 266

7.5 Possible Ongoing Cryovolcanism 269

7.6 Conclusions 272

8 CONCLUSIONS AND FUTURE WORK 275

8.1 How Far Have We Gotten? 275

8.2 Ground Truth: Preliminary Results from *Dawn* and *New Horizons* 277

8.3 Future Steps 280

REFERENCES 282

APPENDIX

A ELEMENTAL ABUNDANCES IN SOLUTIONS, *E. COLI*, AND FIELD SAMPLES 335

APPENDIX Page

B ELEMENTAL COMPOSITION OF CELL COMMUNITIES SEPARATED FROM YNP SEDIMENT 340

C ADDED THERMODYNAMIC DATA FOR SOLIDS 344

LIST OF TABLES

Table Page

1 Comparison between the Trace Element Signal from Sample-Free Digestions and from Separated *E. coli*, in Part per Billion per Mass of Solution Analyzed (Diluted Digestion with 2% HNO_3) 28

2 Cell Recovery Yields for Several Separated Samples Collected at Hot Springs of Yellowstone National Park, as Well as Cultured *E. coli* 31

3 pH, Conductivity, Temperature, and Location of the Hot Springs Sampled . . . 46

4 Major Chemical Composition of the Hot Springs Sampled, as Well as Dissolved P and Mo Content 47

5 Community Composition and Bias due to Cell-Sediment Separation (A) 66

6 Community Composition and Bias due to Cell-Sediment Separation (B) 66

7 Physicochemical Parameters for Laboratory Cultures and Environments for Which the Extended Elemental Composition of Biomass Was Reported in the Literature Cited 89

8 Description of Model Parameters Specific to Dry or Hydrated Silicates 107

9 Description of Model Parameters Not Specific to Dry or Hydrated Silicates . . 109

10 Description of Hydrothermal Circulation Parameters 129

11 Description of Thermal Model Parameters 130

12 Antifreezes Relevant to Icy World Interiors and Eutectic Temperatures and Compositions at 1 Bar of Binary Antifreeze-H_2O Systems 165

13 Parameter Space Sampled in Geochemical Simulations 168

14 Mineral Composition of the Ordinary Chondrite-Type Initial Solid Assemblage 170

15 Mineral Composition of the CM Chondrite-Type Initial Solid Assemblage . . . 171

Table Page

16 Elemental Composition of the Initial Ordinary and CM Chondrite-Type Assemblages 173

17 Thermodynamic Data for Aqueous Solutes Added to the Expanded Database 175

18 Thermodynamic Data for Dissolution Reactions of Gases Added to the Expanded Database 176

19 Condensation Temperatures and Typical Cometary and Disk Abundances of Volatiles 215

20 Composition of the Gas Driving Explosive Volcanism at the Depth Where Positive Buoyancy Is Reached 234

21 Elemental Abundances (by Mass Relative to Sample Dry Mass) in Autoclaved Solutions Used in the Separation Procedure, Unseparated and Separated *E. coli* Cells, and Field Samples 336

22 Elemental Composition of Cell Communities Separated from YNP Sediment . 341

23 Thermodynamic Data for Solids in the Expanded Database 345

LIST OF FIGURES

Figure Page

1 Schematic of a Hydrothermal System 4

2 The Ubiquitous Presence of Water in Contact with Rock in the Solar System, Together with Heat Sources Generating Thermal Gradients, Suggests that Hydrothermal Systems Are Commonplace in Our Planetary Neighborhood . . 7

3 A. Schematic of the Cell-Sediment Separation and Preparation for Elemental Analysis. B. Four Phases of a Separated Sediment Sample: Top Aqueous Layer, Interface Containing Cells, Nycodenz Layer, and Bottom Sediment Pellet, Ideally No Longer Containing Cells 20

4 Relative Enrichment or Depletion of Elements in Cultured Wild-Type *E. coli* that Underwent Separation, Compared with the Same Culture without Separation 25

5 C:N, C:P, and N:P Ratios of Cells Separated from Sediment Collected at Photosynthetic- and Chemosynthetic-Dominated Yellowstone Hot Springs . . . 33

6 Metal Abundances in Cells Extracted from Sediment Samples Collected at a Dozen Photosynthesis- and Chemosynthesis-Dominated Yellowstone Hot Springs 34

7 Example Micrographs of Separated Samples from Two YNP Hot Springs 51

8 Elemental Makeup of Separated and Unseparated Samples Shown on a Ternary Diagram 56

9 Sediment Contribution to Elemental Abundances Measured in Separated Samples 57

10 Relative Abundance of Bacterial Phyla in Unseparated ('Pre') and Separated ('Post') Samples 64

Figure Page

11 (A) C:N, (B) C:P, and (C) N:P Ratios of Material (Mainly Cells) Separated from YNP Hot Spring Sediment Samples 70

12 (A) C:N, (B) C:P, and (C) N:P Ratios in Separated Samples and Bulk Sediment 71

13 Elemental Makeup of YNP Extremophiles Compared to the Known Makeup of Micro-Organisms 72

14 Metal:C Ratios (Molar) for Ni (A; E), Cu (B; F), Zn (C; G), and Mo (D; H) in Separated Cells Show No Correlation with Either Temperature or PH 75

15 Mo:C Ratios (Molar) in Separated Cells Show No Correlation with Hot Spring Dissolved Nitrite (A), Nitrate (B), Ammonium (C), or Sulfide (D) 76

16 (A) Measured Molar Mo:P Ratios in the Separated Cells and Bulk Sediment. (B) Measured Molar Mo:P Ratios in the Separated Cells and Hot Spring Fluid 77

17 CCA Triplots Scaled for OTU Optima Constrained by Cellular C, N, and P (Panel A) or Metal (Panel B) Contents 78

18 Dry (Olivine) and Hydrated (Serpentine) Rock Strengths inside a Ceres-Type Dwarf Planet 104

19 Schematic View of the Phenomena Included in This Study that Influence the Extent of Cracking 110

20 Ceres Geotherms Overlain on the Water Phase Diagram and Silicate Brittle-Ductile Transition Curves 121

21 Upgraded Thermal Evolution Code 124

22 Thermal Evolution and Internal Structure of Ceres with Negligible Antifreezes 132

23 Depth of Cracking inside Ceres' Core over Geologic Time 134

24 Thermal Evolution of Ceres with Antifreezes 138

25 Timescales of Cracking Processes 142

Figure Page

26 Cumulated Radiogenic, Serpentinization (Silicate Hydration), and Gravitational Heating of Ceres through Time 146

27 The Inclusion of Core Cracking and Hydrothermal Circulation in Evolution Models of Ceres (Light Gray Boxes) Enables the Investigation of Key Feedback Loops in Endogenic Processes 154

28 Feedbacks between Geophysical and Geochemical Processes 163

29 Sensitivity of Equilibrium Mineral Assemblages to Starting pH and Redox . . . 179

30 Equilibrium Mineral Assemblages 181

31 Relative Elemental Composition of Equilibrium Solutions 183

32 Equilibrium Gas Compositions 185

33 Fate of N Species 191

34 Fate of K 194

35 Apparent Molar Heat Capacity (A) and Volume (B) of NaCl at Subzero Temperatures as a Function of the Square Root of the NaCl Molality 226

36 Equilibrium Constants for the Dissolution of Carbon Dioxide, Methane, and Argon Gases 227

37 Molality of Key Volatiles with Canonical Starting Abundances (left Panels) and Volumic Vapor Fraction (right Panels) as a Function of Depth for a Charon-Like KBO 229

38 Minimum Crack Length Necessary so that Exsolution Drives Crack Propagation, as a Function of the Initial Abundance of Carbon Monoxide 237

39 Logarithm of the Activities of Cometary Volatiles, Likely to Have Been Accreted by KBOs, as a Function of Redox Conditions in a Subsurface Ocean at 235 K and 1000 Bar 240

40 Time after Which 90% of Aqueous CO Is Consumed to Make Formate, as a Function of pH Relative to Neutrality, for Temperatures between 200 K and 323 K 241
41 Comparison of Timescales for Ascent and Freezing 244
42 Applicability of Current Geochemical Codes in the Pressure-Temperature-Density Space of Relevance to Icy Dwarf Planets 248
43 Differentiation If Ceres Formed 4-7 Myr after CAIs 261
44 Temperatures inside Ceres, versus Depth and Time since Formation (Logarithmic Scale) 267
45 Unveiling the Complexity of Internal Processes Governing the Evolution of Icy Dwarf Planets 276
46 Geologically Active Dwarf Planets 278

Chapter 1

OVERVIEW AND SIGNIFICANCE OF HYDROTHERMAL SYSTEMS

The tantalizing question of whether other worlds are inhabited, or even habitable, remains unanswered after almost forty years of robotic exploration of our solar system. This question has been a key driver of the exploration of Mars by orbital and landed spacecraft, from the *Mariner* and *Viking* era to the Mars Science Laboratory (MSL), through a set of orbiters and landers that "followed the water" (e.g. Squyres *et al.*, 2008). Meanwhile, the *Pioneer* and *Voyager* spacecrafts revealed the potential of icy moons of the giant planets to harbor subsurface oceans (Lewis, 1971; Consolmagno and Lewis, 1978; Plescia, 1987; Croft *et al.*, 1995). This prospect materialized with evidence gathered by *Galileo* of subsurface oceans under Europa and Ganymede's icy shells (Khurana *et al.*, 1998; McCord *et al.*, 1998, 1999; Pappalardo *et al.*, 1999; Kivelson *et al.*, 2000; McCord *et al.*, 2001; Kivelson *et al.*, 2002), and the *Cassini* discoveries of material from an ocean inside Enceladus being vented to space (Porco *et al.*, 2006; Waite *et al.*, 2009; Postberg *et al.*, 2009, 2011; Hsu *et al.*, 2015). Just this year, the first images of the dwarf planets Ceres, Pluto, and Charon returned by the *Dawn* and *New Horizons* spacecrafts have begun to reveal geologically active worlds, seemingly shaped by the action of subsurface liquid having leached material from rock or processed primordial nutrients in energy-producing reactions. Building on these results, current and upcoming solar system missions are on a quest for past or present habitable environments that would provide water, energy, and nutrients, the three ingredients necessary to sustain life (National Research Council, 2011).

Hydrothermal systems are such environments. They constitute the common

thread of this dissertation, which presents results regarding their habitability from the standpoints of both biological demand (Chapters 2 and 3) and environmental supply (Chapters 4 through 7) of the above ingredients. In this opening chapter, I briefly introduce hydrothermal systems, their likelihood of occurrence in the solar system, and their importance in shaping habitable environments. This introduction provides context for Chapters 2 through 7, which have all been published or submitted for publication as individual papers. In Chapter 8, I summarize the results from these papers and suggest avenues for future work.

1.1 Relevant Hydrothermal Processes and Settings

Hydrothermal systems are spatially-confined natural systems where hot (50°C to 500°C) aqueous fluid circulates through rock by convection. Fluid circulation is possible because of rock permeability (Newsom, 1980; Vance *et al.*, 2007; Pinneker, 2010), and because of heat sources creating thermal gradients that drive convection (Turcotte and Schubert, 2014). The fluid, in chemical disequilibrium with the surrounding rock, alters it and leaches and transports mineral and organic solutes (Pirajno, 2009). Fluid and rock physical and chemical properties feed back on each other and on the properties of the hydrothermal system (Farmer, 1996; Pirajno, 2009). The complexity of the geophysical and geochemical processes involved is portrayed in Fig. 1.

A hydrothermal system includes a recharge system, a circulation cell, and a discharge system (Farmer, 1996). On Earth, manifestations of subaerial and subaqueous systems occur at the site of discharge. Surface manifestations of hydrothermal systems include hot springs, geysers, mud pots (all liquid-dominated), and fumaroles (vapor-dominated). Discharge in seafloor hydrothermal systems happens most prominently at

hydrothermal vents. Hydrothermal systems dissipate endogenic heat ultimately arising from energy stored during planetary accretion (by conversion of the potential energy of the planetesimals accreted), and from the radioactive decay of the long-lived radionuclides ^{40}K, ^{232}Th, ^{235}U, and ^{238}U (Turcotte and Schubert, 2014). These radionuclides are assumed present on all solar system bodies in chondritic abundances (Wasson and Kallemeyn, 1988; Lodders, 2003). Hydrothermal systems can also be powered by exogenic sources, both transient (impacts; Newsom, 1980; Newsom *et al.*, 2001; Schwenzer *et al.*, 2012a) and over extended timescales (tidal heating; Czechowski and Leliwa-Kopystynski, 2005; Hsu *et al.*, 2015). Finally, geochemical reactions happening in hydrothermal systems are often exothermic (Vance *et al.*, 2007) and contribute to their total heat input. Hydrothermal circulation lasts as long as liquid water, a permeable matrix, and a thermal gradient coexist.

Circulating fluids alter mafic minerals such as olivines and pyroxenes to yield phyllosilicates (Schwenzer and Kring, 2009) and dissolved species (e.g. silica, carbonates, sulfates, and other salts) that can eventually precipitate out of the fluid if they become supersaturated (Griffith and Shock, 1995; Zolotov and Shock, 2001; Postberg *et al.*, 2009; Hsu *et al.*, 2015). Supersaturation can be caused by changes in temperature (e.g. cooling), water activity (e.g. evaporation or freezing), or chemical composition due to additional inputs of solutes (Fig. 1).

1.2 Occurrence of Hydrothermal Systems in the Solar System

Earth has likely harbored hydrothermal systems throughout its history. While impacts may have been a significant source of hydrothermal activity on early Earth, during the Hadean eon (Newsom, 1980), extant hydrothermal systems are fueled by

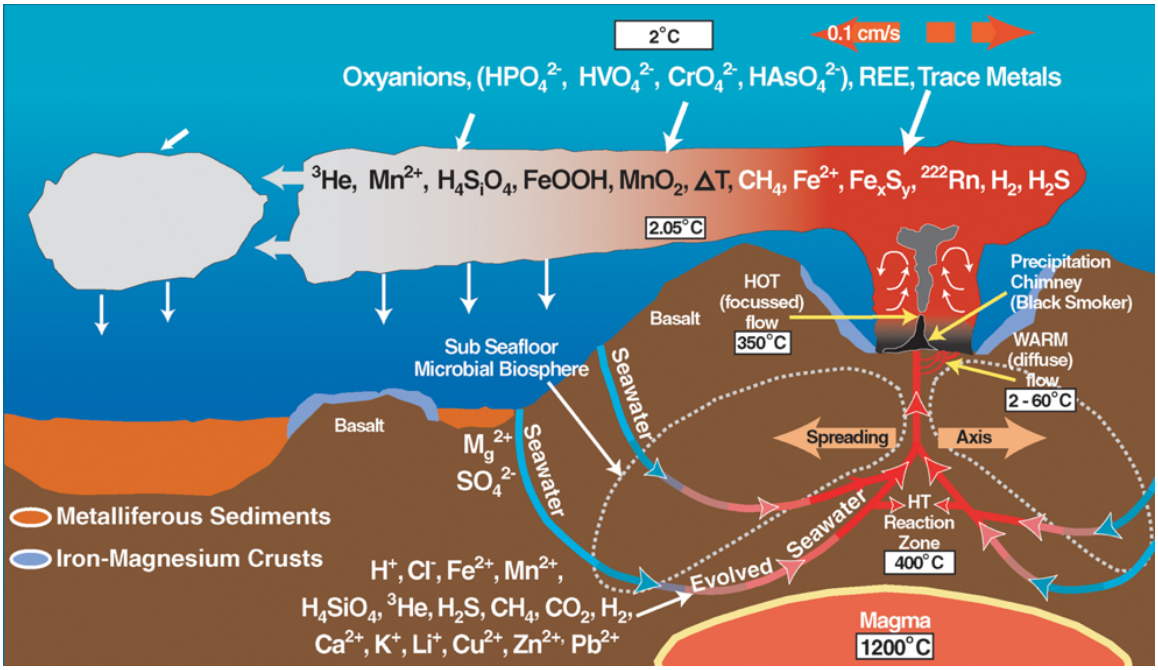

Figure 1: Schematic of a hydrothermal system

This figure illustrates the chemical complexity of these systems which provide energy and nutrients to aqueous settings, enhancing their habitability. In this case, the system is a subaqueous (seafloor) vent.

Source: NOAA.

the dissipation of endogenic heat through hot-spot volcanism and plate tectonics. The predominance of endogenic over exogenic heat sources on present-day Earth is expected: the amount of radiogenic and accretional energy to be dissipated should scale to first order with the size of a solid body, and the Earth is the largest such world in the solar system. As a consequence, many of Earth's hydrothermal systems are located where endogenic heat is dissipated: on hot-spots and near plate boundaries. Prime locations of hydrothermal activity are Yellowstone National Park (Meyer-Dombard *et al.*, 2005; Shock *et al.*, 2010), Iceland (Warner and Farmer, 2010), New Zealand, the Kamchatka peninsula, and seafloor hydrothermal fields such as *Lost City* near the mid-Atlantic ridge (Kelley and Delaney, 1987; Kelley *et al.*, 1993, 2005).

On Mars, there is no definitive evidence of even past hydrothermal activity. However, water and exogenic (impact) or endogenic heat sources (magmatic intrusions or volcanism at hot spots) were likely present at the same place and time during much of Mars' history, as late as 0.18 Ga, the latest age of crystallization from a melt in Martian meteorites (Farmer, 1996). The surface of Mars bears evidence of past and maybe present liquid water (Bridges *et al.*, 2001; Bibring *et al.*, 2006; Ehlmann *et al.*, 2010; Ojha *et al.*, 2015), although pure liquid water is thought to have been thermodynamically unstable at the surface for the past few billion years (Goldspiel and Squyres, 2000). Primary heat sources likely have been both endo- and exogenic (impacts). Both sources have declined over time; therefore, the majority of Mars' hydrothermal systems is expected to have occurred early in Mars' history (Parmentier *et al.*, 2008). Some hydrothermal activity may still occur today (Schulze-Makuch *et al.*, 2007), driven solely by background geothermal heating (Travis *et al.*, 2003). While most water-related morphological and mineralogical features on Mars date back to the Noachian (Schwenzer and Kring, 2009), numerical modeling has shown that even in the Hesperian and Amazonian, systems associated with magmatic intrusions greater than a few hundreds of cubic kilometers could have provided enough water to carve observed surface channels (Gulick, 1998).

Of the other terrestrial planets, Venus and Mercury are likely too water-poor to support extant hydrothermal systems, but Venus may have had extensive hydrothermal activity in its past (Nimmo and McKenzie, 1998). Water melting and hydrothermal fluid flow are thought to have occurred on rocky planetesimals (Grimm and McSween, 1989; Cohen and Coker, 2000; Young, 2001; Young *et al.*, 2003; Palguta *et al.*, 2010), yielding aqueously altered chondritic material that continues to fall on Earth today to be collected as meteorites (Barber, 1981). Detail analysis of the composition of

such fragments provides insights into the conditions of alteration (Larson *et al.*, 1979; Tomeoka and Buseck, 1988; Becker *et al.*, 1997; Alexander *et al.*, 1998, 2007; Zolensky *et al.*, 1999; Hanowski and Brearley, 2001; Howard *et al.*, 2009, 2011; Zolotov, 2012).

Icy bodies are ideally suited to host hydrothermal processes, due to their comparatively higher bulk water abundance, inferred from their bulk density and assumptions on the composition of the accreted material (McKinnon *et al.*, 2008; Zolotov and Kargel, 2009). This is especially the case for icy moons of the giant planets, which are subject to tidal heating, but also for icy dwarf planets (which, by definition, orbit directly the Sun but do not gravitationally dominate other objects sharing their orbit). Indeed, products of alteration of primordial solids or ices abound both on icy moons (McCord *et al.*, 1999; Pappalardo *et al.*, 1999; Postberg *et al.*, 2009, 2011; Hsu *et al.*, 2015; Plescia, 1987; Croft *et al.*, 1995) and on dwarf planets (Jewitt and Luu, 2004; Cook *et al.*, 2007; Milliken and Rivkin, 2009; Rivkin *et al.*, 2012). Evidence for aqueous processes on icy worlds is extensively reviewed in the introductory sections of Chapters 4 through 6.

1.3 Astrobiological Significance of Hydrothermal Systems

Hydrothermal systems are prime astrobiological targets (Schulze-Makuch *et al.*, 2007; Pirajno, 2009; Russell *et al.*, 2014). They provide all the ingredients to make and support life as we know it: water, chemical energy, synthesis of bioavailable nutrients in Fischer-Tropsch and leaching reactions, and synthesis of membranes (Russell *et al.*, 1994, 2014). They are also ideal locations of biosignature preservation (Walter and Des Marais, 1993). We detail these aspects below.

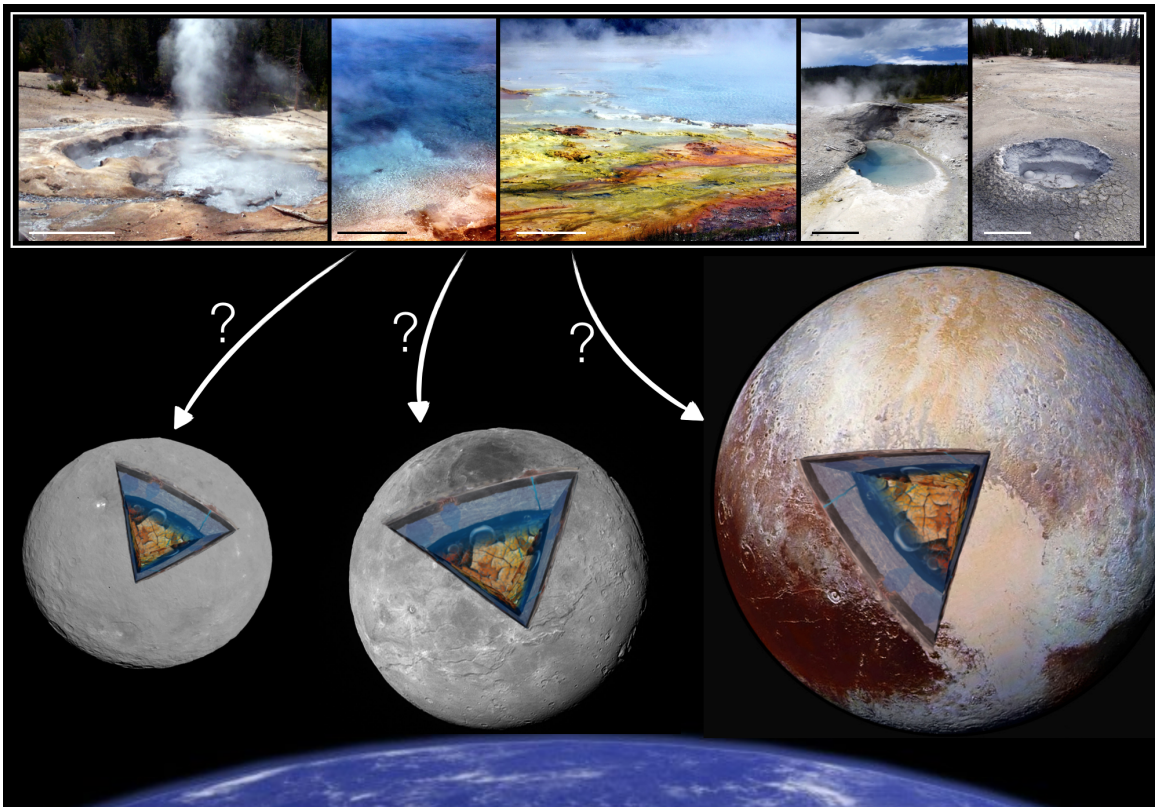

Figure 2: The ubiquitous presence of water in contact with rock in the solar system, together with heat sources generating thermal gradients, suggests that hydrothermal systems are commonplace in our planetary neighborhood

In this dissertation, I characterize hydrothermal systems as habitats from both ends of the "astro-biology" spectrum: biological demand for elements, and occurrence beyond Earth, inside dwarf planets. *Top:* A variety of hot springs in Yellowstone National Park (USA), where microorganisms analyzed in Chapters 2 and 3 were collected. Scale bars: $\approx$ 1 m (foreground). *Bottom:* Recently acquired images of Ceres (left, PIA19562), Charon (center, PIA19932), and Pluto (right, PIA09113), with Earth (bottom) for scale. Overlain are artistic renditions of possibly active interiors, as suggested by the results presented in Chapters 4 through 7.

Sources: NASA Planetary Photojournal, http://photojournal.jpl.nasa.gov (dwarf planet images); NASA (Earth image); the author (Yellowstone photos and artistic renditions).

1.3.1 Hydrothermal Sources of Energy and Nutrients

Hydrothermal systems feature strong chemical redox gradients and disequilibria (Fig. 1) due to the circulation of oxidized aqueous fluid through reduced rock (Schulte *et al.*, 2006; Shock *et al.*, 2010; Russell *et al.*, 2014). These redox gradients can support chemosynthetic organisms (Segerer *et al.*, 1993; Schulte *et al.*, 2006; Shock, 1997), even in large communities (Boston *et al.*, 1992; Varnes *et al.*, 2003). That chemical energy can fuel microbial metabolism without the need for photosynthesis lifts the constraint of illuminated, surface habitats. Thus, Mars or icy worlds may still harbor subsurface life today, without surface expression if chemosynthesis were the sole metabolism present (Shock, 1997; McKay *et al.*, 2014).

In hydrothermal conditions, the prebiotic synthesis of many organic compounds is not only possible, but energetically favored (Shock, 1997; Farmer, 2000). For example, all twenty amino acids used by life on Earth, as well as some proteins used by thermophiles, are more readily formed at high hydrothermal fluid temperatures, and their formation is energetically favored (Amend and Shock, 1998; Holm and Andersson, 2005; Dick, 2008). This suggests that thermophilic organisms spend less energy building biomolecules than microorganisms thriving at cooler temperatures, and is also consistent with very high doubling rates of communities living in seafloor hydrothermal vents on Earth (Lutz *et al.*, 1994).

1.3.2 Emergence and Early Evolution of Life

On Earth, molecular clocks suggest that the earliest identified metabolic pathways involved chemosynthesis at high temperatures (Pace, 1997). Whether Earth's earliest

life also fell into these categories or whether these represent a bottleneck in evolution (e.g. following a major impact event, such as the postulated late heavy bombardment) is unclear (Farmer, 2000; Cavosie, 2014). However, chemosynthetic, thermophilic microorganisms are found today mainly in hydrothermal systems (Amend and Shock, 1998), making these a plausible (but contested; Miller and Lazcano, 1995) environment for life to have originated (Corliss, 1990; Russell *et al.*, 2014).

1.3.3 Biosignature Preservation

Hydrothermal mineral products are prime targets for the search of past microbes or microbial activity (Farmer, 1996, 2000). Organisms thriving in hydrothermal systems are readily incorporated into deposits precipitated from mineral-rich hydrothermal water and preserved as fossils (Walter and Des Marais, 1993; Cady and Farmer, 1996; Cady *et al.*, 2003; Schulte *et al.*, 2006; Allen and Oehler, 2008; Summons *et al.*, 2011), because of the high rate of mineralization of fine-grained hydrothermal precipitates (Farmer and Des Marais, 1999; Farmer, 2000; Goryniuk *et al.*, 2004). Carbonates and silica are highly ordered and chemically stable mineral phases that form an impermeable matrix and closed chemical system protecting microorganisms or their byproducts against further physical or chemical alteration (Farmer and Des Marais, 1999; Allen *et al.*, 2000; Brown *et al.*, 2010). Encasing in mineral or ice matrices also protects biological matter against shocks (Gu *et al.*, 1999; Burchell *et al.*, 2014), bringing about the intriguing possibility of sampling icy world plumes at high velocity during a flyby for biological analysis (McKay *et al.*, 2014).

1.4 Scope of This Dissertation

In this dissertation, I study the potential of hydrothermal systems as a habitat for life beyond Earth from both ends of the "astro-biology" spectrum (Fig. 2). On the biology end, I characterize the biological demand in a few hydrothermal systems on Earth, located in Yellowstone National Park, USA. On the astronomy and planetary science end, I model the internal evolution of dwarf planets to determine if they can harbor hydrothermal systems, and (if so) how such systems may feed back on their long-term evolution.

1.4.1 Biological Demand in Hydrothermal Systems

Chapters 2 and 3 focus on the determination of the bulk elemental composition of microorganisms living in hot springs of Yellowstone National Park (YNP). This determination, performed on sediment and microbial mat communities collected at the hot springs, presents a key challenge: minimizing contributions from non-biological material, such as sediment particles, to the measured elemental composition. To this end, two approaches are possible: using microscopy techniques to measure the elemental composition of individual microbial cells, or using purification methods to eliminate non-biological matter in the collected samples prior to analysis by bulk techniques. I pursued the latter approach.

In Chapter 2, I demonstrate the use of a cell-sediment separation method for sediment samples collected in extreme environments, and the suitability of this method for bulk elemental analyses. In Chapter 3, I use this method to determine the bulk elemental composition of a few dozen hydrothermal microbial communities,

i.e., their elemental requirements. I compare and contrast these requirements with the elemental supply of YNP hot springs to find that, surprisingly, microbial needs in major and trace elements in these hydrothermal systems seem to be similar to those of microorganisms living in more moderate settings, in spite of widely varying physico-chemical conditions at YNP.

1.4.2 Occurrence of Hydrothermal Systems on Dwarf Planets

In Chapters 4 through 7, I use numerical models coupling geophysics and geochemistry to determine how hydrothermal systems might arise and co-evolve with their host dwarf planet. The focus is on dwarf planets largely because these worlds have remained relatively unexplored (until the past few months) compared to Mars or icy moons, and because of the opportunity to inform ongoing exploration by spacecraft. However, some results from Chapter 5 and, to some extent, Chapter 6 are applicable to other worlds bearing hydrothermal systems.

In Chapter 4, I seek to determine the occurrence and extent of hydrothermal processes in space and time. As the spatial extent of water-rock interaction hinges on the area of the water-rock interface, I describe a new geophysical model of core fracturing to determine the depth of cracking inside dwarf planet cores, which provides a first-order estimate of the volume of rock that can be aqueously altered. I couple this model to an existing thermal and geophysical evolution code (Desch *et al.*, 2009) to assess temporal aspects, as well as prevalent hydrothermal conditions such as temperature, pressure, and water-to-rock ratios.

I feed these conditions to geochemical models of water-rock interaction in Chapter 5. Assuming starting liquid and rock compositions similar to those thought to have

been accreted by dwarf planets, I use an existing geochemical code (*PHREEQC*; Parkhurst and Appelo, 2013) to determine the composition of solids, solution, and gas resulting from water-rock interactions proceeding to chemical equilibrium. Specific attention is paid to the fate of antifreezes (which favor liquid persistence over geological timescales by depressing their freezing point) and radionuclides (the chief heat source for dwarf planets, which unlike icy moons are not subject to strong tidal heating): are antifreezes chemically produced or consumed? Are radionuclides leached from the rock into the fluid?

How might we constrain outcomes of such geochemical models? Products of water-rock interaction, which presumably take place below the surface of these worlds, cannot be observed directly unless they are somehow delivered to the surface. Possible transport mechanisms are convection within the shell and eruption of subsurface fluids, or cryovolcanism. In Chapter 6, I model prerequisites for explosive cryovolcanism on dwarf planets.

These models, developed before the exploration by spacecraft of the dwarf planet Ceres and of the Pluto system, are proving to be very relevant to these objects in light of the first images returned by the *Dawn* and *New Horizons* missions, respectively (Fig. 2). These images confirm that Ceres, Pluto, and its moon Charon have all been geologically active, and show signs of ongoing activity. In Chapter 7, I apply the models developed in Chapters 4 through 6 to interpret preliminary data returned by *Dawn* at Ceres, and make predictions to be tested by upcoming measurements.

Chapter 2

PROKARYOTIC CELLS SEPARATED FROM SEDIMENTS ARE SUITABLE FOR ELEMENTAL COMPOSITION ANALYSIS

In this chapter, I describe the first step towards determining the biological demand for elements in hydrothermal systems. As stated in Chapter 1, determining the elemental composition of microbial communities can be achieved by removing the sediment elemental contribution from bulk samples, which include both biological and mineral matter. Here, I test a cell-sediment separation method on samples collected in hydrothermal areas, and demonstrate that the method is suitable for follow-up elemental analysis of the isolated biological matter. The method takes advantage of the density contrast between biological matter (which tends to have a density near that of water) and sediment (which is several times denser).

Co-authors Amisha Poret-Peterson, Zarraz Lee, Ariel Anbar, Jim Elser and I published the contents of this chapter in *Limnology & Oceanography: Methods* (Neveu *et al.*, 2014). A summary of the results as presented in the paper is given below, followed by the text of the paper.

The separation method can be applied to determine the composition of prokaryotic cells. The method uses chemical and physical means to extract cells from benthic sediments and mats. Recovery yields were between 5% and 40%, as determined from cell counts. The method conserves cellular element contents to within 30% or better, as assessed by comparing C, N, P, Mg, Al, Ca, Ti, Mn, Fe, Ni, Cu, Zn, and Mo contents in *Escherichia coli*. Contamination by C, N, and P from chemicals used during the procedure was negligible. Na and K were not conserved, being likely

exchanged through the cell membrane as cations during separation. V, Cr, and Co abundances could not be determined due to large (>100%) measurement uncertainties. We applied this method to measure elemental contents in extremophilic communities of Yellowstone National Park hot springs. The method was generally successful at separating cells from sediment, but does not discriminate between cells and detrital biological or noncellular material of similar density. This resulted in Al, Ti, Mn, and Fe contamination, which can be tracked using proxies such as metal:Al ratios. With these caveats, we present the first measurements, to our knowledge, of the elemental abundances of a chemosynthetic community. The communities have C:N ratios typical of aquatic microorganisms, are low in P, and their metal abundances vary between hot springs by orders of magnitude.

2.1 Introduction

Better understanding of the coupling of major biogeochemical cycles requires knowledge of the cellular elemental composition of microbes (e.g. Williams and Fraústo da Silva, 2000; Haraguchi, 2004; Morel, 2008). Examples of connections between trace metals and macronutrient cycling by microbes abound. Nitrogen is cycled using enzymes that contain Fe, Cu, and Mo (Morel and Price, 2003). Inorganic carbon fixation by photosynthesis requires electron transfer intermediates containing Fe (Morel and Price, 2003), and the pigment chlorophyll contains Mg. Reactive radicals resulting from photosynthesis are managed by superoxide dismutase enzymes with Mn, Fe, Ni, Cu, or Zn cofactors (Bowler *et al.*, 1992). Metalloenzymes with a Zn, Co, or Cd metal center assist microbes with inorganic carbon assimilation (Morel and

Price, 2003). Organically bound phosphorus can be made bioavailable by phosphatase enzymes containing Zn, Mg, or Fe (e.g Stec *et al.*, 2000).

Because of the importance of these microbial processes, we are motivated to study major element cycling in situ by measuring the elemental composition of microbial cells extracted directly from their environment. Carbon, macronutrients (e.g., nitrogen and phosphorus), and micronutrients (e.g., trace metals) need to be taken up from the environment by microbes. In Earth's oceans, the availability of metals, P, and N varies with space and time (Falkowski, 1997; Anbar, 2008; Papineau *et al.*, 2009) and is known to influence element use by cells (Morel, 2008; Dupont *et al.*, 2010). However, in extreme environments such as hot springs, the distribution of elements, their use by extremophilic microorganisms, and the influence of extremophiles on element cycling remain largely unexplored. Hot springs at temperatures above 72°C are also environments where primary production is supported by chemosynthetic processes rather than photosynthesis. Chemosynthesis also involves metals as enzyme cofactors, such as Fe and Ni in hydrogen oxidation. Determining the elemental contents of microbes in such settings will likely advance our understanding of modern biogeochemical processes and potentially those in the past as well.

However, in benthic sediments and microbial mats such as those found in hot springs, it is difficult to determine the composition of microbes because of the contributions of mineral grains and particles. It is especially difficult to determine the microbial content of metals such as Fe, Ni, Cu, Zn, and Mo, which are also found in sediment. However, these elements need to be quantified to extend the stoichiometric analysis beyond the standard "Redfield C:N:P ratio" to a broader suite of elements of biological importance (Twining *et al.*, 2011; Nuester *et al.*, 2012). Removing the sediment contribution from elemental analyses of microbial communities, extremophilic

or otherwise, requires either effective isolation of cells from complex mineral matrices (Havig *et al.*, 2011; Steenbergh *et al.*, 2013) or in situ microscopic analyses (Heldal *et al.*, 2003; Steenbergh *et al.*, 2013).

There is a need to verify that such cell separation procedures do not alter cellular elemental composition before analysis. Cell separation methods usually involve chemical (use of detergents and chelating agents) and physical means (stirring or blending and/or sonication) of disrupting microbe- mineral bonds, followed by density gradient centrifugation (Lindahl and Bakken, 1995; Amalfitano and Fazi, 2008; Kallmeyer *et al.*, 2008; Amalfitano *et al.*, 2009; Poté *et al.*, 2010; Morono *et al.*, 2013). Amalfitano and Fazi (2008) compared combinations of chemical and physical separations. They found that the most efficient method of detaching cells from sediment comprised three steps: (1) stirring of the sample slurry in an extraction mixture containing a detergent and a chelating agent, (2) gentle sonication of the resulting suspension, and (3) centrifugation through a cushion of the density gradient medium Nycodenz (Rickwood *et al.*, 1982) to isolate the cells, which have lower density than sediment. Alternative methods to that of Amalfitano and Fazi (2008) involve blending, dispersion by rotary pestle, or shaking with glass beads (e.g. Lindahl and Bakken, 1995); all of which could contaminate the separated cells with trace metals. This trace metal contamination risk from hardware is minimized in the procedure of Amalfitano and Fazi (2008), which can be carried out entirely in acid-washed plasticware.

For all cell separation methods, there is a trade-off between efficiently breaking the strong cell-sediment bonds and preserving cell integrity (Lindahl and Bakken, 1995). Preserving cell integrity is essential to conserve cellular elemental contents. The method of Amalfitano and Fazi (2008) can affect cellular integrity (Amalfitano *et al.*, 2009), which could lead to problems with measurements of cellular elemental

composition. We tested the ability of the method of Amalfitano and Fazi (2008) to produce accurate information about the elemental contents of *Escherichia coli* cells by comparing elemental abundances in cells that had undergone separation to those in cells that had not. We then separated cells from sediments and mats collected in hot springs of Yellowstone National Park (USA) and measured their elemental makeup using Isotope Ratio Mass Spectrometry (IRMS) for C and N, and Inductively-Coupled Plasma Mass Spectrometry (ICP-MS) for the other elements.

2.2 Materials and Procedures

To evaluate the ability of the cell separation method to pre- serve the elemental content of cells, wild-type *Escherichia coli* in LB broth was cultured to late log or early stationary phase, then divided into 1-mL aliquots and kept frozen at -80°C without addition of any cryoprotectant. Freezing and thawing could result in cell damage. However, when observing thawed *E. coli* cells using epifluorescence microscopy for cell counting, we noticed no physical damage (at least at this limited resolution). Furthermore, cells underwent only one freeze-thaw cycle, and care was taken to thaw cells slowly (10°C, 20-40 min). Freezing is necessary for field samples because cell separations cannot be performed in situ, and in some cases, the distance of field sites from laboratory facilities necessitates sample transport; we therefore applied the same procedure to *E. coli*. We measured the abundances of C, N, P, Na, Mg, Al, K, Ca, V, Cr, Fe, Co, Ni, Cu, Zn, and Mo in *E. coli* before and after separation. We did not mix *E. coli* with sterile sediment before separation because no significant cell-sediment bonding would likely occur (Lindahl and Bakken, 1995). Cell separations, cell counts,

and elemental analyses of *E. coli* were performed on a minimum of three but typically four replicates.

2.2.1 Cell-Sediment Separation Procedure

The separation procedure is the combined $C_{1+2} + P_{1+2}(N)$ procedure of Amalfitano and Fazi (2008), followed by washing and drying of separated cells before elemental analysis. Amalfitano and Fazi's $C_{1+2} + P_{1+2}(N)$ separation procedure consists of two steps: (a) physical and chemical detachment of cells from sediment by vortexing and sonication of the samples in a buffer containing a detergent and a chelating agent, and (b) isolation of the cells by centrifugation of the suspension through a gradient of Nycodenz (Rickwood *et al.*, 1982). Throughout the procedure, polypropylene containers and spatulas were used to prevent sample contamination by trace metals from glass or metallic items. These items were acid-washed and autoclaved before use; care was taken to avoid any physical contact between the plasticware and metals from the autoclave. All solutions were sterilized by autoclaving except sodium pyrophosphate, which was filter-sterilized. Although autoclaving is not considered best practice for trace metal work (Price *et al.*, 1989), the trace metal content of all solutions was negligible compared with abundances measured in *E. coli* (Appendix A).

Cell extraction buffer was prepared as follows. To prepare 50 mL buffer, we used 0.05 g of the chelating agent sodium pyrophosphate (0.1% wt./vol. final concentration), 0.25 mL Tween 20 detergent (0.5% vol./vol. final concentration), and 5 mL phosphate-buffered saline (PBS), brought up to 50 mL with 18 MOhm-cm MilliQ water. The 5 mL PBS contained 1.3 M sodium chloride (0.13 M final concentration in the extraction

buffer), 70 mM sodium phosphate dibasic (7 mM final concentration), and 30 mM sodium phosphate monobasic (3 mM final concentration); the pH of PBS was adjusted to 7.4 with a few drops of concentrated hydrochloric acid or sodium hydroxide. Sodium pyrophosphate was purchased from Sigma-Aldrich (Cat. No. 221368), Tween 20 from Bio-Rad (Cat. No. 170-6531), sodium chloride from Fisher Scientific (Cat. No. S271-500), sodium phosphate dibasic from Mallinckrodt (Cat. No. 7914), sodium phosphate monobasic from EMD Millipore (Cat. No. SX0710-1), and Nycodenz from Axis-Shield (Cat. No. 1002424).

The procedure is depicted in Fig. 3A. Aliquots of *E. coli* were gently thawed in a centrifuge (6000 g, 10°C, 20-40 min). The supernatant was removed. Samples were weighed and transferred into 20-mL beakers. A different beaker was used for approximately every 2 g sediment or microbial mat to avoid overflow during vortexing. In each beaker, extraction buffer (5 mL) was added. The resulting suspensions were then stirred on a large capacity stirrer for 30 min at 720 rpm using acid-washed, autoclaved stir rods. Each sample subsequently underwent sonication in an ice-cold bath (Branson Sonifier 450) with the following parameters: 40% output, 35% duty cycle, 2 min, to not lyse the cells. Amalfitano and Fazi (2008) sonicated cell suspensions for only 1 min; however, initial observations using optical and epifluorescence microscopy showed that more cells were detached from sediment particles in suspensions sonicated for 2 min than in those sonicated for 1 min.

Each suspension was gently homogenized and carefully layered on top of 5 mL of Nycodenz in 15-mL centrifuge tubes. The Nycodenz solution was prepared by dissolving 8 g Nycodenz in 10 mL MilliQ water, which yields a density of 1.3 g mL^{-1} (Poté *et al.*, 2010). The density of the Nycodenz solution, which is intermediate between cells and sediment, allows sediment to migrate through Nycodenz while cells

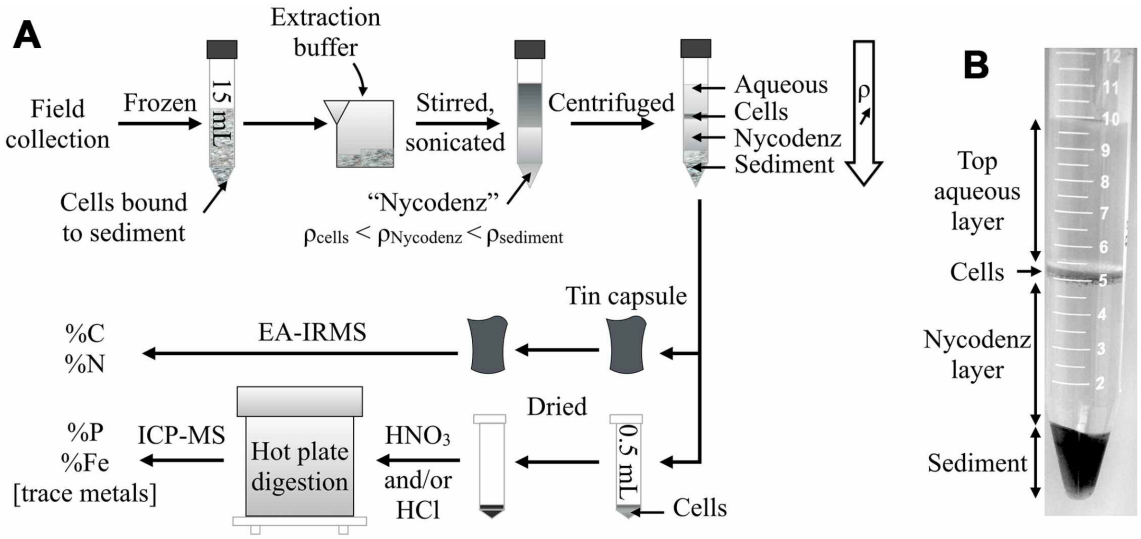

Figure 3: A. Schematic of the cell-sediment separation and preparation for elemental analysis. B. Four phases of a separated sediment sample: top aqueous layer, interface containing cells, Nycodenz layer, and bottom sediment pellet, ideally no longer containing cells

This sample was collected at an outflow of the hot spring in Yellowstone we unofficially named 'Bison Pool'.

remain on top. Each sample was centrifuged at 5000g and 4°C for 30 min using a swing-out rotor. Centrifugation was repeated for an additional 30 min to 1 h until the Nycodenz layer was clear, and distinct phases could be seen. The phases of a separated field sediment sample are shown in Fig. 3B. From bottom to top, these phases are sediment pellet (absent when the procedure is applied to a sediment-free *E. coli* culture); Nycodenz; a thin layer of separated cells (with possible residual detritus of similar density); and the supernatant. The cell layer was pipetted out, transferred into a clean 2-mL tube, and washed three times to remove any Nycodenz or cell extraction buffer, using 0.85% sodium chloride (NaCl) to limit osmotic stress. For each wash, cells were resuspended in 1 mL NaCl solution, then centrifuged (10,000g, 5 min, 4°C), and the supernatant was discarded.

Separated cells, resuspended in a minimal amount (200 to 1000 μL) of 18 MOhm-cm MilliQ water to allow pipetting, were divided into aliquots of 50 μL (IRMS replicates), and 300 μL (ICP-MS replicates) and dried (60°C, overnight) before elemental analysis. Obtaining dry masses of cell fractions was essential to quantify elemental contents in terms of dry cellular mass. *E. coli* cells that did not undergo separation were thawed, washed three times with either 0.85% NaCl or cell extraction buffer (to assess the capacity of these solutions to preserve the cellular makeup), resuspended in a minimal volume (200 to 1000 μL) of 18 MOhm-cm MilliQ water, and dried.

2.2.2 Cell Counting

Cell counting using epifluorescence microscopy helped determine a cell recovery yield. Yields were determined by comparing the amount of cells present before and after centrifugation through Nycodenz. 45-μL aliquots of cell suspensions were removed immediately after the sonication step and again at the end of each NaCl wash. Cells were fixed using 5 μL formaldehyde (37%, final concentration 3.7%) and stored at 4°C until counting. They were stained using 10 μg/mL 4',6- diamidino-2-phenylindole (DAPI), resuspended in 10 mL sterile 18 MOhm-cm MilliQ water, and filtered on a 0.22-μm poly-carbonate membrane for enumeration via epifluorescence microscopy at 1000-fold magnification.

2.2.3 Elemental Analysis

2.2.3.1 Carbon and Nitrogen

We used elemental analysis-isotope ratio mass spectrometry (EA-IRMS) to determine the elemental and isotopic abundances of C and N. A Costech EA-IRMS (Costech International S.p.a.) was used to analyze all samples, calibration standards, and blanks. Before combustion, samples were loaded into 5 $\times$ 9 mm tin capsules (Costech). Freshly separated cells were resuspended in as little 18 MOhm-cm MilliQ water as possible (200 to 1000 μL) and pipetted into tin capsules in 50 μL aliquots, then dried overnight at 60°C. Serial pipetting-drying cycles were required for dilute suspensions; cells awaiting drying were stored at 4°C.

A calibration curve for C and N contents was built using a tomato leaf standard (0.2, 0.5, 1.0, 2.0, 5.0, and 7.0 mg). Glycine standards (0.7 mg) of known light, medium, and heavy C and N isotopic composition were analyzed between samples to determine the accuracy of isotopic determinations. These in-house standards were characterized using the following standards: USGS 40, USGS 41, IAEA NBS 18, and IAEA NBS 19.

2.2.3.2 Phosphorus and Trace Elements

P, Na, Mg, Al, K, Ca, V, Cr, Fe, Co, Ni, Cu, Zn, and Mo abundances were determined by Inductively-Coupled Plasma Mass Spectrometry (ICP-MS). All samples, appropriate multi-element calibration standards, and blanks were analyzed on an X Series quadrupole ICP-MS (Thermo Scientific). Sample preparation was carried out in

a Class-10 clean laboratory, using 1× distilled nitric and hydrochloric acids. Dilutions were made with 18 MOhm-cm water.

Cells dried in microcentrifuge tubes were transferred to acid-cleaned (using concentrated nitric acid followed by concentrated hydrochloric acid) Teflon vessels and digested overnight in 3 mL concentrated nitric acid on a hot plate at 100 to 150°C. The vessels were then uncapped and heated until sample volume decreased to approximately 0.5 mL. The samples were finally diluted to 3.5 mL (the minimum volume required by the ICP-MS to measure the 14 elements specified) with 0.32 M nitric acid in 15 mL acid-cleaned centrifuge tubes. The final dilution volume was weighed to obtain a dilution factor between initial dry mass and mass of solution analyzed.

A calibration curve was built using a phosphorus-enriched black shale standard solution of known elemental composition (characterized using the certified reference material USGS Devonian black shale SDO-1), serially diluted (1:15, 1:35, 1:150, 1:1000, 1:7500, 1:25000) with nitric acid (0.32 M). This standard was chosen because its elemental composition reasonably matched that of (sometimes widely varying) Yellowstone sediment samples and *E. coli*. The standard was not digested along with the samples to test for element recoveries; however, it is routinely run in parallel with samples, with generally excellent recovery, accuracy, and reproducibility. We performed sample-free digestions to check for contamination during digestion, and subtracted the average of the measured values on these digestions from the measured value of each *E. coli* replicate.

2.3 Assessment

2.3.1 Cell Recovery Yields

The yield for *E. coli* aliquots was consistently around 95%. Therefore, only a small portion of cells was either lysed during separation or lost to the aqueous or Nycodenz phases. Amounts of cells washed away in the three washing steps were about 1%, 0.1%, and 0.01%, respectively.

2.3.2 Preservation of Elemental Content

The elemental abundances of unseparated and separated *E. coli* cells are shown in Appendix A, and the relative element enrichments or depletions (i.e., [abundance in separated cells/abundance in non-separated cells] – 1) in *E. coli* due to cell separation are shown in Fig. 4. The measured elemental content of unseparated *E. coli* cells did not depend on whether these cells were washed with 0.85% NaCl or with cell extraction buffer (Appendix A).

C and N contents were systematically depleted by about 10% in separated cells, whereas two elements present as cations in the cells (Na and K, not plotted) were severely depleted in some separated replicates but highly enriched in others. P and trace metal (except V, Cr, and Co) contents were unchanged within 30% or less. V, Cr, and Co contents appeared to be conserved through the separation just as well as Ni, Cu, Zn, or Mo but the precision of our ICP-MS measurements did not allow reliable determination of their abundance (Appendix A). While V, Cr, and Co were

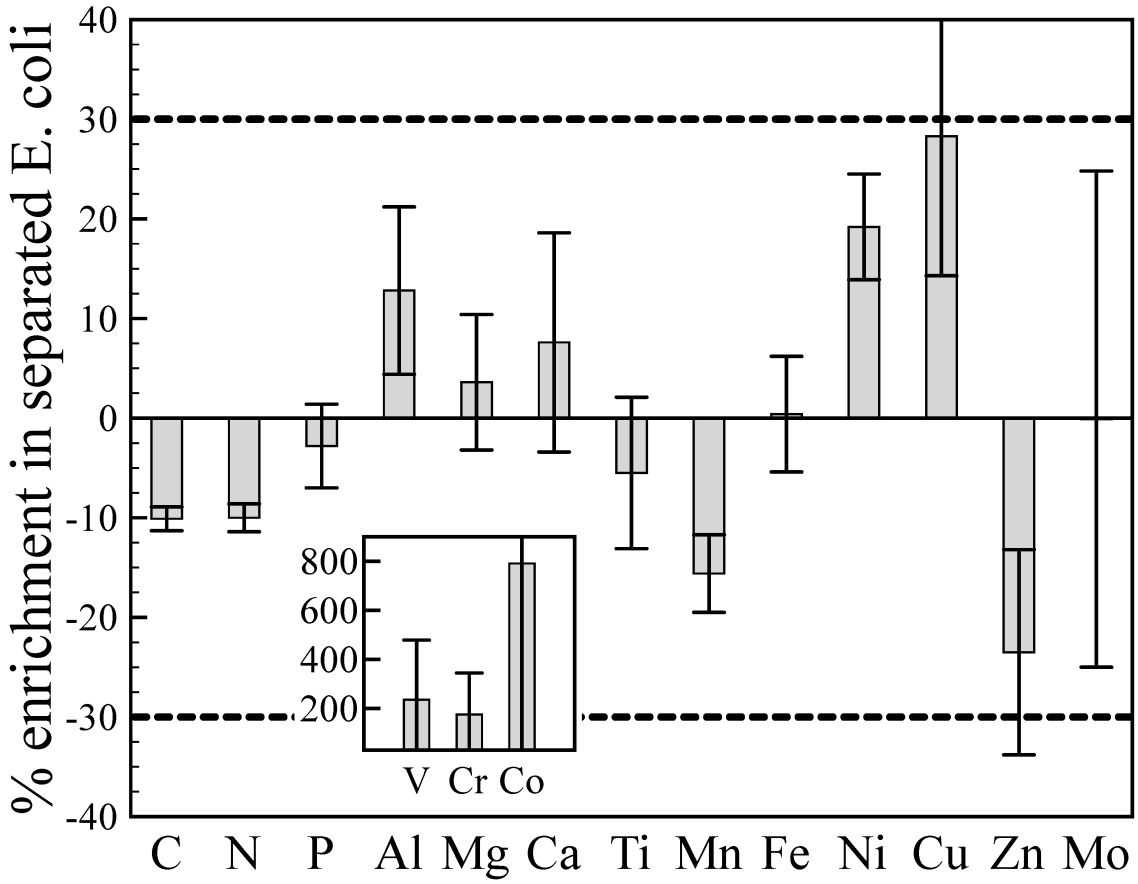

Figure 4: Relative enrichment or depletion of elements in cultured wild-type *E. coli* that underwent separation, compared with the same culture without separation

Error bars show one standard deviation over four replicates (i.e., 2 × the standard error on the mean over four replicates, approximately a 95% confidence limit); standard deviations were propagated through the calculation. The dashed lines at +30% and -30% bracket the range of relative enrichments or depletions.

present at quantifiable levels ($> 10\times$ blank level), the spread between replicates was high.

We note that *E. coli* grown in LB has a high metal content, up to an order of magnitude more than *E. coli* grown in minimal medium (Outten and O'Halloran, 2001). This could mask small variations in metal content due to potential contamination, which may thus have been underestimated. Further investigations may wish to

repeat this experiment with *E. coli* grown in minimal medium to assess potential contamination on a lower scale.

2.3.2.1 Gain of Elements (Contamination)

Artificially high elemental abundances could have resulted if the cells were contaminated by autoclaved solutions used during separation (Steenbergh *et al.*, 2013), or during acid digestion. P- and Na-rich PBS and sodium pyrophosphate, C-rich Tween 20, and C- and N-rich Nycodenz are used in the separation procedure, raising the possibility of contamination by these elements. However, we observed a modest depletion in C and N after separation (Fig. 4), whereas P abundance remained unchanged within the limits of analytical uncertainties. In addition, the C and N isotopic compositions of *E. coli* did not change during separation ($\delta^{13}C_{VPDB}$ = -21.8 ± 0.5‰, $\delta^{15}N_{AIR}$ = 4.0 ± 0.4‰), and were very different from those of Nycodenz ($\delta^{13}C_{VPDB}$ = -30.3 ± 0.7‰, $\delta^{15}N_{AIR}$ = 0.0 ± 0.4‰), further supporting the inference that cell contamination by Nycodenz or Tween 20 was negligible. The isotope measurement errors were determined by measuring the isotopic content of glycine standards of known isotopic composition. Constant P abundances also suggest no contamination from the cell extraction buffer.

Furthermore, the Nycodenz molecule contains 3 atoms of iodine (I), which makes up 46% of its mass. Steenbergh *et al.* (2013) noted that measuring I in separated cells can help estimate Nycodenz contamination, and thus its contribution to the measured C and N. Microorganisms contain 1 to 100 ppm I (Bowen, 1979). Up to 1.4% I by mass (roughly 3% Nycodenz) was measured in the field samples, equivalent to 0.83% C and 0.15% N enrichments from Nycodenz. This falls well within measurement

uncertainties (1.6% for C and 0.6% for N). Since Nycodenz contributes the most C and N of the solutions used in the procedure, we infer that contributions of other chemicals were negligible as well.

The trace element contents of the solutions used in the procedure are shown in Appendix A. Most elemental signals were too noisy (below ten times the instrumental uncertainty on the analytical blank value) to be accurately quantified. The only signals clearly above the noise level were for one isotope of Cu, ^{63}Cu (not confirmed in noisy ^{65}Cu measurements below or around quantification limit) and for K, which was not conserved in *E. coli*. We therefore infer that trace metal contamination due to autoclaving of the solutions used in the cell separation procedure is negligible.

Metal contamination could also occur during sample digestion. We carried out sample-free digestions for each ICP-MS analysis and measured the trace element signal of these procedural blanks. This signal is compared with that of *E. coli* digestions in Table 1, where it can be seen that contamination at this step was negligible.

2.3.2.2 Loss of Elements

Loss of elements from the cells can occur either if cell integrity is compromised by freeze-thaw, osmotic, or mechanical shocks, or if elements can leave through the cell membrane. Indeed, the cell separation procedure of Amalfitano and Fazi (2008) used in this study was found to result in membrane damage for 7 to 30% of cells separated from sediment (Amalfitano *et al.*, 2009).

Separated *E. coli* had C and N abundances that were systematically lowered by about 10%. This depletion might reflect loss of some molecular pools in the cells, where compounds such as sugars, organic acids, nitrates, or amino acids are stored

Table 1: Comparison between the trace element signal from sample-free digestions and from separated *E. coli*, in part per billion per mass of solution analyzed (diluted digestion with 2% HNO_3)

Element	Sample-free digestion				Example-separated
(ppb)	16 Dec. 2011	21 Apr. 2012	4 June 2012	20 Nov. 2012	*E. coli*
^{23}Na	95 ± 25	-0.3 ± 1.1	-20.3 ± 9.5	14.9 ± 0.9	$(2.6 \pm 0.009) \times 10^7$
^{24}Mg	0.4 ± 0.2	0.5 ± 0.1	0.6 ± 0.2	1.31 ± 0.04	$(9.4 \pm 0.04) \times 10^5$
^{27}Al	0.3 ± 1.3	1.9 ± 0.2	7.6 ± 5.1	2.23 ± 0.03	$(6.4 \pm 0.3) \times 10^3$
^{31}P	68 ± 14	41.6 ± 0.9	118 ± 4	42.8 ± 3.6	$(1.9 \pm 0.02) \times 10^7$
^{39}K	5.3 ± 5.8	-7.7 ± 11.2	-38 ± 22	-7.8 ± 1.0	$(2.5 \pm 0.02) \times 10^6$
^{44}Ca	119 ± 58	-6.2 ± 5.8	-63 ± 10	21 ± 11	$(2.0 \pm 0.2) \times 10^5$
^{48}Ti	N/A	0.40 ± 0.06	3.5 ± 0.4	0.05 ± 0.04	$(1.4 \pm 0.2) \times 10^3$
^{51}V	0.004 ± 0.012	0.006 ± 0.024	0.076 ± 0.024	-0.098 ± 0.014	43.3 ± 8.3
^{52}Cr	0.042 ± 0.038	0.075 ± 0.034	0.42 ± 0.03	0.22 ± 0.06	8.3 ± 9.1
^{55}Mn-H_2	N/A	N/A	N/A	0.032 ± 0.008	$(5.1 \pm 0.2) \times 10^3$
^{55}Mn	N/A	N/A	N/A	0.024 ± 0.034	$(4.5 \pm 0.02) \times 10^3$
^{54}Fe	1.1 ± 0.7	4.7 ± 1.6	137 ± 4	2.1 ± 0.6	$(2.1 \pm 0.2) \times 10^5$
^{56}Fe	0.25 ± 0.14	2.0 ± 0.2	0.25 ± 0.79	1.4 ± 0.2	$(2.1 \pm 0.04) \times 10^5$
^{57}Fe	0.32 ± 0.24	1.9 ± 1.1	-26 ± 4	1.6 ± 1.3	$(2.1 \pm 0.2) \times 10^5$
^{59}Co	0.10 ± 0.02	-0.01 ± 0.02	-0.03 ± 0.01	0.000 ± 0.002	$(2.6 \pm 0.04) \times 10^3$
^{58}Ni	0.27 ± 0.08	0.03 ± 0.19	-0.12 ± 0.01	0.007 ± 0.018	$(2.7 \pm 0.07) \times 10^3$
^{60}Ni	0.7 ± 0.2	-0.8 ± 0.2	-0.85 ± 0.05	0.007 ± 0.016	$(3.2 \pm 0.04) \times 10^3$
^{63}Cu	-0.08 ± 0.02	0.63 ± 0.03	2.2 ± 0.7	-0.98 ± 0.04	$(5.3 \pm 0.09) \times 10^3$
^{65}Cu	0.04 ± 0.02	0.37 ± 0.05	0.9 ± 0.7	-0.59 ± 0.04	$(5.0 \pm 0.04) \times 10^3$
^{66}Zn	-0.18 ± 0.12	0.38 ± 0.04	0.9 ± 0.3	0.4 ± 0.1	$(4.6 \pm 0.05) \times 10^4$
^{68}Zn	-0.003 ± 0.044	N/A	0.79 ± 0.39	0.35 ± 0.06	$(4.2 \pm 0.07) \times 10^4$
^{95}Mo	0.11 ± 0.01	-0.12 ± 0.02	0.07 ± 0.01	0.37 ± 0.01	$(4.8 \pm 0.09) \times 10^3$

These values were automatically produced by the mass spectrometer software, which first subtracted the signal from an analytical blank (nondigested, trace metal-free 2% HNO_3 solution) from the physical mass spectrometer measurement, then averaged over three measurements of the same sample. The uncertainty represents the standard deviation between these three measurements of a given sample.

for future use after synthesis or uptake from the environment. Britten and McClure (1962) showed that *E. coli* amino acid pools can be emptied following freeze-thaw or osmotic shocks, and that the C and N contents of these pools can account for 10% of organismal abundances. Regardless of the source of the depletion, the consistent loss of C and N suggests that a correction factor of $\sim$10% should be used to adjust C and N contents of samples analyzed with this procedure.

Epstein and Schultz (1965) and Rhoads and Epstein (1978) showed that osmotic shock during cold cell washing steps deplete the K content of *E. coli*, because intracellular K concentrations depend on osmolarity, and to a lesser extent, temperature of the external medium. This can explain the depletion in *E. coli* cellular K that we measured after some separations. When cell separation caused a K enrichment in *E. coli* cells, we suspect a contamination by trace K^+ from the extraction buffer: we measured 10-fold differences in K abundances in solutions between the buffer and supernatant phases, where most buffer should end up. Finally, the mismatch in *E. coli* Na is not surprising, given its ubiquity in the buffer and wash solution and the fact that Na^+ can pass through the cell membrane.

2.3.3 Application to Field Samples

2.3.3.1 Cell-Sediment Separation

Due to ongoing research projects at hot springs within Yellowstone National Park (Cox *et al.*, 2011; Havig *et al.*, 2011), we sought to determine cellular elemental ratios in samples from the area's diverse hot spring ecosystems. Field sediment samples were collected in July and August 2009 at hot springs with temperatures ranging from 20°C to boiling (∼93°C). The pH of the springs ranged from 1 to 9. Four replicate 15-mL tubes were filled with sediment to 5 mL. Sediment samples without a cryoprotectant added were kept on ice in the field and then frozen at -20°C until transport back to Arizona State University, where samples were transferred to a -80°C freezer.

Cells were separated using the same method as for the *E. coli* samples. Visual examination of the freshly separated samples confirmed the applicability of the cell-

sediment separation method for hot spring sediment samples (Fig. 3B). Four phases – aqueous, cell, Nycodenz, and sediment – could be seen after centrifugation of all samples, although the cell phase was at times difficult to distinguish in samples with low bulk biomass content.

For each cell separation of field-collected samples, we also separated a 1-mL *E. coli* aliquot, not mixed with any sediment, from the same culture as that used in the above element conservation studies. This extra *E. coli* separation was an independent check on the integrity of the method, allowing us to track anomalous element variations or recovery yields.

2.3.3.2 Cell Recovery Yields

Cell recovery yields were estimated for a few samples using the same method as for *E. coli* cells. Cell counting also provided an opportunity to examine the isolated and resuspended cell fraction to check for the presence of detrital and sedimentary particles. Cell counts for the field-collected samples indicated recovery yields between 5 and 40% (Table 2). These rates, lower than the 95% *E. coli* recovery rate, likely indicate that a significant fraction of the cells was still bound to sediment. Different sediment characteristics, such as humic content and grain size, may affect the cell separation efficiency. Moreover, the 0.85% NaCl wash solution may not always closely match the osmolarity of field samples given their considerable compositional diversity; the resulting osmotic stress may have lysed some cells. However, the reported yield percentages are in line with literature data (Lindahl and Bakken, 1995; Kallmeyer *et al.*, 2008; Morono *et al.*, 2013).

Table 2: Cell recovery yields for several separated samples collected at hot springs of Yellowstone National Park, as well as cultured *E. coli*

Sample	T_{spring} (°C)	pH (spring)	Site description	Cell concentration in unseparated sample (per g sediment)	Cell concentration in separated sample (per g sediment separated)	Cell recovery yield (±SD)
'Bison Pool'	66.2	8.1	Outflow of siliceous sinter spring, phototrophic site	$(3.6 \pm 2.8)10^8$	$(9.8 \pm 6.0)10^7$	28 ± 27%
'Green Cheese'	57.4	6.1	Phototrophic site	$(2.9 \pm 1.2)10^8$	$(1.5 \pm 0.1)10^7$	5 ± 2%
'Tinkerbell'	61.4	4.7	Red, turbid, Al-rich spring, chemotrophic site	$(7.5 \pm 2.4)10^8$	$(2.8 \pm 0.9)10^7$	37 ± 16%
'Mr. Clean'	76.4	6.1	Black, turbid spring, chemotrophic site	$(3.7 \pm 1.3)10^8$	$(2.8 \pm 1.2)10^7$	8 ± 4%
E. coli	N/A	N/A	Cell culture	$(2.4 \pm 0.03)10^{10}$[a]	$(2.2 \pm 0.03)10^{10}$[b]	95 ± 2%

Uncertainties are one standard deviation over three replicates and were propagated for the recovery yields. Note that the names given to sampling sites are unofficial and correspond only to our own sampling program. All samples were frozen following sampling and thawed before separation. [a] Sum of the numbers of *E. coli* cells in all four separation phases and all three washes for 1 g *E. coli* culture separated. [b] Number of *E. coli* cells in cell layer only (Fig. 3B) for 1 g *E. coli* culture separated.

2.3.3.3 Elemental Composition of Cells Separated from Sediment

When the separated cell phase was too small for quantitative analysis by both IRMS and ICP-MS, determination of C and N content by IRMS of three to four replicates was given priority, but we still kept one replicate for ICP-MS analysis. This was the case for seven Yellowstone samples out of the eleven separated.

Sample preparation for elemental analysis was carried out as described previously for *E. coli*. Samples for ICP-MS analysis were considered digested if the solution was clear. Turbid solutions were digested again by repeating the addition of 3 mL nitric acid and heating overnight (usually 2 repeats). If turbidity was still observed, aqua regia (1 mL of concentrated nitric acid and 3 mL of concentrated hydrochloric

acid) was added and samples heated overnight for up to 10 repeats, until the turbidity disappeared. Rarely, samples contained particles that resisted digestion. These particles, considered residual sediment, were weighed and discarded; their mass was subtracted from those of the samples to calculate final element concentrations but was usually negligible.

Exemplary results are presented in Figs. 5 and 6 and Appendix A, in which all elemental abundances are reported as a percentage or part-per-million (ppm) of dry mass. The C:N:P relationships for four communities are shown in Fig. 5. C and N abundances were corrected to account for the 10% loss measured in *E. coli*. The hot spring photosynthetic communities sampled had C:N:P ratios in the range normally reported for microorganisms (see Sterner and Elser (2002) for a review). The chemosynthetic community sampled had C:N:P molar ratios of 850:109:1. Thus, its C:N ratio of 7.8 is similar to that measured by Redfield (1958) for marine phytoplankton (C:N = 106:16 = 6.6). To our knowledge, these data constitute the first measurement of the C:N:P ratios of a hot spring chemosynthetic community.

The abundances of metals in Yellowstone cells collected at a dozen sites are shown in Fig. 6. Most metal abundances (Mg, Al, Ca, Ti, Mn, Fe, Cu, and Mo) varied from site to site by orders of magnitude whereas others (Ni and Zn) were similar across all the sites. Al, Ca, and Fe tended to be the most abundant metals. The Al content of cells should be on the order of 1 ppm (Bowen, 1979; Bruland *et al.*, 1991) but was measured at 0.1 to 1% in the samples. Such artificially high abundances can result from non-biomass sediment matter (e.g., particles with similar densities to cells) remaining in the cell fraction. In the bulk sediment, the amount of Al was 1 to 5% of the dry mass, ten times higher than in the separated cell fraction. If 100% of

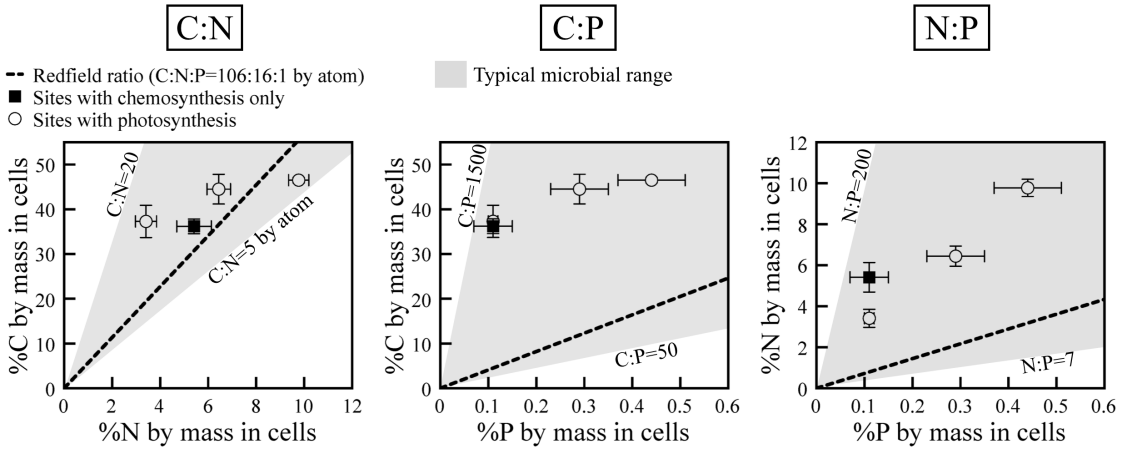

Figure 5: C:N, C:P, and N:P ratios of cells separated from sediment collected at photosynthetic- and chemosynthetic-dominated Yellowstone hot springs

Error bars show one standard deviation uncertainties determined from both instrumental uncertainties by co-measurement of standards with the samples, and from one standard deviation over a minimum of three replicates. C and N abundances were corrected for a 10% loss during cell-sediment separation. Elemental abundances are reported as percentages of dry mass.

the Al measured in the cell fraction was sediment, then sediment comprised 10% of the dry mass of separated sample analyzed, the rest being cells. This 10% mineral contribution is roughly represented by the segmented line in Fig. 6, calculated as the geometric average over all field samples of the sediment contribution, assuming sediment makes up 10% of the dry mass of separated sample analyzed. Because sediment abundances vary significantly between field samples, this line should only be taken as a guide to the eye. As shown on Fig. 4, sediment accounts for most of the measured Ti and Mn in the separated samples, and part of the measured Mg, Ca, and Fe. However, sediment contribution is negligible for C, N, P, Ni, Cu, Zn, and Mo. For all bioessential metals (Mg, Ca, Mn, Fe, Ni, Cu, Zn, and Mo), the metal:Al ratio is several-fold higher in separated samples compared with bulk sediment; whereas the

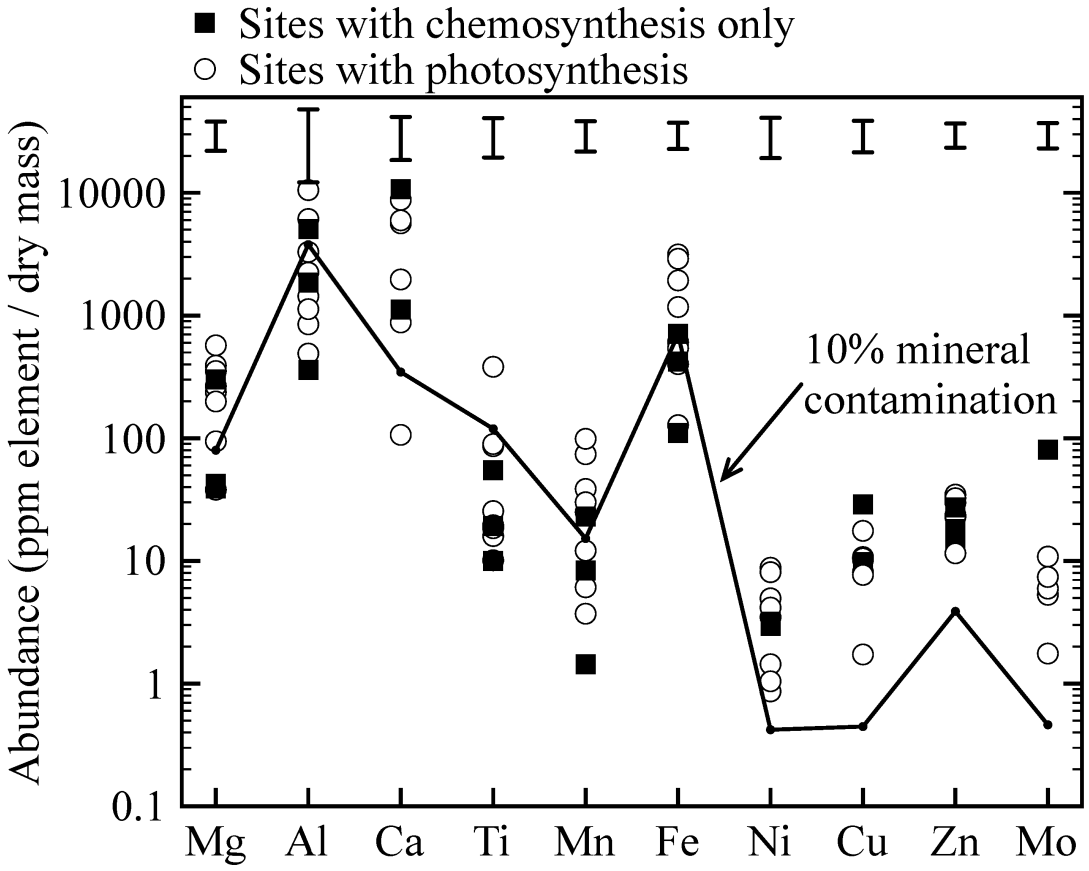

Figure 6: Metal abundances in cells extracted from sediment samples collected at a dozen photosynthesis- and chemosynthesis-dominated Yellowstone hot springs

Elemental abundances are reported as ppm of dry mass. To avoid clutter, indicative error bars show typical one standard deviation uncertainties for this sample set, determined from both instrumental uncertainty by co-measurement of a standard with the samples, and from one standard deviation over at least three replicates. If not enough replicates were available, uncertainties were determined from one standard deviation over at least four replicates of *E. coli* separated and prepared along with the samples. As can be seen in Appendix A, the variability between replicates for *E. coli* and field samples is comparable and tends to scale with abundance. Therefore, the error bars provide an indicative estimate of the variability between replicates anywhere on the y-axis. The segmented line represents the mineral contribution to elemental abundances if the samples analyzed consist of 10% sediment and 90% cells, as estimated from the Al content measured in separated samples compared to that measured in bulk sediment (see text for details).

Ti:Al is several-fold lower. We take this to indicate removal of at least part of the sediment contribution to measured elemental abundances in separated samples.

2.4 Discussion

These data show that the cell separation method we applied is successful at separating microbial cells from hot spring sediments, and based on the *E. coli* assessments, promising for retaining composition across a broad suite of biologically important elements.

The cell recovery yield was low for some field sites. Because our original samples were relatively large, these recovery yields were satisfactory to obtain sufficient material to determine an elemental composition profile of the sediment community. However, some microorganisms in a given community might be more easily separated than others from the sediment matrix; therefore there is likely to be further heterogeneity in elemental composition that this method cannot resolve. Such data can only be obtained by methods such as single-cell analyses via X-ray fluorescence (Heldal *et al.*, 2003; Steenbergh *et al.*, 2013).

This technique cannot separate detrital material (biogenic or otherwise) with a density similar to cell material, but a different element stoichiometry, from intact cells. In some samples, detrital and sedimentary particles were observed along with cells even after separation; however, the amount of detritus was much smaller compared with unseparated samples. Another point of uncertainty arises from possible cell damage due to freezing and thawing of the samples before separation. We minimized this factor by freezing the samples only once, in the field, since separations cannot be performed there; we also thawed the samples gently.

Cellular C and N contents can be determined but appear to require correction of measured abundances for a 10% depletion during separation. Abundances of P, Mg, Al, Ca, Ti, Mn, Fe, Ni, Cu, Zn, and Mo were conserved during separation and could be determined by ICP-MS with an accuracy of 30% (1 SD) or better. Whereas V, Cr, and Co contents are likely conserved as well during separation, their cellular abundances were too low in our samples to obtain an accurate determination by ICP-MS.

Trace element abundances in field-collected samples show that there remains significant sediment contamination for elements enriched in sediments and depleted in cells, such as Al, Ti, Mn, and Fe, after the separation procedure (Fig. 4). Provided that the mineralogy of the sediment samples is accurately known, it may be possible to apply an assumed correction factor for sedimentary contribution, for example by using Al or Ti as a lithogenic tracer (Frew *et al.*, 2006). We attempted to use Al, assumed nonbiological in origin, to estimate the extent of mineral contamination of purified cells. Aluminum abundances by mass range between 1 ppm and 0.1% in microorganisms, but between 0.9% and 30% in rocks, soil, and sediment (Bowen, 1979; Bruland *et al.*, 1991). *E. coli*, not mixed with sediment, had an average Al content of 5 $\pm$ 2.5 ppm, both with and without separation. (Uncertainties for both *E. coli* and field samples are 1 SD). These amounts are consistent with Al trapped in the cell membrane of *E. coli*, as measured by Coughlin *et al.* (1983). Al could also have been-picked up in minute amounts during autoclaving of the LB solution, although Al is not part of LB medium itself. Al was present in sample-free digestions at levels of about 0.1% of that measured in *E. coli*, which makes the possibility of contamination during digestion unlikely. In half of the field samples, Al abundances were above 0.1%, reaching up to 1 $\pm$ 0.5%. The bulk field sediment samples contained 1 to 5% Al. Therefore, assuming 100% of the Al in separated cell fractions is from

sediment, the separated cell fractions contained about 10% (up to 20%) sediment. However, the widely varying mineralogy of Yellowstone National Park hot springs complicates the determination of corrections based on metal:Al ratios in sediment and cells. We consider Al a worst-case contamination proxy, because Al^{3+} ions are more easily mobilized than other metal ions by ligands, such as the pyrophosphate used in the procedure (Williams, 1996).

Another useful criterion is to reject data for samples or elements for which the metal:Al ratios closely mimic sedimentary ratios. Cu, Zn, Mo, and (to a lesser extent) Ni are systematically much higher than the sediment level (even if sediment constituted up to 50% of the separated fraction). For these metals, analyses can be interpreted relatively unambiguously in terms of cellular content, provided that supporting data (such as high Cu:Al, Zn:Al, and Mo:Al compared with sediment) are reported.

For the purposes of determining the C:N:P stoichiometry of samples, rejection of separated samples with a C content less than typical for microbes (35% to 50% Sterner and Elser, 2002) should suffice. This assumes that carbonates are not a major component of the sediment sample; if they are, a carbonate removal step before separation can be added (Kallmeyer *et al.*, 2008). In practice, detrital biological material with a C:N:P stoichiometry different from that of the cells but with a similar density could also bias the measured C:N:P ratios of cells; this is a fundamental limitation of this method. Thus, with further refinement, this cell separation method enables the determination of elemental contents, in mass per dry cell mass, of C, N, P, and key trace biological elements in sediment communities. This procedure is complementary to laborious electron microscopy methods that investigate the elemental composition of single cells (Heldal *et al.*, 2003; Steenbergh *et al.*, 2013). However, using both approaches would allow comparison of element distributions

across broad components of a microbial community with those of the individual cells comprising the biomass.

This method will help quantify the multi-element stoichiometric envelope within which microbes operate (Sterner and Elser, 2002; Ho *et al.*, 2003; Twining *et al.*, 2011; Cameron *et al.*, 2012; Nuester *et al.*, 2012). It will also allow comparisons of microbial elemental compositions with those of their environment to determine their mutual influence (Havig *et al.*, 2011).

2.5 Comments and Recommendations

Overall, we suggest that this method for separating microbial cells from sediment and analyzing their elemental contents at the community level should be applicable to samples from a wide variety of environments, such as soils, soil crusts, or lacustrine or riverbed sediments. Because high temperatures and pH extremes of hot springs result in low biomass of microbial cells, the abiotic contents of key elements can be unusually high, increasing the risk of elemental contamination of cells during separation. The possibility of contamination is likely lower for samples collected in milder conditions. This method should also be applicable for water samples containing high concentrations of suspended sediments, provided that enough sample is collected and filtered to obtain sufficient biomass for elemental analyses. Based on our studies, here is a set of recommendations for future applications:

1. Energy parameters for the sonication step should be considered as approximate values. As Lindahl and Bakken (1995) pointed out, the sonicator output depends on the age of the electromechanical converter, due to changes in its crystal structure.

2. Precise measurement of cellular dry masses is key to the normalization of elemental abundances to mass and eventual determination of elemental ratios. Mass spectrometers measure the elemental masses in a sample more precisely than most balances measure dry masses of a few milligrams. Thus, we recommend to use a balance of microgram precision to measure the dry mass of recovered cell phases.
3. For future analyses of samples from a specific location, standards used to determine the ICP-MS calibration curve and digestion recovery should be chosen as close to sample composition as possible to yield measurements as accurate as possible.
4. As a coarse means of screening out contamination, we suggest discarding samples of C content too low to be biological (lower limit of about 35 to 40% Sterner and Elser, 2002). However, even minute amounts of sediment can significantly alter the metal content of the recovered cell fraction. Therefore, the use of complementary, more precise contamination indicators is advised. We recommend developing a correction factor for metal abundances based on lithogenic tracers such as Al or Ti (Frew *et al.*, 2006) if the mineralogy of the samples is relatively uniform. Reporting of metal:Al or metal:Ti ratios is also advised to assess the reliability of a measurement.
5. Finally, we recommend that follow-up work focuses on determining the extent of the selective biases due to over-representation of microorganisms that are more easily separated from sediment grains relative to those that contribute the most to the measured community composition. Energy-dispersive X-ray spectroscopy of single cells that remain in the sediment fraction may help (Heldal *et al.*, 2003; Steenbergh *et al.*, 2013).

Chapter 3

ORDINARY STOICHIOMETRY OF EXTRAORDINARY MICROORGANISMS

The results presented in the previous chapter provided a useful means of determining the elemental composition of microorganisms living in hydrothermal settings. In this chapter, I make extensive use of this method to determine the elemental composition (biological demand) of microbial communities collected at diverse hydrothermal sites. I relate the measured microbial compositions to those supplied by the hydrothermal environments, and characterize biological elemental patterns to inform the search for life in extraterrestrial settings.

This chapter was published as a paper in *Geobiology* with co-authors Amisha Poret-Peterson, Ariel Anbar, and Jim Elser (Neveu *et al.*, 2015c). The text of this paper is provided below.

All life on Earth seems to be made of the same chemical elements in relatively conserved proportions (stoichiometry). Whether this stoichiometry is conserved in settings that differ radically in physicochemical conditions (extreme environments) from those commonly encountered elsewhere on the planet provides insight into possible stoichiometries for putative life beyond Earth. Here, we report measurements of elemental stoichiometry for extremophile microbes from hot springs of Yellowstone National Park (YNP). Phototrophic and chemotrophic microbes were collected in locations spanning large ranges of temperature (24°C to boiling), pH (1.6–9.6), redox (0.1–7.2 mg L^{-1} dissolved oxygen), and nutrient concentrations (0.01–0.25 mg L^{-1} NO_2^- , 0.7–12.9 mg L^{-1} NO_3 , 0.01–42 mg L^{-1} NH_4^+, 0.003–1.1 mg L^{-1} P mostly as phosphate). Despite these extreme conditions, the microbial cells sampled had a major

and trace element stoichiometry within the ranges commonly encountered for microbes living in the more moderate environments of lakes and surface oceans. The cells did have somewhat high C:P and N:P ratios that are consistent with phosphorus (P) limitation. Furthermore, chemotrophs and phototrophs had similar compositions with the exception of Mo content, which was enriched in cells derived from chemotrophic sites. Thus, despite the extraordinary physicochemical and biological diversity of YNP environments, life in these settings, in a stoichiometric sense, remains much the same as we know it elsewhere.

3.1 Introduction

Living organisms all rely on a common core biochemistry that depends on nucleic and amino acid polymers, lipids, and carbohydrates (Fraústo da Silva and Williams, 2001). This results in an organismal elemental composition largely centered around the proportions of the major elements carbon, nitrogen, and phosphorus that make up these macromolecules in their normal range of allocation (Sterner and Elser, 2002). In addition, many metabolic functions (including those that are processes in major element cycles) are mediated by metalloenzymes whose active sites feature one or several transition metal ions or clusters (e.g Sunda, 1989; Morel and Price, 2003). Thus, these metals are present in low and variable amounts in cells (Fraústo da Silva and Williams, 2001). Both major and trace elements are available in the environment in proportions that often differ considerably from those in cells (Hecky *et al.*, 1993; Morel and Price, 2003; Novoselov *et al.*, 2013). A notable exception is the open ocean, where carbon, nitrogen, and phosphorus are present both in plankton and as solutes in relatively fixed proportions of C:N:P = 106:16:1 (molar), the so-called Redfield

ratio (Redfield, 1934, 1958, 1963; Sterner and Elser, 2002). Although deviations from the Redfield ratio have been reported (e.g. Redfield, 1958; Weber and Deutsch, 2010; Martiny *et al.*, 2013; Frigstad *et al.*, 2014), the broad concordance of C:N:P compositions of organisms with environmental resources highlights the fundamental interplay between life and its environment on a planetary scale.

However, because the availability of chemical elements varies with time and space, one would expect to observe some degree of variation in the elemental makeup of organisms as well, including that resulting from long-term evolutionary adaptation to the supplies of key chemical elements (Sunda, 1989; Zimmerman *et al.*, 2014). Indeed, phylogenomic analyses of protein structures reveal that biological utilization of transition metals likely varied with the availability of metals through the history of life on Earth (Quigg *et al.*, 2003; Zerkle *et al.*, 2005; Dupont *et al.*, 2010). For example, the presumed increased availability of Zn and decreased availability of Fe in Earth's oceans over time, due to a change in ocean chemistry from anoxic in the Archean and sulfidic in the Proterozoic (though perhaps only intermittently in continental margin settings; Poulton and Canfield, 2011) to modern oxic conditions, seems to have resulted in greater use of Zn in enzymes, reflecting the evolution of eukaryotic cells (Fraústo da Silva and Williams, 2001; de Baar and La Roche, 2003; Saito *et al.*, 2003), and in use of Fe in decreased amounts in the photosystem of eukaryotic phototrophs (Raven, 1990). In the late Archaean, limited supply of Ni from the Earth's mantle to the oceans may have curbed biological methane production (Konhauser *et al.*, 2009). Decreased availability of free Fe and Mo ions in the Proterozoic sulfidic ocean, due to their speciation as metal-sulfide complexes (Saito *et al.*, 2003), may have reduced the use of N-fixation enzymes by prokaryotes, thereby limiting the supply of N (Anbar and Knoll, 2002; Zerkle *et al.*, 2006; Glass *et al.*, 2009). Selection for efficient element

use appears to be embedded even in patterns of amino acid usage in the proteomes of micro- and macro-biota (Baudouin-Cornu *et al.*, 2001; Elser *et al.*, 2011). In modern aqueous environments, low trace metal concentrations limit phytoplankton growth (Morel *et al.*, 1991; Saito *et al.*, 2002, 2004; de Baar and La Roche, 2003; Morel and Price, 2003; Morel, 2008); these scarce metals are accumulated via membrane transport systems involving the use of ligands (Hudson and Morel, 1993; Tortell *et al.*, 1999; Saito *et al.*, 2005). Metal scarcity drives selection pressures that can result in the use of substitute metals, such as Cd or Co instead of Zn (Yee and Morel, 1996; Lane *et al.*, 2005; Xu *et al.*, 2007; Morel, 2008), or even in the ability to decrease metalloenzyme production altogether (Saito *et al.*, 2011). Fe and Mn are more readily available in the suboxic zone than in surface oxic water where they form insoluble oxides (Nealson and Saffarini, 1994). In the ocean, metal utilization by phytoplankton varies between taxa and regions (Sunda, 1989; Twining and Baines, 2013), and is sensitive to chemical parameters such as pH or pCO_2 (Xu *et al.*, 2012). An extreme case of potential spatial variation is the consideration of environments beyond Earth conducive to life, the subject matter of astrobiology (Novoselov *et al.*, 2013). Potentially habitable exoplanets have been found in stellar systems whose bulk elemental abundances differ widely from those of our solar system (Young *et al.*, 2014). Could life as we know it cope with the different elemental availabilities and physicochemical conditions found in such environments?

To explore how living organisms adjust their chemical makeup to extreme environmental diversity, we sampled sediment microbial communities in the hot springs of Yellowstone National Park (YNP) and used a method to separate microbial cells from associated sediments (Neveu *et al.*, 2014) to quantify the multi-element stoichiometries of microbes from these diverse environments, targeting both phototrophic and

chemotrophic assemblages. The YNP springs sampled have widely varying temperature (ambient to boiling) and chemical properties (e.g., pH from 1 to 9; see Tables 3 and 4). This high physico-chemical diversity generates selective pressures that result in a corresponding diversity of microbes (Meyer-Dombard *et al.*, 2005) and microbial metabolisms (Shock *et al.*, 2010). The physical, chemical, and biological variety of these settings contrasts with that of most environments, such as the surface ocean or freshwater lakes, investigated during previous work on the interplay between environmental and microbial elemental contents. Nonetheless, many such previous studies have found that micro-organisms, especially photoautotrophs, can significantly adapt their major elemental composition to the environmental context (Rhee, 1978; Goldman *et al.*, 1979; Shuter, 1979; Fourqurean *et al.*, 1992; Koerselman and Meuleman, 1996; Hillebrand and Sommer, 1999; Sterner and Elser, 2002; Klausmeier *et al.*, 2004; Lee *et al.*, 2015). The tremendous metabolic diversity observed at YNP (Shock *et al.*, 2010) suggests the possibility of comparable diversity in major element and trace metal use by microbes. Thus, one would expect the elemental composition of YNP hot spring micro-organisms to cover a considerable range, possibly as wide as any environment on Earth allows.

In the following sections, we summarize our efforts to separate and analyze cells from sediment samples collected from the hot springs of YNP while considering the mineral contamination challenges inherent to the method. We then compare elemental compositions and stoichiometries of separated biomass to those of micro-organisms living in more moderate environments, and explore correlations (or lack thereof) between microbial compositions and environmental parameters. We briefly conclude with consideration of the implications of a relatively uniform stoichiometry of life on Earth for ongoing efforts to search for it elsewhere.

3.2 Methods

3.2.1 Sample Collection

All field sediment and mat samples were collected in July and August 2009 from hot springs located in YNP. The exact location and physicochemical conditions of the springs are detailed in Tables 3 and 4. At each location, handheld meters, connected to probes that were introduced directly into the hot springs, were used to measure pH and temperature (WTW 330i, WTW, Weilheim, Germany) as well as conductivity (YSI 30, YSI, Yellow Springs, OH, USA). Following these measurements, a sampling scoop was used to obtain hot spring water and sediment samples. Hot spring water was filtered through tandem 0.8 and 0.2 μm Supor membrane filters (Pall Corporation, Port Washington, NY, USA). For sediment samples, typically, four replicate 15-mL tubes were filled with sediment to 5 mL. Sediment samples were kept on ice in the field, then frozen at -20°C until transported back to Arizona State University, where they were transferred to a -80°C freezer. No cryoprotectant was added prior to freezing.

Clues about the possible presence or absence of photosynthesis were obtained visually by noting the presence or absence of green, orange, brown, yellow (in association with green), and/or purple photosynthetic pigments in hot springs following Cox *et al.* (2011). As noted in their study, this coarse method is unlikely to generate a false positive (strictly chemosynthetic site mimicking signs of phototrophic pigmentation) but could produce a false negative at a low abundance of phototrophs. These visual criteria could be improved by extracting and identifying pigments, as well as genes associated with photo- and chemotrophy, in collected samples (Cox *et al.*, 2011). For

Table 3: pH, conductivity, temperature, and location of the hot springs sampled

Sample ID	Unofficial Name	pH	Conductivity (μS)	Temperature (°C)	Latitude x (12T)	Longitude y (UTM)	Elevation (ft)	Photosynthesis?
090725D1	'Octopus Outflow 3'	8.2	2975	67.3	0516030	4931221	7354	Yes
090730V1	'Goldilocks Outflow 1'	2.4	3580	41.0	0518643	4949659	7402	Yes
090802W1	'Green Cheese'	6.1	804	57.4	0544535	4939787	7896	Yes
090726O1	'Old Blue Eyes Outflow 2'	9.0	3444	71.4	0515028	4929589	7403	Yes
090804P1	'Rabbit Creek Outflow 1'	9.2	3140	62.5	0514888	4929694	7428	Yes
090804J1	'Buddha's Belly'	7.7	2816	63.1	0514713	4928920	7371	Yes
090728A1	'Boulder Source'	8.4	4000	92.8	0512421	4933943	7287	Yes[a]
090729Q1	'Bumpy Butt'	6.3	2311	65.9	0514902	4917998	7712	No
090730C1	'Blondie Source'	2.7	2085	36.9	0518672	4949708	7409	No
090723K	'Obsidian Pool Black Mat'	5.4	930	57.6	0544541	4939799	7896	No
090723F	'Figure 8 Pool'	4.2	4146	68.3	0544482	4939773	7894	No
090730T1	'Avocado Source'	6.3	4169	73.1	0518575	4949713	7437	No
090723C	'Skippy's Bathtub Source'	4.8	2905	68.1	0544553	4939854	7895	No
090728D1	'Boulder Outflow 3'	8.7	3040	66.1	0512427	4933961	7218	Yes
090724QA	'Mound Spring Marsh'	9.6	1685	24.0	0511044	4934592	7275	Yes
090730U1	'Goldilocks Source'	2.4	2380	52.9	0518630	4949651	7421	No
090724OA	'Mound Spring Outflow W1'	8.3	3589	87.7	0511112	4934623	7258	No
090728RA	'Mockturtle'	1.6	15710	79.9	0541070	4944511	7840	No
090730UA	'Lil' Hottie'	2.1	6500	83.9	0518478	4949609	7442	No
090725DA	'Skippy's Bathtub Outflow'	5.2	3161	63.6	0544553	4939858	7889	No
090726N1	'Old Blue Eyes Outflow 1'	9.0	3630	74.2	0515035	4929586	7397	No
090730XA	'Lobster Claw'	2.1	6740	87.7	0518360	4949589	7503	No
090730Z1	'Danny Boy'	2.6	2730	71.5	0518168	4949641	7501	No
090802NA	'Fraggle Rock'	7.7	4760	92.8	0539333	4903284	7564	No
090802OA	'Mouse Graveyard'	7.2	3980	80.8	0539328	4903325	7550	No
090802PA	'Sore Foot Blues'	8.0	4362	92.4	0539356	4904316	7527	No
090802QA	'Wounded Knee'	6.5	3448	80.3	0539392	4904324	7519	No

The hot spring names are unofficial and correspond to our own sampling program.
[a] The sample was collected from a photosynthetic mat on an overhanging rock wall regularly splashed with hot spring water from the source pool. The temperature reading is for the hot spring source pool.

future investigations, it may be informative to extract pigments from the samples (e.g., chlorophyll *a* and several bacteriochlorophylls with acetone) and quantify their abundances using ultraviolet spectrophotometry. Regardless of the accuracy of pigment identification, the presence of pigments does not necessarily imply that communities are solely using light to fix carbon. Moreover, sites that display obvious signs of photosynthetic pigments may also host chemotrophs. Because of these caveats, the binary distinction between 'chemotrophic' and 'phototrophic' sites in the present

Table 4: Major chemical composition of the hot springs sampled, as well as dissolved P and Mo content

Sample ID	DIC (ppm C)	DOC (ppm C)	O_2 (aq) (mg/L)	NO_3^- (mg/L)	NO_2^- (mg/L)	NH_4^+ (mg/L)	Fe^{2+} (mg/L)	S^{2-} (mg/L)	SiO_2 (mg/L)	P (μg/L)	Mo (μg/L)	Alkalinity (mg/L)
090725D1	59.70 ± 1.79	0.18 ± 0.01	N/A	N/A	N/A	N/A	N/A	N/A	N/A	6.0	25	N/A
090730V1	7.81 ± 0.39	1.44 ± 0.12	5.50	1.70	0.040	1.63	1.44	37	340	36	1.3	BDL
090802W1	N/A	N/A	N/A	N/A	N/A	N/A	N/A	N/A	N/A	N/A	0.84	N/A
090726O1	35.81 ± 1.43	0.24 ± 0.01	N/A	N/A	N/A	N/A	N/A	N/A	N/A	11.5	29	N/A
090804P1	N/A	0.23 ± 0.01	1.20	0.70	0.020	0.01	0.03	BDL	521	3.7	29	154
090804J1	78.67 ± 3.15	0.53 ± 0.02	0.80	2.10	0.145	0.08	BDL	14	274	6.8	31	340
090728A1	1.76 ± 0.11	0.36 ± 0.01	N/A	N/A	N/A	N/A	N/A	N/A	N/A	6.1	44	N/A
090729Q1	8.08 ± 0.26	0.46 ± 0.03	1.80	1.60	0.075	0.08	0.01	12	346	4.1	117	38.9
090730C1	N/A	1.52 ± 0.12	N/A	N/A	N/A	N/A	N/A	N/A	N/A	41	0.18	N/A
090723K	18.32 ± 0.55	3.43 ± 0.15	1.10	2.30	0.114	0.42	1.02	194	299	210	3	4.4
090723F	16.42 ± 0.82	2.35 ± 0.10	2.90	2.90	0.001	BDL	0.74	123	353	62	59	BDL
090730T1	94.05 ± 3.76	0.12 ± 0.01	0.54	11.10	0.057	1.6	BDL	612	311	3.0	16.7	300
090723C	20.60 ± 0.62	2.23 ± 0.10	1.00	4.50	0.085	0.07	0.57	143	445	43	27	32
090728D1	36.11 ± 1.08	0.28 ± 0.01	1.30	7.60	0.063	N/A	0.02	374	354	6.0	48.1	251
090724QA	41.97 ± 0.84	0.71 ± 0.05	7.20	1.40	0.269	0.02	BDL	5	496	7.4	32	306
090730U1	> 45	1.31 ± 0.10	0.10	2.30	0.019	2.17	3.22	626	275	58	1.15	BDL
090724OA	31.87 ± 0.64	0.18 ± 0.01	0.70	12.90	0.056	BDL	0.02	875	412	4.4	28	261
090728RA	11.84 ± 0.24	> 24	N/A	N/A	0.010	17.7	2	53900	354	1100	0.08	BDL
090730UA	0.79 ± 0.04	1.09 ± 0.09	0.80	1.80	0.046	5	2.07	118	422	34	0.52	BDL
090725DA	11.44 ± 0.34	1.21 ± 0.05	2.60	1.60	0.026	0.11	0.26	73	444	32	26	18.4
090726N1	36.18 ± 1.45	0.27 ± 0.01	0.60	3.30	0.046	BDL	BDL	134	331	9.0	29	148
090730XA	2.93 ± 0.15	0.86 ± 0.07	0.31	3.40	0.040	42.6	6	682	N/A	88	3.5	N/A
090730Z1	N/A	N/A	0.82	2.30	0.035	41	1.2	1536	202	9.6	0.25	BDL
090802NA	N/A	N/A	N/A	N/A	N/A	N/A	N/A	N/A	N/A	6.1	83	N/A
090802OA	N/A	N/A	N/A	N/A	N/A	N/A	N/A	N/A	N/A	8.9	82	N/A
090802PA	42.24 ± 0.84	0.23 ± 0.01	0.35	3.80	0.098	0.1	BDL	40	522	5.1	76	224
090802QA	60.77 ± 1.22	0.45 ± 0.02	0.88	3.90	0.086	0.02	BDL	BDL	511	6.7	72	232

Uncertainties on Dissolved Inorganic Carbon (DIC) and Dissolved Organic Carbon (DOC) are ± 1 standard deviation. In spring water samples for which phosphate was measured above detection limit separately by ion chromatography (IC; in addition to the P abundances reported here measured by ICP-MS), most P seemed to be present as phosphate. Method details for IC measurements were provided by Shock *et al.* (2010). "N/A": not available, "BDL": below detection limit.

study should only been taken as qualitative. This distinction does not affect the main conclusions of this article.

Most measurements of solute concentrations reported in Table 4 were carried out in the field using a visible (400–880 nm) spectrophotometer (Hach DR/2400; Hach, Loveland, CO, USA): dissolved oxygen was measured using an indigo carmine method, nitrate with a Cd reduction method, nitrite with a diazotization method, total

ammonia with a salicylate method, ferrous iron with a 1,10-phenantroline method, total sulfide with a methylene blue method, and dissolved silica with a silicomolybdate method. Alkalinity was determined using a Hach Digital Titrator (Hach, USA) with a colorimetric indicator and reported as calcium carbonate. Spectrophotometry and titration measurements carry an uncertainty of 5–10%, with contributions coming from interferences, analytical uncertainties, and operator error (Windman *et al.*, 2007; Shock *et al.*, 2010). Further details on field measurement methods were provided by Shock *et al.* (2010).

Shortly after the field campaign, dissolved organic and inorganic carbon (DOC and DIC, respectively) were measured at Arizona State University using an OI Analytical 1010 Wet Oxidation TOC Analyser (OI Analytical, College Station, TX, USA). Concentrations were quantified using CO_2 obtained following the reaction of water samples with either sodium persulfate (DOC) or phosphoric acid (DIC). Total concentrations of phosphorus, as well as all other elemental abundances in bulk samples, were measured by inductively coupled plasma mass spectrometry (ICP-MS; Thermo Element 2, Thermo Fisher Scientific, Waltham, MA, USA). Prior to ICP-MS analysis, samples were stored in acid-washed 60-mL Nalgene bottles until they were acidified with 400 μL of OmniTrace®UltraTM (Fisher Scientific, Pittsburgh, PA, USA) high-purity 69–70% HNO_3 just before analysis (Havig, 2009).

3.2.2 Cell-Sediment Separation

Microbes in benthic sediments and mats tend to be physically and chemically bound to mineral grains. Thus, minerals make up a significant fraction of such samples (Havig, 2009). Because the metals present in trace amount in cells can be major rock-

forming elements (e.g., Mg, Fe, Mn), even small amounts of minerals can overwhelm the microbial signal in an elemental analysis (Martin and Knauer, 1973). Therefore, we separated cells from sediment following a method modified from a previously described approach (Amalfitano and Fazi, 2008; Neveu *et al.*, 2014). If possible, we performed cell-sediment separations on several replicate samples ('biological replicates') for each given location for independent analysis as separate samples.

We used trace-metal clean, sterile solutions, and autoclaved plasticware to avoid sample contamination by trace metals and micro-organisms. Frozen field samples were gently thawed in a centrifuge (6000 g, 10°C, 20–40 min). The supernatant was removed. Samples were transferred into 20-mL beakers. A different beaker was used for approximately every 2 g sediment or microbial mat to avoid overflow during subsequent stirring. The samples were stirred (720 rpm, 30 min), using autoclaved stir rods, in 5 mL phosphate buffer saline (0.13 M sodium chloride, 7 mM sodium phosphate dibasic, 3 mM sodium phosphate monobasic, pH adjusted to 7.4 with a few drops of concentrated hydrochloric acid or sodium hydroxide) with added detergent (0.5% vol./vol. Tween 20, final concentration) and chelating agent (0.1% wt./vol. sodium pyrophosphate, final concentration). Sodium pyrophosphate was purchased from Sigma-Aldrich (Cat. No. 221368; St. Louis, MO, USA), Tween 20 from Bio-Rad (Cat. No. 170-6531; Hercules, CA, USA), sodium chloride from Fisher Scientific (Cat. No. S271-500), sodium phosphate dibasic from Mallinckrodt (Cat. No. 7914; Damastown, Mulhuddart, Ireland), and sodium phosphate monobasic from EMD Millipore (Cat. No. SX0710-1; Billerica, MA, USA).

The samples were then gently sonicated (40% output, 35% duty cycle, 2 min) in an ice-cold bath. The resulting cell-sediment suspension was gently homogenized and carefully pipetted atop a 5-mL layer of NycodenzTM (Axis-Shield, Dundee, UK,

Cat. No. 1002424, 4 g dissolved in 5 mL water), of density (1.3 g mL^{-1}) between the density of cells and that of sediment grains, in 15-mL centrifuge tubes. During the subsequent centrifugation step (5000 *g* at 4°C for 30 min using a swing-out rotor), cells did not undergo migration through the Nycodenz layer, whereas sediment grains did unless their density was low. Centrifugation was repeated for an additional 30 min to 1 h until the Nycodenz layer was clear and distinct phases could be seen. From bottom to top, these phases are sediment pellet, Nycodenz, a thin layer of separated cells (with possible residual detritus of similar density), and supernatant.

Following centrifugation, the layer of separated cells was pipetted out and washed three times (using 0.85% NaCl to limit osmotic stress) to remove any Nycodenz or stirring solution. For each wash, cells were resuspended in 1 mL NaCl solution, then centrifuged (10000 *g*, 5 min, 4°C), and the supernatant was discarded.

Cell recovery yields were also determined by staining pre- and post-separated samples with 10 μg mL^{-1} 4',6-di-amidino-2-phenylindole (DAPI) and imaging via epifluorescence microscopy. Most yields were estimated on hot spring sediment samples other than those analyzed here, but collected in the same or adjacent hot springs during the same sampling campaign, following the sampling methods described above. Example epifluorescence micrographs of separated samples stained with DAPI are shown in Fig. 7. On field sediment samples, we typically obtained cell separation yields of 5–40% (Table 2). The lowest recovery yields were obtained when the cell density in sediment was lowest, as previously observed (Morono *et al.*, 2013).

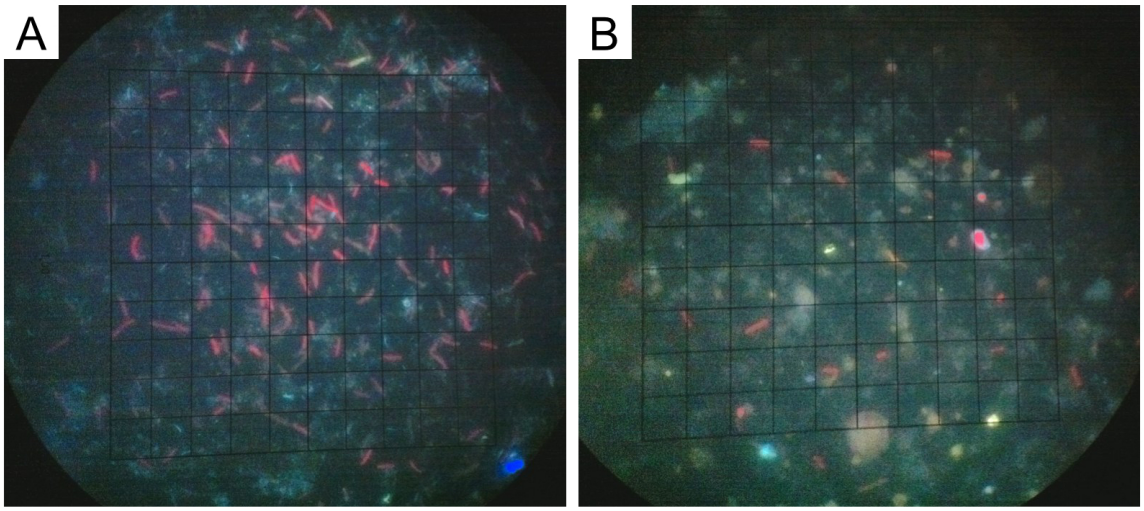

Figure 7: Example micrographs of separated samples from two YNP hot springs

(A) "Bison Pool", which fell just below the 20% C cutoff (see text) and was not part of this study but was collected and separated as described in the Methods section; (B) "Green Cheese" (sample 090802W1). The hot spring names are unofficial and correspond to our own sampling program. A grid square measures 10 μm x 10 μm. The blue color arises from the DAPI stain (see text); other colors are due to the natural fluorescence of certain cells (red) and minerals (yellow-green in panel B).

3.2.3 Elemental Analysis

Elemental analysis was largely conducted following a method previously described by Neveu *et al.* (2014). To ensure that the microbial elemental content was not altered during the procedure, wild-type *E. coli* of known elemental composition were separated and analyzed along with each sample. For each sample, a fraction of the recovered bio-mass was combusted to measure C and N from CO_2 and N_2 using an Elemental Analyzer (Costech, Cernusco sul Naviglio, Italy) coupled to an Isotope Ratio – Mass Spectrometer (IRMS; Finnigan DELTAplus Advantage, Thermo Fisher Scientific, USA). Before combustion, samples were loaded into 5 $\times$ 9 mm tin capsules (Costech).

Freshly separated cells were resuspended in as little 18 MOhm-cm MilliQ water as possible (200–1000 μL) and pipetted into tin capsules in 50 μL aliquots, then dried overnight at 60°C. Serial pipetting-drying cycles were required for dilute suspensions; separated material awaiting drying was stored at 4°C. The mass of each tin capsule was measured using a balance of microgram precision, both before pipetting the cell suspension and after all drying cycles, to obtain a net dry mass of separated material. All elemental abundances reported in this article are normalized to the net dry mass of the corresponding sample. A calibration curve for C and N contents was built using a tomato leaf standard (0.2, 0.5, 1.0, 2.0, 5.0, and 7.0 mg). Glycine check standards (0.7 mg) were analyzed between samples to determine the accuracy of the elemental measurements. The in-house calibration and check standards were characterized using standards USGS 40, USGS 41, IAEA NBS 18, and IAEA NBS 19. A minimum dry mass of approximately 1 mg was necessary to yield quantitative IRMS measurements (within the calibration curve). When a given separation clearly did not yield enough cell material to carry out IRMS analyses on several biological replicates, we combined the cells of replicate separations to obtain a single measurement, giving priority to the measurement of C and N abundances.

The remainder of the separated material was analyzed by ICP-MS (Thermo X-series, X-series 2, and iCap Q, Thermo Fisher Scientific, USA) to determine its trace element abundances. Separated material was first pipetted and dried in micro-centrifuge tubes (200 μL volume) overnight at 60°C. Similarly to tin capsules, several pipetting-drying cycles were required for dilute suspensions; separated material awaiting drying was stored at 4°C. All micro-centrifuge tubes were weighed both empty and after the last drying cycle, using a balance of microgram precision, to obtain a net dry mass of separated material to which all measured elemental abundances were normalized. To

obtain accurate masses, it was essential to use as light a container as possible: the 200-μL micro-centrifuge tubes were both light and not subject to acid leaching of potential trace metals (as established by performing sample-free preparations and analyses). The remaining steps of the sample preparation were carried out in a Class-10 clean laboratory. The dry samples were transferred to acid-cleaned (using concentrated HNO_3 followed by concentrated HCl) Teflon vessels. 3 mL of 1x-distilled HNO_3 were added to all vessels, which were tightly capped and placed on a hot plate for overnight digestion at 100–150°C. The vessels were then uncapped and heated until the sample volume decreased to approximately 0.5 mL. If there remained any undigested material (that is, any turbidity or solid particle) in the vessels, additional overnight cycles of digestion were performed using, in this order, 3 mL of 1x-distilled HNO_3, 1 mL HNO_3 and 3 mL HCl (aqua regia), and aqua regia with 100 μL H_2O_2 at 100–150°C for up to 2 weeks. Any undigested residue was weighed, then discarded; the residue mass was always too low to be measured by a balance of microgram precision.

The samples were finally diluted to 3.5 mL (the minimum volume required by the Thermo X-series ICP-MS to measure the elements specified) in 15-mL acid-cleaned (using concentrated HNO_3 followed by concentrated HCl) centrifuge tubes, using 0.32 M nitric acid in 18 MOhm-cm water. The final dilution volume was weighed to obtain a dilution factor between initial dry mass and mass of solution analyzed. A calibration curve was built using a phosphorus-enriched black shale standard solution of known elemental composition (characterized using the certified reference material USGS Devonian black shale SDO-1), serially diluted (1:15, 1:35, 1:150, 1:1000, 1:7500, 1:25000) with nitric acid (0.32 M). This standard was chosen because its elemental composition reasonably matched that of (sometimes widely varying) YNP sediment samples and *E. coli*. The standard was not digested along with the samples to test

for element recoveries; however, it is routinely run in parallel with samples, with generally excellent recovery, accuracy, and reproducibility. We performed sample-free digestions to check for contamination during digestion, and subtracted the average of the measured elemental abundances on these digestions from the measured abundances of each sample. Unseparated sediment was similarly analyzed.

Separation of a given sample (one 15-mL tube filled to 5 mL with sediment) yielded between 0.03 and 3 mg of dried cells, depending on the location of sample collection. Obtaining enough biomass was especially an issue for samples collected at chemotrophic locations. Even after combining biological replicates, many samples fell below the lowest IRMS calibration standard: while we separated samples from 50 locations, quantitative C and N abundances could be determined for only 25 samples. Of these, 14 had carbon contents higher than 20%, indicating that the analyzed samples were mostly biomass. They were collected at the locations reported in Tables 3 and 4, and their elemental abundances are given in Table 22 (Appendix B) along with the number of biological replicates analyzed. (Two samples were collected at 'Goldilocks Outflow 1' from a black mat near the spring and from green filaments in the spring's outflow channel.) The other eleven samples were likely contaminated by low-density, porous sediment grains (see below).

Of the 25 samples for which C and N abundances could not be obtained, nineteen still yielded enough material for measurement by ICP-MS on at least one biological replicate. Fourteen of these samples (listed in Tables 3, 4, and 22 in Appendix B) showed acceptably low levels of mineral contamination (see below). For these samples, we determined which elements could not be excluded as arising from mineral contamination.

3.2.4 Quantification of Sediment Contamination

It has been shown that *E. coli* cells separated by the Nycodenz density gradient method (Amalfitano and Fazi, 2008) conserve their elemental content in C, N, P, Mg, Al, Ca, Ti, Mn, Fe, Ni, Cu, Zn, and Mo to within 30% or better (Neveu *et al.*, 2014). However, cells separated from sediment are not systematically free of residual sediment because a density gradient separation cannot discriminate between cells and low-density fractal dust particles or porous sediment grains. As a consequence, the analyzed samples still likely contained material that was not biological, yet had a density similar to that of cells. Prior to analysis and interpretation of elemental data, we applied several filters to the C, N, P, and trace metal data sets to minimize the contribution of sediment contamination. Separated material with C contents less than 20% of the sample dry mass were considered to be likely contaminated by sediment. We choose this threshold of 20% of the sample dry mass because aquatic bacteria have a typical C content of 30–60% (Fagerbakke *et al.*, 1996). Shifting this cutoff to lower C contents would increase the likelihood of contamination by sediment material. Shifting the cutoff to higher C contents (e.g., 30%), while leading to the rejection of four additional samples showing no signs of photosynthesis (Fig. 8), does not alter the conclusions drawn from the results presented below.

Despite our rejection of samples with C abundances incompatible with high biomass content, sediment material may still account for most of the measured trace elements, which are major rock-forming elements, in separated samples of high C content. Therefore, even small amounts of sediment contamination may significantly affect

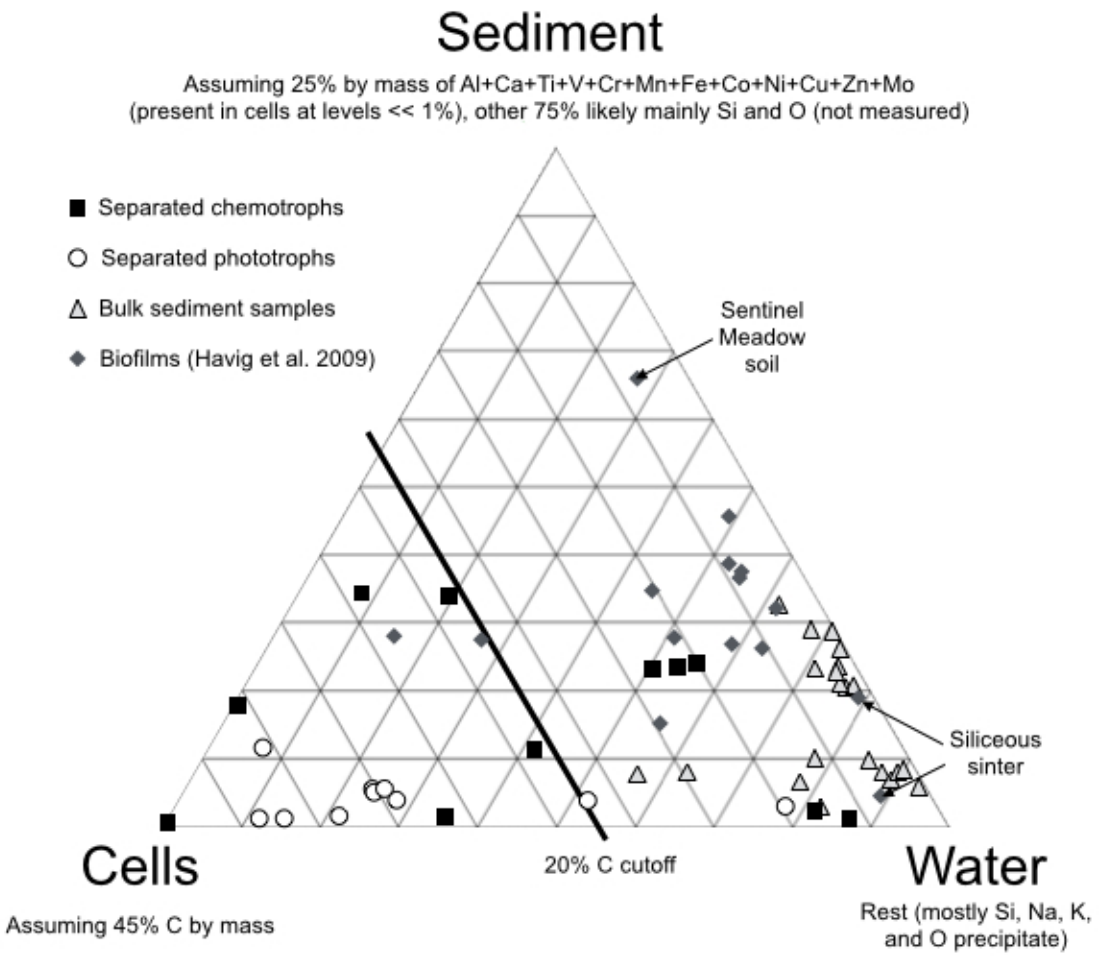

Figure 8: Elemental makeup of separated and unseparated samples shown on a ternary diagram

The three apices represent the cell component (scaled to 45% C), the sediment component (scaled to 25% of the sum of all the transition metals, which along with Si and O are rock-forming elements), and the water component (rest, assumed to be precipitated silica and salts in the hydrothermal YNP springs). Separated samples (circles, "phototrophs": sites where phototrophy was clearly present; squares, "chemotrophs": sites with no clear evidence of phototrophy) are richer in C than unseparated sediment (triangles) or biofilms (diamonds). A slanted black line shows the 20% C cutoff for the separated samples whose elemental abundances are further discussed in this study. Adapted from Havig (2009).

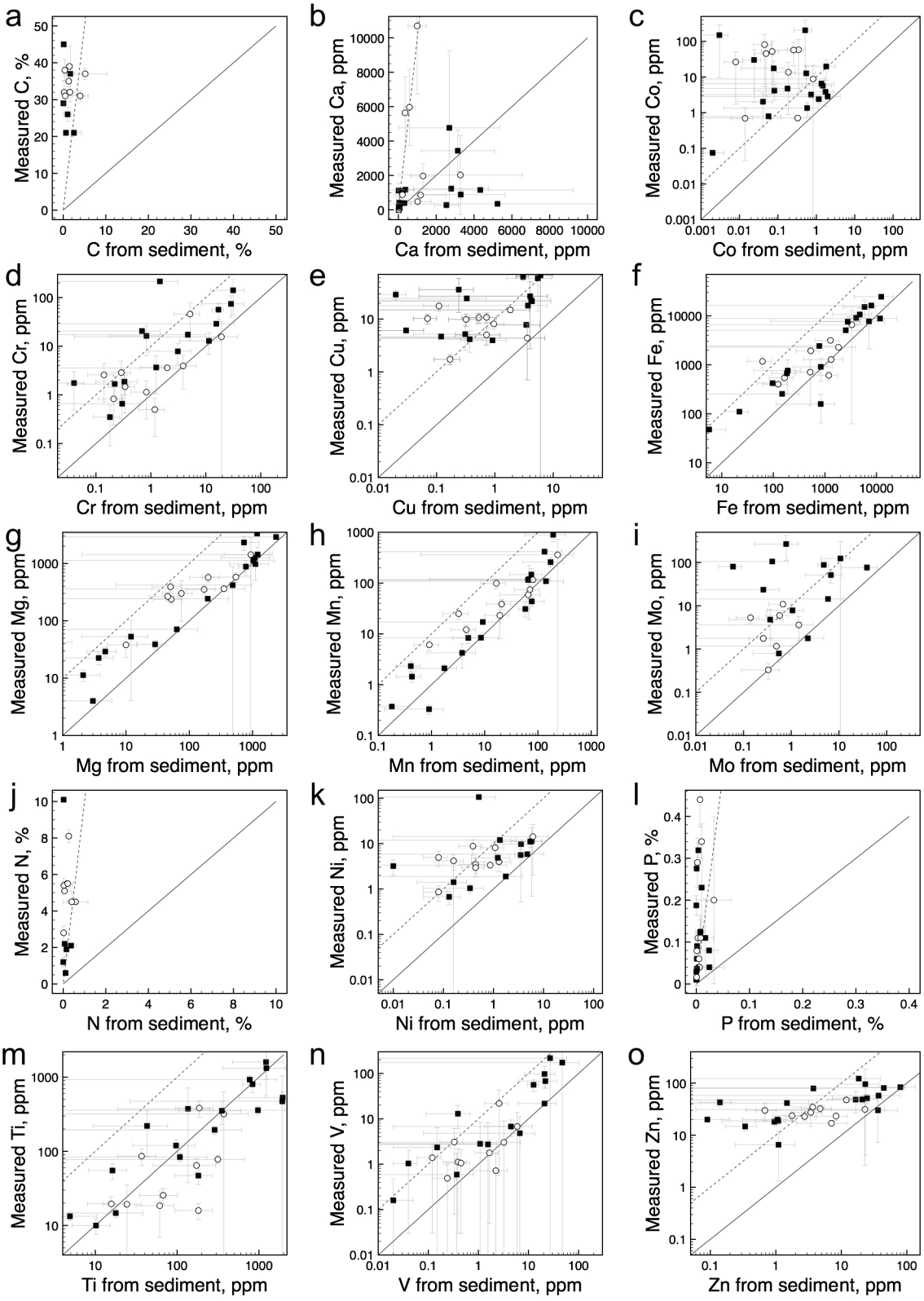

Figure 9: Sediment contribution to elemental abundances measured in separated samples

Figure 9: (Continued from previous page.) The sediment contribution for an element X was estimated using the X:Al ratio of the bulk sediment, assuming 100% of the sample Al came from sediment (see text for details). The dashed and solid lines indicate sediment contributions of 10% and 100%, respectively. Circles represent locations with obvious signs of phototrophy and squares locations with no obvious phototrophy. Elemental abundances are reported as either percent or part per million of the sample dry mass. Uncertainties shown by error bars are as described in Figs 11 and 12 and were propagated when calculating Al normalizations. Note the linear scale on panels (A), (B), (J), and (L).

the measured trace element composition of a separated sample. We tracked this sediment contamination based on Al content, which we assumed to be contributed solely by sediment and which is easily measured by ICP-MS. This method seems to provide reasonable estimates of abiotic contamination (Collier and Edmond, 1984), although the susceptibility of Al to the separation procedure may depend on the chemical properties of the sample, such as redox or pH. This bias could be mitigated by measuring other rock-forming elements, such as Si or Fe, along with Al. However, Si is difficult to reliably measure by ICP-MS because of its high ionization potential, and Fe, of prime biological interest, cannot be assumed to come entirely from sediment.

To our knowledge, there is no satisfactory alternative method for contamination tracking. Contamination by mineral matter of density similar to cells could be estimated by spiking sterile sediment with a given mass of microbes of known elemental composition, such as *E. coli*. By comparing the elemental composition of such a mixture following separation and analysis to that of *E. coli* alone, the sediment contribution may be quantified. However, although sterile sediment is devoid of live organisms, it still contains dead cellular material that will be separated along with *E. coli*; this prevents such an experiment from discriminating the biological contribution from that of abiotic material. A third alternative could involve lysing cells in a sediment sample (e.g., by strong sonication) and filtering the sample to discard intracellular metals

and measure only the abundance of sediment-bound metals. However, this method does not dispose of metals either in membrane-bound proteins or trapped in the cell membrane debris (Martin and Knauer, 1973; Coughlin *et al.*, 1983).

Short of more satisfactory alternative methods, we thus chose to use Al as a proxy for sediment contamination. We scaled the elemental composition of the sediment, $X_{\text{bulk sed}}$, by the ratio of Al abundance in the separated sample, $\text{Al}_{\text{sep sample}}$, to Al abundance in the bulk sediment, $\text{Al}_{\text{bulk sed}}$. Assuming that Al is entirely non-biological, and that the X:Al ratio of the sediment component of the analyzed sample is identical to that of the bulk sediment, the abundance of an element X contributed from sediment in a separated sample, $X_{\text{sed, sep sample}}$, is then:

$$X_{\text{sed, sep sample}} = X_{\text{bulk sed}} \times \text{Al}_{\text{sep sample}}/\text{Al}_{\text{bulk sed}} \tag{3.1}$$

We compared this sediment contribution to the measured abundances for 15 elements (C, N, P, Mg, Ca, Ti, V, Cr, Mn, Fe, Co, Ni, Cu, Zn, and Mo).

Mineral contamination varied with sample location and element of interest (Fig. 9). For elements Mg, Ca, V, Cr, Mn, and Fe, the sediment contribution ranged from 20% to 100% for most samples (Appendix B, Table 22). We conclude that biomass abundances cannot be derived for these elements even at an order-of-magnitude accuracy. These are also the elements for which concentrations in the separated material and bulk sediment were most strongly correlated, although log-log diagrams give a stronger visual impression of linear relationship than those with a linear scale (compare Fig. 9B and D, where the distribution of data points is relatively similar, using the dashed and solid lines as a guide). R^2 coefficients of determination for linear regressions of all combined (phototrophic and chemotrophic) samples for each panel

of Fig. 9 are provided in Table 22 (Appendix B). Ti seemed essentially contributed by sediment, which is expected since this element seems to have little biological role.

Our results pertain to the elements for which the estimated contamination from sediment was generally low: C, N, P, Ni, Cu, Zn, and Mo. For these elements, as well as Co, the sediment contribution was around 10% or less for most of the samples and was close to 100% for no more than two of these samples (Appendix B, Table 22). We therefore consider these elemental abundances as contributed by biomass and accurate to within an order of magnitude. This is accurate enough for comparison with previously published values, given the relatively larger range of abundances covered for any given element. Co abundances are not considered further, because it has not been ascertained that this element is conserved during the separation procedure (Neveu *et al.*, 2014).

The elemental makeup of the samples for which we obtained both IRMS and ICP-MS measurements is shown in Fig. 8. Using C content as a proxy for biomass shows that separated samples are richer in biological material than unseparated bulk sediment or biofilms (Havig, 2009). However, some separated samples still had a C content of a few percent of the sample dry mass, too low to be solely biomass.

3.2.5 Statistical Analyses of Elemental Stoichiometries

Two types of statistics, least-squares linear correlations and t-tests, were used to assess correlations between elemental stoichiometries and environmental parameters. Least-squares linear regressions were performed for phototrophs and chemotrophs together; coefficients of determination (R^2) are reported along with the sample size. Parametric correlations (Welch approximate two-sample t-tests) were performed to

assess possible relationships between elemental stoichiometries and the presence or absence of obvious signs of phototrophy. The Welch approximate t-test differs from that for Student t distributions by not assuming that the two distributions have equal variance (Zar, 2010). Thus, the Welch t-test was appropriate to the sample distributions we tested, which had variances that differed by a factor of a few in some instances. All t-tests were carried out assuming two-tailed normal distributions. The validity of these assumptions and sizes of the distributions are discussed along with t-test results.

3.2.6 16S rRNA Gene V4 Region Sequencing

To determine which organisms were present in sediment and mat samples, as well as whether the separation procedure introduced any significant bias in the distribution of microbial taxa, we sequenced 16S ribosomal RNA gene libraries for six samples, both pre- and post-separation from sediment/mat material. These six samples were collected at the same time and location as those subjected to elemental analysis. They underwent cell-sediment separation at a different time, as we were unable to recover enough material from cell separations on a single sample to carry out both an elemental analysis and a DNA extraction: DNA from initial aliquots of separated material was neither visible on a gel, nor quantifiable via fluorometry.

DNA was extracted from sediment/mat and separated material using the FastDNATM SPIN Kit for Soil (MP Biomedicals, Solon, OH, USA) following the manufacturer's protocol. Prior to amplification, DNA was checked for integrity using gel electrophoresis and quantified by fluorometry using the Qubit®Assay (Invitrogen, Carlsbad, CA, USA). The V4 Region of the 16S rRNA gene was amplified with

primers (515F and 806R; Caporaso *et al.*, 2012) barcoded for each sample. Triplicate PCR reactions contained at least 10 ng of purified DNA, 1X High Fidelity PCR buffer, 2 mM $MgSO_4$, 200 mM dNTP mix, 200 μg mL^{-1} acetylated BSA, 250 nM of the forward and reverse primers, and 1 μM of Platinum®Taq High Fidelity DNA polymerase (Invitrogen, Carlsbad, CA, USA). PCR reactions were carried out using the following thermal cycler parameters: (i) initial denaturation at 94°C for 2min, (ii) 30 cycles of 94°C for 30s, 50°C for 30s, and 68°C for 2 min, and (iii) final extension for 5 min at 68°C. Following amplification, PCR products were gel-purified using the Wizard®SV Gel and PCR Clean-Up System (Promega, Madison, WI, USA), quantified by fluorometry, pooled to equimolar concentrations, and prepared as a single library for 29250 bp paired-end sequencing on the Illumina MiSeq (Illumina, San Diego, CA, USA) at the DNASU Genomics Core Facility at Arizona State University. The 16S rRNA gene amplicon library was sequenced in the same run as samples for metagenomic and other amplicon analyses with about 10% of the lane devoted to amplicon libraries.

The quality of reads was checked with *FastQC* (Andrews, 2010) and paired with *PANDASeq* (Masella *et al.*, 2012), resulting in 149004 sequences. These sequences were then demultiplexed, trimmed of barcodes and primers, and analyzed in *mothur* (Schloss *et al.*, 2009), generally following the guidelines of Kozich *et al.* (2013). During processing, de-replicated sequences were aligned to the *Silva* v119 SSU reference (Quast *et al.*, 2012), checked for chimeras, clustered into Operational Taxonomic Units (OTUs) at a 0.03 cutoff, and classified using *Greengenes 13_8* (DeSantis *et al.*, 2006). Library sizes ranged from 2968 to 20381 sequences after processing. Singleton OTUs were removed and samples were then subsampled to the smallest library size for each pre- and post-separated pair. OTUs with differential abundance were then detected using a

two-sided Fisher's exact test implemented in the software package *Statistical Analysis of Metagenomic Profiles* (*STAMP*; Parks *et al.*, 2014). Differences in OTU abundances were considered statistically significant if the Benjamini-Hochberg corrected P-value was less than 0.001 and the effect size (differences between proportions) was greater than 1. Canonical correspondence analyses (CCA) followed by permutation (999) were used to determine the presence of any significant correlations between taxonomic composition and cellular C, N, P, Ni, Cu, Mo, and Zn contents (Buttigieg and Ramette, 2014). CCA and permutation analysis were implemented in *R* using the *vegan* software package (Oksanen *et al.*, 2007; *R* Core Team, 2014), following the method described by Borcard *et al.* (2011). Following CCA, we performed a permutation analysis (999 permutations) to test for the significance of any correlations between taxonomic composition and cellular elemental contents. Only the metal contents that could be reliably attributed to a cellular origin were used (Ni, Cu, Zn, and Mo). Two CCA analyses were conducted using either C, N, and P or only metals as environmental variables. The Mo content of sample 090728A1, which was below detection limit, was set to a value of 0 for these analyses. OTU abundances in the pre-separated samples were used as response variables. Sequences were processed as described in the main text, but subsampled to the smallest size across all pre-separated libraries using *mothur* (Schloss *et al.*, 2009). OTU abundances were imported into *R* (*R* Core Team, 2014) using the *phyloseq* software package (McMurdie and Holmes, 2013), and CCA and permutation analyses were performed using the *vegan* software package (Oksanen *et al.*, 2007). Sequences were deposited into the National Center for Biotechnology Information (NCBI) databases under the following accession numbers: 090802W1 (KM679418–KM712112), 090804P1 (KM712113–KM734438), 090730V1-Green Fil-

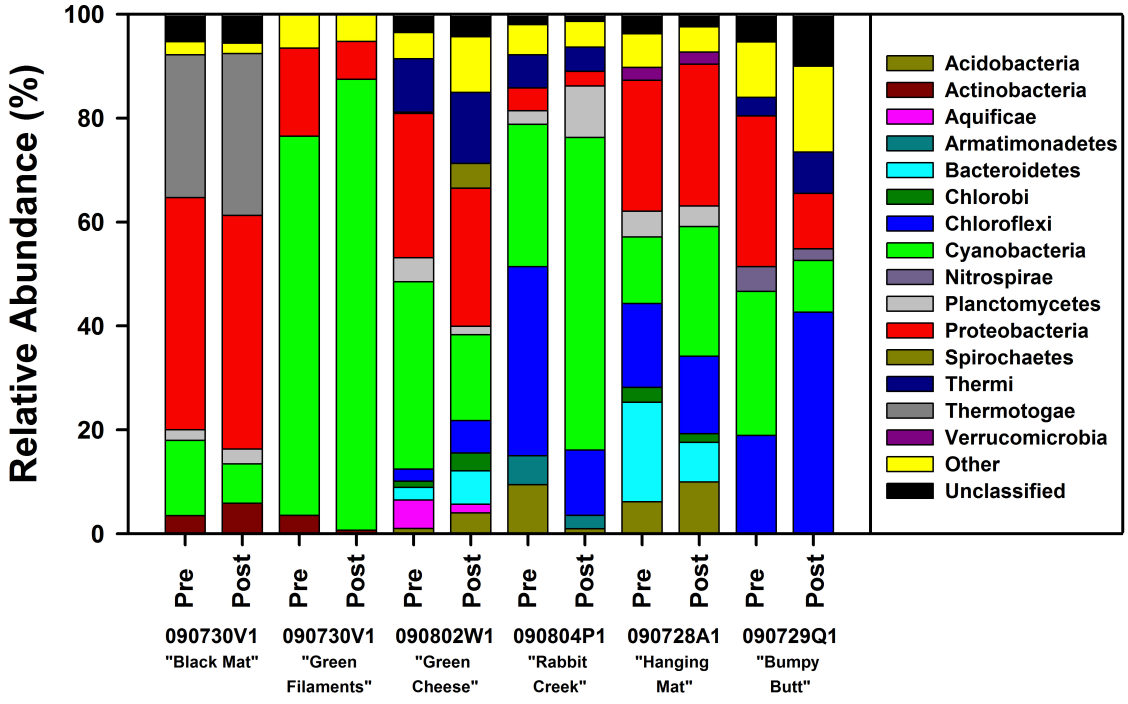

Figure 10: Relative abundance of bacterial phyla in unseparated ('Pre') and separated ('Post') samples

All sequences (including those comprising singleton OTUs) were included for determination of community composition. Phyla with an abundance of 2% or more in either the unseparated or separated libraries are shown. The remaining phyla are categorized as 'Other.' The phyla that comprise this category differ between sites.

aments (KM734439–KM755386), 090729Q1 (KM75 5387–KM767863), 090728A1 (KM767864–KM804064), 090730V1-Black Mat (KM804065–KM816404).

The relative abundance of different bacterial phyla in 16S rRNA gene libraries of pre- and post-separated samples is depicted in Fig. 10. Archaea are not shown, as they were generally present at low abundances ($< 1\%$). All sequenced samples except one (090729Q1) were collected at locations displaying obvious signs of phototrophy, but spanning a broad range of pH (2.4–9.2; Table 3). Phototrophs (Cyanobacteria

and Chloroflexi) comprised 14–73% of the pre-separated libraries. Most sites were dominated by Bacteria (> 99%), with the exception of a low-pH site (090730V1-'Black Mat') in which Archaea (mostly affiliated with Thermoplasmata) comprised ≈7.2% of the pre-separation 16S rRNA amplicons and where a large portion of OTUs classified as Cyanobacteria were derived from chloroplasts (≈75% of the cyanobacterial OTUs). Other abundant OTUs in this site were designated as Thermotogae or Proteobacteria (e.g., sulfur-respiring deltaproteobacterium *Desulfurella* or fermentative alphaproteobacterium *Acidiphilium*). Sample 090730V1-'Green Filaments' was dominated by a single OTU (an unclassified cyanobacterium). In general, OTUs designated as phototrophs were assignable to the rank of genus (e.g., Gloeobacter, Roseiflexus, and Chloroflexus). OTUs classified as Proteobacteria were the third most abundant phylum across samples (up to 44%) and many of these sequences were affiliated with taxa that cycle sulfur.

Our primary goal in sequencing 16S rRNA genes was to determine whether the cell separation procedure introduced any significant bias in community composition. While Archaea were generally less than 1% of the 16S rRNA sequences pre-separation, in samples 090802W1-'Green Cheese' and 090729Q1-'Bumpy Butt', archaeal abundance increased to 4.7 and 8.1%, respectively, in post-separation samples. At the bacterial phylum level, the presence of taxa was broadly similar between pre- and post-separated libraries; however, the relative abundance of some bacterial phyla appeared to change after cell separation (Fig. 10). These changes were reflected in the alpha diversity (measured as the Inverse Simpson Index) of samples (Tables 5 and 6), which tended to differ between pre- and post-separation libraries. To determine which OTUs were driving these apparent differences, we used a Fisher's exact test to compare the abundance of OTUs in pre- and post-separation libraries that contained no singleton

Table 5: Community composition and bias due to cell-sediment separation (A)

A		OTUs		Inverse Simpson Index	
Sample	N_{seqs}	Pre-separation	Post-separation	Pre-separation	Post-separation
090730V1 (black mat)	2871	120	120	8.98	5.9
090730V1 (green filaments)	6968	157	145	1.91	1.35
090802W1	11849	561	693	13.72	36.70
090804P1	5229	173	170	10.78	6.80
090728A1	15905	530	478	17.14	12.42
090729Q1	5033	213	246	7.40	14.10

Table 6: Community composition and bias due to cell-sediment separation (B)

B		Taxonomy (Domain; Phylum; Class;	% Relative abundance		Effect	95% CI	
Sample	OTU	Order; Family; Genus)	Pre-sep.	Post-sep.	size	Lower	Upper
090730V1 (black mat)	Otu_22	Bacteria; Proteobacteria; Alphaproteobacteria; Rhodospirillales; Acetobacteraceae; *Acidiphilium*	11.2	24.3	-13.1	-15.0	-11.1
	Otu_14	Bacteria; Thermotogae; MS9; V5; unclassified	24.9	30.7	-5.8	-8.1	-3.5
	Otu_33	Bacteria; Proteobacteria; Alphaproteobacteria; Rhodospirillales; Acetobacteraceae; *Acidiphilium*	7.8	4.0	3.8	2.5	5.0
	Otu_18	Bacteria; Proteobacteria; Deltaproteobacteria; Desulfurellales; Desulfurellaceae; *Desulfurella*	13.9	10.0	3.9	2.2	5.6
	Otu_48	Bacteria; Cyanobacteria; Chloroplast; Stramenopiles; unclassified	8.3	1.2	7.1	6.0	8.2
090730V1 (green filam.)	Otu_1	Bacteria; Cyanobacteria; unclassified	74.1	87.9	-13.9	-15.2	-12.6
	Otu_36	Bacteria; Proteobacteria; Gammaproteobacteria; RCP1-48; unclassified	16.7	7.3	9.4	8.3	10.4
	Otu_83	Bacteria; Actinobacteria; Acidimicrobiia; Acidimicrobiales; unclassified	3.4	0.7	2.7	2.2	3.2
090802W1	Otu_32	Bacteria; Cyanobacteria; Nostocophycideae; Nostocales; Nostocaceae; unclassified	0.8	8.3	-7.5	-8.0	-7.0
	Otu_16	Bacteria; [Thermi]; Deinococci; Thermales; Thermaceae; *Meiothermus*	7.0	11.1	-4.1	-4.9	-3.4
	Otu_50	Archaea; Euryarchaeota; Thermoplasmata; A10; Thermoplasmatales; unclassified	0.1	3.6	-3.5	-3.9	-3.2
	Otu_46	Bacteria; OP8; OP8_1; OPB95; unclassified	0.3	3.7	-3.4	-3.7	-3.0
	Otu_68	Bacteria; Spirochaetes; Spirochaetes; Spirochaetales; Spirochaetaceae; *Treponema*	0.1	2.3	-2.2	-2.5	-2.0
	Otu_43	Bacteria; Planctomycetes; Planctomycetia; Gemmatales; Gemmataceae; *Gemmata*	2.0	0.5	1.5	1.2	1.8
	Otu_1	Bacteria; Cyanobacteria; unclassified	3.2	1.7	1.5	1.1	1.9
	Otu_34	Bacteria; Proteobacteria; Deltaproteobacteria; Syntrophobacterales; Syntrophaceae; *Desulfomonile*	2.4	0.4	2.0	1.8	2.3
	Otu_40	Bacteria; Proteobacteria; Deltaproteobacteria; Desulfobacterales; Desulfobacteraceae; *Desulfatirhabdium*	3.4	0.5	2.9	2.6	3.3
	Otu_19	Bacteria; Aquificae; Aquificae; Aquificales; Hydrogenothermacea; unclassified	5.3	1.5	3.8	3.3	4.2
	Otu_29	Bacteria; Cyanobacteria; Synechococcophycideae; Synechococcales; Acaryochloridaceae; *Thermosynechococcus*	4.3	0.5	3.8	3.4	4.2
	Otu_15	Bacteria; Proteobacteria; Deltaproteobacteria; Syntrophobacterales; Syntrophobacteraceae; *Thermodesulforhabdus*	5.3	1.0	4.2	3.8	4.7
	Otu_10	Bacteria; Cyanobacteria; Oscillatoriophycideae; unclassified	23.4	1.6	21.8	21.1	22.6
090804P1	Otu_2	Bacteria; Cyanobacteria; Gloeobacterophycideae; Gloeobacterales; Gloeobacteraceae; *Gloeobacter*	12.9	32.0	-19.1	-20.6	-17.5
	Otu_3	Bacteria; Cyanobacteria; Gloeobacterophycideae; Gloeobacterales; Gloeobacteraceae; *Gloeobacter*	7.4	14.8	-7.4	-8.6	-6.2

Table 6: (Continued.)

Sample	OTU	Taxonomy (Domain; Phylum; Class; Order; Family; Genus)	% Relative abundance Pre-sep.	% Relative abundance Post-sep.	Effect size	95% CI Lower	95% CI Upper
	Otu_17	Bacteria; Planctomycetes; Planctomycetia; Gemmatales; Gemmataceae; *Gemmata*	2.0	8.8	-6.8	-7.7	-6.0
	Otu_7	Bacteria; Cyanobacteria; unclassified	3.7	8.2	-4.5	-5.4	-3.6
	Otu_25	Bacteria; Cyanobacteria; Gloeobacterophycideae; Gloeobacterales; Gloeobacteraceae; *Gloeobacter*	1.0	3.0	-2.0	-2.6	-1.5
	Otu_13	Bacteria; [Thermi]; Deinococci; Thermales; Thermaceae; *Thermus*	5.0	2.8	2.2	1.5	2.9
	Otu_5	Bacteria; Chloroflexi, Chloroflexi; [Roseiflexales]; [Roseiflexaceae]; *Roseiflexus*	4.6	2.2	2.4	1.7	3.1
	Otu_9	Bacteria; Chloroflexi, Chloroflexi; Chloroflexales; Chloroflexaceae; *Chloroflexus*	5.9	3.3	2.5	1.7	3.1
	Otu_20	Bacteria; Armatimonadetes; OS-L; unclassified	5.4	2.7	2.7	1.9	3.5
	Otu_39	Bacteria; Chloroflexi; Anaerolineae; WCHB1-50; unclassified	3.2	0.4	2.8	2.4	3.4
	Otu_30	Bacteria; Acidobacteria; [Chloracidobacteria]; [Chloracidobacterales]; [Chloracidobacteraceae]; *Ca. Chloracidobacterium*	9.1	0.7	8.3	7.5	9.2
	Otu_8	Bacteria; Chloroflexi, Chloroflexi; [Roseiflexales]; [Roseiflexaceae]; *Roseiflexus*	21.8	5.9	15.9	14.7	17.2
090728A1	Otu_7	Bacteria; Cyanobacteria; unclassified	4.4	12.3	-7.9	-8.5	-7.3
	Otu_4	Bacteria; Proteobacteria; Alphaproteobacteria; Rhizobiales; unclassified	14.5	19.9	-5.4	-6.2	-4.5
	Otu_11	Bacteria; Acidobacteria; [Chloracidobacteria]; [Chloracidobacterales]; [Chloracidobacteraceae]; *Ca. Chloracidobacterium*	4.5	9.0	-4.5	-5.1	-4.0
	Otu_21	Bacteria; Cyanobacteria; Synechococcophycideae; Pseudanabaenales; Pseudanabaenaceae; *Pseudanabaena*	2.3	4.9	-2.7	-3.1	-2.3
	Otu_90	Bacteria; Proteobacteria; Deltaproteobacteria; NB1-j; unclassified	1.5	0.2	1.4	1.2	1.6
	Otu_62	Bacteria; Bacteroidetes; unclassified	1.5	0.04	1.5	1.3	1.7
	Otu_54	Bacteria; Bacteroidetes; Cytophagia; Cytophagales; unclassified	2.2	0.1	2.2	1.9	2.4
	Otu_12	Bacteria; Bacteroidetes; [Saprospirae]; [Saprospirales]; Saprospiraceae; unclassified	12.5	5.3	7.2	6.6	7.9
090729Q1	Otu_9	Bacteria; Chloroflexi, Chloroflexi; Chloroflexales; Chloroflexaceae; *Chloroflexus*	2.3	10.5	-8.2	-9.1	-7.3
	Otu_73	Archaea; Euryarchaeota; Thermoplasmata; E2; DHVEG-1; unclassified	0.4	6.9	-6.5	-7.2	-5.8
	Otu_5	Bacteria; Chloroflexi, Chloroflexi; [Roseiflexales]; [Roseiflexaceae]; *Roseiflexus*	14.3	18.7	-4.4	-5.9	-3.0
	Otu_13	Bacteria; [Thermi]; Deinococci; Thermales; Thermaceae; *Thermus*	3.3	7.2	-3.8	-4.7	-3.0
	Otu_27	Bacteria; Chloroflexi, Chloroflexi; Chloroflexales; Chloroflexaceae; *Chloronema*	0.4	4.2	-3.8	-4.4	-3.3
	Otu_61	Bacteria; Chloroflexi; Anaerolineae; OPB11; unclassified	0.4	3.4	-3.0	-3.6	-2.5
	Otu_80	Bacteria; unclassified	0.3	3.2	-2.9	-3.5	-2.4
	Otu_45	Bacteria; Nitrospirae; Nitrospira; Nitrospirales; [Thermodesulfovibrionaceae]; *Thermodesulfovibrio*	3.3	1.6	1.6	1.0	2.2
	Otu_42	Bacteria; Proteobacteria; Betaproteobacteria; Rhodocyclales; Rhodocyclaceae; *Hydrogenophilus*	2.8	1.2	1.6	1.1	2.2
	Otu_3	Bacteria; Cyanobacteria; Gloeobacterophycideae; Gloeobacterales; Gloeobacteraceae; *Gloeobacter*	24.4	6.9	17.5	16.1	18.9
	Otu_15	Bacteria; Proteobacteria; Deltaproteobacteria; Syntrophobacterales; Syntrophobacteraceae; *Thermodesulforhabdus*	21.2	3.6	17.6	16.3	18.8

Tables 5 and 6: (Continued from previous page.) (A) After removal of singleton OTUs, each pairwise unseparated and separated sample was subsampled to the smallest library size (N_{seqs}), the number of OTUs observed at a cutoff of 0.03 was noted, and the Inverse Simpson Index was calculated. (B) The abundances of OTUs in each pre- and post-separation sample were compared using a two-sided Fisher's exact test with a Benjamini-Hochberg correction of the P-value. OTUs detected as significantly different ($P < 0.001$ and effect size greater than 1) between pre- and post-separation libraries are listed along with their taxonomic classification based on the *Greengenes* database and relative abundance in the subsampled libraries. 'CI': Confidence Index.

OTUs and were subsampled to equal library sizes. The number of OTUs identified as differentially abundant using the Fisher's exact test ($P < 0.001$ and effect size of 1%) ranged from 3 to 13 (Tables 5 and 6); however, many of these OTUs had differences in relative abundance between the pre- and post-separation libraries (effect sizes) of less than 5%. At all the sites except 090728A1-'Hanging Mat', at least one typically abundant OTU showed a 10% or greater difference in relative abundance between pre- and post-separated samples. Generally, OTUs classified as the same phylum and in some cases genus (e.g., Proteobacteria/Acidiphilium and Cyanobacteria/Gloeobacter) did not show the same pattern of enrichment or depletion in the post-separation libraries within or across samples.

Thus, taxa found in the in situ and separated communities can differ in relative abundance, as previously observed (Maron *et al.*, 2006; Holmsgaard *et al.*, 2011; Portillo *et al.*, 2013). This may result in the elemental composition of separated samples not entirely reflecting that of the in situ hot spring sediment and mat communities, particularly if a taxon that constitutes a large proportion of the pre-separated community is absent from the separated sample. However, given that many taxa differed by less than 5% relative abundance, this may not result in a detectable effect on the measured elemental composition.

3.3 Results

3.3.1 C:N:P Stoichiometries

Molar C:N ratios were between 5 and 28 (C:N was 50 for one sample but with high uncertainty), molar C:P ratios between 230 and 2200, and molar N:P ratios between 12 and 400 (Fig. 11). C:N ratios for the separated samples generally fell close to the canonical Redfield value of ≈6.6 (molar). For two samples collected from chemotrophic sites (090723F 'Figure 8 Pool' and 090730T1 'Avocado Source'), the C:N ratios are above previously reported ranges (Bruland *et al.*, 1991; Hecky *et al.*, 1993; Elser and Hassett, 1994; Fagerbakke *et al.*, 1996; Elser *et al.*, 2000; Ho *et al.*, 2003; Cleveland and Liptzin, 2007; Nuester *et al.*, 2012). Aside from these two samples, the C:N ratios of the separated material seem to roughly match those of the bulk sediment (Fig. 12). The C:P and N:P ratios were generally much higher than the respective Redfield values of 106:1 and 16:1. In fact, a few samples showed C:P or N:P ratios that exceeded previously reported ranges. These extremely high C:P and N:P ratios were generally uncorrelated with those of bulk sediment collected at the same locations (coefficient of determination $R^2 < 0.005$ on least-squares linear regressions over 14 samples, in both cases done for phototrophic and chemotrophic locations together); however, similarly high ratios were also reached in the bulk sediment (Fig. 12).

C, N, and P abundances relative to dry mass of separated material are shown in Fig. 13 and compared to previously reported ranges. By design (C cutoff at 20% by mass to ensure samples are mainly biomass), C abundances match previously reported ranges for aquatic bacteria (Fagerbakke *et al.*, 1996). N abundances also

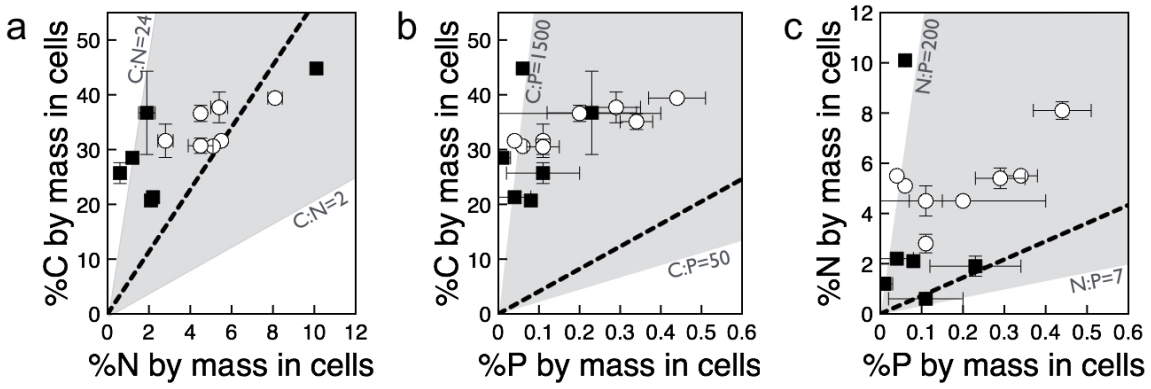

Figure 11: (A) C:N, (B) C:P, and (C) N:P ratios of material (mainly cells) separated from YNP hot spring sediment samples

Chemotrophic locations are shown by squares and phototrophic locations by circles. Overlain are the typical molar ranges (shaded) for aquatic micro-organisms (Bruland *et al.*, 1991; Hecky *et al.*, 1993; Elser and Hassett, 1994; Fagerbakke *et al.*, 1996; Elser *et al.*, 2000; Ho *et al.*, 2003; Cleveland and Liptzin, 2007; Nuester *et al.*, 2012) and, for reference, the molar Redfield ratio of marine phytoplankton (dashed line). Uncertainties shown by error bars are the maximum between the standard deviation from the mean over n biological replicates (Appendix B, Table 22) and the standard error on separated *E. coli*. The latter uncertainty estimation is useful when a separation yielded enough sample to analyze only one replicate.

match reported ranges for microbial soil biomass (Cleveland and Liptzin, 2007), marine phytoplankton (Ho *et al.*, 2003), and a marine N fixer (Nuester *et al.*, 2012), although the two samples mentioned above (090723F and 090730T1) had N contents below these ranges. P abundances match the lower end of reported abundances for microbial soil biomass (mostly from grassland and forest soil in climates ranging from arctic to tropical; Cleveland and Liptzin, 2007), with values as low as 100–200 ppm by mass, similar to those reported by Wolfe-Simon *et al.* (2011) for a P-limited bacterium, and up to values approaching 5000 ppm (0.5%) by mass as reported by Nuester *et al.* (2012) and compiled by Bruland *et al.* (1991) for marine micro-organisms. The P abundance ranges we measured remain below more commonly reported values for

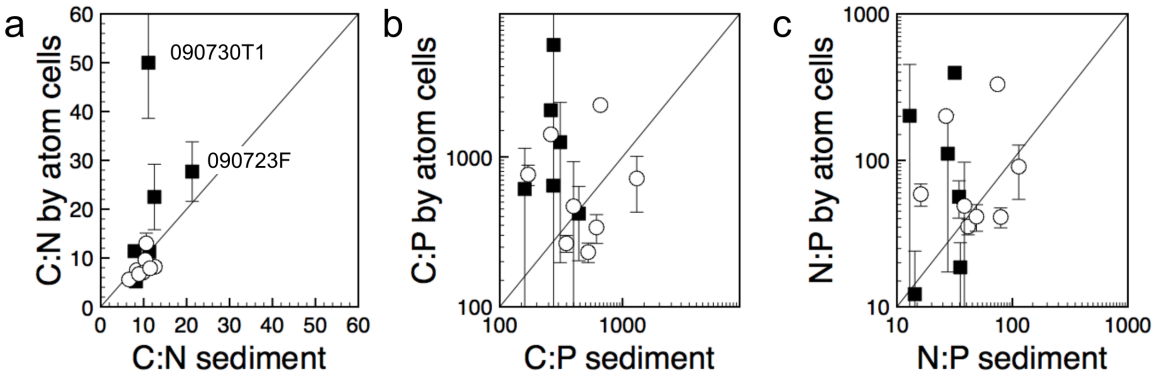

Figure 12: (A) C:N, (B) C:P, and (C) N:P ratios in separated samples and bulk sediment

A 1:1 line is overlain on each panel. Circles show samples from locations with obvious photosynthesis and squares show samples collected at locations with no obvious sign of photosynthesis. Uncertainties on cellular ratios shown by vertical error bars are those described in Fig. 11 and were propagated for the calculation of the ratios. Uncertainties on sediment ratios were estimated as the standard deviation over analytical replicates; they are smaller than the symbol size. Note the logarithmic scale on panels (B) and (C).

microbes, on the order of a few percent (Rouf, 1964; Ho *et al.*, 2003; Twining *et al.*, 2004, 2011; Cameron *et al.*, 2012).

3.3.2 Trace Element Stoichiometries

The measured elemental abundances for Cu, Ni, Zn, and Mo in separated material are shown on Fig. 13 and compared to previously reported ranges. The abundances of these trace elements in extremophile microbes (except Mo at sites showing no obvious signs of phototrophy) matched the ranges previously reported for microbes living in more moderate conditions. This is surprising, given the tremendous diversity in physicochemical conditions and trace element supply in YNP hot springs.

Based on measured Al, there remained a few samples in which close to 100%

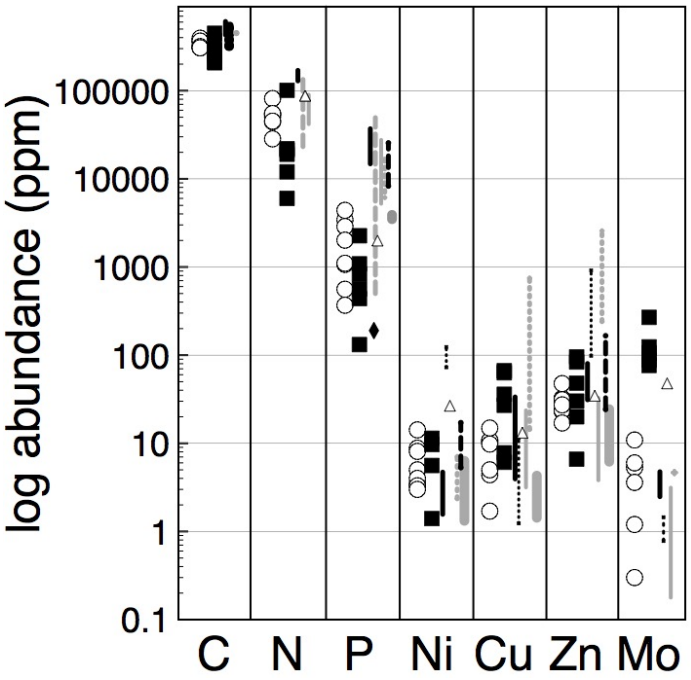

Figure 13: Elemental makeup of YNP extremophiles compared to the known makeup of micro-organisms

Logarithm of the abundances of seven major and trace elements (normalized to dry mass of analyzed material) for separated samples collected in hot spring sediment at chemotrophic (squares) and phototrophic sites (circles) of YNP. Error bars are not shown for clarity, but are shown on Fig. 9. Other symbols and bars represent abundance ranges previously reported for microbes: diverse bacteria (dotted grey bars; Rouf, 1964), *E. coli* (thin black bars; Rouf, 1964; Cameron *et al.*, 2012, this work), marine phytoplankton (thick grey bars: Bruland *et al.* (1991), and references therein; dashed black bars: Twining *et al.* (2004, 2011)), marine phytoplankton excluding Ca-rich shells (thin grey bars; Ho *et al.*, 2003)), cultured hyperthermophilic archaea (dotted black bars; Cameron *et al.*, 2012)), a marine N fixer (triangles; Nuester *et al.*, 2012)), microbial soil biomass (dashed grey bars; Cleveland and Liptzin, 2007), aquatic bacteria (thick black bar; Fagerbakke *et al.*, 1996), and P-limited GFAJ-1 (black diamond; Wolfe-Simon *et al.*, 2011). For literature sources that reported only C:element ratios, the element content was estimated assuming a C content of 45% by mass. These data are consistent with a previous compilation (Novoselov *et al.*, 2013).

of the Ni, Zn, and Mo appeared to be contributed by sediment despite our down-selection of samples based on a bulk C content above 20%. Given order-of-magnitude uncertainties on trace metal content (Fig. 9), we have chosen not to correct the sample abundances shown in Fig. 13 for the sediment contributions. Such corrections are unlikely to change our finding that the metal contents of hot spring microbes are ordinary. Despite the additional variability and uncertainty introduced by these potentially large corrections, abundances would likely remain within the biological ranges involved.

Ni, Cu, and Zn abundances in separated samples spanned less than two orders of magnitude (Fig. 13). They matched the lower end of previously reported ranges; in particular for *E. coli* (Rouf, 1964; Cameron *et al.*, 2012, as well as data –not shown– from *E. coli* check standards analyzed along with our samples), marine phytoplankton (Bruland *et al.*, 1991; Ho *et al.*, 2003; Twining *et al.*, 2004, 2011) and, for Ni and to some extent Cu, diverse bacteria (Rouf, 1964). Cameron *et al.* (2012) reported Cu abundances for cultured hyperthermophilic archaea similar to those measured in our separated samples; however they reported Ni and Zn abundances higher than those we measured. The Mo abundances we measured spanned three orders of magnitude and matched the ranges reported by Rouf (1964), Ho *et al.* (2003), and Cameron *et al.* (2012). However, all samples from chemotroph-dominated locations had Mo abundances higher than the highest microbial Mo abundance we found in the literature: that measured in a marine N fixer by Nuester *et al.* (2012).

Only Mo showed a difference in abundance between chemotrophic and phototrophic communities (Fig. 13): Mo was higher in cells extracted from chemotrophic sites (Welch's t-test on separated samples: $t = 2.94$, df $= 12$, $P < 0.05$ ('df' = degrees of freedom), assuming the distributions of seven phototrophic sites and 12 chemotrophic

sites are normal and two-sided). The lower abundance of Mo in separated material collected at sites showing obvious signs of phototrophy compared to sites that did not was also reflected in the lower ratios of Mo:C (Welch's t-test: $t = 3.59$, df $= 4$, $P < 0.05$, assuming the distributions of six phototrophic sites and five chemotrophic sites are normal and two-sided), and to a lesser extent Mo:P ($t = 1.35$, df $= 12$, $P < 0.2$, assuming the distributions of seven phototrophic sites and 12 chemotrophic sites are normal and two-sided), as shown in Figs 14 through 16. For the three t-tests reported above, the assumption of normal distributions seems justified for the phototrophic sites, but may be an approximation for the chemotrophic sites (especially for the distribution of Mo:C): for phototrophic sites the distribution minima were 1.0 (for Mo), 1.0 (for Mo:C), and 0.8 (for Mo:P) standard deviations (σ) below the mean and the maxima were, respectively, 1.9, 1.5, and 1.8 σ above the mean; for chemotrophic sites, the minima were respectively 0.9, 0.4, and 0.8 σ below the mean and the maxima 2.7, 3.3, and 1.7 σ above the mean.

Overall, cellular Mo:C and Mo:P ratios seemed insensitive to concentrations of hot spring sulfide or nitrogen species (Fig. 15; coefficients of determination $R^2 < 0.1$ on least-squares linear regressions over phototrophic and chemotrophic sites together: 14 samples for S_2^-, 16 samples for NO_3^- and NO_2^- , and 13 samples for NH_4^+). The contrast in Mo:C and Mo:P ratios between phototrophic and chemotrophic cells appeared to be driven by Mo abundances rather than C and P, which did not differ as much between cells (Fig. 13; Relative Standard Deviation = 152% for Mo for 20 samples, compared to RSD = 93% for P for 28 samples and RSD = 21% for C for 14 samples; relative standard deviations determined together for phototrophic and chemotrophic

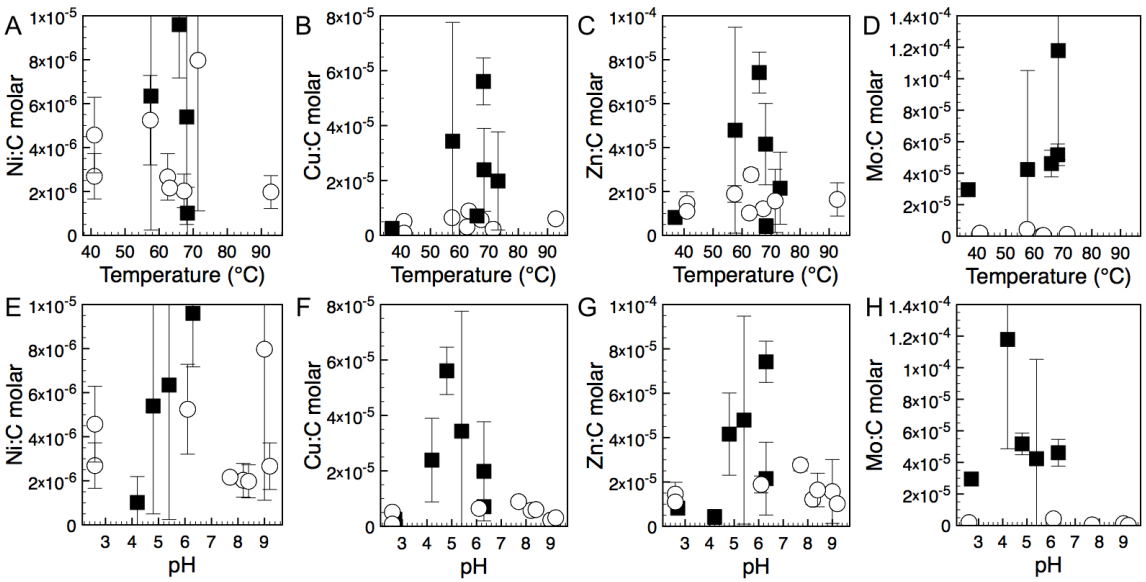

Figure 14: Metal:C ratios (molar) for Ni (A; E), Cu (B; F), Zn (C; G), and Mo (D; H) in separated cells show no correlation with either temperature or pH

Coefficients of determination R^2 on least-squares linear regressions are below 0.1 for all panels; for each panel tests were done with phototrophs and chemotrophs together. Samples collected at locations showing obvious signs of photosynthesis are represented by open circles; those collected at locations displaying no such signs are represented by squares. (Note that the "photosynthetic" data point at a temperature above 90°C was collected in a mat splashed by hot spring water, but not submerged in it; see Table 3.) Error bars represent uncertainties as described in Fig. 11 and Fig. 12. Uncertainties were propagated in ratio calculations.

sites). Moreover, Mo:P ratios were higher at phototrophic sites regardless of the concentration of Mo in hot spring water (Fig. 16B). We also did not observe any strong correlations between metal abundances or metal:C ratios and temperature (Fig. 14A–D; coefficients of determination $R^2 < 0.15$ on least-squares linear regressions over phototrophic and chemotrophic sites together: 12 samples for Ni:C, 14 samples for Cu:C and Zn:C, and 11 samples for Mo:C), pH (Fig. 14E–H; $R^2 < 0.1$ using the same statistics), or sediment availability of the metal except perhaps for Zn (Fig. 9E,I,K,O; R^2 of 0.26 for Ni, 0.46 for Cu, 0.67 for Zn, and 0.36 for Mo using the same statistics). We did not observe any relationships between metal: C/N/P stoichiometries and

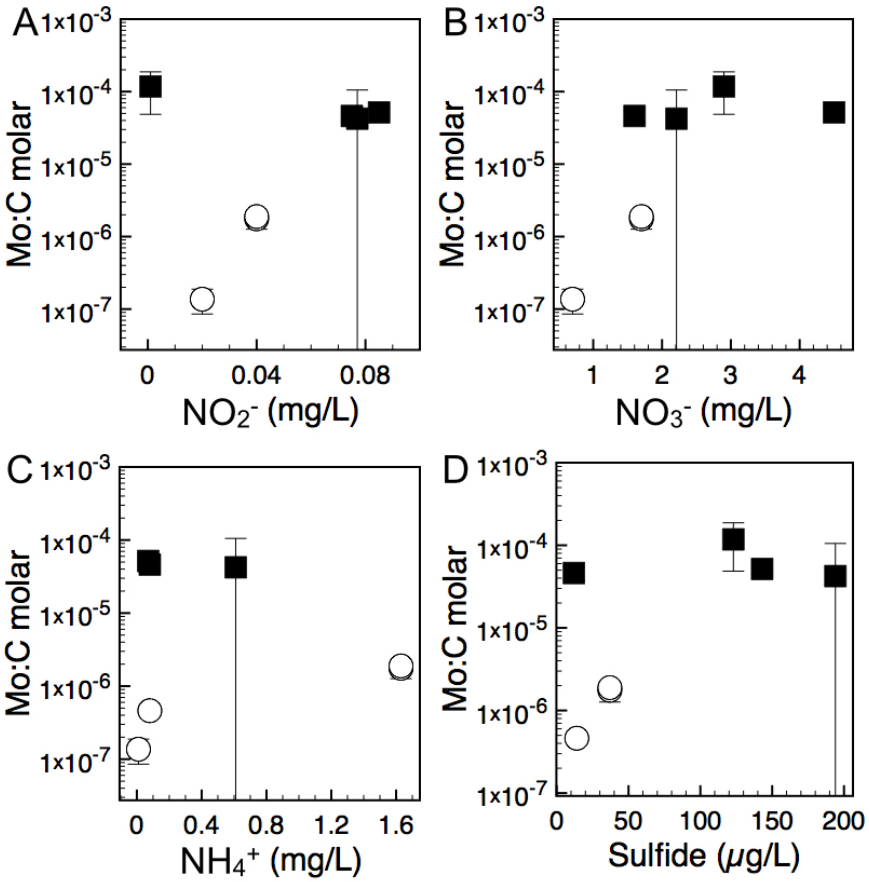

Figure 15: Mo:C ratios (molar) in separated cells show no correlation with hot spring dissolved nitrite (A), nitrate (B), ammonium (C), or sulfide (D)

Samples collected at locations showing obvious signs of photosynthesis are represented by open circles; those collected at locations displaying no such signs are represented by squares. For all panels, error bars represent uncertainties as described in Fig. 11 and Fig. 12. Uncertainties were propagated in ratio calculations.

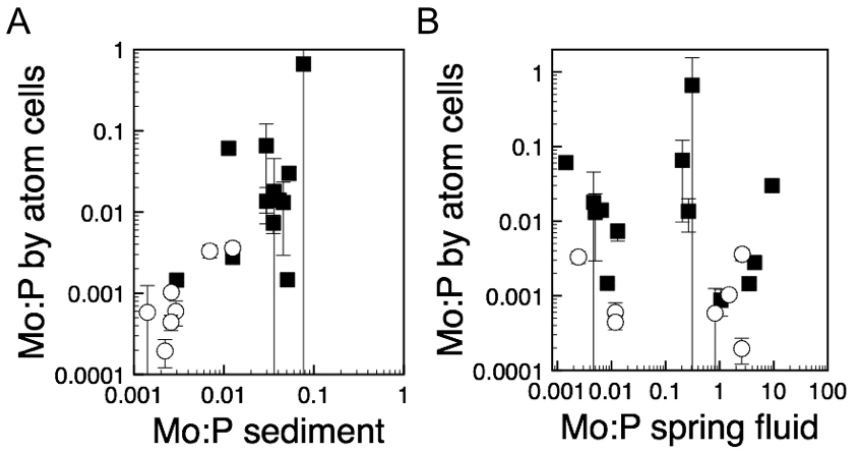

Figure 16: (A) Measured molar Mo:P ratios in the separated cells and bulk sediment. (B) Measured molar Mo:P ratios in the separated cells and hot spring fluid

Samples collected at locations showing obvious signs of photosynthesis are represented by open circles; those collected at locations displaying no such signs are represented by squares. Error bars represent uncertainties as described in Fig. 11 and Fig. 12. Uncertainties were propagated in ratio calculations.

nutrient concentrations or other geochemical parameters listed in Table 4 (data not shown with the exception of Mo).

3.3.3 Elemental Abundances and Microbial Community Composition

We did not identify any significant correlations between cellular elemental abundances and microbial community composition, using CCA followed by permutation analysis ($P > 0.496$; Fig. 17), for any of the six samples for which gene sequencing was performed. Despite the lack of significant correlation, OTUs in 090730V1 'Green Filaments' appear associated with high cellular N content and OTUs in sites 090802W1, 090729Q1, and 090804P1 seem associated with high cellular Mo and Zn contents (Fig. 17). Material separated from the two low-pH samples (pH 2.4) had higher C (>38% by mass), N (>5%), and P (>0.3%) than the four other locations (≤32% C; ≤5%

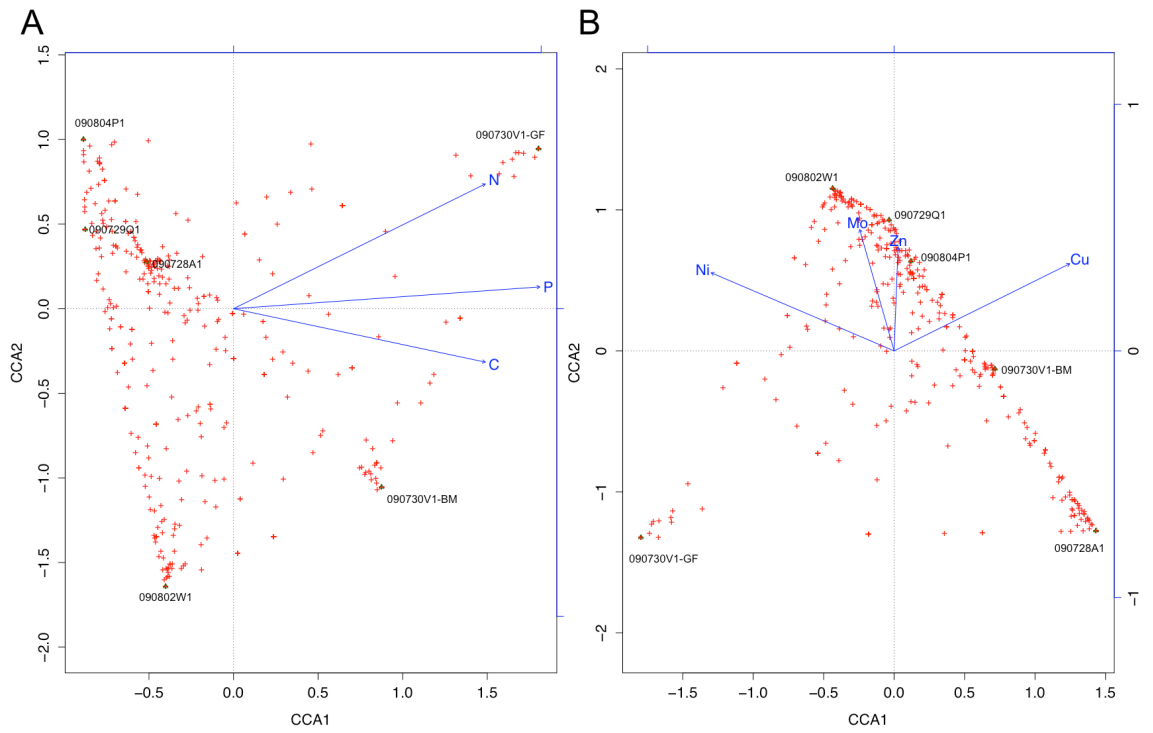

Figure 17: CCA triplots scaled for OTU optima constrained by cellular C, N, and P (panel A) or metal (panel B) contents

Green triangles show the position of sites and red crosses show the position of OTUs. Based on permutation analyses, apparent correlations between OTUs and elemental contents are not significant ($P > 0.496$). BM: Black Mat; GF: Green Filaments.

N; $\leq$0.11% P), but whether these differences in C, N, and P abundances are due to taxonomic composition is unclear (Fig. 17). The community composition seems to differ between the two low-pH sites as much as it does across all six locations (Fig. 10 and Fig. 17). Trace element abundances did not exhibit any clear pattern across all six sites (Appendix B, Table 22). Mo and Zn abundances seem to be correlated, but this observation appears driven by the high Mo and Zn contents of cells extracted from site 090729Q1 (Appendix B, Table 22).

3.4 Discussion

In this study, we sought to explore if and how living organisms adjust their chemical makeup in response to extreme environmental diversity. To this end, we quantified the elemental composition of microbial cells separated from sediment collected in the hot springs of Yellowstone National Park (YNP). Although the tremendous physical, chemical, and metabolic diversity observed at these springs seemed to suggest a large diversity in the major element and trace metal content of microbes, we measured microbial elemental abundances within the range of those previously observed in more moderate settings. Before discussing the implications of this finding, we investigate patterns in the major and trace element abundances reported above.

3.4.1 What Causes High Biomass C:P and N:P Ratios?

The measured C:P and N:P ratios in separated biomass are relatively high compared to the canonical Redfield values, but comparable to those seen in suspended materials in P-limited lakes (Hecky *et al.*, 1993; Elser and Hassett, 1994; Elser *et al.*, 2000). For several samples, the measured ratios even exceed the high C:P and N:P values reported by these authors and, to our knowledge, are the highest reported.

What might cause such high ratios? Because low phosphorus concentrations were also measured in the springs sampled (Table 4), the low P abundances in separated material may reflect a scarcity of P (compared to C and N) in YNP environments (Adams *et al.*, 2008, J. Priscu, pers. comm.).

Another interpretation for such high ratios is that part of the carbon may not originate in biomass. One possible carbon source may lie in small, porous carbonate

particles of similar density as cells. However, the two separated samples with C:N ratios above previously reported ranges (090723F and 090730T1) were collected in acidic locations incompatible with any substantial persistence of carbonate minerals in sediment. Moreover, the presence of non-biological carbon would not explain the observed relatively high N:P ratios, and would likely lead to higher C:N ratios than observed.

The high C:N values for samples 090723F and 090730T1 reflect their low N content (rather than high C content). It may be that biological N was diluted due to significant amounts of sediment still present in these samples. Based on the C content of these two communities (29% and 26%, respectively) and assuming all C is biological (Appendix B, Table 22), the contribution from sediment to separated material cannot exceed 50% by mass in these samples. In this case, and if all the measured N is biological (Appendix B, Table 22), the biomass N content should be twice that measured, i.e., 2.4% for 090723F and 1.2% for 090730T1. Even in this extreme case of possible contamination, these upper limits on biomass N are at the lower end of previously reported ranges (Ho *et al.*, 2003; Cleveland and Liptzin, 2007; Nuester *et al.*, 2012), suggesting that these two communities were severely N-limited. Indeed, the bulk sediment N content for these samples was the lowest of the 14 samples for which we report C, N, and P abundances in Figs 11 through 13. Consequently, their bulk sediment C:N ratios were high (Fig. 12A), even though the dissolved N levels in the corresponding hot spring waters were generally in line with the other springs sampled (Table 4).

Thus, we favor the interpretation of low biomass N and P contents being due to a deficiency of N in a few springs and of P in most. In turn, these low abundances

cause high biomass C:N ratios in two samples and high biomass C:P and N:P ratios at most locations sampled.

A final possible interpretation is that under extreme physicochemical conditions, microbial cells may tend to grow slowly. As slow-growing cells have a lower reliance on P-rich biomolecules such as (ribosomal) RNA (Sterner and Elser, 2002), their P content may be lower than that of micro-organisms growing in more moderate environments. In this case, the low P content we measured in hot spring micro-organisms would be a consequence of a harsh environment limiting their growth rate rather than of a limited P supply, although these interpretations are not mutually exclusive. In addition, low P and N contents have been associated with acclimation to high temperatures due to a lower demand for enzymes and ribosomes under warm conditions, as enzymatic and ribosomal processes run more rapidly at higher temperatures (Woods *et al.*, 2003). Thus, relatively low N and P contents may reflect high temperature acclimation in the hot spring biota.

3.4.2 Patterns in Trace Element Abundances

Differences in the relative usage patterns of Ni, Cu, Zn, and Mo by microbial communities may relate to specific metabolic processes at play in hot springs because these four metals are often used as enzyme cofactors (Morel and Price, 2003). For example, we measured lower P:Mo ratios in the separated biomass of sites that do not support phototrophy due to the higher Mo content of chemotrophic cells (Fig. 16A). It may be that the cellular demand for Mo in chemotrophic communities is higher, perhaps for N cycling, formate oxidation, or sulfur oxidation, since Mo is present in enzymes key to these pathways (Morel and Price, 2003; Sauvé *et al.*, 2007; Windman

et al., 2007; Cabello *et al.*, 2009; Madigan *et al.*, 2012). Cellular Mo:C ratios were unrelated to concentrations of hot spring sulfide or nitrogen species (Fig. 15), but it is more likely that a response to resource availability would affect enzyme activity (which does not impact cellular requirements for Mo) rather than enzyme abundance. High Mo concentrations may also be due to Mo-bearing nanoparticles that escaped separation from cells (Brinza *et al.*, 2008).

Ni, Cu, and Zn abundances seem insensitive to the presence or absence of photosynthesis (Fig. 13). This is understandable in that these trace metals are not expected to be present at different abundances in photo- or chemotrophic organisms. For example, although Cu and Zn can be used for the dismutation of superoxide resulting from photosynthesis (Madigan *et al.*, 2012), Cu is also used in multiple chemotrophic pathways such as Fe oxidation, nitrification, anammox, and methanotrophy (Madigan *et al.*, 2012), while Zn plays a role in processing orthophosphate (Morel and Price, 2003; Paytan and McLaughlin, 2007). Ni may be dominant in chemosynthetic pathways (e.g. methanogenesis), but can also be used by phototrophs to catalyze the enzymatic dismutation of superoxide (Madigan *et al.*, 2012). In contrast, Mg is present in chlorophyll but plays little role in most chemosynthetic pathways (Madigan *et al.*, 2012); therefore we expect higher cellular Mg at locations that display signs of photosynthesis. However, such a correlation could not be assessed in our samples, as Mg was mainly contributed by sediment (Fig. 9).

We emphasize again here that the communities termed 'phototrophic' (i.e., which display visual signs of photosynthetic pigments) likely host chemotrophs as well. The contribution of these chemotrophs to the overall elemental composition of the community is unknown. Whether their contribution may affect the trends (or lack thereof) described above could be elucidated by measuring elemental compositions of

single cells (Heldal *et al.*, 2003; Steenbergh *et al.*, 2013), correlating these compositions with abundances per cell type (as determined, e.g., by morphology or fluorescence, see Fig. 7), and associating cell types to a taxonomic identification, e.g., by using Fluorescence In-Situ Hybridization (FISH) probes (e.g. Pernthaler *et al.*, 2001). Such a valuable (but time-consuming) approach would be complementary to ours. That trace element abundances or metal:C ratios seem unaffected by temperature (Fig. 14A–D), pH (Fig. 14E–H), sediment availability of the metal (Fig. 9E,I,K,O), or nutrient concentrations (data not shown) is surprising, given the extreme breadth in the ranges exhibited by the hot spring environments sampled regarding these parameters. This is further discussed below.

3.4.3 Ordinary Major and Trace Element Stoichiometries

The YNP hot springs from which we obtained samples spanned a much broader range of physicochemical conditions than natural environments for which elemental compositions of microbial biomass have previously been reported (Fig. 13). This can be seen by comparing Tables 3 and 4 with Table 7. In particular, the environmental ranges of temperatures (24°C to boiling near 93°C) and pH (1.6–9.6) in the YNP springs sampled are much wider than those indicated in Table 7 for natural samples, i.e., temperatures from -0.5°C to ≈30°C and pH generally between 7 and 8.5, with a few acidified lakes of pH as low as 4.5 (Hecky *et al.*, 1993). It is more difficult to compare other quantities (dissolved O_2, nutrients, and conductivity), which were infrequently reported by previous investigations [Table 7; this was also noted by Cleveland and Liptzin (2007)]. For microbial compositions reported for marine organisms, the composition of surface ocean water provides a useful guide. In surface oceans, the

range of dissolved oxygen abundances (3.2–5.7 mg L^{-1}; Matear and Hirst, 2003) is much narrower than that encountered in our sampling (0.1–9.2 mg L^{-1}). The dissolved Fe concentrations reported in Table 4 are much higher than those measured in seawater (Table 4), as expected given the dearth of Fe in the ocean (e.g. Twining *et al.*, 2004) and the hydrothermal nature of the springs. Some hot springs were much richer in nitrate (up to 13 mg L^{-1}) or ammonia (up to 42 mg L^{-1}) than any lake or marine environment reported in Table 4, for which dissolved N concentrations did not exceed 3 mg L^{-1}. Only the ranges of dissolved C and P (mostly phosphate) concentrations spanned by this and previous studies are similar. The composition of culture media from which elemental compositions of microbial biomass were reported is difficult to establish, largely because culture media contained ingredients of unknown elemental composition such as yeast. All reported media pH were close to 7, and only one study (Cameron *et al.*, 2012) reported elemental compositions for cultures grown at temperatures higher than 37°C (i.e., 85°C and 98°C).

Despite the large physicochemical variability of YNP hot springs compared to that of environments for which microbial elemental compositions have previously been reported, both the major and trace element stoichiometries of YNP hot spring microbes appear to be quite ordinary (that is, these stoichiometries are within the range of abundances measured in micro-organisms from moderate environments) regardless of the type of hot spring sampled and its taxonomic composition. Even though some communities have extremely high C:P and N:P ratios (which seem to result from adaptation to extreme nutrient limitation), these ratios seem to be pushing the stoichiometric envelope rather than being completely outside the norm. In the broadest sense, these relatively ordinary stoichiometries suggest a common core of organic and inorganic biochemistry that leads to elemental abundances constrained within a

common envelope typical of all microbes, at least for C, N, P, Ni, Cu, Zn, and Mo. This stoichiometric envelope spans several orders of magnitude in abundance for P and trace metals (Fig. 13), perhaps due to microbial adaptation to a variety of elemental supply conditions (Nealson and Saffarini, 1994; Fraústo da Silva and Williams, 2001; Saito *et al.*, 2003; Glass *et al.*, 2009; Dupont *et al.*, 2010; Twining and Baines, 2013). Careful attention should be paid to this variability within the stoichiometric envelope when modeling biogeochemical cycles of these elements, especially in light of strong couplings between biomass trace metal content and major element cycling (Morel and Price, 2003). For example, attempts at parameterizing biological fluxes of elements should explore model sensitivities to microbial abundances of trace elements spanning three or more orders of magnitude (Fig. 13). Regardless of their position on the phylogenetic tree and of their environment, microbial stoichiometries seem bound by this envelope. These constrained compositions may offer insight into the stoichiometric underpinnings of life on Earth. As reviewed in detail by Sterner and Elser (2002), the constrained relative proportions of the major elements C, N, and P in micro-organisms reflect the allocations of essential biomolecules to fulfill the requirements of life, such as nucleic acids for information storage, proteins for metabolism, and lipids for seclusion.

Does the (more loosely) constrained stoichiometry of trace elements satisfy a similar requirement? Like major elements, transition metals are essential to life. This crucial role arises from their redox sensitivity: in enzyme cofactors, they help transfer electrons whose exchange lies at the heart of metabolic processes that yield energy for growth (Vaccaro *et al.*, 2009). Because metalloenzymes are used in major element cycling (Morel and Price, 2003), one might expect a coupling between major and trace element requirements (Anbar and Knoll, 2002; de Baar and La Roche, 2003; Shaked *et al.*, 2006). However, unlike major elements, trace metals can in some instances

be substituted for one another without loss of their biological function (Sunda and Huntsmann, 1995; Yee and Morel, 1996; Lane *et al.*, 2005; Xu *et al.*, 2007; Morel, 2008; Dupont *et al.*, 2010). Thus, the specific physical and chemical properties of any given transition metal do not seem as narrowly specified for particular biological processes as those of major non-metals such as C or P. Moreover, similarities have been noted between the trace metal stoichiometry of life and that suspected to have prevailed in aqueous environments on Earth during the emergence of life (Fraústo da Silva and Williams, 2001; de Baar and La Roche, 2003; Novoselov *et al.*, 2013). Therefore, the ranges in trace metal stoichiometries of life on Earth may have been determined at the outset by those of its environment. That these starting stoichiometric ranges have been altered only in a minor way over the subsequent billions of years, as environmental conditions changed and life colonized a tremendous diversity of niches, suggests that the fundamental biochemical machinery built during life's emergence may have constrained its extended elemental composition. Nonetheless, one may hypothesize that life has been (and still is) pushing its stoichiometric envelope throughout its evolution.

If the trace element stoichiometry of life on Earth is but a sort of chemical 'vestigial characteristic' of the environment in which it emerged, one might expect lifeforms in extraterrestrial environments to use trace metals for redox metabolism in proportions that also mirror the environment of their emergence. Some extrasolar environments seem to provide an elemental supply radically different from Earth's (Young *et al.*, 2014); thus, we do not expect the trace elemental ranges reported in this study to hold for putative life that may have emerged in such exotic planetary settings.

3.5 Conclusion

We have reported measurements of major and trace element abundances of microbial communities collected in hot springs featuring a tremendous diversity of physico-chemical conditions. In spite of this diversity, microbial abundances of C, N, P, Ni, Cu, Zn, and Mo fell within the wide range of abundances measured in micro-organisms living in more moderate environments, albeit with extremely high C:P and N:P ratios in some communities. That even extremophilic micro-organisms have a rather ordinary stoichiometry for these elements indicates the existence of a common microbial stoichiometric envelope. While life's stoichiometric signature may vary somewhat with environmental conditions (Sterner and Elser, 2002; Dupont *et al.*, 2010; Zimmerman *et al.*, 2014) and was likely shaped by the initial palette of elements supplied as life emerged (Novoselov *et al.*, 2013), this signature appears to nevertheless remain anchored by biochemical constraints, even under the extreme range of selective pressures encompassed by our hot spring sampling. While we do not expect the elemental ranges reported here to hold for putative life that may have emerged in environments drastically different from Earth's, such as those suggested by recent observations of extrasolar systems (Young *et al.*, 2014), constrained elemental distributions may prove a useful means of detecting extant or extinct Earth-like life. Multi-element deviations from mineral background abundances at the spatial scales of cells or microbial mats (Storrie-Lombardi and Nealson, 2003) along with comparison of such elemental patterns against biological elemental ranges that seem robust to much of Earth's entire environmental spectrum (Fig. 13) may provide a biosignature. The sophisticated elemental instrumentation now in place on Mars (Yen *et al.*, 2005;

Gellert *et al.*, 2009; Meslin *et al.*, 2013) sets the stage for such analyses to emerge perhaps sooner than many have previously imagined.

Table 7: Physicochemical parameters for laboratory cultures and environments for which the extended elemental composition of biomass was reported in the literature cited

Sample name	Medium / Location	pH	T (°C)	Photo-synthesis?	C (ppm by mass)	N ($mg\ L^{-1}$)	O_2 (aq) ($\mu g\ L^{-1}$)	Fe ($\mu g\ L^{-1}$)	P analysis	Mo	Biomass
					Cultures						
E. coli (aerobic)[R64]	Glucose, salts	7.1	30	No	N/A	N/A	N/A	N/A	570000	N/A	AAS
Bacteria[R64]	Glucose, peptone, yeast, metals	7.1	30	No	N/A	N/A	N/A	N/A	N/A	N/A	AAS
Marine phytoplankton[H03]	Aquil medium [a]	N/A	19 ± 1	Yes	N/A	N/A	N/A	N/A	N/A	9.5	CHN, ICP-MS
E. coli[C12]	Lysogeny broth, trace metals	7	37	No	N/A	N/A	N/A	N/A	N/A	4000	ICP-MS
Methanococcus jannaschii[C12]	Cysteine, salts, trace metals	7	37	No	N/A	N/A	N/A	N/A	N/A	N/A	ICP-MS
Pyrococcus furiosus[C12]	Yeast, salts, trace metals	7	98	No	N/A	N/A	N/A	N/A	N/A	N/A	ICP-MS
					Natural samples						
Lake particulate matter[H93]	Arctic to tropical	> 4.5	N/A	Yes	0.13–50, median 0.45	0.016–3 [b]	N/A	N/A	1.8–240 [b]	N/A	CHN, Sp.
Lakes[EH94]	NE U.S & Canada	N/A	N/A	Yes	N/A	0.17–1.18 [c]	N/A	N/A	1.7–33 [c]	N/A	N/A
Marine and estuarine sites[EH94]	NW Atlantic, NE & SE Pacific	N/A	N/A	Yes	N/A	0.47–0.78 [c]	N/A	N/A	5.5–70 [c]	N/A	N/A
Marine plankton[T04]	Southern Ocean, 170°W	N/A	−0.5–5	Yes	N/A	0.28–0.32 as NO_3^-	N/A	$\sim 510^{-6}$	N/A	N/A	SXRF
Marine plankton[T11]	Equatorial Pacific Ocean	N/A	23–26	Yes	N/A	N/A	N/A	4–23 10^{-6}	N/A	N/A	SXRF, ICP-MS
Trichodesmium (N fixer)[N12]	Sargasso Sea	N/A	29	Yes	N/A	N/A	N/A	N/A	N/A	N/A	CHN, ICP-MS
	Indicative seawater (e.g Broecker, 1982; Levitus et al., *1993; Pilson, 2012; Matear and Hirst, 2003)*										
		7.5–8.5	0–30	Yes	DIC: ≈30, DOC: ≈1	0.08–0.33 as NO_3^-	3.2–5.7	510^{-6}	12–50	∼2	

Table 7: (Continued from previous page.) The corresponding biomass compositions were obtained by the technique reported in the "biomass analysis" column. An indicative seawater composition, relevant to marine samples, is provided for reference. [C12] Cameron *et al.* (2012). [EH94] Elser and Hassett (1994). [H93] Hecky *et al.* (1993). [H03] Ho *et al.* (2003). [N12] Nuester *et al.* (2012). [R64] Rouf (1964). [T04] Twining *et al.* (2004). [T11] Twining *et al.* (2011). Detailed environmental data were unavailable for biomass compositions reported in the references cited by Bruland *et al.* (1991) for North Pacific plankton (biomass analyses by atomic absorption spectrophotometry), as well as by Fagerbakke *et al.* (1996) for Scandinavian lake bacteria (biomass analyses by CHN and X-ray microscopy), and from the reviews by Cleveland and Liptzin (2007) for soil biomass, mostly from grassland and forest in climates ranging from arctic to tropical, and by Elser *et al.* (2000). AAS: Atomic Absorption Spectrophotometry. SXRF: Synchrotron X-Ray Fluorescence. Sp.: Spectrophotometry (for P). N/A: Not available. [a] Price *et al.* (1989). [b] Particulate nitrogen and phosphorus. [c] Total N and P, the sum of dissolved and particulate N and P.

Chapter 4

CORE CRACKING AND HYDROTHERMAL CIRCULATION CAN PROFOUNDLY AFFECT CERES' GEOPHYSICAL EVOLUTION

The previous two chapters were concerned with the microbial demands for elements in hydrothermal settings. In this and following chapters, we no longer characterize hydrothermal habitats from the perspective of biological requirements, but from that of environmental supply. We focus in particular on the occurrence of hydrothermal activity on dwarf planets for reasons provided below.

As stated in Chapter 1, hydrothermal systems require liquid water, a permeable matrix, and a thermal gradient to drive fluid circulation. In this chapter, I couple numerical thermal evolution models, which constrain the availability of liquid water and thermal gradients through space and time, to analytical models of rocky core fracturing, which constrain the permeability of the rock matrix through space and time. I apply these models to the dwarf planet Ceres. This chapter, which quantifies the extent of hydrothermal activity, is a first step towards coupling geophysical and geochemical processes in models of dwarf planet evolution; the subsequent steps are described in following chapters.

This chapter was published in the *Journal of Geophysical Research* with co-authors Steve Desch and Julie Castillo-Rogez. A summary of the results is provided below, followed by the text of the paper.

Observations and models of Ceres suggest that its evolution was shaped by interactions between liquid water and silicate rock. Hydrothermal processes in a heated core require both fractured rock and liquid. Using a new core cracking model coupled

to a thermal evolution code, we find volumes of fractured rock always large enough for significant interaction to occur. Therefore, liquid persistence is key. It is favored by antifreezes such as ammonia, by silicate dehydration which releases liquid, and by hydrothermal circulation itself, which enhances heat transport into the hydrosphere. The effect of heating from silicate hydration seems minor. Hydrothermal circulation can profoundly affect Ceres' evolution: it prevents core dehydration via "temperature resets", core cooling events lasting ∼50 Myr during which Ceres' interior temperature profile becomes very shallow and its hydrosphere is largely liquid. Whether Ceres has experienced such extensive hydrothermalism may be determined through examination of its present-day structure. A large, fully hydrated core (radius 420 km) would suggest that extensive hydrothermal circulation prevented core dehydration. A small, dry core (radius 350 km) suggests early dehydration from short-lived radionuclides, with shallow hydrothermalism at best. Intermediate structures with a partially dehydrated core seem ambiguous, compatible both with late partial dehydration without hydrothermal circulation, and with early dehydration with extensive hydrothermal circulation. Thus, gravity measurements by the *Dawn* orbiter, whose arrival at Ceres is imminent, could help discriminate between scenarios for Ceres' evolution.

4.1 Introduction

The imminent exploration by spacecraft of the dwarf planet Ceres has motivated recent extensive telescopic observations (Thomas *et al.*, 2005; Li *et al.*, 2006; Carry *et al.*, 2008; Drummond and Christou, 2008; Milliken and Rivkin, 2009; Rousselot *et al.*, 2011; Küppers *et al.*, 2014; Drummond *et al.*, 2014), as well as the development of models of Ceres' geophysical evolution and present state (McCord and Sotin, 2005;

Castillo-Rogez and McCord, 2010; Castillo-Rogez, 2011; Zolotov, 2014). Observations and models both suggest that liquid water may have persisted in the interior of Ceres over geological timescales, possibly until present (Castillo-Rogez and McCord, 2010; Rivkin *et al.*, 2012; McCord *et al.*, 2012). Liquid persistence may be enabled below 273 K by salt or volatile antifreezes such as methanol or ammonia (Hussmann *et al.*, 2006; Desch *et al.*, 2009; Castillo-Rogez and McCord, 2010; Sohl *et al.*, 2010).

If present over such extended timescales, liquid water could have played a major role in shaping the geophysical evolution of Ceres. For example, interactions between liquid water and Ceres' rocky core could have occurred, altering physical and chemical properties of the silicates. Common products of such interactions, carbonates and clay minerals, are seen on Ceres' surface (Milliken and Rivkin, 2009; Rivkin *et al.*, 2012). Water-rock interactions may have influenced Ceres' geophysical evolution in several ways. First, dry silicates may have hydrated once in contact with liquid water at lower temperatures. Hydration causes rock to swell and tends to decrease its thermal conductivity (Horai, 1971; Castillo-Rogez and McCord, 2010), resulting in a larger core that better retains heat. Second, hydration reactions tend to be highly exothermic (Cohen and Coker, 2000), adding to Ceres' heat budget. Third, chemical interactions between water and rock may leach out radiogenic elements, such as potassium, from core silicates (Castillo-Rogez and Lunine, 2010; Castillo-Rogez and McCord, 2010). Similarly, salt or volatile antifreezes such as ammonia, invoked as a requirement for liquid over the long term (e.g. Desch *et al.*, 2009; Castillo-Rogez and McCord, 2010; Rubin *et al.*, 2014), may be produced or consumed in water-rock reactions (Matson *et al.*, 2007; Fortes *et al.*, 2007; Glein *et al.*, 2009). Finally, water can circulate through pores or fractures in the core and efficiently transport heat outwards in a convective pattern known as hydrothermal circulation (Young, 2001; Young *et al.*, 2003).

The major part of water-rock interactions presumably occurs in core macro- and micro-fractures (connected pores), because these offer a much greater area of water-rock interface than the core's outer surface ("seafloor"), as well as higher temperatures that speed up kinetically-controlled chemical reactions. Moreover, core fractures could feature chemical disequilibria at water-rock interfaces. The availability of chemical energy and presence of liquid water make long-lived core cracks a potential habitat for life as we know it.

The extent of fracturing in Ceres' core is unknown, and, to our knowledge, neither the extent of core fracturing nor the effects of water-rock interaction have been investigated in models of Ceres' evolution. A key reason for this is that models of core fractures on icy bodies have focused on cooling cracks (Vance *et al.*, 2007), while models of Ceres suggest that by the time the core starts cooling the icy shell is mostly frozen (Castillo-Rogez and McCord, 2010). However the problem is still worth visiting, first because long-term liquid may persist due to antifreezes, and second because cracking can also result from heating (Norton, 1984), which on Ceres likely occurred concurrently with the presence of liquid (Castillo-Rogez and McCord, 2010).

Coupled geophysical-geochemical evolution models have so far focused on the evolution of planetesimals (Cohen and Coker, 2000; Grimm and McSween, 1989; Palguta *et al.*, 2010) or icy moons (Travis *et al.*, 2012). Local hydrothermal systems around magmatic intrusions on Martian volcanoes or impact craters have also been modeled (e.g. Newsom, 1980; Gulick, 1998; Rathbun and Squyres, 2002; Abramov and Kring, 2005; Pope *et al.*, 2006; Barnhart *et al.*, 2010; Schwenzer *et al.*, 2012b). Several of these studies have used numerical codes developed for Earth applications, such as SUTRA (Voss and Provost, 2010) and HYDROTHERM (Hayba and Ingebritsen, 1994), which model fluid flow in porous media. A third code, MAGHNUM, was

developed to model local hydrothermal systems on planets (Travis *et al.*, 2003), and later expanded as a global planetary thermal evolution code (e.g. Travis *et al.*, 2012). Although MAGHNUM incorporates the effects of hydrothermal circulation, it does not account for silicate hydration or dehydration. A geophysical model of the present state of potential hydrothermal systems on water-rich bodies has been developed (Vance *et al.*, 2007; Sohl *et al.*, 2010), but this model has not been applied to Ceres and neglects time evolution. This model is further discussed below. Finally, time-evolution models developed by Malamud and Prialnik (2013, 2015) and applied to Enceladus, Mimas, and Kuiper belt objects include the rock swelling and heating effects due to serpentinization, the flow of water liquid and vapor, and a detailed treatment of rock and ice porosity by means of equations of state. These models therefore offer an opportunity for comparison with those presented here.

There exist recent, sophisticated models of hydrothermal systems in the Earth sciences. These generally focus on a specific aspect of these systems, such as 3D fluid flow in porous or fractured media (Person *et al.*, 2012), vapor-brine phase separation and salinity (Han *et al.*, 2013), or transport of reactive fluid (Steele-MacInnis *et al.*, 2012; Ord *et al.*, 2012). In practice, these aspects feed back on one another. However, their integration into a single detailed model of the physics and chemistry of local or globally-averaged hydrothermal systems remains a challenge to existing computational capabilities (Ingebritsen and Appold, 2012). Most of these models do not discuss the appearance or disappearance of pores or fractures, mainly because the feedbacks with reactive hydrothermal flow are not well understood (Ingebritsen *et al.*, 2010), but also because many models focus on simulating hydrothermal systems limited in their spatial extent and lifetime. The models that focus on spatially variable or anisotropic porosity and permeability generally assume that these properties remain invariant

over time (Xu and Pruess, 2001; Jones *et al.*, 2004), or consider simple geometries of restricted spatial extent (Bolton *et al.*, 1999).

In the following sections, we first briefly review the global thermal evolution model on which we base this study (Desch *et al.*, 2009). Next, we present a model for core fracturing which expands on the work of Vance *et al.* (2007) and suggestions of Travis *et al.* (2012), and which is inspired by models of hydrothermal systems on Earth. We then explain how this model is incorporated as a cracking subroutine into the thermal evolution code of Desch *et al.* (2009), along with the inclusion of silicate hydration and dehydration, and hydrothermal circulation in the porous layer. The level of detail in the resulting code is similar to that of Malamud and Prialnik (2013, 2015), albeit with a different approach in the treatment of differentiation, porosity, and hydrothermal heat transfer. We apply the model to Ceres and investigate the influence of fracturing and physical water-rock processes on its evolution.

4.2 Thermal Evolution Code

The code of Desch *et al.* (2009) performs time-dependent calculations of the internal temperature profile and structure of bodies made of rock and ice. It is applicable to objects roughly 300 to 1500 km in radius, as it neglects porosity (significant below this radius range) and the compressibility of rocky and icy materials (significant above this range) as well as high-pressure phases of ice.

Inputs to the code are body radius, density, ammonia content, surface temperature, initial temperature (isothermal radial profile), and time of formation, as well as the total simulation time. From the density input, a bulk rock-to-ice ratio is determined. The initial structure is assumed homogenous and undifferentiated, and mass is distributed

assuming spherical symmetry on a fixed-volume 1D grid, with a specified number of zones evenly distributed in radius (typically 200). The internal energy in each grid zone is computed from the initial temperature using equations of state, detailed by Desch *et al.* (2009), for rock and ice (which includes water ice I, liquid water, liquid ammonia, and ammonia dihydrate I). It is assumed that any accretional heating has been dissipated before the starting time of the simulation.

From this initial state, the internal energy E_i in each grid zone i of outer radius r_i is updated after a time step Δt. This time step (typically fixed at 50 years) must satisfy a Courant condition $\Delta t < \min[(\Delta r)^2/(2\kappa_d)]$, where κ_d is the thermal diffusivity. Energy changes are due to heat fluxes F_i out of each zone, radiogenic heating $Q_{i,\mathrm{rad}}$, and gravitational energy release $Q_{i,\mathrm{grav}}$:

$$\frac{E_i(t+\Delta t) - E_i(t)}{\Delta t} = 4\pi r_{i-1}^2 F_{i-1} - 4\pi r_i^2 F_i + Q_{i,\mathrm{rad}}(t) + Q_{i,\mathrm{grav}} \tag{4.1}$$

Heat fluxes, assumed conductive, are computed using a finite-difference scheme as:

$$F_i = -\frac{k_i + k_{i+1}}{2} \frac{T_{i+1} - T_i}{(r_{i+1} - r_{i-1})/2} \tag{4.2}$$

Here, k_i are the thermal conductivities in each grid zone; chosen expressions are given by Desch *et al.* (2009) and in Table 11. In the ice shell, possible heat transfer by solid-state convection, rather than conduction, is accounted for by parameterizing k_i in terms of the Rayleigh number in the shell (Desch *et al.*, 2009). Vigorous convective heat transfer is also assumed to occur in any grid zone containing more than 2% liquid ("slush"); in this case the thermal conductivity is set arbitrarily to a value of 400 W m^{-1} K^{-1}, high enough to obtain a near-isothermal temperature profile across the slush layer. T_i are the temperatures, computed such that E_i is the energy required to raise the mix of rock and ices from 0 K to T_i, including phase transitions, using the

equations of state mentioned above. The boundary conditions are zero heat flux at the center (by symmetry), and a fixed temperature (i.e., fixed energy) at the surface as determined in the input.

The heating term $Q_{i,\mathrm{rad}}(t)$ due to the decay of radionuclides j is given by:

$$Q_{i,\mathrm{rad}}(t) = M_{rock,i} \sum_j N_j \ \Delta E_j \ \ln(2)/t_{1/2,j} \ \exp(-\ln(2)/t_{1/2,j} \ \times \ t) \qquad (4.3)$$

where $M_{rock,i}$ is the mass of silicate rock in a zone i, N_j is the number of atoms of the nuclide j per kg of rock, ΔE_j is the energy produced per decay, and $t_{1/2,j}$ is the nuclide half-life. These parameters are given by Desch *et al.* (2009) for the long-lived radionuclides ^{40}K, ^{232}Th, ^{235}U, and ^{238}U. ^{26}Al decay heating is also accounted for, assuming a half-life of 716000 years, a ^{26}Al/^{27}Al atomic fraction of 5×10^{-5} (Castillo-Rogez *et al.*, 2007), an initial abundance of 8.41×10^4 Al atoms per 10^6 Si atoms (Lodders, 2003), and a calculated energy heat per decay ΔE of 3.177 MeV (within 2% of the value estimated by Castillo-Rogez and Lunine (2010) using the same method, but slightly different assumptions on neutrino energies (Desch *et al.*, 2009)). These values yield an initial heating rate $\Delta E_j(\ln 2/t_{1/2})$ $(N_j/10^6)/(151\ m_{\mathrm{nucleon}})$ of 0.26 μW/kg of rock, assuming that rock contains on average 151 nucleons for every Si atom.

Ice-rock differentiation occurs if the temperature in a zone exceeds a threshold T_{diff}. Physically, it is assumed that differentiation is initiated by ice melting at a temperature of first melt (solidus) that depends on initial ammonia content. For non-negligible amounts of ammonia (arbitrary mass fraction of 10^{-2} with respect to H_2O), we set $T_{\mathrm{diff}} = 176$ K; otherwise we set $T_{\mathrm{diff}} = 273$ K. In practice, melting first occurs in the central zones and differentiation proceeds outward. In all the zones exceeding T_{diff}, the code redistributes mass by first filling the innermost zones with rock, then the

zones surrounding this rocky core with liquids and ammonia dihydrate, and finally the outermost differentiated zones with pure water ice. This approach ensures mass conservation. Volume changes are precluded by choosing fixed densities for liquid water and ammonia, slightly different from their actual values: the density of liquid water $\rho_{\mathrm{H2O\ (l)}}$ is equated to that of ice $\rho_{\mathrm{H2O\ (s)}}$, and the density of ammonia $\rho_{\mathrm{NH3\ (l)}}$ is determined by mass balance: ${\rho_{\mathrm{NH3\ (l)}}}^{-1} = {\rho_{\mathrm{H2O\ (l)}}}^{-1} + ({\rho_{\mathrm{H2O\ (s)}}}^{-1} + {\rho_{\mathrm{ADH\ (s)}}}^{-1})/X_c$, where ${\rho_{\mathrm{ADH\ (s)}}}^{-1}$ is the density of ammonia dihydrate and $X_c = 0.321$ is the eutectic ammonia mass fraction. Density values are provided by Desch *et al.* (2009).

Differentiation leads to a gravitationally unstable configuration, with an ice mantle underneath a denser, undifferentiated crust. Such a configuration is prone to Rayleigh-Taylor instabilities, which Rubin *et al.* (2014) showed act on geological timescales in zones where $T_i > T_{\mathrm{diff}} \approx 140$ K. This value of T_{diff} is adopted in the late stages of differentiation.

Differentiation generates heat due to gravitational energy release. The gravitational potential energy U_g is calculated at each time step:

$$U_g = -G \int_0^{R_{\mathrm{P}}} 4\pi r^2 \rho(r) \frac{M(r)}{r} dr \tag{4.4}$$

where $M(r)$ is the mass enclosed within a sphere of radius r and G is the gravitational constant. If differentiation has redistributed mass and changed U_g during a time step, this energy difference ΔU_g is redeposited uniformly throughout all differentiated shells, out to a radius R_{diff}. The corresponding heating term $Q_{i,\mathrm{grav}}$ in equation (4.1) is given by:

$$Q_{i,\mathrm{grav}} = \frac{\Delta U_g}{\Delta t} \frac{r_i^3 - r_{i-1}^3}{R_{\mathrm{diff}}^3} \tag{4.5}$$

This thermal evolution code, which accounts for ice-rock differentiation and ammonia antifreeze, is our starting point for exploring consequences of the persistence of liquid water interacting with a rocky core over geological timescales. We now proceed to quantify the extent of these interactions using a core fracturing model, which we describe below.

4.3 Geophysical-Geochemical Model of Core Fracturing

Modeling the extent of macro- and microfracturing in the cores of icy worlds over geologic time provides an estimate of the extent of hydrothermal circulation. In turn, such estimates constrain the magnitude of the coupling between geophysical and geochemical processes in icy world evolution. In this section, we describe a new model of core fracturing.

We assume that icy body cores are made of ferromagnesian silicate minerals, either dry or hydrated. Such compositions are typical of Earth's upper mantle (Sohl *et al.*, 2010), and also compose ordinary and carbonaceous chondrites. Therefore, we do not account for alkali-rich minerals.

We model five phenomena which may influence core fracturing on small and large scales: (1) the brittle-ductile transition in hydrated rock; micro-cracking by (2) thermal expansion mismatch of mineral grains and (3) expansion of pore water upon heating; and micro- and macro-crack shrinking due to (4) rock swelling during hydration (as well as crack widening during dehydration) and (5) precipitation of mineral species (as well as widening due to dissolution). We account for elastic opening and closing of cracks. Many other phenomena may affect cracking, such as compaction and thermal expansion of the solid rock matrix (Germanovich *et al.*, 2001), increases in

fluid pressures from precipitation clogging (Germanovich *et al.*, 2001), exsolution of volatiles from water (Kelley *et al.*, 1993), pressure solution of species (Bolton *et al.*, 1999), anisotropy in the permeability of rock (Bolton *et al.*, 1999), multi-phase flows (Goldfarb and Delaney, 1988; Xu and Pruess, 2001; Ingebritsen *et al.*, 2010; Han *et al.*, 2013), and exogenous impacts (Bowling *et al.*, 2014). We neglect these phenomena in this simple approach.

4.3.1 Brittle-Ductile Transition in Hydrated Rock

The extent of core cracking is limited by the healing timescale of cracks. Cracks heal when rock accommodates stresses in a ductile or plastic fashion at high pressure and temperature. We do not distinguish between the brittle-ductile and brittle-plastic transitions (Kohlstedt *et al.*, 1995), and will refer to the transition as brittle-ductile. This transition occurs when the brittle and ductile rock strengths are equal. Such a model successfully predicts the strength profile of Earth's lithosphere with depth (Kohlstedt *et al.*, 1995; Escartin *et al.*, 1997a).

The frictional strength of brittle rock, τ, is given as a function of normal stress σ by (e.g. Kohlstedt *et al.*, 1995):

$$\tau = \mu_{\mathrm{f}} \left(\sigma - P_w\right) + C_{\mathrm{f}} \tag{4.6}$$

where μ_{f} is the coefficient of friction, P_w is the fluid pressure, and C_{f} is the frictional cohesive strength. Empirically, μ_{f} and C_{f} are found to be similar regardless of rock type (Byerlee, 1978), leading to a relationship called Byerlee's rule: $\tau = 0.85\ \sigma$ for $\sigma < 200$ MPa, and $\tau = 50 + 0.6\ \sigma$ between 200 and 1700 MPa ($C_f = 50$ has units of MPa). Hydrated clays are exceptions to this rule (Brace and Kohlstedt, 1980): for serpentine

rock (lizardite, antigorite or chrysotile), Escartin *et al.* (1997b, 2001) found that a brittle strength with $\mu_\mathrm{f} = 0.3$ to 0.5 and $C_\mathrm{f} = 0$ better fitted data from deformation experiments at pressures up to 1 GPa. The dependence of μ_f on temperature is unclear, with reports of both increases (Moore *et al.*, 1997) and decreases within a large range of 0.1 to 0.85 (Hirth and Guillot, 2013). Strengths $\tau \approx 0.4\ \sigma$ also seem to apply to rocks that are just slightly serpentinized (Escartin *et al.*, 2001). We adopt values of 0.4 for μ_f and set $C_\mathrm{f} = 0$ for hydrated silicates, use Byerlee's rule for dry silicates, and combine linearly the dry and hydrated rock strengths for partially hydrated silicates. We neglect changes in these parameters with temperature. To derive a rock strength value, we assimilate the normal stress as the confining pressure $P(r)$. In practice, P_w can be taken as 0 since the brittle-ductile transition occurs above the dehydration temperature of rock (see below and Fig. 25), such that water does not affect the frictional behavior of rock.

The ductile behavior of crystalline rock at temperature T and pressure P is described by a flow (creep) law of the form (e.g. Weertman *et al.*, 1978; Kohlstedt *et al.*, 1995):

$$\dot{\epsilon} = A\sigma^n d^{-p} \exp\left(-\frac{Q + PV}{RT}\right) \tag{4.7}$$

Here, $\dot{\epsilon}$ is the strain rate of the material, σ the differential stress necessary for creep to occur at this rate, A is a dimensionless material parameter, d is the grain size, p is the grain size exponent, Q and V are the creep activation energy and volume of the material, and R is the ideal gas constant. Although typical Earth mantle rheologies incorporate several creep mechanisms in parallel or series combinations (Kohlstedt *et al.*, 1995), experimental measurements on serpentine in the ductile regime are scarce. At the temperatures, pressures, and differential stresses typical of icy dwarf planet

cores (T = 200 to 1500 K, P = 10 to 4000 MPa, $\sigma < 1$ GPa), the relevant flow regime is diffusion creep, even for mm-sized grains. Rutter and Brodie (1988) found equation (4.7) to describe the diffusion creep of serpentinite for T between 573 and 873 K, P between 180 and 300 MPa, grain sizes between 0.1 and 60 μm, and differential stresses between about 5 and 170 MPa, with $A = 10^{5.62}$, $n = 1$, $p = 3$, $Q = 240$ kJ, and $V = 0$ (with σ in MPa and d in microns). These values yield a flow law close to that of wet diffusion creep of olivine compiled by Korenaga and Karato (2008), which included data collected at temperatures from 1473 K to 1573 K, confining pressures from 100 MPa to 2100 MPa, differential stresses from 4 to 410 MPa, strain rates from 10^{-3} to 0.7×10^{-6} s^{-1}, and grain sizes from 1 to 70 μm. Above the dehydration temperature of serpentine, 730 to 900 K (Perrillat *et al.*, 2005; Evans *et al.*, 2013), the relevant flow law becomes that of diffusion creep in olivine in dry conditions. Such a law was also compiled by Korenaga and Karato (2008) and the flow parameters are very similar to those of wet diffusion and those of Rutter and Brodie (1988). We therefore adopt the flow parameters of Rutter and Brodie (1988), short of measurements at lower T and lower strain rates more representative of conditions inside dwarf planets. The ductile strength τ is the differential stress σ that causes creep. The ductile strength is typically insensitive to P and $\dot{\epsilon}$ (Kohlstedt *et al.*, 1995), but very sensitive to T, contrary to the brittle strength which is sensitive to P, but not to T.

The rock strength is the lower of its brittle and ductile strengths. It is highest at the brittle-ductile transition (Fig. 18). In practice, we find the strain rate $\dot{\epsilon}$ for which the brittle and ductile strengths are equal, and assume cracks are healed past a time $1/\dot{\epsilon}$. At each time step, in cracked grid zones, this $1/\dot{\epsilon}$ timescale is compared to the time elapsed since cracking last occurred; the zone is assumed no longer cracked if the time elapsed is greater than $1/\dot{\epsilon}$. Because $\dot{\epsilon}$ in a given grid zone changes at each time

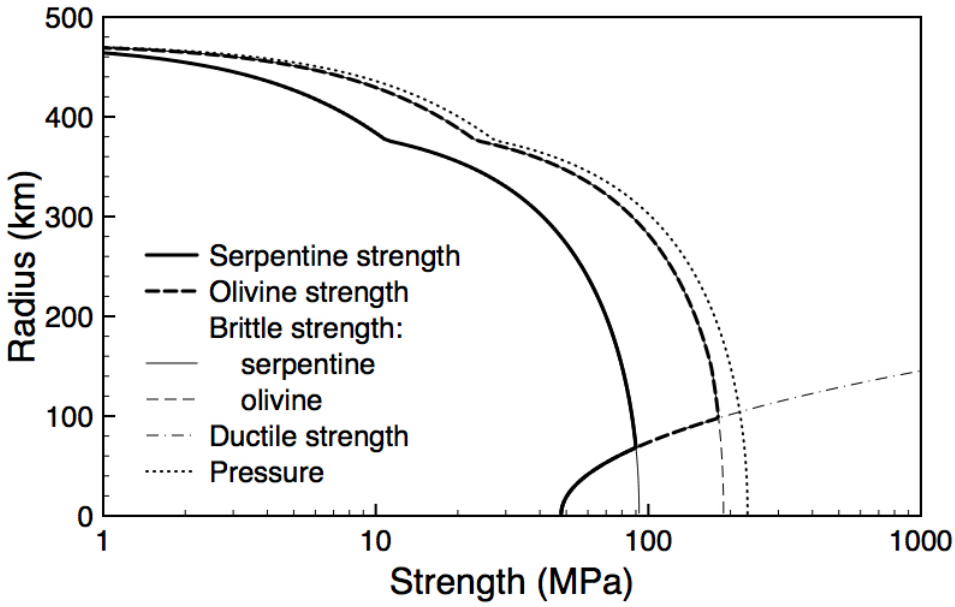

Figure 18: Dry (olivine) and hydrated (serpentine) rock strengths inside a Ceres-type dwarf planet

The olivine brittle strength follows Byerlee's law. The serpentine brittle strength is $\tau = 0.4\ P$ (Escartin *et al.*, 1997b). The ductile strength $\tau = \dot{\epsilon}\ A\ d^p \exp[Q/(R\ T)]$ is derived from Rutter and Brodie (1988); a strain rate of $(10\ \text{Myr})^{-1}$ and a grain size of 1 μm are assumed. The kink in the curves at radius 375 km marks the rocky core - icy mantle boundary in this model.

step (primarily due to temperature changes), the code heals cracks by a fractional factor (time elapsed since cracking)$\times\dot{\epsilon}(t)$ at each time step and cracks are removed once the cumulative fraction is 1. Except for this estimation of crack lifetime, the healing fraction has no effect on the geophysics and geochemistry included in the code (e.g., no impact on crack size).

4.3.2 Micro-Cracking by Thermal Expansion Mismatch

Core micro-cracks can develop when a rocky core either heats up and expands, or cools and contracts. Vance *et al.* (2007) modeled the cooling and contraction aspects, but their model holds for heating and expansion as well. We summarize their model, adapted from Evans and Clarke (1980) and Fredrich and Wong (1986).

Thermal expansion anisotropies between square silicate grains result in a mean stress $\overline{\sigma}$ that depends on the cooling rate $\dot{T}$ (Fig. 19a). $\overline{\sigma}$ is given by:

$$\frac{d\overline{\sigma}}{dT} = \frac{96\Omega D_0 \delta_b E}{3^{1/2} k_b d^3 \dot{T}} \frac{e^{-\frac{Q_{\rm gb}}{RT}}}{T} \overline{\sigma} - \frac{\beta E \Delta\alpha}{1+\nu} \tag{4.8}$$

This equation includes stress relaxation by creep (first right-hand term) and elastic processes (second term). The threshold temperature at which stress starts accumulating is T', defined such that $\overline{\sigma}(T') = 0$. An approximate analytical expression for T' is:

$$T' \approx \frac{Q_{\rm gb}}{R} \left[\ln \left(\frac{96\Omega D_0 \delta_b E}{3^{1/2} n k_b d^3 \dot{T}} \right) \right]^{-1} \tag{4.9}$$

In equations (4.8) and (4.9), Ω is the atomic volume, D_0 and δ_b are the grain boundary diffusion coefficient and width, E is Young's modulus for all grains, k_b is Boltzmann's constant, $Q_{\rm gb}$ is the activation enthalpy for grain boundary sliding, β is the boundary angle, $\Delta\alpha$ is the thermal expansion anisotropy, ν is Poisson's ratio, and n is a fitting parameter.

Let us consider an inclusion within a matrix. If the thermal expansion coefficient of the inclusion is higher than that of the matrix, compressive or tensile stresses will develop upon heating or cooling, respectively. This can also occur between two adjacent grains similar in mineralogy, but differing in orientation, that do not undergo

isotropic thermal expansion: Bouhifd *et al.* (1996) showed that thermal expansion coefficient anisotropies could be on the order of $\sim 10^{-6}$ K^{-1}. Micro-fractures occur when the stress intensity K_I exceeds a critical value, the fracture toughness K_{IC}. K_I is estimated from T and P:

$$K_I = \sqrt{\frac{2}{\pi a}} \int_0^a \frac{\sigma_{yy}(x, T, T')\ x^{1/2}}{(a-x)^{1/2}} dx - P_c \cdot (\pi a)^{1/2} \tag{4.10}$$

where a flaw of size $a < d$ extends from the grain boundary (x=0) to $x = a$. P_c is the confining pressure, which tends to reduce stress, and $\sigma_{yy}(x, T, T')$ is the normal stress along the x-axis:

$$\begin{aligned} \sigma_{yy}(x, T, T') = \frac{E\Delta\alpha(T'-T)}{2\pi(1-\nu^2)} \Bigg(& \frac{d^2}{d^2+(d-x)^2} \\ & - \frac{d^2}{d^2+x^2} + \ln\left[\frac{d-x}{x}\right] \\ & - \frac{1}{2}\ln\left[\frac{d^2+(d-x)^2}{d^2+x^2}\right] \Bigg) \end{aligned} \tag{4.11}$$

K_I and K_{IC} are substituted to differential stress σ and rock strength τ because crack propagation depends on the product of the differential stress and the square root of flaw length (Griffith, 1921).

The flaw size $a < d$ is chosen so as to maximize K_I. To avoid the calculation of the integral in equation (4.10) at each grid zone and time step, we tabulate values of $a(K_{Imax})$ separately from the main code for a range of P and T.

Parameter values can be found in Tables 8 and 9. Vance *et al.* (2007) used parameters for olivine, although one expects cracking to occur also in hydrated serpentine. With increasing hydration, Young's modulus decreases from 200 to 35 GPa and Poisson's ratio increases from 0.25 to 0.35 at room temperature (Christensen, 1966). The values for both parameters increase only by about 10% or less from 50

Table 8: Description of model parameters specific to dry or hydrated silicates

Parameter	Description	Value	Units	References and Notes
			Dry silicates	
E	Young's modulus	200	GPa	Christensen (1966); Hirth and Kohlstedt (1995)
ν	Poisson's ratio	0.25		Christensen (1966, 1996)
μ_f	Friction coefficient	0.85		Byerlee (1978); $P < 200$ MPa
		0.6		$P > 200$ MPa
C_f	Cohesive strength	0	MPa	Byerlee (1978); $P < 200$ MPa
		50	MPa	$P > 200$ MPa
K_{IC}	Fracture toughness	1.5	MPa $m^{1/2}$	DeMartin *et al.* (2004); Balme *et al.* (2004)
ρ	Density	3800	kg m^{-3}	Chung (1971)
			Hydrated silicates	
E	Young's modulus	35	GPa	Christensen (1966); Hirth and Kohlstedt (1995)
ν	Poisson's ratio	0.35		Christensen (1966, 1996)
μ_f	Friction coefficient	0.4		Escartin *et al.* (1997b)
K_{IC}	Fracture toughness	0.4	MPa $m^{1/2}$	Tromans and Meech (2002); Funatsu *et al.* (2004); Backers (2005); Wang *et al.* (2007)
ρ	Density	2600	kg m^{-3}	Tyburczy *et al.* (1991); Auzende *et al.* (2006); Nestola *et al.* (2010)

to 1000 MPa (Christensen, 1966), and $\partial E/\partial T$ and $\partial \nu/\partial T$ for olivine seem small at room temperature (Kumazawa and Anderson, 1969). Therefore, we neglect the changes in E and ν with P and T, but not their change with hydration. We adopt values of E and ν linearly interpolated between olivine and serpentine end members (Table 8), depending on the degree of hydration of the silicates. While these values are appropriate for bulk silicates, loosely consolidated rock can have a much smaller Young's modulus.

The fracture toughness of olivine in hydrothermal areas was experimentally determined to be $K_{IC} \approx 0.6 \pm 0.3$ MPa $m^{1/2}$ (DeMartin *et al.*, 2004), which is the value used by Vance *et al.* (2007). However, K_{IC} for olivine may be as high as 2 MPa $m^{1/2}$ (Balme *et al.*, 2004; Backers, 2005). The fracture toughness of clays and salts ranges from 0.1 to 1.5 MPa $m^{1/2}$ (Tromans and Meech, 2002; Backers, 2005; Wang *et al.*, 2007). Funatsu *et al.* (2004) found that the fracture toughness of sandstone is relatively insensitive to temperature but increases linearly with pressure, from 0.5 to 2.5 MPa $m^{1/2}$ between atmospheric pressure and 10 MPa, which is half of the pressure expected at Ceres' seafloor (Fig. 18). In view of these results, we set a canonical

value of K_{IC} of 0.4 MPa $m^{1/2}$ for hydrated silicates and 1.5 MPa $m^{1/2}$ for dry silicates. Again, we interpolate linearly between these two end members, depending on the degree of hydration.

Fredrich and Wong (1986) used values of E, $\Delta\alpha$, ν, d, and K_{IC} close to those chosen by Vance *et al.* (2007) and those used here. They showed that the above equations provide a temperature mismatch for the onset of cracking compatible with thermal cracking experiments performed from room temperature up to 1000°C, with typical total increases of order 100°C. Similar temperature changes are predicted by thermal evolution models of Ceres (Castillo-Rogez and McCord, 2010), albeit at a much slower rate than in the experiments of Fredrich and Wong (1986). Slow heating allows the rock matrix to relax; this is captured by the use of the temperature of zero stress T' (Evans and Clarke, 1980) instead of an initial temperature T_0 in the equations of Fredrich and Wong (1986).

4.3.3 Expansion of Pore Water upon Heating

In hydrated areas, pore fluid is at confining pressure P_c. However, fluid can expand upon heating. Expansion increases fluid pressure, creating a differential stress that can open micro-cracks if this stress is higher than the rock strength (Paterson and Wong, 2005; Travis *et al.*, 2012) (Fig. 19b). We account for pore fluid expansion following Norton (1984) and Le Ravalec and Guéguen (1994) (see also Dutrow and Norton (1995) and Norton and Dutrow (2001)). For a temperature increase dT, the fluid pressure P_{fluid} increases by $\partial P/\partial T \times dT$. $\partial P/\partial T$ can be expressed as the ratio of the thermal expansivity of liquid water α_w to its isothermal compressibility β_w (Norton, 1984; Bizzarri and Cocco, 2006). Furthermore, because of the elongated

Table 9: Description of model parameters not specific to dry or hydrated silicates

Parameter	Description	Value	Units	References
		General parameters		
D_i	Initial subgrid crack width	10^{-2}	m	
D	Crack width		m	
τ	Rock strength		Pa	
P_c	Confining pressure		Pa	
		Brittle-ductile transition		
n	Flow law index	1		Rutter and Brodie (1988)
p	Grain size exponent	3		Rutter and Brodie (1988)
d	Grain size	500	μm	Vance *et al.* (2007)
Q	Flow law activation energy	240 ± 40	kJ	Rutter and Brodie (1988)
A	Flow law coefficient	$10^{5.62}$		Rutter and Brodie (1988)
V	Flow law activation volume	0	m^3	Rutter and Brodie (1988)
$\dot{\epsilon}$	Flow law strain rate		s^{-1}	
		Thermal expansion and contraction mismatch		
a	Flaw size	$a < d$	m	Vance *et al.* (2007)
$D_0\delta_b$	Grain boundary diffusion coefficient × Width	$1.5 \times 10^{-0.8}$	$m^2\ s^{-2}$	Hirth and Kohlstedt (1995)
K_I	Stress intensity		MPa $m^{1/2}$	
n	Fitting parameter	23		Vance *et al.* (2007)
Q_{gb}	Activation energy for grain boundary sliding	3.15×10^5	J mol^{-1}	Hirth and Kohlstedt (1995)
$\Delta\alpha$	Thermal expansion anisotropy	3.1×10^{-6}	K^{-1}	Bouhifd *et al.* (1996)
β	Boundary angle	$\pi/6$	radians	Vance *et al.* (2007)
Ω	Atomic volume	1.23×10^{-29}	m^3	Hirth and Kohlstedt (1995)
T'	Temperature at zero stress		K	
		Thermal pressurization of pores		
b_p/a_p	Pore aspect ratio	10 to 10^4		Norton (1984); Le Ravalec and Guéguen (1994)
α_w	Thermal expansivity of water		K^{-1}	Wagner and Prüß (2002)
β_w	Compressibility of water		Pa^{-1}	Wagner and Prüß (2002)
$P_{\mathrm{fluid\ eff}}$	Effective fluid pressure		Pa	
		Hydration		
$T_{\mathrm{dehydr.\ min}}$	T at onset of dehydration	700	K	
$T_{\mathrm{dehydr.\ max}}$	T at onset of hydration	850	K	
$D_{\mathrm{H2O}}(T)$	Diffusion rate of water in rock	$4.5 \times 10^{-5}\ \mathrm{e}^{-45000/(RT)}$	$m^2\ s^{-1}$	MacDonald and Fyfe (1985)
		Dissolution and precipitation		
Ea_{silica}	Activ. energy, silica dissolution	62.9 ± 2	kJ	Rimstidt and Barnes (1980)
Ea_{chrys}	Activ. energy, chrysotile diss.	70 ± 10	kJ	Thomassin *et al.* (1977)
Ea_{magn}	Activ. energy, magnesite diss.	32.1 ± 3	kJ	Pokrovsky *et al.* (2009)
V_{silica}	Molar volume of silica	29.0×10^{-6}	$m^3\ mol^{-1}$	Helgeson (1978)
V_{chrys}	Molar volume of chrysotile	108.5×10^{-6}	$m^3\ mol^{-1}$	Helgeson (1978)
V_{magn}	Molar volume of magnesite	28.018×10^{-6}	$m^3\ mol^{-1}$	Helgeson (1978)
μ_i	Rate law parameter	1 or 4 (magnesite)		Pokrovsky and Schott (1999); Xu and Pruess (2001)
A/V	Area-to-volume ratio	$2/D$	m^{-1}	Rimstidt and Barnes (1980)
ρ_w	Density of water	1000	kg m^{-3}	
R_i	Rate of reaction		mol $m^{-3}\ s^{-1}$	
k_i	Rate constant		mol $m^{-2}\ s^{-1}$	
a_i	Activity	Dimensionless or mol m^{-3} if ideality		
Q_i	Activity product			
K_i	Equilibrium constant			Helgeson (1978)

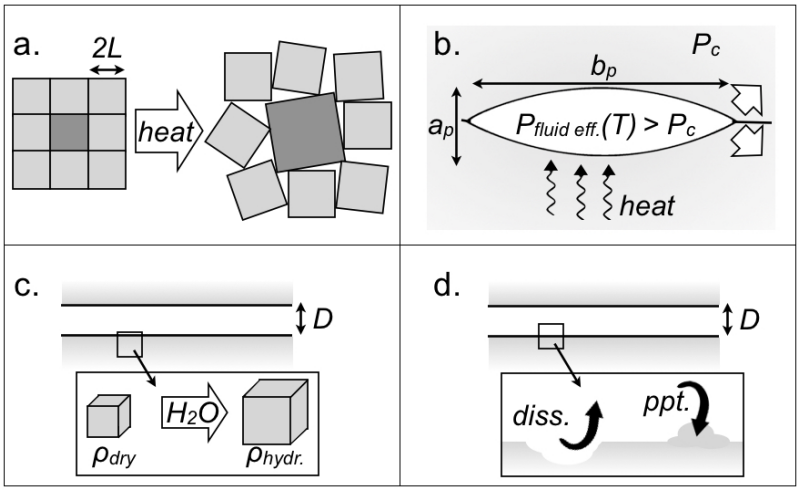

Figure 19: Schematic view of the phenomena included in this study that influence the extent of cracking

a. Micro-cracking by thermal expansion mismatch of mineral grains. *b.* Micro-cracking by expansion of pore water upon heating. *c.* Micro- and macro-crack shrinking by hydration swelling of silicates (or widening by dehydration). *d.* Dissolution and precipitation of mineral species can widen, shrink, or even clog micro- and macro-conduits.

shape of pores, the effective stress capable of opening cracks is leveraged at the pore tip by a geometric factor $1 + 2\ b_p/a_p$, where b_p/a_p represents the pore aspect ratio, or ratio of the long axis over short axis (Norton, 1984). Thus, assuming the fluid is pure water, the effective fluid pressure at the pore tip is:

$$P_{\text{fluid eff}} = P_c + \frac{\alpha_w(T, P_c)}{\beta_w(T, P_c)}\ dT \times (1 + 2\ b_p/a_p) \tag{4.12}$$

where the subscript w denotes properties for pure water.

For elliptical pores of high aspect ratios, in the limit where microporosity is low and the confining pressure is negligible compared to the rock's Young modulus ($P_c \ll E$), relaxation of the rock matrix mitigates the fluid pressure increase with temperature such that (Le Ravalec and Guéguen, 1994, equation 12):

$$\frac{\partial P}{\partial T} = \alpha_w(T, P_c) \times \left(\beta_w(T, P_c) + \frac{b_p}{a_p} \frac{3(1-2\nu)}{E} \right)^{-1} \tag{4.13}$$

where $E/[3(1-2\nu)]$ is the rock bulk modulus. Because $\beta_w \; E \approx 40$ (unless rock is loosely consolidated, in which case E is smaller), the relaxation term is not negligible for aspect ratios b_p/a_p above this threshold. As before, the effective fluid pressure is $P_{\text{fluid eff}} = (\partial P/\partial T) \; dT \times (1 + 2 \; b_p/a_p)$.

Cracks open when the differential stress $P_{\text{fluid eff}} - P_c$ exceeds the rock strength τ. This condition is valid in the frame of linear elastic fracture mechanics provided that pore flaw lengths are of order $(K_{IC}/\tau)^2 \sim 1$ mm, such that the differential stress can be assimilated to a stress intensity K_I.

$\alpha_w(T, P_c)$ and $\beta_w(T, P_c)$ are computed from the IAPWS95 equation of state for water (Wagner and Prüß, 2002) using the software package *CHNOSZ* (Dick, 2008). In the model, we set the pore aspect ratio b_p/a_p from 10 (Le Ravalec and Guéguen, 1994) to 10^4 (Norton, 1984). The magnitude of the aspect ratio dictates that of the differential stress $P_{\text{fluid eff}} - P_c$, even though it also favors the elastic relaxation of pores in equation (4.13).

4.3.4 Hydration Swelling and Dehydration Shrinking

Incorporation of water molecules into a dry silicate matrix results in swelling of the rock (Evans *et al.*, 2013). Dehydration leads to shrinking. These phenomena are not often taken into account in models of Earth's hydrothermal systems; perhaps due to the local spatial extent of such models, for which rock is always hydrated. In icy bodies, where hydrothermal systems may extend through the entire core (Vance *et al.*,

2007; Castillo-Rogez and Lunine, 2010), the swelling effects of hydration cannot be neglected. We provide a simple set of equations to describe hydration swelling.

Because our 1D model cannot account for this phenomenon, we incorporate it using a sub-grid model: where rock is cracked, we attribute an initial micro- or macro-crack width D_i, left as a free parameter, to a 2D crack of infinite length. We assume that hydration occurs in cracked areas to a degree that depends on temperature: full hydration below 700 K, no hydration above 850 K, and a linear decrease between 700 and 850 K. If the degree of hydration has increased since the previous time step, we consider the change in volume of a cube of rock of edge length a undergoing hydration, $a^3_{\rm hydr} - a^3_{\rm dry}$, where the subscripts "*hydr*" and "*dry*" refer respectively to more hydrated and drier rock (Fig. 19c). This change in volume can be related to a change in crack width D: $\Delta D = -2\ \Delta a$, with $\Delta a = [(a_{\rm hydr} - a_{\rm dry})/a_{\rm dry}]\ a_{\rm dry}$. The first term can be expressed in terms of the ratio of volumes or densities: $a_{\rm hydr}/a_{\rm dry} - 1 = (\rho_{\rm hydr}/\rho_{\rm dry})^{-1/3} - 1$. The second term, the cube edge length a, is also the mean distance $\bar{x}$ traveled by a hydration front into the rock after a time step Δt. Thus,

$$\Delta D = -2 \left[\left(\frac{\rho_{\rm hydr}}{\rho_{\rm dry}} \right)^{-1/3} - 1 \right] \times \bar{x} \tag{4.14}$$

The values for $\rho_{\rm hydr}$ and $\rho_{\rm dry}$ depend on the degree of hydration of the silicates. They are linearly interpolated between the values of 2600 kg m^{-3} for hydrated silicates (Tyburczy *et al.*, 1991; Auzende *et al.*, 2006; Nestola *et al.*, 2010) and 3800 kg m^{-3} for dry silicates (Chung, 1971).

We compute $\bar{x}(T)$ following the estimates of MacDonald and Fyfe (1985) from measurements of diffusivities of water molecules in serpentinized peridotites. They found a diffusivity $D_{\rm H2O}(T)$ of 10^{-12} m^2 s^{-1} at 300 K, varying with temperature as

$D_{\mathrm{H2O}}(T) \approx 4.5 \times 10^{-5}$ exp$[-(45$ kJ$)/(RT)]$. They then estimated the mean distance of diffusive penetration of a hydration front into rock as $\bar{x}(T) \approx (2\ D_{\mathrm{H2O}}(T)\ \Delta t)^{1/2}$. After a time step $\Delta t = 50$ years, their approach yields values of $\bar{x}$ of 4 cm at 300 K, up to 4 m at 600 K. Diffusion slows down as $t^{-1/2}$ over longer timescales, relevant for global hydration (see section 5.3.4).

If hydration swelling causes a crack to close, residual swelling generates compression stresses that can open new cracks. The compression stress σ is given by Hooke's law, $\sigma = E\epsilon$, where E is Young's modulus of the rock (Table 8) and $\epsilon = (\Delta D - D)/\bar{x}$ is the compression strain. Cracks open if the differential stress (compression stress minus confining pressure) exceeds the rock strength:

$$E \times \frac{\Delta D - D}{\bar{x}} - P_c(r) > \tau(r) \tag{4.15}$$

This is a simplification of the analytical compression cracking model of Sammis and Ashby (1986), which successfully reproduced experimental results on the nucleation and growth of cracks on circular pores. Equation (4.15) holds for grain-sized (mm) cracks (in order to scale rock strength and stress intensity) growing on pores of negligible size.

Dehydration is also accompanied by volume changes in the rock, leading to stresses given by:

$$\sigma_{\mathrm{dehydr}} = E \times \left[\left(\frac{\rho_{\mathrm{hydr}}}{\rho_{\mathrm{dry}}} \right)^{-1/3} - 1 \right] \tag{4.16}$$

If the stress in a given layer exceeds the sum of the confining pressure and rock strength, cracks open. Open cracks may be widened due to dehydration, following equation (4.14).

4.3.5 Dissolution and Precipitation of Mineral Species

Once cracks are open, circulation of a chemically reactive aqueous fluid can result in mineral dissolution or precipitation. Dissolution erodes conduit walls and widens micro- and macro-cracks, whereas precipitation narrows or even clogs them. These chemical processes are function of fluid and rock composition, temperature, and pressure. We consider a small number of species: amorphous silica (e.g., from a previous episode of precipitation), the serpentine chrysotile, and the carbonate magnesite. This choice is dictated by two considerations. First, hydrated minerals (perhaps brucite) and carbonates have been observed on the surface of Ceres (Milliken and Rivkin, 2009). Second, the dissolution reactions involving these species cover a wide range of equilibria (as estimated using thermodynamic data from Helgeson (1978)) and kinetic rates (Rimstidt and Barnes, 1980; Thomassin *et al.*, 1977; Pokrovsky *et al.*, 2009), and therefore can be used as proxies to explore the impact of other reactions on crack width. No attempt was made at accurately modeling the chemistry of water-rock reactions, such as chemical feedbacks between reactions or the effect of pH. We consider the following reactions:

$$\underset{\textit{amorphous silica}}{\mathrm{SiO_{2\ (s)}}} \rightarrow \underset{\textit{aqueous silica}}{\mathrm{SiO_{2\ (aq)}}}$$

$$\underset{\textit{chrysotile}}{\mathrm{Mg_3Si_2O_5(OH)_{4(s)}}} + \mathrm{H_2O_{(l)}} \rightarrow \underset{\textit{aqueous silica}}{\mathrm{2\ SiO_{2(aq)}}} + \mathrm{3\ Mg^{2+}_{(aq)}} + \mathrm{6\ OH^-_{(aq)}}$$

$$\underset{\textit{magnesite}}{\mathrm{MgCO_{3\ (s)}}} \rightarrow \mathrm{Mg^{2+}{}_{(aq)}} + \mathrm{CO_3^{2-}{}_{(aq)}}$$

These reactions are reversible (precipitation). Each has an equilibrium constant $K_i(T, P)$, determined at local temperature and pressure using the software package *CHNOSZ* (Dick (2008); thermodynamic data from Helgeson (1978)). Above the transition temperature of amorphous silica (622 K), we consider the dissolution of quartz, which is the stable SiO_2 species between 622 K and 867 K for $P < 5$ kbar. (Above 850 K, the rock is assumed dehydrated and dissolution is irrelevant.) α- and β-quartz are considered in their stability regimes (Helgeson, 1978).

At low temperatures possible in dwarf planet oceans (200 K $< T <$ 273 K), we assume water remains liquid due to the presence of antifreezes. Thermodynamic data below 273 K are scarce, and the equation of state for pure water, needed for *CHNOSZ* computations, has to be extrapolated (Wagner and Prüß, 2002; Neveu *et al.*, 2015b). Therefore, where local temperatures are below 261 K, we set $T = 261$ K for the determination of $K_i(T, P)$. We neglect the heats of dissolution and precipitation in the local heat budget.

At such low temperatures, chemical reactions may be controlled by kinetics rather than thermodynamic equilibria. Modeling suggests that kinetics can dominate equilibrium even for Earth's hydrothermal systems (Bolton *et al.*, 1999). The kinetics of silica dissolution have been studied by Rimstidt and Barnes (1980), who found the precipitation rate $R_{\mathrm{SiO2\ ppt}}$ to be proportional to the activity of dissolved aqueous silica $a_{\mathrm{SiO2\ (aq)}}$ and to the ratio A/V of fluid-rock contact surface area to fluid volume (assuming a constant fluid density $\rho_w = 1000$ kg m^{-3}). Thus:

$$R_{\mathrm{SiO2\ ppt}} = k_{\mathrm{SiO2\ ppt}}(T)\ (A/V)\ a_{\mathrm{SiO2\ (aq)}} \tag{4.17}$$

The proportional term, $k_{\mathrm{SiO2\ ppt}}(T)$, is a rate "constant" (units of mol m^{-2} s^{-1}) which

follows an Arrhenius law $\exp[-E_a/(RT)]$, where E_a is an activation energy and R the ideal gas constant.

Likewise, the dissolution rate is proportional to the activity of solid silica, which is 1 for the pure crystalline solid. We assume an activity of 1 for amorphous silica as well. The net dissolution rate $R_{\mathrm{SiO2}} = (\partial a_{\mathrm{SiO2\ (aq)}}/\partial t)_{P,T,V}$ (dissolution minus precipitation) is therefore:

$$R_{\mathrm{SiO2}} = (A/V)\ [k_{\mathrm{SiO2\ diss}}\ a_{\mathrm{SiO2\ (s)}} - k_{\mathrm{SiO2\ ppt}}\ a_{\mathrm{SiO2\ (aq)}}] \tag{4.18}$$

where the subscript "*diss*" denotes dissolution. This expression can be simplified using the activity product $Q_i = \prod a_i^{\nu_i}$, where ν_i are the stoichiometric coefficients. With $a_{\mathrm{SiO2\ (s)}} = 1$, we have $Q_{\mathrm{SiO2}} = a_{\mathrm{SiO2\ (aq)}}$. Therefore:

$$R_{\mathrm{SiO2}} = (A/V)\ k_{\mathrm{SiO2\ diss}}\ \left[1 - \frac{Q_{\mathrm{SiO2}}}{K_{\mathrm{SiO2}}(T,P)}\right] \tag{4.19}$$

At equilibrium, $Q_{\mathrm{SiO2}} = K_{\mathrm{SiO2}}$ and the net rate is zero. The dissolution and precipitation rate constants are linked via the equilibrium constant: $k_{\mathrm{SiO2\ ppt}}(T) = k_{\mathrm{SiO2\ diss}}(T)/K_{\mathrm{SiO2}}(T,P)$, so the precipitation rate constant depends on pressure. For any reaction where the reactants have an activity of 1, equation (4.19) becomes:

$$R_i = (A/V)\ k_{i\ \mathrm{diss}}\ \left[1 - \left(\frac{Q_i}{K_i(T,P)}\right)^{\mu_i}\right] \tag{4.20}$$

We have followed the derivation of Rimstidt and Barnes (1980). Xu and Pruess (2001) provided a more general version of equation (4.20) that takes into account, for example, the effect of mineral reactive surface area at different water saturations. Sometimes, the dependence of R_i on Q_i/K_i is non linear and experimental data are fitted by a law with $\mu_i \neq 1$ (Xu and Pruess, 2001).

The activation energies of the dissolution rate constants at atmospheric pressure have been determined experimentally: 62.9 kJ for amorphous silica (Rimstidt and Barnes, 1980), about 70 kJ for chrysotile (Thomassin *et al.*, 1977; Bales and Morgan, 1985, Fig. 4), and about 32 kJ for magnesite (Pokrovsky *et al.*, 2009, Table 4). The magnesite value is valid at a pH of 5.4 and decreases with both pH and (to a lesser extent) pCO_2; based on the Fig. 2 of Pokrovsky and Schott (1999), a more general expression for the rate constant of magnesite dissolution may be $k_{\mathrm{MgCO3\ diss}} = 10^{-0.3\ (\mathrm{pH}-5.4)} \times \exp[-E_a/(RT)]$. Because these reactions do not involve gases, their rates do not depend much on pressure. For silica and chrysotile $\mu_i = 1$, but for magnesite $\mu_i = 4$ (Pokrovsky and Schott, 1999).

To account for the impact of chemical reactions on crack width, we adopted the same sub-grid approach as for the hydration process. Thus, the crack width D changes as a result of both hydration and dissolution (Fig. 19d). For our 2D crack geometry, the area to volume ratio A/V is $2/D$ (Rimstidt and Barnes, 1980). The net change in crack width after a time Δt due to chemical processes is (equation 61 of Rimstidt and Barnes, 1980; Martin and Lowell, 2000):

$$\Delta D = \sum_{i=1}^{\mathrm{N\ species}} \frac{R_i\ \Delta t\ V_i(T,P)}{[A/V]} \tag{4.21}$$

where V_i is the molar volume of the mineral species dissolved, which we take at 298 K and 1 bar from Helgeson (1978). We assume negligible salinity, so that activities are assimilated as molalities (moles per kg of water) and R_i has units of mol m^{-3} s^{-1}. The change in species activity (molality) after a time Δt is $\Delta a_i = \nu_i\ R_i\ \Delta t/\rho_w$. If a species precipitates entirely, $\Delta a_i = -a_i$ and the variation in D from the precipitation of this species is:

$$\Delta D_i = \frac{\Delta a_i \ \rho_w \ V_i(T,P)}{\nu_i \ [A/V]} \tag{4.22}$$

In the code, we allow chemical reactions only in zones of hydrothermal circulation. Changes in D_i, R_i, and a_i feed back on each other on timescales possibly shorter than the geophysical code time step (typically 50 years). To capture these feedbacks, we iterate calculations of crack widths, dissolution rates, and activities using equations (4.20) through (4.22) over a short chemical time step, typically 10^{-6} times the main geophysical time step. After a few iterations, ΔD_i and Δa_i may converge toward values that are then scaled to the geophysical time step. Alternatively, precipitation may occur, either because T and P have changed since a previous time step at which species were in solution, or because the reaction timescale is much shorter than even the chemical time step. In the former case, the crack is closed. In the latter case, dissolution and precipitation cancel each other: the net sum of D_i in equations (4.21) and (4.22) is zero. In this case, chemical processes are decoupled from cracking processes and have no influence on geophysics.

4.3.6 Neglected Effects

4.3.6.1 Thermal Expansion of the Rock Matrix

Rock can expand upon heating; this affects cracking. Thermal expansion coefficients of silicates are of order $10^{-5}K^{-1}$, about two orders of magnitude smaller than that of water (Germanovich *et al.*, 2001). A temperature increase of 100 K will thus cause a relative rock volume increase of 0.1%. This is small compared to the rock volume

increase resulting from hydration, $\rho_{\text{hydr}}/\rho_{\text{rock}} - 1 \approx 30\%$. Thermal pressurization of pores is also likely to dominate rock expansion even at low water-to-rock ratios.

4.3.6.2 Fluid Pressure Changes Linked to Conduit Size

Any pressure change due to a change in crack size should bear mostly on the fluid, because the compressibility of even highly porous serpentine is two orders of magnitude lower than that of water (Hilairet *et al.*, 2006; Walsh, 1965; Kelemen and Hirth, 2012). We assume that fluid percolates away before precipitation causes the rock to become cemented, such that "geyser"-like conduits never occur.

4.3.6.3 Anisotropy in Rock Permeability

We do not consistently model the geometry, orientation, and connectivity of cracks, and do not account for anisotropies in rock permeability. At the sub-mm scale, the degree of anisotropy in crack orientation seems low (Boudier *et al.*, 2010; Hanowski and Brearley, 2001). Bolton *et al.* (1997, 1999) considered the impact of a non-homegenous and anisotropic permeability on hydrothermal flow, and found that fluids flow so as to connect regions of higher permeability.

4.3.6.4 Gas Processes and Multi-Phase Flows

The presence of vapor can lead to brine segregation in the liquid phase, which favors precipitation. Vaporization of fluid in segregated pores results in large pore pressure increases, leading to fracturing. Liquid-vapor equilibria also influence fluid

chemistry and fluid-rock interactions. For these reasons, all state-of-the-art models of hydrothermal systems incorporate gas effects (Goldfarb and Delaney, 1988; Xu and Pruess, 2001; Ingebritsen *et al.*, 2010; Han *et al.*, 2013). At this time we have ignored gas processes, including volatile exsolution (Kelley *et al.*, 1993), gas diffusion in the rock matrix, gas-solute reactions and resulting fluid pressure changes, two-phase permeabilities, and capillary pressure (Ingebritsen *et al.*, 2010). This choice is justified in part because hydrothermal systems may be cooler on icy dwarf planets than on Earth, at a given pressure. If the brittle-ductile transition occurs below the critical temperature for pure water, supercritical effects are irrelevant (Fig. 20). On the other hand, Ceres formed further away from the Sun than the Earth, and could have accreted a higher proportion of volatiles (Desch *et al.*, 2009; Castillo-Rogez and McCord, 2010; Sohl *et al.*, 2010), some of which have a lower vapor pressure than water. Thus, careful treatment of gas processes should include not only water vapor, but also primordial volatiles and those formed as a consequence of endogenic activity, such as ammonia, methane, molecular hydrogen, or carbon dioxide (Neveu *et al.*, 2015b). We leave the inclusion of these species for future work.

Although we do not model phase separation, Goldfarb and Delaney (1988) suggested that brines precipitate preferentially on conduit walls and cracks close from the outside in, with the smaller conduits shutting off first; this is an implicit assumption of our model.

4.3.6.5 Species Transport

Species transported in the hydrothermal flow may not dissolve and precipitate in the same place. One expects more dissolution at depth, and precipitation in shallower

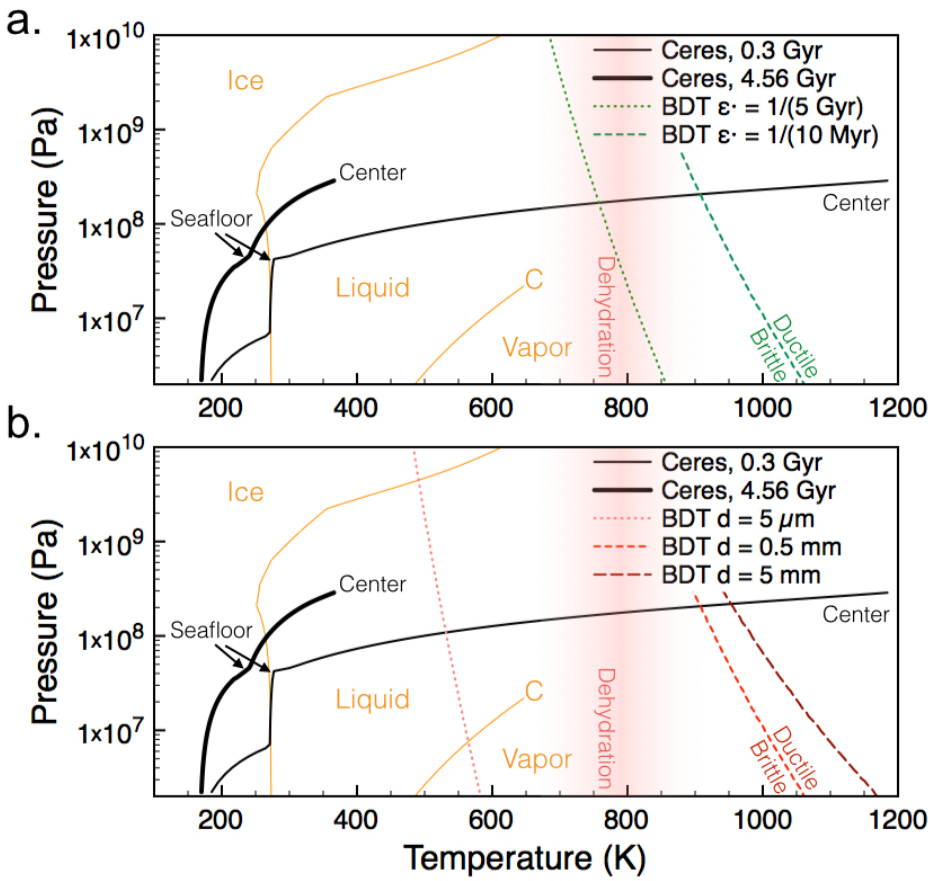

Figure 20: Ceres geotherms overlain on the water phase diagram and silicate brittle-ductile transition curves

a., dashed and dotted curves: Brittle-ductile transition (BDT) in silicates for various strain rates, assuming a grain size of 500 μm (Rutter and Brodie, 1988). *b., dashed and dotted curves:* BDT for various grain sizes, assuming a strain rate of $(10\ \mathrm{Myr})^{-1}$. *Solid black curves:* Pressure-temperature ($P-T$) profiles inside Ceres obtained using the present thermal evolution model, after 0.3 Gyr (hottest profile) and 4.56 Gyr of evolution. *Solid orange curves:* Phase diagram of pure water. Dehydration and the brittle-ductile transition both occur above (but close to) the critical temperature of pure water for most parameters.

layers where solubilities are decreased at lower temperatures and pressures. In our code, typical grid spacing and time step are 2 km and 50 years. The timescale of hydrothermal transport can be estimated using equation (4.26). Setting $\kappa = 10^{-15}$ m^2, $\mu = 10^{-3}$ Pa s, $\Phi = 0.01$, and $\partial P/\partial r = 10^3$ Pa m^{-1}, one finds $v = 10^{-7}$ m s^{-1} or 160 m in 50 years, an order of magnitude less than the grid spacing. Therefore, the approximation of no transport holds for permeabilities of 10^{-15} m^2 or lower. If 1D vertical velocities are much higher than 1 km per century, one can assume that concentrations are homogenized in circulating layers. If the ratio of grid spacing to time step is comparable to flow velocity, tracking concentrations with transport equations is necessary (e.g. Travis *et al.*, 2012), as chemical stratification occurs in the long term. *A posteriori*, our simulations of Ceres do suggest permeabilities consistent with non-negligible species transport and possible chemical stratification. As previously mentioned, such accurate modeling of hydrothermal chemistry falls outside the scope of this chapter and is left for future work.

4.3.6.6 Anisotropy in Serpentine Properties

The crystalline structures of serpentine minerals are anisotropic; this is reflected in their physical properties (Hilairet *et al.*, 2006). We assume that in large volumes of rock, these properties are averaged over all possible directions. This assumption holds for macroscopic cracking phenomena, such as compressive stresses resulting from hydration swelling. For microscopic phenomena, such as thermal expansion mismatch at grain boundaries and thermal pore pressurization, stress buildup and brittle deformation occur in a preferred direction. Elasticity and failure properties quoted in Table 8 were determined from experiments on macroscopic samples, and

thus account empirically for anisotropy. For example, measured values of K_{IC} are likely those for the weakest axis, along which brittle failure first occurs (Escartin *et al.*, 1997b).

4.4 Inclusion in Thermal Evolution Code

To study feedbacks between core cracking and thermal evolution, we have modified the code of Desch *et al.* (2009) to include the cracking model described above. The upgrades are shown in Fig. 21. The updated code is freely available at https://github.com/MarcNeveu/IcyDwarf.

4.4.1 Rock Hydration and Dehydration

The cracking model accounts for silicate hydration, which was not modeled by Desch *et al.* (2009). We have modified their 1D code so that hydrated silicates in a given layer dehydrate if the temperature of that layer exceeds 700 K. To smooth out the transition between dry and hydrated rock, we have defined a degree of hydration $X_{\rm hydr}$ in each layer, which is 0 if the silicates in this layer are completely dehydrated and 1 if the silicates are fully hydrated. For dehydrating silicates, $X_{\rm hydr}$ decreases linearly with temperature between 700 K and 850 K. $X_{\rm hydr}$ is allowed to increase in a given layer only if (a) the temperature of this layer is below 850 K and decreasing, (b) this layer is cracked, as well as all core layers above, so that it is possible for liquid water above the seafloor to flow down core cracks to reach the layer, and (c) there is enough liquid to hydrate this layer.

Upon hydration or dehydration, heat is produced or consumed, respectively. The

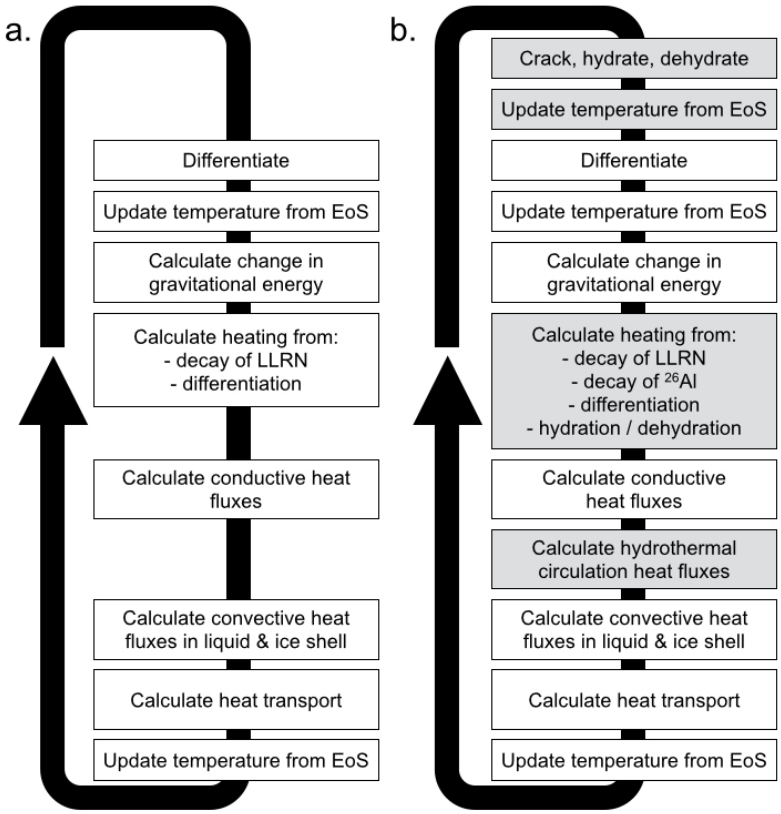

Figure 21: Upgraded thermal evolution code

a. Calculations carried at each time step in the thermal evolution code of Desch *et al.* (2009). *b.* Updates to the code are shown in grey boxes. *EoS* = equation of state; *LLRN* = long-lived radionuclides.

amount of heat released, H_{hydr}, was estimated using *CHNOSZ* by calculating enthalpies of reaction $\Delta_r H$ at temperatures between 700 and 850 K and pressures between 100 and 5000 bar (10 and 500 MPa), for the following two hydration reactions:

$$\underset{\textit{forsterite}}{3\ \mathrm{Mg_2SiO_{4(s)}}} + \underset{\textit{aqueous silica}}{\mathrm{SiO_{2(aq)}}} + 4\ \mathrm{H_2O_{(l)}} \rightarrow 2\ \underset{\textit{chrysotile}}{\mathrm{Mg_3Si_2O_5(OH)_{4(s)}}}$$

$$\underset{\textit{forsterite}}{2\ \mathrm{Mg_2SiO_{4(s)}}} + 3\ \mathrm{H_2O_{(l)}} \rightarrow \underset{\textit{chrysotile}}{\mathrm{Mg_3Si_2O_5(OH)_{4(s)}}} + \underset{\textit{brucite}}{\mathrm{Mg(OH)_{2(s)}}}$$

At these temperatures and pressures, enthalpies of reaction range between -450 and -700 kilojoules per kilogram of forsterite consumed, with similar values if the serpentine product is antigorite. The mid-range value, -575 kJ (kg^{-1} dry silicate), was arbitrarily chosen for H_{hydr}. The net heating rate Q_{hydr} is calculated in each layer with rock mass M_{rock} as:

$$Q_{\mathrm{hydr}} = \Delta X_{\mathrm{hydr}} \times M_{\mathrm{rock}} \times (-H_{\mathrm{hydr}})/\Delta t \tag{4.23}$$

This heat of hydration is added to those arising from radioactive decay and changes in gravitational potential in equation (4.1).

The degree of hydration of silicates influences their thermal conductivity. Hydrated rocks and chondritic material have conductivities of 0.5 to 1.5 W m^{-1} K^{-1} (Yomogida and Matsui, 1983; Clauser and Huenges, 1995; Opeil *et al.*, 2010); for dry silicates a value of 4.2 W m^{-1} K^{-1} has been adopted by many modelers (Ellsworth and Schubert, 1983; McCord and Sotin, 2005; Robuchon and Nimmo, 2011; Guilbert-Lepoutre *et al.*, 2011). We choose the values of 1 W m^{-1} K^{-1} for hydrated rock and 4.2 W m^{-1} K^{-1} for dry rock. The thermal conductivity of partially hydrated rock varies linearly with X_{hydr} between these two values.

The hydration and dehydration subroutines move mass and internal energy of water and rock on the 1D grid, but do not update grid temperatures. Thus, after these subroutines are called, temperatures are updated in each grid zone using the relevant equations of state for each material (Fig. 21).

4.4.2 Hydrothermal Circulation in the Cracked Layer

If parts of the core in contact with a liquid ocean are cracked, cooler water can circulate down into the core fractures, warm up, and return to the ocean in a convective pattern known as hydrothermal circulation. This phenomenon results in mass and energy transfer in and out of the core. In our models, hydrothermal circulation occurs in the cracked layers in contact with the ocean if (a) there is enough liquid to be circulated (i.e., the volume of liquid is greater than the volume of pores in the cracked rock); and (b) the Rayleigh number Ra exceeds the critical Rayleigh number for convection in a porous medium with a permeable top, about 30 (Lapwood, 1948; Ribando *et al.*, 1976; Cherkaoui and Wilcock, 2001). In a porous medium, Ra can be expressed as (Phillips, 1991):

$$Ra = \frac{\alpha_w \ \rho_w^2 \ c_p \ g \ \Delta T \ \kappa \ \Delta r}{k_w \ \mu} \tag{4.24}$$

with $c_p = 4188.5$ J kg^{-1} K^{-1} the heat capacity of water, g the gravitational acceleration, calculated in the middle of the hydrothermal layer of thickness Δr, ΔT the temperature gradient across the layer, κ the permeability of the medium (in m^2), $k_w = 0.61$ W m^{-1} K^{-1} the thermal conductivity of liquid water, and μ the dynamic viscosity of the fluid.

We model circulation in a greatly simplified fashion. Mass transfer is neglected under the assumption of negligible species transport and steady-state fluid circulation. Convective heat transfer is not modeled explicitly, but parameterized in the form of an increased effective thermal conductivity for the layers experiencing hydrothermal circulation. This effective thermal conductivity, k_{hydro}, is derived from the following equations:

$$\frac{\partial T}{\partial t} = \frac{1}{\rho_w \; c_p} \frac{\partial}{\partial r} \left(k_{\text{hydro}} \frac{\partial T}{\partial r} \right) \tag{4.25}$$

$$v = \frac{dr}{dt} = \frac{1}{\Phi} \frac{\kappa}{\mu} \frac{\partial P}{\partial r} \tag{4.26}$$

Equation (4.25) describes conductive heat transport. Equation (4.26), Darcy's law, describes fluid flow in a porous medium in response to a pressure gradient $\partial P/\partial r$. v is the 1D fluid velocity and Φ is the dimensionless bulk medium (rock) porosity. We assume for simplicity that the fluid is moved by the lithostatic pressure gradient. In reality, the pressure of fluid circulating through cracks should follow a hydrostatic gradient several-fold shallower (Kelley and Delaney, 1987). However, thermal expansion of the fluid increases its pressure at depth, which steepens the fluid pressure gradient up to several fold, depending on core temperatures.

Assuming temperature and pressure variations ΔT and ΔP are small across a layer, these equations can be rearranged to give k_{hydro}:

$$k_{\text{hydro}} = \frac{\rho_w \; c_p}{\Phi} \frac{\kappa}{\mu} \Delta P \tag{4.27}$$

With $\Phi = 30\%$, $\kappa = 10^{-12}$ to 10^{-15} m^2, $\mu = 10^{-3}$ Pa s, $\rho_w = 1000$ kg m^{-3}, $c_p = 4188$ J kg^{-1} K^{-1}, $\Delta P = 10^5$ to 10^6 Pa, one finds $k_{\text{hydro}} = 1$ to 10^4 W m^{-1} K^{-1}.

In practice, we cap k_{hydro} at 100 W m^{-1} K^{-1} to avoid destabilizing the code with large energy transfers by violating the Courant condition. If k_{hydro} is much larger than material thermal conductivities, its exact value matters little: even at 100 W m^{-1} K^{-1}, layers undergoing circulation quickly become nearly isothermal, the bottleneck of heat transfer being in non-hydrothermal solid layers. In the calculation of k_{hydro}, we assume $\Phi = 0.01$ and that κ varies as the square of crack size D (Millington and Quirk, 1961): $\kappa = 10^{-15} \times [D/(1 \text{ mm})]^2$ m^2 (Table 10). In zones that are not cracked, the code

prevents hydrothermal circulation from taking place; this is equivalent to setting $\Phi = 0$ and $\kappa = 0$. The value of Φ in cracked zones is chosen low enough that circulation is not impeded by lack of liquid, in case liquid contained in a thin layer must circulate through the entirely cracked (porous) core. The value of κ for 1 mm cracks is anchored arbitrarily in the middle of the range of measured seafloor rock permeabilities, which spans over ten orders of magnitude (Fisher, 1998). The importance of choosing an appropriate order of magnitude for κ is mitigated in our approach by the need to cap $k_{\rm hydro}$. This coarse treatment of permeability and hydrothermal heat transfer could be improved, but at the expense of modeling hydrothermalism on a global scale and over geologic time, as meeting the Courant condition at high $k_{\rm hydro}$ would require coarsening the grid or decreasing the time step by orders of magnitude.

The viscosity of the liquid, $\mu(T)$, is key in determining the effective thermal conductivity. At low temperature, water-ammonia liquids have much larger viscosities, 10 to 100 Pa s, than does liquid water at 293 K (1.00×10^{-3} Pa s). We adopt the empirical formulation of Kargel *et al.* (1991) for $\mu(T)$ in Pa s. This fit to their experimental data matches their measurements to 15% or less, for ammonia mass fractions X from 0 to 100% and temperatures from 176 K to 340 K:

$$\mu = \exp(A + B/T) \tag{4.28}$$

with, for $T > 240$K:

$$A = -10.8143 + 0.711062X - 22.4943X^2 + 41.8343X^3 - 18.5149X^4 \tag{4.29}$$

$$B = 1819.86 + 250.822X + 6505.25X^2 - 14923.4X^3 + 7141.46X^4 \tag{4.30}$$

and for $T < 240$ K:

Table 10: Description of hydrothermal circulation parameters

Parameter	Description	Value	Units	References and Notes
Φ	Bulk porosity of fractured silicate layer	0.01		
κ	Permeability of fractured silicate layer	10^{-15}	m^2	Fisher (1998)
k_{hydro}	Max. effective thermal conductivity of layers experiencing hydrothermal circulation	100	W m^{-1} K^{-1}	May be lower than actual value to keep code stable
Ra_{cr}	Critical Rayleigh number for convection in a porous medium	30		Lapwood (1948); Ribando *et al.* (1976); Cherkaoui and Wilcock (2001)

$$A = -13.8628 - 68.7617X + 230.083X^2 - 249.897X^3 \tag{4.31}$$

$$B = 2701.73 + 14973.3X - 46174.5X^2 + 45967.6X^3 \tag{4.32}$$

Other model parameters relevant to hydrothermal circulation are listed in Table 10.

We coarsely model heat transfer by convection in liquid, following Desch *et al.* (2009), by imposing an effective thermal conductivity of 400 W m^{-1} K^{-1} wherever the melt fraction exceeds 2%. This allows us to run the code with a reasonably large time step without violating the Courant condition, and results in a temperature gradient across the convecting liquid layer of less than 5 mK km^{-1} for a typical heat flux of 2 mW m^{-2}, which is negligible compared to that across silicate, hydrothermal, or icy layers. Such a negligible temperature drop is consistent with more sophisticated simulations of subsurface ocean convection (Goodman and Lenferink, 2012; Travis *et al.*, 2012); therefore, even our crude treatment should provide a good approximation of spatially-averaged heat transfer across potential liquid layers.

Table 11: Description of thermal model parameters

Parameter	Description	Value	Units	References and Notes
t_0	Accretion time after CAIs	2, 3, or 5	Myr	Castillo-Rogez and McCord (2010)
$T_{\rm surf}$	Surface temperature	168	K	Effective temp. at 2.7 AU with albedo 0.02
$T_{\rm init}$	Initial temperature	168	K	Assumed no accretional heat
$T_{\rm diff}$	Final differentiation temperature	140	K	Rubin *et al.* (2014)
R	Radius	475	km	$R_{\rm mean} = 471 \pm 5$ km (Drummond *et al.*, 2014)
ρ	Bulk density	2077	kg m^{-3}	Castillo-Rogez and McCord (2010)
X	NH_3/H_2O mass fraction	10^{-10}, 0.01		Desch *et al.* (2009); Castillo-Rogez and McCord (2010)
$(X_{\rm hydr})_0$	Initial degree of hydration	1		Fully hydrated (Castillo-Rogez and McCord, 2010)
$k_{\rm dry}$	Thermal conductivity, dry rock	4.2	W m^{-1} K^{-1}	Ellsworth and Schubert (1983)
$k_{\rm hydr}$	Thermal conduct., hydrated rock	1	W m^{-1} K^{-1}	Clauser and Huenges (1995)

4.5 Results

4.5.1 Thermal and Geophysical Evolution of Ceres

We have modeled the thermal and geophysical evolution of Ceres from immediately after its accretion until present (4.56 Gyr). Canonical parameters were assumed for the cracking model (Tables 8 and 9) and for the thermal model (Tables 10 and 11). We assumed that Ceres accreted “cold" (no heat of accretion), from hydrated planetesimals.

Three scenarios illustrate different outcomes in Ceres' evolution depending on the amount of internal heating from the decay of the short-lived radionuclide ^{26}Al. Major ^{26}Al heating occurs if Ceres accretes at $t_0 = 2$ Myr after the formation of calcium-aluminum inclusions (CAIs); this is scenario (a). In scenario (b), $t_0 = 3$ Myr and ^{26}Al heating is more moderate. In scenario (c), $t_0 = 5$ Myr and ^{26}Al heating is even lower. These three scenarios were chosen identical to those investigated by Castillo-Rogez and McCord (2010) to facilitate comparisons between model outcomes.

In all three scenarios, differentiation occurs quickly. It is initiated by ice melting

in the central regions of Ceres, which occurs between 0.1 Myr (scenario a) and 18 Myr (scenario c), even in the absence of antifreezes, out to a radius of at least 375 km. This leads to a gravitationally unstable configuration, with an undifferentiated outer shell overlying an icy mantle. Rubin *et al.* (2014) have shown that in this situation, differentiation then proceeds by Rayleigh-Taylor instabilities (foundering) at temperatures $T_{\rm diff} = 140 \pm 20$ K. This is lower than Ceres' starting and surface temperatures, set at 168 K. Therefore, differentiation is instantaneous once the Rayleigh-Taylor configuration is set up. We consider that differentiation proceeds by foundering once Ceres' interior is differentiated out to a radius $R/2$.

4.5.1.1 Simulations with Negligible NH_3 Amounts

Here, the ice component is assumed to contain negligible amounts of ammonia (mass fraction 10^{-10} with respect to water). Results for the three scenarios are shown in Fig. 22.

In scenario (a), ^{26}Al decay delivers enough heat to immediately crack the entire hydrated core by pore water pressurization, no matter the pore aspect ratio. ^{26}Al decay heating also triggers dehydration of the silicate core after about 0.5 Myr (Fig. 22a). Dehydration is complete by 2.5 Myr, also fractures the entire core, and consumes much radiogenic heat. However, it releases liquid water as an ocean surrounding the core, and the hydrosphere of Ceres is almost entirely melted. Past 2.5 Myr, only the upper 10 km of the core are cracked (Fig. 23a): there, the highest temperatures reached are still low enough ($T < 400$ K) that rock remains brittle on timescales much longer than the age of the solar system (Fig. 25). Hydrothermal circulation is prevented in these brittle layers by mineral precipitation, which clogs cracks in

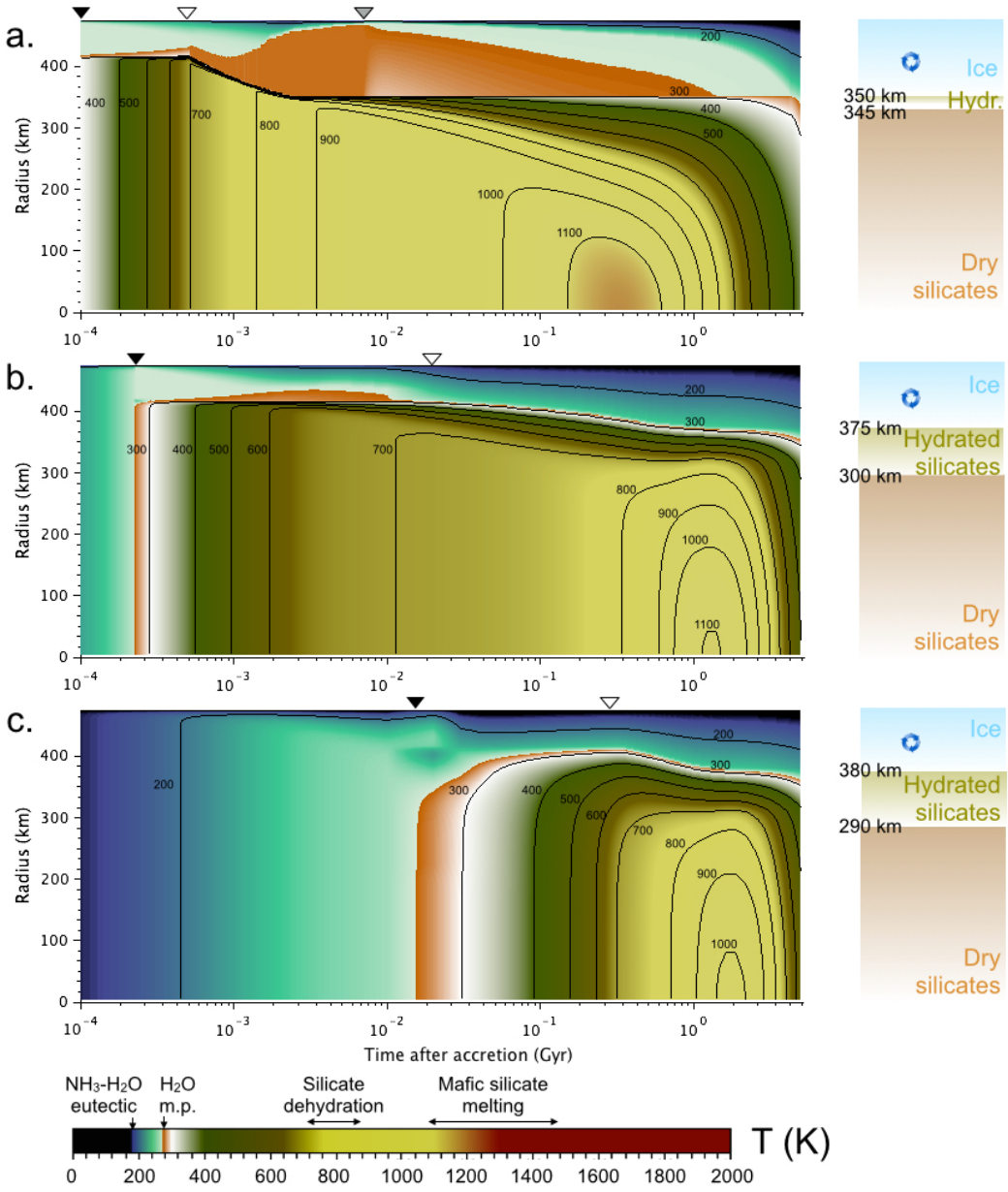

Figure 22: Thermal evolution and internal structure of Ceres with negligible antifreezes

Left panels: Thermal evolution of Ceres in three cases: accretion 2 Myr (*a.*), 3 Myr (*b.*), and 5 Myr (*c.*) after the condensation of Ca-Al inclusions (CAIs). A negligible NH_3/H_2O mass fraction of 10^{-10} is assumed. Black arrows on top of each panel indicate the onset of differentiation. White arrows indicate the onset of dehydration, around 700 K. On panel (a), the gray arrow indicates a brief episode of hydrothermal circulation. *Right panels:* Present-day structures of Ceres. Circular arrows indicate convective heat transfer in the corresponding layers.

the second outermost core layer (Fig. 23a). Inner core regions keep heating until about 300 Myr (peak temperature around 1180 K). Subsequently, Ceres quickly cools as a whole. Past 1.2 Gyr, temperatures in the entire core are low enough to allow rehydration. Surprisingly however, despite large amounts of liquid, rehydration does not occur. This is because thermal contraction mismatch does not yield high enough stresses to further crack core silicates. Stress intensities K_I from contraction mismatch range from a few 10^5 Pa $m^{1/2}$ just below the cracked layer to 10^4 Pa $m^{1/2}$ further down. This is close to, but lower than the fracture toughness K_{IC} for dry and hydrated silicates. Thus, core cooling occurs slowly enough that stresses arising from thermal expansivity mismatch between adjacent grains of differing mineralogy are accommodated by diffusion creep before cracking occurs. Since rehydration does not occur, the final core radius is small: 350 km. Outer hydrosphere layers slowly refreeze and subsolidus convection in ice is initiated after 4.25 Gyr, once liquid convection and hydrothermal circulation cease. Together, solid-state convection in ice, convection in the ocean, hydrothermal circulation, and the high thermal conductivity of dehydrated silicates all contribute to cooling Ceres to a greater extent than in the other two scenarios, yielding a cold present state (central temperature around 385 K at 4.56 Gyr). Present-day hydrosphere temperatures range between 168 K and 220 K, too low to maintain liquid without antifreezes.

In scenario (b), the entire hydrated core is still cracked by pore pressurization immediately after differentiation at 0.2 Myr. Due to weaker heating by ^{26}Al decay, core dehydration is much slower, starting at 20 Myr and stopping at 1.2 Gyr when peak core temperatures are reached. Dehydrating areas are fractured. Dehydration is incomplete and yields a dry inner core of radius 300 km surrounded by a hydrated outer core 75 km thick. Cracks that opened prior to core dehydration heal quickly

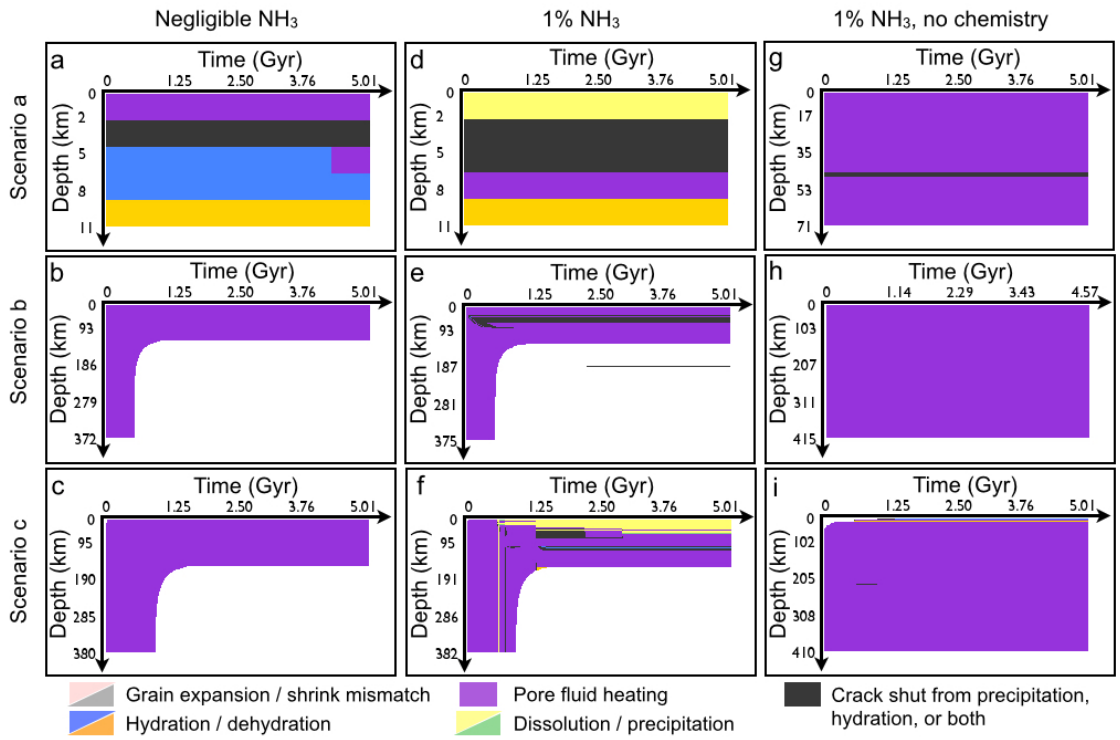

Figure 23: Depth of cracking inside Ceres' core over geologic time

The depth is 0 at the seafloor and increases toward the center. Note the different vertical scales, which depend on maximum cracked depth (core radii are shown on Figs. 22 and 24). Cracking by thermal pore pressurization generally dominates. Dehydration cracking is also widespread (see text), but not shown here if it occurs in zones already fractured by pore pressurization. Cracking by hydration swelling seldom occurs, and cracking by thermal mismatch does not occur. In panel (a), precipitation shuts off cracks in the second outermost zone (grid resolution 2.4 km), preventing circulation in the underlying zones. In panels (b), (c), (e), and (f), cracks heal due to ductile creep in the hot central zones. In panels (d), (e), and (f), crack clogging by precipitation, sometimes aided by hydration swelling, yields impermeable layers in the core (see text for details). In panel (g), a layer is made impermeable solely by hydration swelling, as precipitation was disabled in this simulation. In panels (h) and (i), the entire core remains fractured until the present day.

in the dehydrated zone, where temperatures are above 850 K (Fig. 25), but persist in the hydrated layers (Fig. 23b). Liquid convection is initiated as soon as Ceres differentiates but ceases after only 10 Myr, short of liquid as the hydrosphere refreezes. Ice convection, also initiated immediately after differentiation, persists weakly until present. Hydrothermal circulation never occurs. Present-day core temperatures are higher than in scenario (a), with a central temperature around 550 K. Although this is cold enough for the core to be rehydrated, late hydration does not occur since there is no liquid.

In scenario (c), differentiation and core cracking take more time. The brittle, hydrated core is entirely cracked by pore thermal pressurization after 20 Myr (Fig. 23c). Partial dehydration is initiated after 300 Myr (Fig. 22c), cracking the dehydrating zones. It ceases around 1.7 Gyr when peak central temperatures of about 1015 K are reached; the core then reaches its present-day state, consisting of an inner dry core of radius 290 km and an outer hydrated core of radius 380 km. No melting occurs in this scenario in the absence of antifreezes, as in scenario (b). Liquid convection and hydrothermal circulation are therefore never initiated. As a result, the core is never rehydrated, even as it cools below 700 K. In the hydrosphere, heat is transported by solid-state convection of ice, which continues on today, albeit even less vigorously than in scenario (b). Thus, present-day central temperatures (620 K) are the highest of all three scenarios.

4.5.1.2 Simulations with $NH_3/H_2O = 0.01$ by Mass

Ceres could have accreted ammonia at a level up to 14% with respect to water (Dodson-Robinson *et al.*, 2009). Subsequently, ammonia may have speciated into

ammonium salts (Fortes *et al.*, 2007; Marion *et al.*, 2012) or been oxidized to N_2 in hydrothermal reactions (Matson *et al.*, 2007; Glein *et al.*, 2009). Ammonia could also have reacted with silicates and become integrated into the rock in saponite form; saponite may have been observed on Ceres' surface (King *et al.*, 1992) but this is now contested (Cohen *et al.*, 1998; Rivkin *et al.*, 2006; Milliken and Rivkin, 2009). Given these uncertainties on the fate of ammonia, we have chosen to investigate its effects for an arbitrary content of 1% by mass (1.06% by mole) with respect to water.

Ammonia does not affect the internal structure of Ceres if present at this level, despite minor differences (e.g., earlier time of differentiation because melting is easier). Ceres' dry inner core, hydrated outer core, and hydrosphere have same radii as in ammonia-free runs. However, ammonia enables liquid persistence until the present day in the form of a partially molten layer whose mass scales with ammonia content. For a 1% bulk ammonia content in ice, this layer is a few kilometers thick if the melt mass fraction is 70%, but up to 100 km if the melt mass fraction is only 2%, the cutoff for liquid convection in the code. Convection in such a thick, partially molten layer is initiated only in scenario (a) and contributes to cooling Ceres to the point where its present-day central temperature is only 315 K. For the other two scenarios, convection in the liquid is never initiated because early ^{26}Al heating never melts a layer thick enough (the Rayleigh number scales with the cube of the liquid layer thickness). Surprisingly, the presence of liquid does not always lead to hydrothermal circulation, because upper cracked layers may be clogged by mineral precipitation and isolate the cracked layers beneath from the seafloor above (Fig. 23d through f). Thermal histories are therefore similar to ammonia-free runs (Fig. 22).

That hydrothermal circulation may be impeded by mineral precipitation could be a spurious feature of the 1D code: in practice, precipitation is likely localized

in latitude and longitude. Therefore, we have also run the 1% NH_3 scenarios with mineral dissolution and precipitation disabled, in order to investigate the maximum effect of hydrothermal circulation on thermal evolution (Fig. 24).

In scenario (a), the entire core is differentiated and cracked in the first Myr, leading to extensive hydrothermal circulation and melting. ^{26}Al heating is sufficient to dehydrate part of the core; however, efficient convective cooling in the outer core and hydrosphere prevent dehydration in a layer 45 km thick. Early rehydration at 45 km depth causes rock to swell and shut off cracks in that layer, preventing the underlying layers from further rehydrating (Fig. 23g). Therefore, a structure with an inner dry core of radius 320 km, an outer hydrated core 45 km thick, a partially molten layer ("slush") 25 km thick, and an icy crust 85 km thick is established after only 10 Myr and persists to the present day. While the inner core cools by conduction, the outer core and partially molten layer cool primarily by convection. Circulation in the outer core is intermittent, as it is fueled by conductive thermal gradients that it quickly dissipates. This causes the thickness and temperature of the liquid layer to fluctuate slightly (Fig. 24a).

Temperature profiles in scenarios (b) and (c) exhibit a curious cyclic behavior, characterized by ∼50 Myr intervals during which internal temperatures are cold (below 300 K). These "temperature resets" are caused by episodes of vigorous hydrothermal circulation. Liquid is allowed to circulate through the entire core because core cracks never heal due to insufficient radioactive decay heating, except in the central regions in scenario c (Fig. 23h and i).

Thus, hydrothermal circulation results in efficient heat transfer (occurring by convection, but modeled as enhanced conduction) in both scenarios (b) and (c), cooling down the core and heating up the hydrosphere: only about 50 Myr after

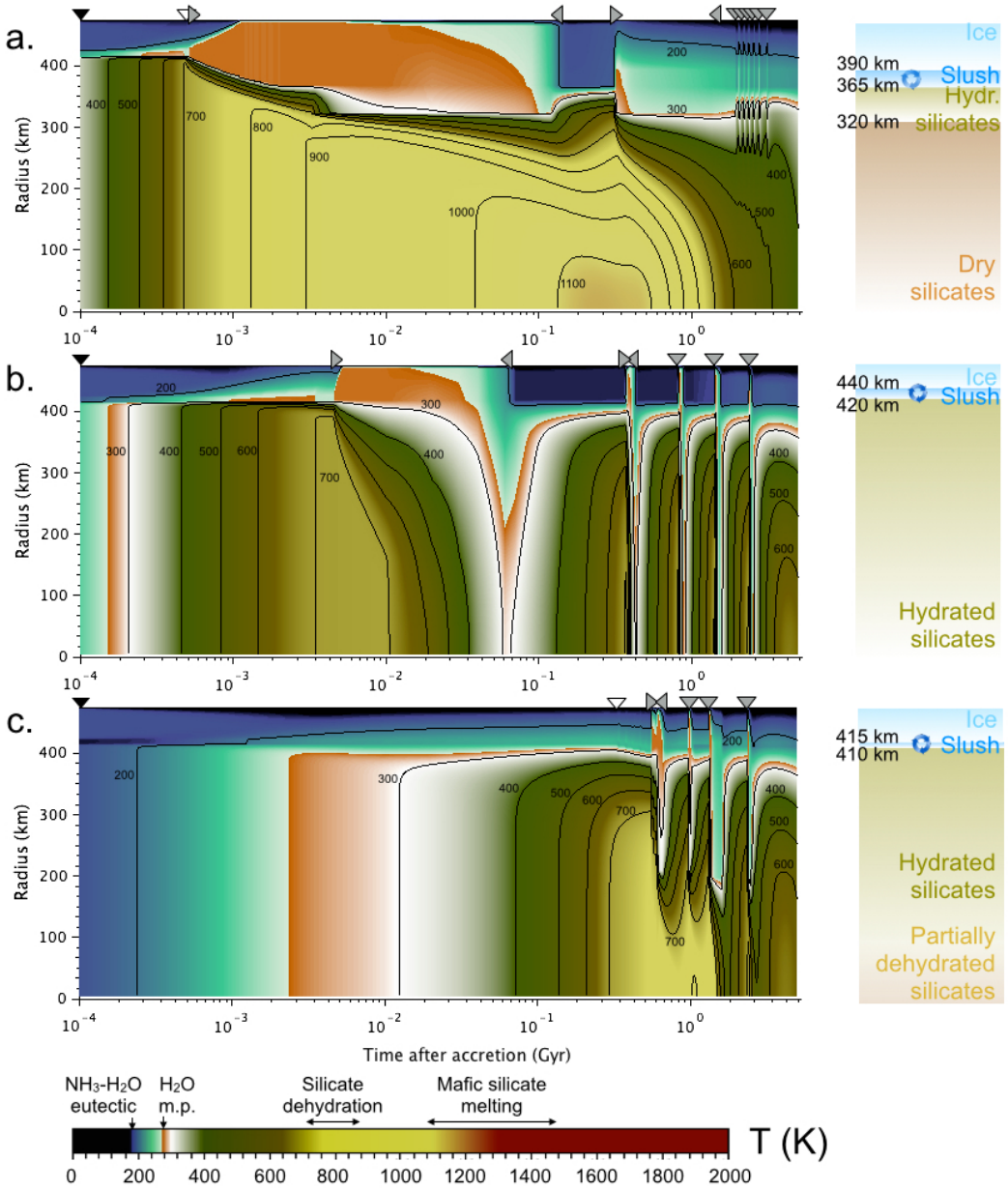

Figure 24: Thermal evolution of Ceres with antifreezes

Left panels: Thermal evolution of Ceres in three cases: accretion 2 Myr (*a.*), 3 Myr (*b.*), and 5 Myr (*c.*) after the condensation of Ca-Al inclusions (CAIs). A bulk NH_3/H_2O mass fraction of 10^{-2} is assumed. Black arrows on top of each panel indicate the onset of differentiation. White arrows on panels (a) and (c) indicate the onset of dehydration, around 700 K (dehydration seldom occurs in scenario b). Gray arrows indicate episodes of hydrothermal circulation. *Right panels:* Present-day structures of Ceres. Circular arrows indicate convective heat transfer in the corresponding layers. “Slush" indicates a partially (at least 2%) liquid convective layer.

circulation is initiated (gray arrows in Fig. 24), the temperature profile becomes very shallow. This brief phenomenon almost appears like a series of temperature resets between 0.5 and 3 Gyr in Fig. 24b and c due to the logarithmic scale for time, but the smooth nature of the temperature changes is more clearly visible in Fig. 24b between 10^{-2} and 10^{-1} Gyr. This phenomenon persists as long as hydrothermal circulation operates, i.e., until the thermal gradient becomes shallow enough that the Rayleigh number drops below its critical value of 30. A steep rise in internal temperatures follows, because of slow conductive heat transfer in hydrated rock. This re-heating can cause several subsequent episodes of ice melting and hydrothermal cooling. Past a few Gyr, heating by long-lived radionuclides becomes too weak to initiate new hydrothermal episodes, thus unlikely to occur at the present day or in the near-future. In both scenarios, the present-day Ceres is structured into a large hydrated core (radius 410 to 420 km), surrounded by a partially molten layer, itself topped by an icy crust.

4.5.2 Cracking Model Sensitivity to Free Parameters

The cracking model described above has a number of free or poorly constrained parameters: the fracture toughness K_{IC}, initial subgrid crack width D_i, grain size d, and pore aspect ratio b_p/a_p. We explore the model sensitivity to these parameters.

Crack healing depends on grain size (Fig. 20b). Even for grain sizes of 1 μm and strain rates of $(4.56\ \text{Gyr})^{-1}$ that minimize ductile strength, the brittle-ductile transition occurs at radii of 310 km or lower at the highest temperatures experienced. This has little bearing on the structures shown in Fig. 22: running scenario (b) with $d = 5$ μm yields a cracked depth decreased by one grid layer (about 2 km).

Thermal mismatch cracking is more important at shallower core depths where relatively low confining pressures yield the highest K_I. This process may help connect the seafloor to a cracked zone at depth. However, since shallow core regions are already cracked in our simulations, thermal mismatch has no influence on our results. Thermal mismatch cracking is most sensitive to K_{IC}: even the lowest reasonable values of 0.1 MPa $m^{1/2}$ for hydrated rock and 0.5 MPa $m^{1/2}$ for dry rock preclude cracking, because K_I is never higher than these values. K_I increases linearly with $\Delta\alpha$, the difference in thermal expansion coefficient between adjacent mineral grains. For olivine, Fredrich and Wong (1986) used $\Delta\alpha = 1.9 \times 10^{-6}$ K^{-1} and Vance *et al.* (2007) used 3.1×10^{-6} K^{-1}; but values for $\Delta\alpha$ could be up to 5×10^{-6} K^{-1}, assuming the case of an olivine grain with $\alpha \approx 26.5 \times 10^{-6}$ K^{-1} (Osako *et al.*, 2010) surrounded by lizardite grains with $\alpha \approx 32.8 \times 10^{-6}$ K^{-1} (Gregorkiewitz *et al.*, 1996). Such values would yield stress intensities as high as 0.6 MPa $m^{1/2}$, enough to crack hydrated and, possibly, dry silicates in shallow core regions.

Early core cracking occurs in all scenarios because of heating, which causes silicate dehydration and pore water pressurization. Heating rates are stronger for higher silicate densities. The dehydration cracking equation (4.16) has no free parameter, but the pore pressurization equation (4.13) has one: the pore aspect ratio b_p/a_p. Pore pressures are nearly proportional to the aspect ratio for values of b_p/a_p above 10. Pressures accumulate as long as cracking does not occur. They reach values comparable to the confining pressure and silicate brittle strength much faster than the inelastic relaxation time of silicates for the whole range of temperatures for which rock is hydrated ($T < 850$ K). Thus, the pore aspect ratio does not influence whether cracking occurs in our simulations. However, cracking occurs faster for higher values of b_p/a_p, but no later than 3×10^5 years after core differentiation even for $b_p/a_p = 10$

and an accretion time 5 Myr after CAIs, which produce the weakest heating of the scenarios investigated (Fig. 25).

Dissolution and precipitation occur in hydrothermal areas. The extent of hydrothermal circulation is increased by a low porosity of the cracked silicates, which decreases the amount of liquid needed for circulation in the fractured layers. The vigor of circulation is also increased, because Ra scales with the circulation depth, even though it also scales with porosity via $k_{\rm hydro}$ in equation (4.27). Chemical processes are highly dependent on temperature (Fig. 25), via both the equilibrium "constant" $K_i(T, P)$ and the Arrhenius term $k_{i\rm diss}$ for a given reaction (equation 4.20). Because K_i and $k_{i\rm diss}$ vary by many orders of magnitude with temperature, free parameters such as initial crack size D_i and area-to-volume ratio A/V do not affect much the fate of cracks. Similarly, hydration and dehydration only have a minor influence on the sub-grid crack width D. The high dependence of clogging on temperature makes this process somewhat arbitrary. Clogging does not always happen in adjacent layers, creating at times impermeable layers in the core below which hydrothermal circulation is impeded. Such layering may be a spurious feature of the 1D code, as precipitation could be localized in latitude and longitude. Discussing the distribution of impermeable precipitates is beyond the scope of our study; but given its potential impact on hydrothermal circulation, this distribution would be worth exploring in further detail with 2D or 3D models.

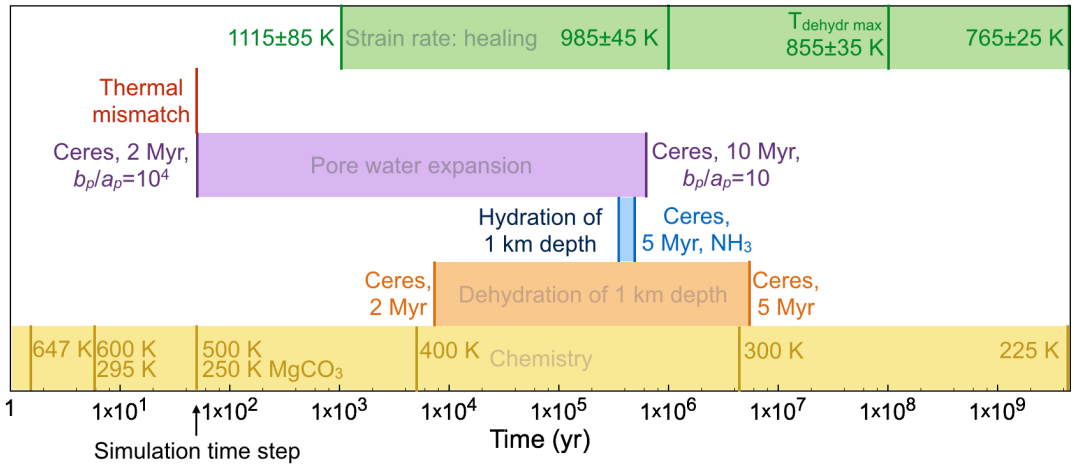

Figure 25: Timescales of cracking processes

Shaded regions show the timescale ranges determined from our simulations. "Ceres, x Myr" denotes the time of accretion. b_p/a_p denotes the pore aspect ratio. Chemistry timescales assume product activities a_i of 0.

4.5.3 Timescales of Cracking Processes

4.5.3.1 Fracture Healing

Cracks heal where rock is ductile. Rock yields by diffusion creep if its ductile strength is lower than its brittle strength. We find brittle strengths and temperatures from 10 MPa and 200 K at Ceres' seafloor to 200 MPa and 1200 K at its center (Figs. 18, 22, and 24). Corresponding strain rates (healing timescales) vary tremendously with temperature, as exp(-1/T), but only linearly with strength. In Ceres' core, strain rates range from $(10^3 \text{ yr})^{-1}$ around 1150 K to $(4.6 \text{ Gyr})^{-1}$ around 765 K for grain sizes of 500 μm, increasing by about three orders of magnitude for every 200 K increase (Fig. 25). These temperatures may shift by up to 100 K depending on brittle strength.

4.5.3.2 Thermal Mismatch

Thermal mismatch depends on the rate of heating and cooling; i.e., the magnitude of temperature changes estimated over a given timescale. In our simulations, this timescale is the time step, typically 50 years (Fig. 25).

4.5.3.3 Pore Water Pressurization

Pore pressurization timescales range from less than a 50-year time step to 5×10^5 years after differentiation (Fig. 25). These timescales depend on early heating rate and pore aspect ratio. The heating rate depends in turn on short-lived radioisotope content (time of accretion), to which the cracking timescale is very sensitive. For an aspect ratio of 10, pore pressurization cracking happens a few thousand years after differentiation if Ceres accretes 2 or 3 Myr after CAIs; but 0.3 to 0.5 Myr for accretion at 5 or 10 Myr after CAIs. Cracking happens first at mid-core depths where the combination of heating rate and brittle strength, which both increase with depth, is most favorable.

4.5.3.4 Core Hydration and Dehydration

The core dehydration front advances 1 km on timescales of 10^4 (Fig. 22a) to 5×10^6 years (Fig. 22c). The hydration front migrates by 1 km in 4 to 5×10^5 years (Fig. 24c). These velocities depend on heating and cooling rates. Dehydration timescales are shorter than those determined by Castillo-Rogez and McCord (2010) by one to several orders of magnitude, perhaps because their models assumed early hydration during

differentiation; consequently, the heat from ^{26}Al was consumed in melting ice and any residual heat was damped by convection. MacDonald and Fyfe (1985) measured diffusion coefficients of water in serpentinite and inferred that hydration fronts advance by 1 km in $\sim 10^9$ years at room temperature to $\sim 10^6$ years at 573 K. Extrapolating these timescales to the temperatures at which hydration and dehydration take place in our models (700 to 850 K) yields timescales of order 10^5 years, compatible with our findings.

4.5.3.5 Dissolution and Precipitation

Kinetic chemical processes cover a wide range of timescales, from seconds to over 4.6 Gyr, due to two factors. First, reaction rates vary hugely with temperature, as exp(-1/T) (Fig. 25). Reaction timescales also vary considerably between mineral species, due to differences in activation energies for dissolution. Thus, the dissolution of a crack wall thickness of 1 cm into pure liquid water, estimated using equations (4.20) through (4.22), takes about 10^8 years at 250 K for silica or chrysotile, but only 10^3 years for magnesite.

Second, equilibrium constants depend considerably on temperature and pressure. In the ranges 260-1000 K and 1-2500 bar, the equilibrium constants for the dissolution of silica, chrysotile, and magnesite vary by 3.5, 150, and 95 orders of magnitude, respectively, as calculated using the software package *CHNOSZ* (Dick, 2008) with thermodynamic data from Helgeson (1978). Thus, the timescales shown on Fig. 25, where the K_i play no role, can be profoundly modified for nonzero product activities if equilibrium dominates kinetics. In practice, two cases may occur. First, timescales may be such that some dissolution occurs during a time step. In this case, activities

are usually high enough that precipitation and clogging will likely occur at a later time step. Second, the timescale for mineral dissolution and precipitation can be much shorter than the simulation time step. In this case, cracks are not affected because everything that dissolves during a time step also precipitates back: crack width changes ΔD_i in equations (4.21) and (4.22) are equal. Thus, when chemical processes occur on timescales too different from the ranges of other processes displayed in Fig. 25, they do not affect cracking in the model.

4.5.4 Material Compressibility

In our simulations, in which volume changes are forbidden, we have implicitly assumed that the compressibility of rocky and icy materials can be neglected. To verify this assumption, we have computed the effect of material compression on density and pressure profiles inside Ceres generated by the thermal evolution code at 4.56 Gyr. Using these input profiles, we have solved the third-order Birch-Murnaghan equation of state (Birch, 1947) for silicates (Chung, 1971; Auzende *et al.*, 2006) and ammonia dihydrate ice (Fortes *et al.*, 2003), as well as a pressure-dependent equation of state for liquid water and ice Ih (Choukroun and Grasset, 2010), to generate output profiles accounting for material compression.

The compacted density profiles do not differ much from those that neglect compression: the radii of the inner dry core, outer hydrated core, and ice shell differ by less than 10 km in all scenarios. Pressures differ by less than 15%, with the largest discrepancies at the center. These results support *a posteriori* our assumptions that Ceres' interior experiences little compression. Errors arising by not accounting for compression are less than those linked to the assumption that Ceres is spherically

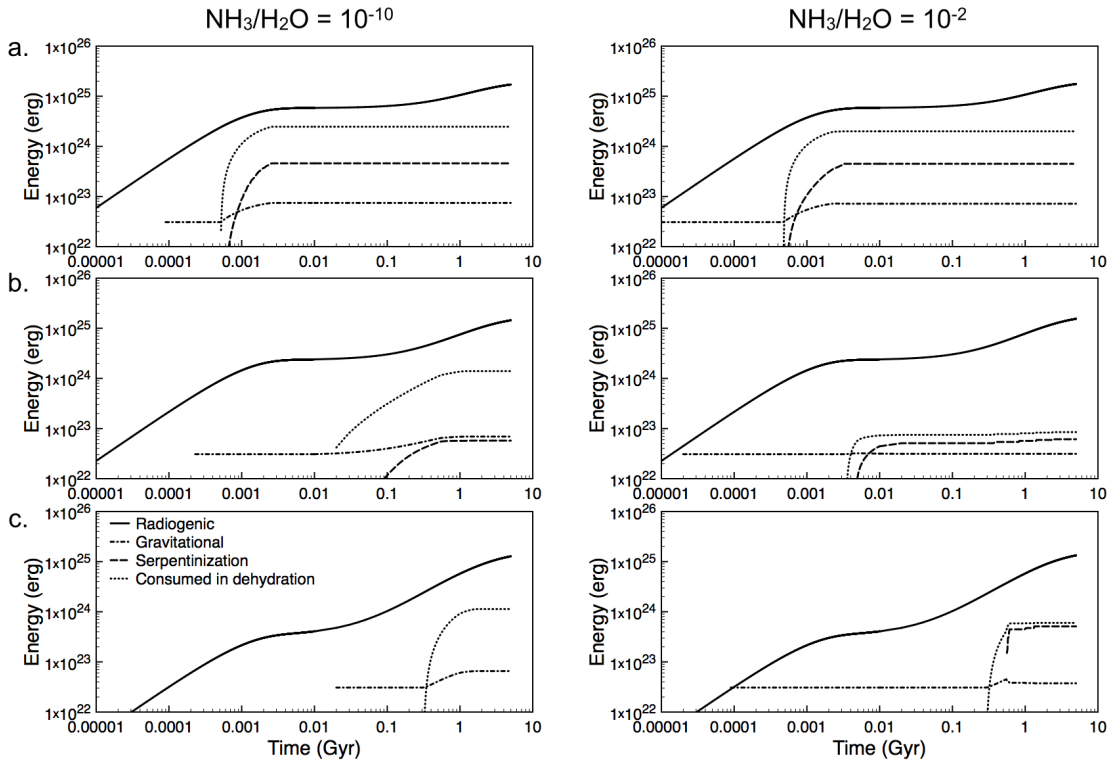

Figure 26: Cumulated radiogenic, serpentinization (silicate hydration), and gravitational heating of Ceres through time

Three scenarios are considered: accretion 2 Myr (*a.*), 3 Myr (*b.*), and 5 Myr (*c.*) after the condensation of Ca-Al inclusions (CAIs). Results are shown for simulations with NH_3/H_2O by mass of 10^{-10} (*left*) and 10^{-2} (*right*). Heat consumption by silicate dehydration is also plotted.

symmetric, since Ceres' short and long axes have radii that differ by about 40 km (Drummond *et al.*, 2014).

4.5.5 Heat Sources

In all scenarios, most of the heat budget is contributed by long-lived radionuclides, which produce two orders of magnitude more cumulated heat than the release of potential energy. Short- and long-lived radionuclide heating can be seen on Fig. 26 as

separate increases in heat produced. ^{26}Al decay heating dominates the cumulative heat budgets in all scenarios for the first 10 Myr. Gravitational heating occurs during differentiation and core dehydration.

Serpentinization is not a significant heat source. This could be due to a lack of either fractures (scenario a) or liquid (scenarios b and c with negligible NH_3); however, even when both persist over geological time scales, radiogenic heating still dominates (scenario (c) with 1% NH_3). Interestingly, serpentinization heating is most prominent in scenario (a) for which Ceres' core is most dehydrated (Fig. 26). This is because hydrothermal circulation is pervasive early on during dehydration, which is slowed down by partial rehydration due to circulating fluids. Dehydration is a significant heat sink in almost all scenarios, and contributes to keeping Ceres' core from reaching melting temperatures.

Locally, hydration and dehydration can lead to changes in heat content two orders of magnitude higher than those caused by radioactivity. Gravitational heating due to contraction of silicate layers from dehydration is locally only an order of magnitude lower than radiogenic heating.

4.6 Discussion

4.6.1 Comparison with Results of Previous Studies

4.6.1.1 Core Cracking Models of Vance et al. (2007)

To our knowledge, only Vance *et al.* (2007) have modeled cracking in the cores of icy worlds. They assumed that cracks develop in a dry rocky core by thermal

contraction mismatch. Structures for most bodies were provided by the steady-state models of Hussmann *et al.* (2006). Vance *et al.* (2007) assumed present-day cooling rates of 1 K yr^{-1} to 1 K Gyr^{-1}, and grain sizes of 0.1 to 10 mm. For a cooling rate of 1 K yr^{-1}, a grain size of 1 mm, and $K_{IC} = 0.6$ MPa $m^{1/2}$, they predicted that bodies the size of Enceladus (radius 250 km) to Oberon (radius 760 km) may experience core cracking depths of 100 to 170 km. These depths were doubled for a ten-fold increase in grain size, and were four-fold lower for cooling rates of 1 K Gyr^{-1}. Their results suggested that the core of Ceres-sized bodies may be entirely cracked (Castillo-Rogez and McCord, 2010).

We suggest that thermal mismatch plays little role in cracking Ceres' core. Cooling rates are of order 10 K Gyr^{-1} at the present day in outer core layers, at the lower end of the range assumed by Vance *et al.* (2007). Assuming such a cooling rate, a grain size of 500 μm, and all other parameter values equal to those in their study ($E = 197$ GPa, $K_{IC} = 0.6$ MPa $m^{1/2}$), we do find thermal mismatch cracking depths in dry silicate of 5 to 20 km. However, our simulations show that the upper core is more likely hydrated, in which case silicate Young moduli E are as low as 35 GPa (Christensen, 1966; Hirth and Kohlstedt, 1995). This six-fold decrease in E is enough to prevent thermal mismatch cracking in our models.

4.6.1.2 Models of McCord and Sotin (2005)

McCord and Sotin (2005) studied the thermal evolution of Ceres for two scenarios: undifferentiated and differentiated. They concluded that Ceres must have differentiated into a rocky core and an icy mantle, with little internal porosity. We support these conclusions. They also suggested that the core may be entirely hydrated, in which case

Ceres would cool faster (by conduction through a thinner ice shell) than with a dry silicate core. We show that cooling actually seems to occur mainly by convective heat transport through the upper core and hydrosphere. McCord and Sotin (2005) did not predict iron-silicate differentiation since internal temperatures did not exceed 900 K in their models. Melting experiments on fragments of the Allende carbonaceous chondrite, a possible analog to Ceres' primordial rocky material, suggest that temperatures above 1400 K would be required (Agee *et al.*, 1995). Such temperatures are not reached in our simulations either. McCord and Sotin (2005) pointed out that a metal core may form if accretional heating produces the temperatures needed; we consider this unlikely, especially since many past estimates of accretional heating have assumed accretion from heliocentric impactors (Safronov, 1978), a model now obsolete.

4.6.1.3 Models of Castillo-Rogez and McCord (2010)

Castillo-Rogez and McCord (2010) investigated scenarios similar to those explored here. They suggested that hydrothermal circulation, along with the time of formation, could be a major evolution driver; however they did not explicitly model hydrothermal processes. We show here that hydrothermal activity could persist in the outer core over geological timescales due to long-lived cracking in the rocky core, not just during early evolution as they suggested. Heat is thus transferred out of the core and keeps the hydrosphere melted. This in turn favors heat loss by vigorous convective heat transfer, resulting in lower present-day core and hydrosphere temperatures than in their models.

Another impact of hydrothermal circulation expected by Castillo-Rogez and McCord (2010) was rock hydration, which results in heat production, volume changes,

and decreased rock thermal conductivity. All these phenomena occur if conditions for circulation are favorable: high NH_3 content, highly fractured core (no dehydration), and little mineral precipitation. If so, the impact on Ceres' thermal evolution is significant (Fig. 24). Otherwise, hydrothermal effects are small (Fig. 22) because late hydration is prevented for three reasons. First, there may not be enough liquid. Second, thermal contraction mismatch, the only core cracking process in cooling regions, is ineffective. Third, even cracks that open before cooling starts, and do not heal, can be clogged by precipitated minerals.

4.6.1.4 Models of Malamud and Prialnik (2015)

Malamud and Prialnik (2015) modeled the thermal evolution of the Ceres-sized Kuiper belt object Orcus (radius 459 km) with a level of detail similar to that presented here, including serpentinization. When comparing simulation outcomes, one must bear in mind a few differences. First, the bulk density of Orcus is only 1530 kg m^{-3}, implying a rock/ice mass ratio of 3 (with their chosen densities), twice as low as that we derive for Ceres (6.25). Second, the surface temperature of Orcus is only 41 K, assuming the albedo value used by Malamud and Prialnik (2015). Third, ^{26}Al heating is likely negligible at the accretion timescales of the Kuiper belt, of order 10^7 years (Kenyon and Bromley, 2012). Finally, silicate-ice differentiation is very gradual in the models of Malamud and Prialnik (2015), proceeding as the diffusion of ice and volatiles through a rock matrix. In the present code, differentiation occurs when the temperature of a given layer exceeds a threshold; every layer below is rearranged instantaneously into a core and mantle.

Despite these differences, some modeling results of Malamud and Prialnik (2015)

for Orcus are similar to our scenario (c) with negligible NH_3. Orcus' present-day central temperature is 550 K (620 K for Ceres). The temperature gradient is steeper in Orcus' core, due to a colder ice-rich shell and slow conductive heat transport through the highly porous outer core. The peak temperature reached inside Orcus is 890 K around 2 Gyr after formation; Ceres reaches 1015 K around 1.6 Gyr. Malamud and Prialnik (2015) do not allow for silicate dehydration; therefore Orcus' core remains hydrated throughout their simulation. The outer core, which spans radii of 200 km to 350 km, is highly porous; Ceres' cracked zone spans radii from 290 km to 380 km. Thus, the volumes of fractured or porous rock are very similar. Malamud and Prialnik (2015) found Orcus' ice shell to be highly porous, which is reasonable at frigid near-surface temperatures; on Ceres, the porosity is likely negligible except in the surface regolith (McCord and Sotin, 2005).

Serpentinization is a major heat source in the model of Malamud and Prialnik (2015), which assumes silicates to be initially dehydrated. A hydration heat pulse is released after about 200 Myr as differentiation occurs in their simulation. This pulse seems to exceed radiogenic heating for a brief period, releasing about a tenth of the long-lived radiogenic heat produced over 4.6 Gyr. In our models, serpentinization is usually less prominent, perhaps because hydrothermal circulation is more efficient at removing that heat.

4.6.2 Geophysical and Geochemical Feedbacks

Our models of core cracking make the essential link between geophysical and geochemical processes, elucidating some feedbacks shown in Fig. 27. Crack formation is favored by high heating or cooling rates and core dehydration, but hindered by high

core temperatures and by precipitates of leaches resulting from water-rock interactions. Cracking seems insensitive to hydration swelling of rock.

Liquid can be generated not only by melting ice, but also by dehydrating silicates. The relative importance of each source depends on the extent of core dehydration. Up to 60% of the long-lasting liquid originates from dehydration in scenario a, with or without NH_3 antifreeze. In scenarios (b) and (c) with negligible NH_3, any liquid originating in core dehydration is refrozen in 10 Myr or less; with 1% NH_3, little or no dehydration occurs and all present-day liquid originates in melting ice.

Provided liquid persists, core cracking can greatly speed up heat transfer out of the core and into the hydrosphere, due to hydrothermal circulation in the fractured zone (Fig. 24). Hydrothermal circulation and ocean convection are tightly linked, because hydrothermalism warms the ocean, which in turn provides liquid to circulate. An unintuitive consequence of convective heat transfer on Ceres' evolution is that a hotter birth seems to lead to a cooler present state. However, strong hydrothermal heat transfer is eventually self-limiting as it both smoothes out the thermal gradients by which it is fueled, and causes liquid to refreeze. On Fig. 27, this is shown by two negative feedback loops. A first loop links hydrothermal circulation, heat transfer in rock, and heating. A second loop links hydrothermal circulation, heat transfer in rock, rock temperature, heat transfer in water, and freezing.

Finally, the extent of cracking determines that of water-rock interactions. Surprisingly, these often seem to result in crack clogging in the present model, preventing further interaction. The possibility of such an inhibiting effect was noted by McKinnon and Zolensky (2003). However, more detailed and faithful chemical modeling is needed to explore water-rock reaction outcomes. Unknown consequences on the distribution of solute antifreezes and radionuclides remain to be investigated (Fig. 27). Follow-up

geochemical calculations are likely to use water to rock ratios as an input. Our simulations suggest bulk mass ratios (mass of liquid / mass of cracked rock, assuming all the liquid is circulated) between 0.005 and 0.015 when hydrothermal circulation occurs through a large portion of the core (all 1% NH_3/H_2O cases), and between 0.1 and 5 if water is circulated only in a few upper core layers (scenario (a) with negligible NH_3).

4.6.3 Testing Predictions with *Dawn* Observations

4.6.3.1 Gravity Measurements

Two parameters of Ceres' internal structure seem key to understanding its origin. The first is the core size, which seems to depend on Ceres' time of formation. In the absence of late hydration, the final core size is set by the extent of silicate dehydration, which in turn depends on the amount of ^{26}Al heating in our simulations. The long-term evolution of the core may be further affected by leaching of the ^{40}K in water-rock reactions, taking away part of the core's radiogenic fuel (Castillo-Rogez and McCord, 2010). Core sizes of 370 km or less may suggest both an early time of formation near Ceres' current heliocentric distance, and little hydrothermal activity. The second parameter is the amount of liquid involved in crack circulation, directly proportional to antifreeze content in our calculations. In turn, the amount of volatile antifreezes accreted depends on Ceres' place of formation, with larger amounts accreted if Ceres formed further away from the Sun (Dodson-Robinson *et al.*, 2009). However, salt compounds leached from silicates during hydrothermal alteration may also act as antifreeze; this remains to be explored.

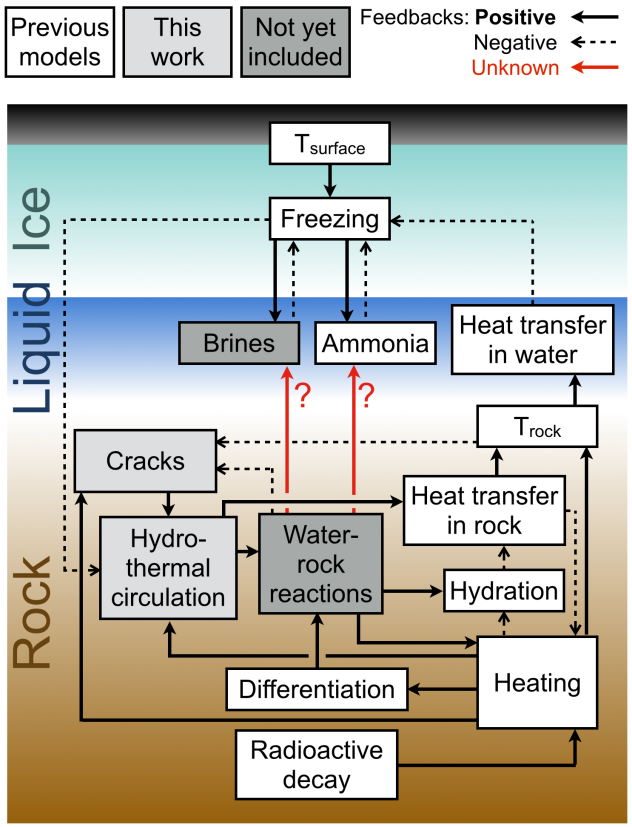

Figure 27: The inclusion of core cracking and hydrothermal circulation in evolution models of Ceres (light gray boxes) enables the investigation of key feedback loops in endogenic processes

Such loops were suggested, but not explicitly modeled, in previous work (McCord and Sotin, 2005; Castillo-Rogez and McCord, 2010). A full understanding of the coupled geophysical-geochemical evolution of Ceres will require investigation of the fate of ammonia and brine antifreezes, as well as the possibility of radionuclide leaching via water-rock reactions (Castillo-Rogez and Lunine, 2010) (dark gray boxes).

Constraints on the internal structure of Ceres will be obtained by gravimetry via Doppler tracking of the *Dawn* spacecraft. Ceres' bulk density and gravitational moment J_2 should be measured to respectively 1% and 0.001% (Russell and Raymond, 2011; Russell *et al.*, 2012); to the extent that the assumption of hydrostatic equilibrium can be applied to Ceres, the measurement of J_2 may provide an estimate of its moment of inertia. Similar constraints on the internal structures of Titan and Enceladus have recently been obtained by tracking of the *Cassini* orbiter (Iess *et al.*, 2012, 2014). The gravitational signature of a liquid layer inside Ceres may be difficult to detect if this layer also contains substantial amounts of water ice and ammonia. Evidence for subsurface liquid could have been collected with a magnetometer able to detect an induced field on Ceres due to salt water. Unfortunately, *Dawn*'s magnetometer was descoped (Russell and Raymond, 2011).

4.6.3.2 Compositional Mapping

Finer constraints on Ceres' evolution may be obtained by inferring the temperature and pressure at which formed the surface carbonates and clays, likely products of aqueous alteration (Milliken and Rivkin, 2009). Our results suggest two possible settings. First, hydrated minerals form early on during differentiation, or perhaps even in the primordial bodies accreted by Ceres (Zolotov, 2014). Water-rock interaction products are circulated upwards into the ocean, then brought to the surface by ice convection. Second, hydrated minerals are formed in the cracked outer core layers experiencing hydrothermal circulation as late as 3 Gyr after Ceres' formation, then brought to the surface by ice convection.

Discriminating between these scenarios requires age estimates of the surface

deposits. Estimates may be obtained using spectra acquired by *Dawn*'s Visible and InfraRed spectrometer (VIR) (De Sanctis *et al.*, 2011, 2012), imaging by *Dawn*'s Framing Camera (Sierks *et al.*, 2011), and models of crater relaxation (Bland, 2013; Dombard and Schenk, 2013).

Timing, physical, and chemical constraints on the fluid-rock reactions that formed Ceres' surface minerals could be obtained with geochemical speciation or reaction path models coupled to a geophysical code. Such modeling could allow interpretation of compositional measurements in terms of constraints on Ceres' evolution and present state. Spectral observations of Ceres' surface at high spatial resolution may allow pinpointing of local heterogeneities from current global averages, which may have hindered previous interpretations of spectra. More complex or yet unidentified species may be detected. For example, the current absence of salts in spectra of Ceres (Zolotov, 2014) does not preclude their existence on the surface: salts are harder to detect than hydrated minerals, because higher degrees of hydration yield shallower reflectance features (McCord *et al.*, 2002; De Sanctis *et al.*, 2012). Infrared remote sensing probes a depth of only a few wavelengths, bringing about the need to discriminate between an endogenic or exogenic source of the materials observed. *Dawn*'s Gamma-Ray and Neutron Detector, *GRaND* (Prettyman *et al.*, 2011) will help with this issue. *GRaND*'s objective is to map abundances of major rock-forming elements (O, Na, Mg, Al, Si, K, Ca, Fe) to 20% precision at a resolution of 1.5 times the mapping altitude, within a depth of order 1 m. Salt-forming elements P, S, and Cl may also be observed. Correlations between *VIR* and *GRaND* measurements will establish the contribution of endogenic materials in *VIR* spectra.

4.6.3.3 Possible Cryovolcanic Activity

Küppers *et al.* (2014) recently reported observations of water vapor expelled from Ceres. The vapor sources seem both spatially and temporally confined. Whether these sources arise from sublimation of near-surface ice or from cryovolcanism is unknown. Cryovolcanism may be favored by freezing, which could pressurize liquid water reservoirs (Fagents, 2003; Neveu *et al.*, 2015b). Our results suggest that under certain conditions (late accretion, presence of antifreezes) it might be possible for Ceres to undergo global freezing at the present day (Fig. 24b and c). Even if Ceres' interior is currently frozen and the current activity is not cryovolcanic, Ceres' surface might show evidence of periodic cryovolcanism over geologic time, which could be linked to the ending of the periodic hydrothermal episodes suggested by some of our simulations.

4.7 Conclusions

We have described new geophysical evolution models for icy dwarf planets, applied to Ceres, that focus on core cracking and hydrothermal circulation. The models account for the following fracturing processes: brittle-ductile transition in dry and hydrated rock, thermal mismatch of mineral grains, thermal pressurization of pores, silicate swelling and shrinking upon hydration and dehydration, and mineral dissolution and precipitation.

We have found that the depth of the fractured zone depends mainly on peak core temperatures. While the entire core is initially cracked due to either pore pressurization or dehydration shrinking stresses, only core layers that never experience temperatures

higher than about 800 K remain fractured on geological timescales; otherwise, cracks heal from the ductile creep of silicates. It is unlikely that core cracking occurs as Ceres cools, because thermal contraction mismatch seems ineffective at fracturing silicates. Present-day cracked depths, of 5 to 420 km in our simulations, suggest a significant volume of rock available to interact with liquid, if present.

The presence of liquid hinges on antifreeze content, on silicate dehydration (which releases liquid), and on hydrothermal circulation itself (which efficiently transports core heat into the hydrosphere). The heat of serpentinization seems too small to significantly help liquid persist.

If liquid persisted over geological timescales, hydrothermal circulation may have profoundly affected Ceres' thermal and geophysical evolution. If shallow, hydrothermal circulation helped sustain liquid by efficiency tapping the core's heat, yet not cooling the core too quickly. If reaching deep into the core, hydrothermal circulation may have prevented core dehydration through "temperature resets", global cooling events lasting about 50 Myr during which Ceres' interior temperature profile was very shallow and the hydrosphere was largely melted.

Hydrothermalism may have left its mark on Ceres' present-day structure. A large, fully hydrated core (radius 420 km) suggests that extensive hydrothermal circulation prevented core dehydration. A small, dry core (radius 350 km) suggests early dehydration from short-lived radionuclides, with shallow hydrothermalism at best. Intermediate structures with a partially dehydrated core seem more ambiguous, being compatible both with late partial dehydration without hydrothermal circulation, and with early dehydration with extensive hydrothermalism. While current shape data do not allow discrimination between these possible structures (Castillo-Rogez and McCord, 2010), gravity measurements by the *Dawn* mission may.

As a final note, our estimates of the cracking depth constrain not only the extent of water-rock interactions, but also the potential of icy dwarf planets to support the emergence and persistence of chemotrophic microbes (Vance *et al.*, 2007). The habitability of subseafloor hydrothermal areas depends on their elemental inventory and the speciation of these elements, as well as on the amount of chemical energy available. Possible hydrothermal chemistries inside Ceres and other icy dwarf planets will be the topic of the next chapter.

Chapter 5

AQUEOUS GEOCHEMISTRY IN ICY WORLD INTERIORS: FATE OF ANTIFREEZES AND RADIONUCLIDES

In the previous chapter, I constrained the occurrence of hydrothermal activity in dwarf planet interiors, thereby characterizing the strength of the coupling between geophysical and geochemical processes. In particular, I determined the influence of geophysical evolution on the conditions under which water and rock interact, such as temperature, pressure, and water-to-rock ratio. However, as expanded on below, the chemistry of water-rock interaction can itself feed back on geophysics in two major ways. First, chemical reactions can produce or consume antifreezes, which can control or even enable the persistence of liquid water over geological timescales. Second, hydrothermal fluids might leach radionuclides, affecting the spatial distribution of this chief endogenic heat source for dwarf planets. Though critical for dwarf planets, which are deprived of a tidal heat source and may require antifreezes to maintain subsurface liquid, these two processes are also relevant to icy moons.

In this chapter, I quantify these two feedbacks of geochemistry on geophysics through numerical simulations of chemical equilibria between fluid and rock of compositions thought to have been accreted by icy worlds. These results have been submitted for publication in *Geochimica et Cosmochimica Acta* with co-authors Steve Desch and Julie Castillo-Rogez. A summary of the results from this paper is provided below, followed by the text of the paper.

The geophysical evolution of many icy moons and dwarf planets seems to have provided opportunities for interaction between liquid water and rock (silicate and

organic solids). Here, we explore two ways by which water-rock interaction can feed back on geophysical evolution: the production or consumption of antifreeze compounds, which affect the persistence and abundance of cold liquid, and the potential leaching into the fluid of lithophile radionuclides, affecting the distribution of a long-term heat source. We model numerically the interaction of chondritic rock with pure water and with C, N, S-bearing cometary fluid, thought to be the materials initially accreted by icy worlds, and describe the resulting equilibrium fluid and rock assemblages. Our findings suggest that water-rock interaction can strongly alter the nature and amount of antifreezes, resulting in solutions rich in reduced nitrogen, mildly oxidized sulfur, and (sometimes) reduced carbon that can remain partially liquid down to around 211 K or even 176 K, the respective eutectic temperatures of the H_2SO_4-H_2O and NH_3-H_2O systems. The prominence of Cl in solution seems to hinge on its primordial supply in ices. Equilibrium assemblages, rich in serpentine and saponite clays, retain thorium and, at low temperatures and low water:rock ratios ($W{:}R$), uranium radionuclides. However, the radionuclide ^{40}K can be leached at high pH and/or high $W{:}R$. We recommend the inclusion of these effects in future models of the geophysical evolution of ocean-bearing icy worlds. Applied to Ceres, our simulations suggest that if Ceres' hydrated surface minerals are confirmed to include NH_4-phyllosilicates, they may result from alteration of chondritic material by cold N-bearing fluids at any depth ($T < 100$°C, pH 7–10 and $-6 \leq fO_2 \leq 3$ at equilibrium, independently of $W{:}R$ and P). Carbonates, which seem prominent on Ceres, are present in some simulations outputs with alkaline equilibrium pH values ($\geq$11), but remain in solution. Thus, carbonate formation on Ceres may have required precipitation induced by either freezing or sublimation.

5.1 Introduction

The bulk densities of most known icy moons and dwarf planets larger than about 250 km in radius, estimated from measurements of their mass and size, are intermediate between those of water ice (918 to 935 kg m^{-3}; Croft *et al.*, 1988) and chondritic rock (2100 to 3730 kg m^{-3}, including porosity; Britt and Consolmagno, 2003). This suggests icy worlds accreted a mixture of these materials. Thermal models suggest that radiogenic heating alone can partially melt ice in their interiors, producing subsurface liquid that may have persisted over several Gyr in contact with silicates and organics (Desch *et al.*, 2009; Robuchon and Nimmo, 2011; Malamud and Prialnik, 2015; Travis *et al.*, 2015; Neveu *et al.*, 2015a, view). If so, substantial interaction between liquid water and "rock" (solid silicates and organics of chondritic composition) is expected to have driven the chemical evolution of these objects. The extent of interaction scales with the water-rock interface area, which is higher if rocky cores are fractured or unconsolidated (Neveu *et al.*, 2015a; Roberts, 2015) or if rock is in the form of suspended fines (Travis *et al.*, 2015; Neveu *et al.*, view). Observational clues of extensive water-rock interaction on icy worlds are building up. Surface salts on Europa may result from such interaction (McCord *et al.*, 1998; Kargel *et al.*, 2000; Zolotov and Shock, 2001; Hand and Carlson, 2015). Salts and aqueously precipitated silica seem to be ejected from an ocean inside Enceladus (Postberg *et al.*, 2009, 2011; Hsu *et al.*, 2015). Ceres' warm surface, where unstable ice cannot mask silicates, is blanketed by mineral products of aqueous alteration (Rivkin *et al.*, 2012, and references therein). Thus, water-rock interaction may have been pervasive in icy world interiors, as predicted by Ransford *et al.* (1981).

The occurrence of aqueous geochemistry inside icy worlds has major implications

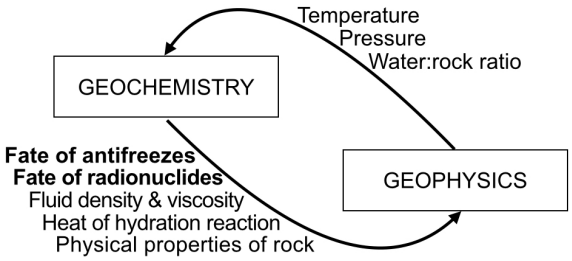

Figure 28: Feedbacks between geophysical and geochemical processes

Current geophysical models of icy world interiors suggest and constrain settings under which aqueous geochemical reactions can take place. Although some effects of geochemistry on geophysics have been investigated, the fates of antifreezes and radionuclides (bold) and their consequences on long-term geophysical evolution have not been quantified.

for their habitability. The progressive oxidation of reduced mineral assemblages by aqueous fluids generates redox gradients, an energy source widely used on Earth by chemoautotrophic microorganisms (Swan *et al.*, 2011). This energy source, together with liquid water and chondritic organics over geological timescales, may provide a habitat for such lifeforms (Kargel *et al.*, 2000; Shock and Holland, 2007; Vance *et al.*, 2007; Abramov and Mojzsis, 2011; Russell *et al.*, 2014; Holm *et al.*, 2015). As over 80 icy dwarf planets have been discovered in the Kuiper belt as of July 2015 (M. Brown, http://web.gps.caltech.edu/∼mbrown/dps.html), the number of potential abodes for life in the solar system could increase from a dozen planets and moons to nearly a hundred worlds.

Water-rock interaction may also shape the internal evolution of icy worlds. Constrained by their thermal and geophysical state, they can feed back on their geophysical evolution in several ways (Fig. 28). First, the long-term persistence of subsurface liquid may hinge on its antifreeze content. In current geophysical models, antifreezes such as ammonia (NH_3) remain in the liquid (Desch *et al.*, 2009; Malamud and

Prialnik, 2015; Neveu *et al.*, 2015a), despite geochemical model suggestions (Kargel, 1992) that NH_3 could be lost by oxidation to N_2 (Matson *et al.*, 2007; Glein *et al.*, 2009) or formation of NH_4^+ salts (Engel *et al.*, 1994; Fortes *et al.*, 2007; Zolotov, 2009; Castillo-Rogez and McCord, 2010). Second, radionuclides such as ^{40}K, ^{232}Th, ^{235}U, and ^{238}U, assumed to be present solely in rock, may be leached into the fluid, changing the internal distribution of heat sources (Kirk and Stevenson, 1987; Engel *et al.*, 1994; Castillo-Rogez and Lunine, 2010). Third, leached minerals can enrich the fluid in salts, which may not only decrease the fluid eutectic temperature, but also affect its density and viscosity and therefore its ability to convectively transport heat and mix material (Travis *et al.*, 2012). Fourth, the hydration of mafic silicates tends to be exothermic, and may significantly increase heat production (Cohen and Coker, 2000; Vance *et al.*, 2007; Malamud and Prialnik, 2013, 2015), although perhaps not always (Palguta *et al.*, 2010; Neveu *et al.*, 2015a). Finally, the alteration of mineral assemblages changes their physical properties, lowering silicate densities and thermal conductivities by 30% and several-fold, respectively (Castillo-Rogez and McCord, 2010; Neveu *et al.*, 2015a).

A few models of water-rich bodies account for the potentially major effects of aqueous geochemistry on icy world geophysics, such as heats of serpentinization (Cohen and Coker, 2000; Vance *et al.*, 2007; Wakita and Sekiya, 2011; Malamud and Prialnik, 2013, 2015; Neveu *et al.*, 2015a) and the changes in rock properties following hydration or dehydration (Abramov and Mojzsis, 2011; Neveu *et al.*, 2015a). However, to our knowledge, no published model yet accounts for the geochemical production or consumption of antifreezes, and the possible leaching of radionuclides has been modeled only in geochemically unconstrained cases (Castillo-Rogez and McCord, 2010). Likewise, the outcomes of water-rock interaction have largely been explored independently of any feedbacks on geophysical evolution (Shock and McKinnon, 1993;

Table 12: Antifreezes relevant to icy world interiors and eutectic temperatures and compositions at 1 bar of binary antifreeze-H_2O systems

Antifreeze	Molar mass (g mol^{-1})	Eutectic T at 1 bar (K)	Eutectic composition at 1 bar (mass% salt)	(molal)
CH_3OH [a]	32.042	157	80.3	127
NH_3 [b]	17.031	176	32.1	27.76
HCl [c,d]	36.46	$\approx$ 187	21.8	7.64
$Ca(ClO_4)_2$ [e]	238.98	198.5	49.9	4.16
$Mg(ClO_4)_2$ [e]	223.21	205	43.7	3.48
H_2SO_4 [d,f]	98.079	211	35.8	5.68
$HClO_4$ [e]	100.46	213	40.6	6.8
$AlCl_3$ [g]	133.34	218	25.3	2.54
$CaCl_2$ [c,h]	110.98	221	30.2	3.90
HNO_3 [d]	63.01	230	32.7	7.71
$FeCl_2$ [i]	126.75	237	30.4	3.45
$FeCl_3$ [j]	162.2	238	28.7	2.485
$NaClO_4$ [e]	122.44	239	53.0	9.20
$MgCl_2$ [c,h]	95.211	240	21.0	2.79
NaCl [c,h]	58.44	251	23.3	5.20
$(NH_4)_2SO_4$ [c,k,l]	132.14	253	40	5
$NaNO_3$ [d]	84.995	255.5	38	7.3
NH_4NO_3 [k]	80.043	256	42.3	9.15
NH_4Cl [c,k,l]	53.491	258	19	4.4
$Al_2(SO_4)_3$ [g]	342.15	261	27.2	1.092
KCl [c]	74.551	262.5	19.7	3.3
CH_2O [l]	30.031	263	6 to 20	2.1 to 8.3
$KHCO_3$ [m]	100.115	267.5	17.0	2.04
NH_4HCO_3 [k]	79.056	269	9.51	1.33
$MgSO_4$ [n]	120.37	270	17	1.7
KNO_3 [d]	101.10	270	10.8	1.2
NH_4ClO_4 [k]	116.48	270.5	9.8	0.93
$NaHCO_3$ [m]	84.007	271	6.25	0.795
Na_2CO_3 [m]	105.99	271	5.84	0.585
$FeSO_4$ [i]	151.91	271	12.7	0.96
$MgCO_3$ [m]	84.314	271.5	3.25	0.398
K_2SO_4 [c,n]	174.26	271.5	6.67	0.410
Na_2SO_4 [c,n]	142.04	272	4.035	0.296
$KClO_4$ [e]	138.55	273	0.74	0.054
$CaSO_4$ [n]	136.14	273	0.18	0.013

Data from [a] Miller and Carpenter (1964), [b] Leliwa-Kopystynski *et al.* (2002), [c] Yatsenko and Chudotvortsev (2002), [d] Marion (2002), [e] Marion *et al.* (2010), [f] Carlson *et al.* (1999), [g] Marion *et al.* (2009), [h] Barduhn and Manudhane (1979), [i] Marion *et al.* (2003), [j] Marion *et al.* (2008), [k] Marion *et al.* (2012), [l] Kargel (1992), [m] Marion (2001), and [n] Marion and Farren (1999). Several of these authors also report data for ternary or higher-order antifreeze-H_2O systems; usually eutectic T are within a few K of the lower of those species' eutectic T. A notable exception is the system CH_2O-NH_3-H_2O: NH_3 reacts with CH_2O to form $(CH_2)_6N_4$ of eutectic T=264 K with 30% by mass (or 3.1 molal) $(CH_2)_6N_4$ (Kargel, 1992). Studies of several systems at pressures up to 3 kbar have shown eutectic T vary by $\lessapprox$ 10 K (Leliwa-Kopystynski *et al.*, 2002; Marion *et al.*, 2005).

Zolotov and Shock, 2001; McKinnon and Zolensky, 2003; Zolotov, 2009, 2014; Glein *et al.*, 2015; Glein, 2015; Marion *et al.*, 2014, and references therein).

In this chapter, we report attempts at modeling the fate of antifreezes (Table 12) and long-lived radionuclides as a result of aqueous alteration of chondritic rock, at chemical equilibrium under conditions relevant to icy world interiors. In the following sections, we first describe our geochemical models and simulations, constrained by data returned by spacecraft, laboratory analyses of meteorites, and spectroscopy of cometary volatiles. We then describe outcomes of water-rock interaction under a vast set of physico-chemical conditions, with particular focus on antifreezes and radionuclides. We discuss the implications of these results for geophysical models, and explore applications to cryovolcanism and to Ceres. Finally, we conclude on these impacts of aqueous geochemistry on icy world evolution.

5.2 Geochemical Models and Simulations

5.2.1 Geochemical Model, Code, and Starting Conditions

To investigate equilibrium fluid and rock compositions under conditions relevant to icy world interiors, we used the freely available geochemical modeling software *PHREEQC 3.1.2* (Parkhurst and Appelo, 2013). Our use of *PHREEQC* was restricted to its basic capabilities: fluid speciation, and computation of equilibrium fluid, rock, and gas assemblages. These calculations were performed using *PHREEQC*'s implementations of an extended Debye-Hückel equation to compute solute activity coefficients (Pitzer and Brewer, 1961; Helgeson, 1969; Anderson, 2005), and of a Peng-Robinson equation to compute gas fugacity coefficients (Peng and Robinson,

1976). Fluid-rock compositions were computed iteratively using a Newton-Raphson algorithm until all species present in the solid assemblage were supersaturated with respect to the speciated solution. Temperatures T and pressures P remained constant throughout each calculation, but pH, redox (as set by the electron potential pe=$-$log a_{e^-}, where a_{e^-} is the electron activity), and water:rock ratio ($W{:}R$) could vary. Input files and the thermodynamic database (see below) can be found at https://github.com/MarcNeveu/IcyDwarf.

Initial ranges of T, P, pH, pe, and $W{:}R$ are shown in Table 13. Ranges of T, P, and $W{:}R$ are constrained by geophysical models (Robuchon and Nimmo, 2011; Neveu *et al.*, 2015a, view). The pH of subsurface fluids is unconstrained; however, because the interaction between mafic silicates and liquid water may generate alkaline solutions (Vance *et al.*, 2007; Glein *et al.*, 2008), we explored neutral (7) to highly alkaline (14) initial values. We varied the starting pe, assuming the oxygen fugacity fO_2 remained within 6 log units of the value buffered by equilibrium between the minerals fayalite, magnetite, and quartz (FMQ buffer). This allowed us to cover a wide range of redox conditions thought to occur in the interiors of the Earth (Ballhaus *et al.*, 1990; Kasting, 1993) and other planetary bodies (Shock and McKinnon, 1993; Zolotov and Shock, 2001; Glein *et al.*, 2009), including the parent bodies of chondritic material (Wadhwa, 2008).

For a given set of input fluid and rock compositions, we performed simulations for 7 starting values of T and P, 8 values of pH, 13 values of pe, and 3 values of $W{:}R$, totaling 15288 runs (Table 13). While simulations were usually quick ($<$ 1 second on a 2.3 GHz Intel Core i7 processor), the Newton-Raphson algorithm was not always able to determine the equilibrium state for a parameter space of over 1000 physico-chemical variables, despite the built-in capability to automatically adjust numerical method

Table 13: Parameter space sampled in geochemical simulations

Parameter	Unit	Min.	Max.	Step
Temperature T	°C	0 [a]	300	50
Pressure P	bar [b]	200	3200	500
pH		7	14	1
log fO_2 (input as pe)		FMQ-6 [c]	FMQ+6	1
Water:rock ratio [d]	by mass	0.1	10	$\times 10$ [e]

[a] We were unable to perform simulations at 0°C; therefore the minimum temperature simulated was 5°C. [b] 1 bar = 0.1 MPa. [c] FMQ: Fayalite-Magnetite-Quartz buffer. [d] Input as mass of water for a rock mass of 1 kg. [e] Geometric step.

parameters such as tolerance thresholds. Such unsuccessful simulations usually took over a minute before being abandoned. To keep computation times reasonable (∼3 weeks), we executed several *PHREEQC* instances in parallel (8 threads) via a routine coded in C using *IPhreeqc* modules (Charlton and Parkhurst, 2011), available at https://github.com/MarcNeveu/IcyDwarf.

Simpler simulations were run to assess the ability of the code to converge towards equilibrium compositions for every set of parameters. These runs involved a simplified chondritic composition (8 minerals) reacting with pure water, in the Fe-Mg-Al-Si-Ca-Na-O-H system. Convergence occurred quickly for almost every set of input parameters.

The large number of physico-chemical variables raises the possibility that the algorithm may output metastable (rather than stable) equilibrium compositions. However, the smoothly varying nature of most compositional outputs with input conditions robustly indicates that computed equilibria are stable.

5.2.2 Initial Rock and Fluid Compositions

The initial mineral assemblages were chosen to match representative elemental (Wasson and Kallemeyn, 1988) and mineralogical compositions of ordinary (McSween *et al.*, 1991) or CM chondrites (Howard *et al.*, 2009, 2011) to within a few percent for each element and mineral group. The detailed initial mineralogical compositions are shown in Table 14 for ordinary chondrites and in Table 15 for CM chondrites. All elements more abundant than about 500 ppm were included (Al, C, Ca, Co, Cr, Fe, H, K, Mg, Mn, Na, Ni, O, P, S, Si and Ti), plus N and a few trace elements (Table 16).

We performed simulations with two possible initial fluid compositions: either pure water, or aqueous fluid of cometary composition. The cometary fluid comprises 5 mol% C, 2 mol% N, 0.5 mol% S, and 520 mol ppm (for the CM rock composition) or 600 mol ppm (ordinary chondrite composition) of Cl. C, N, and S abundances were chosen to roughly match observed abundances of cometary carbon, nitrogen, and sulfur gases, whose ranges span about an order of magnitude across comets (Mumma and Charnley, 2011). Chlorine abundances are the difference between abundances measured in CI chondrites (680 ppm; Wasson and Kallemeyn, 1988), presumably the major chondrite type for which contributions from fluids to the elemental composition are the highest, and those measured either in ordinary (Table 14) or CM chondrites (Table 15). In simulations involving cometary fluid, C, N, S, and Cl are mainly contributed by the fluid; therefore their relative contribution to the water-rock system depends on *W:R*.

Table 14: Mineral composition of the ordinary chondrite-type initial solid assemblage

Species	Formula in *PHREEQC* database	Mass% in initial assemblage	Reported mass%
Major mineral groups			
Feldspars			
K-feldspar	$KAlSi_3O_8$	0.60	0.6 [a]
Albite	$NaAlSi_3O_8$	7.9	7.9 [a]
Anorthite	$CaAl_2(SiO_4)_2$	1.6	1.6 [a]
Pyroxenes			*29.2* [b]
Diopside	$CaMgSi_2O_6$	4.7	4.8 [a]
Enstatite	$MgSiO_3$	15.8	
Ferrosilite	$FeSiO_3$	8.4	
Olivines			*43.0* [a]
Forsterite	Mg_2SiO_4	26.3	
Fayalite	Fe_2SiO_4	16.0	
Tephroite [c]	Mn_2SiO_4	0.5	
Metals			*10.7* [a]
Fe	Fe	9.6	
Ni	Ni	1.0	
Sulfides			
Troilite	FeS	5.8	5.7 [a]
Covellite	CuS	0.012	
Sphalerite	ZnS	0.007	
Other minerals			
Hydroxyapatite	$Ca_5(OH)(PO_4)_3$	0.59	0.6 [a]
Chromite	$FeCr_2O_4$	0.77	0.8 [a]
Ilmenite	$FeTiO_3$	0.19	0.2 [a]
Halite [d]	NaCl	0.013	
Organics [e]			
"Kerogen C292" [f]	$C_{292}H_{288}O_{12}$	0.10	
Pyridine	C_5H_5N	0.027	
Trace species [g]			
Mo	Mo	1.7×10^{-4}	
Co [h]	Co	0.08	
B [i]	B	5.0×10^{-5}	
EuO [h]	EuO	8.1×10^{-6}	
Gd_2O_3 [h]	Gd_2O_3	3.5×10^{-5}	
Eucryptite [j]	$LiAlSiO_4$	3.1×10^{-3}	
Sc [j]	Sc	7.9×10^{-4}	
Sm_2O_3 [h]	Sm_2O_3	2.1×10^{-5}	
Thorianite [h]	ThO_2	4.8×10^{-6}	
Uraninite [h]	UO_2	1.4×10^{-6}	

[a] Typical normative mineralogy from McSween *et al.* (1991). [b] Sum of diopside and hypersthene (orthopyroxene) as reported by McSween *et al.* (1991). [c] Proxy for Mn substitution of Fe and Mg in olivine and sulfide (Allen and Mason, 1973). [d] Zolensky *et al.* (1999). [e] The mixture of specific (theoretical) organic compounds was chosen to match measured organic contributions to the bulk C and N contents of ordinary chondrites (Alexander *et al.*, 1998). [f] Helgeson *et al.* (2009). [g] These elements, except Mo, may be detected on Ceres using *Dawn*'s Gamma Ray and Neutron Detector (T. Prettyman, personal communication). [h] Lodders (2003, Table 9). [i] In practice B is likely present as reedmergnerite feldspar (Lauretta and Lodders, 1997), for which we were unable to find thermodynamic data. [j] Used in place of, respectively, Li_4SiO_4 and Sc_2O_3 (Lodders, 2003, Table 9), for which we could not find thermodynamic data.

Table 15: Mineral composition of the CM chondrite-type initial solid assemblage

Species	Formula in *PHREEQC* database	Mass% in initial assemblage	Reported mass%
Phyllosilicates		64.2	67 to 88 [a]
Serpentines			
Antigorite	$Mg_{48}Si_{34}O_{85}(OH)_{62}$	24.3	
Amesite	$Mg_4Al_4Si_2O_{10}(OH)_8$	0.31	
Cronstedtite	$Fe_4SiO_5(OH)_4$	23.6	
Smectites			
High (Fe,Mg)-smectite	$Ca_{.025}Na_{.1}K_{.2}Fe_{.7}-Mg_{1.15}Al_{1.25}Si_{3.5}O_{10}(OH)_2$	1.5	
Mg-Nontronite	$Mg_{.165}Fe_2Al_{.33}Si_{3.67}O_{10}(OH)_2$	2.5	
Ca-Nontronite	$Ca_{.165}Fe_2Al_{.33}Si_{3.67}O_{10}(OH)_2$	2.5	
K-Nontronite	$K_{.33}Fe_2Al_{.33}Si_{3.67}O_{10}(OH)_2$	0.13	
Na-Nontronite	$Na_{.33}Fe_2Al_{.33}Si_{3.67}O_{10}(OH)_2$	2.5	
Ca-Saponite	$Ca_{.165}Mg_3Al_{.33}Si_{3.67}O_{10}(OH)_2$	0.54	
Na-Saponite	$Na_{.33}Mg_3Al_{.33}Si_{3.67}O_{10}(OH)_2$	0.87	
Ca-Montmorillonite	$Ca_{.165}Mg_{.33}Al_{1.67}Si_4O_{10}(OH)_2$	0.21	
K-Montmorillonite	$K_{.33}Mg_{.33}Al_{1.67}Si_4O_{10}(OH)_2$	0.042	
Na-Montmorillonite	$Na_{.33}Mg_{.33}Al_{1.67}Si_4O_{10}(OH)_2$	0.31	
Chlorites			
Clinochlore	$Mg_5Al_2Si_3O_{10}(OH)_8$	2.5	
Daphnite	$Fe_5Al_2Si_3O_{10}(OH)_8$	2.4	
Zeolites			
Ca-Clinoptilolite	$Ca_{1.7335}Al_{3.45}Fe_{.017}-Si_{14.533}O_{36} \cdot 10.922\ H_2O$	0.30	
K-Clinoptilolite	$K_{3.467}Al_{3.45}Fe_{.017}-Si_{14.533}O_{36} \cdot 10.922\ H_2O$	0.079	
Na-Clinoptilolite	$Na_{3.467}Al_{3.45}Fe_{.017}-Si_{14.533}O_{36} \cdot 10.922\ H_2O$	1.0	
Carbonates, sulfates, salts, oxides, feldspars			
Apatite	$Ca_5(OH)(PO_4)_3$	0.49	
Calcite	$CaCO_3$	1.1	1.1 [a]
Gypsum	$CaSO_4 \cdot 2H_2O$	0.39	0.4 [a]
Halite [b]	NaCl	0.026	
Albite	$NaAlSi_3O_8$	1.2	
Magnetite	Fe_3O_4	1.8	0.6 to 5.2 [a]
Chromite	Fe_2SiO_4	0.71	0.7 [c]
Pyroxenes		4.2	0.0 to 7.5 [a]
Enstatite	$MgSiO_3$	2.1	
Ferrosilite	$FeSiO_3$	1.3	
Wollastonite	$CaSiO_3$	0.33	
Na_2SiO_3	Na_2SiO_3	0.55	
Olivines			
Forsterite	Mg_2SiO_4	9.5	3.6 to 21 [a]
Fayalite	Fe_2SiO_4	0.40	0.0 to 3.1 [a]
Tephroite [d]	Mn_2SiO_4	0.32	
Tochilinite [e]	$6(FeS) \cdot 5(Fe,Mg)(OH)_2$	6.5	Up to 6–7 [a]
Sulfides		3.2	1 to 4 [f]
Troilite	FeS	1.5	
Millerite [g]	NiS	1.8	
Covellite	CuS	0.017	
Sphalerite	ZnS	0.027	
Ca-Al rich inclusions (CAIs)		1.2	0.1 to 3 [h]
Akermanite	$Ca_2MgSi_2O_7$	0.62	
Gehlenite	$Ca_2Al_2SiO_7$	0.23	
Grossular	$Ca_3Al_2(SiO_4)_3$	0.076	
Corundum	Al_2O_3	0.17	
Rutile	TiO_2	0.10	

Species	Formula in *PHREEQC* database	Mass% in initial assemblage	Reported mass%
Organics [i]		3.1	2 [j]
"Kerogen C515" [k]	$C_{515}H_{596}O_{72}$	0.022	
"Kerogen C128" [k]	$C_{128}H_{68}O_7$	1.5	
Pyridine [l]	C_5H_5N	0.85	
"[(6)(CB)(CB)>S]" [m]	S	0.36	
"[(aro)-O-(aro)]" [n]	O	0.40	
Trace species [o]			
Mo	Mo	15×10^{-4}	
Co [p]	Co	5.8×10^{-3}	
B [q]	B	6.0×10^{-5}	
EuO [p]	EuO	8.4×10^{-6}	
Gd_2O_3 [p]	Gd_2O_3	3.2×10^{-5}	
Eucryptite [r]	$LiAlSiO_4$	2.5×10^{-3}	
Sc [r]	Sc	8.1×10^{-4}	
Sm_2O_3 [p]	Sm_2O_3	2.3×10^{-5}	
Thorianite [p]	ThO_2	4.5×10^{-6}	
Uraninite [p]	UO_2	1.3×10^{-6}	

(Continued from previous page.) [a] Howard *et al.* (2011). [b] Barber (1981). [c] Metzler *et al.* (1992). [d] Proxy for Mn substitution of Fe and Mg in olivine and sulfide (Allen and Mason, 1973). [e] Since measurements of thermodynamic data for tochilinite are unavailable (Zolensky *et al.*, 1989; Browning and Bourcier, 1996) aside perhaps from heat capacities between 298 and 720 K (Gooding and Zolensky, 1987), we input tochilinite as its Mg end-member: 6 × brucite ($Mg(OH)_2$) + 5 × troilite (FeS), assuming ideal mixing between the hydroxide and sulfide layers (Zolensky *et al.*, 1989; Browning and Bourcier, 1996). [f] Howard *et al.* (2009). [g] Proxy for pentlandite $(Fe,Ni)_9S_8$. [h] Area% (Hezel *et al.*, 2008). [i] The mixture of specific (theoretical) organic compounds was chosen to match measured organic elemental molar ratios of H:C=0.68, O:C=0.19, N:C=0.03, and S:C=0.07 (Alexander *et al.*, 1998, 2007). We set N:C = 0.06 rather than 0.03 to match measured bulk N abundances (Wasson and Kallemeyn, 1988). [j] Busemann *et al.* (2006). [k] Helgeson *et al.* (2009). [l] Helgeson *et al.* (1998). [m] Richard (2001). [n] Richard and Helgeson (1998). [o] These elements, except Mo, may be detected on Ceres using *Dawn*'s Gamma Ray and Neutron Detector (T. Prettyman, personal communication). [p] Lodders (2003, Table 9). [q] In practice B is likely present as reedmergnerite feldspar (Lauretta and Lodders, 1997), for which we were unable to find thermodynamic data. [r] Used in place of, respectively, Li_4SiO_4 and Sc_2O_3 (Lodders, 2003, Table 9), for which we could not find thermodynamic data.

Table 16: Elemental composition of the initial ordinary and CM chondrite-type assemblages

Element	ppm by mass in input OC composition	Reported ppm by mass in OCs [a]	ppm by mass in input CM composition	Reported ppm by mass in CMs [a]
Al	11870	11300–12200	12196	11800
B	0.5	0.4–0.5	0.60	0.60
C	1069	900–1200	21784	22000
Ca	13403	12500–13100	13043	12700
Cl	80	76–130	160	160
Co	812	490–810	576	575
Cr	3580	3660–3880	3276	3050
Cu	81	80–90	114	115
Eu	0.073	0.073–0.078	0.076	0.076
Fe	259168	185000–275000	220121	210000
Gd	0.300	0.299–0.310	0.28	0.28
H	101	N/A	13819	14000
K	846	780–825	413	400
Li	1.7	1.7–2.1	1.36	1.36
Mg	134356	140000–153000	120608	117000
Mn	2594	1630–2620	1731	1700
Mo	1.7	1.1–1.7	1.5	1.5
N	48	43–70	1497	1520
Na	6948	6400–7000	3953	4100
Ni	9814	10200–17500	11557	12000
O	352410	357000–400000	401235	432000
P	1097	850–1080	910	900
S	21197	20000–23000	31358	33000
Sc	7.9	7.9–8.6	8.1	8.2
Si	179985	169000–189000	140832	129000
Sm	0.185	0.185–0.200	0.20	0.20
Th	0.042	0.042–0.043	0.040	0.040
Ti	612	600–630	620	580
U	0.012	0.012–0.013	0.011	0.011
Zn	48	46–50	184	185

[a] Wasson and Kallemeyn (1988). The range for ordinary chondrite indicates the compositional envelope spanned by H, L, and LL chondrites; we optimized our input ordinary chondrite composition to match that of H chondrites.

5.2.3 Thermodynamic Data

The thermodynamic data used for our calculations are mainly those compiled by J. Johnson and converted to *PHREEQC* format by G. Anderson in the

llnl.dat database (Parkhurst and Appelo, 2013). This database is distributed at http://wwwbrr.cr.usgs.gov/projects/GWC_coupled/phreeqc. It contains thermodynamic data for over a thousand solutes and minerals, as well as gases of low molecular weight. We complemented this database in order to study the potential incorporation of N into ammoniated minerals, the fate of organics, the behavior of salts, and pressure effects. If added thermodynamic data were present in two or more databases, we confirmed that these data matched. The resulting *core5.dat* thermodynamic database can be found at https://github.com/MarcNeveu/IcyDwarf. All database species were allowed to form in each simulation.

The mineral data present in *llnl.dat* were complemented with the mineral, salt, and solid organic data shown in *PHREEQC* format in Table 23 (Appendix C). The salt data added were primarily those determined by Marion *et al.* (2014, and references therein) in their development of the *FREZCHEM* code. No data were added for clathrate hydrates, which are absent from our calculations. [Under conditions producing methane-rich solutions, methane clathrates could form, as most of the subsurface liquid colder than 300 K lies in their stability field (Mousis *et al.*, 2015).]

Added data for small organic (and Fe-bearing) solutes (Table 17) were taken from the *OBIGT* database of the *CHNOSZ* geochemical software package, freely available at http://www.chnosz.net (Dick, 2008). Values for the $\mathring{a}_i$ solute parameter (*–llnl_gamma* in the *llnl.dat* database), specific to the L. Livermore National Laboratory solute model, were taken from the *data0.sup* database of the *EQ3/6* code (Wolery, 1992), which reports thermodynamic data in a format similar to that used here. Data for added organic gases (Table 18) were taken either from the *phreeqc.dat* database, or from the *OBIGT* database (Shock, 1993; Helgeson *et al.*, 1998).

To account for pressure effects on solutes, molar volume parameters for the

Table 17: Thermodynamic data for aqueous solutes added to the expanded database

Species	From reaction	$\log K = a_1 + a_2\,T + a_3/T + a_6\,T^2$, T in K				T range	$\mathring{a}$ [a]
		a_1	a_2 (K^{-1})	a_3 (K)	a_6 (K^{-2})	(K)	
$HCOOH$ [b]	$HCO_3^- + H^+ = HCOOH + 0.5\,O_2$	-85.32	0.1936	0	-1.22×10^{-4}	273–623	3.0
$HCOO^-$ [b]	$HCOOH = HCOO^- + H^+$	-6.456	0.01694	0	-2.71×10^{-5}	273–623	3.5
CH_3COOH [b]	$2\,HCO_3^- + 2\,H^+ = CH_3COOH + 2\,O_2$	-303.1	0.6829	0	-4.57×10^{-4}	273–623	3.0
$CO(NH_2)_2$ [c]	$2\,NH_3 + HCO_3^- + H^+ = CO(NH_2)_2 + 2\,H_2O$	15.98	-0.0441	0	-4.25×10^{-5}	273–623	3.0
C_2H_6 [d,e]	$2\,HCO_3^- + 2\,H^+ + H_2O = C_2H_6 + 3.5\,O_2$	-539.9	1.2150	0	-8.296×10^{-4}	273–623	3.0
C_3H_8 [d]	$3\,HCO_3^- + 3\,H^+ + H_2O = C_3H_8 + 5\,O_2$	-804	1.877	0	-1.33×10^{-3}	273–623	3.0
CH_3OH [d]	$H_2O + HCO_3^- + H^+ = CH_3OH + 1.5\,O_2$	-262.54	0.6159	0	-4.375×10^{-4}	273–623	3.0
CH_3CH_2OH [d]	$H_2O + 2\,HCO_3^- + 2\,H^+ = CH_3CH_2OH + 3\,O_2$	-475.1	1.069	0	-7.284×10^{-4}	273–623	3.0
CH_2O [d]	$HCO_3^- + H^+ = CH_2O + O_2$	-184.9	0.4178	0	-2.817×10^{-4}	273–623	3.0
$Fe(OH)_2^+$ [f]	$2\,H_2O + Fe^{3+} = Fe(OH)_2^+ + 2\,H^+$	6.872	0	-3739	0	273–298	4.0
$Fe(OH)_3$ [f]	$3\,H_2O + Fe^{3+} = Fe(OH)_3 + 3\,H^+$	5.619	0	-5431	0	273–298	3.0
$Fe(OH)_3^-$ [f]	$3\,H_2O + Fe^{2+} = Fe(OH)_3^- + 3\,H^+$	-8.788	0	-6621	0	273–298	4.0
$Fe(OH)_4^-$ [f]	$4\,H_2O + Fe^{3+} = Fe(OH)_4^- + 4\,H^+$	1.700	0	-6946	0	273–298	4.0
$FeCO_3$ [g]	$Fe^{2+} + CO_3^{2-} = FeCO_3$	6.367	0	-592.8	0	N/A	4.0
$FeOH^+$ [f,g]	$H_2O + Fe^{2+} = FeOH^+ + H^+$	0.1706	0	-2883	0	273–298	4.0

These data were added to *PHREEQC*'s *llnl.dat* database to create the expanded *core5.dat* database. [a] From the *data0.sup* database of the *EQ3/6* software package (Wolery, 1992). [b] Shock (1995). [c] Shock and McKinnon (1993). [d] Shock and Helgeson (1990). [e] Although log K data for C_2H_6 (aq) were already available in the *llnl.dat* database, we noticed a discrepancy between those data and those provided in the *data0.sup* database of *EQ3/6* and the *OBIGT* database of *CHNOSZ*, even though all three databases quote the same source for those data (Shock and Helgeson, 1990). We found and confirmed with D. Parkhurst (pers. comm.) that this discrepancy may be resolved if the a_1 term provided in *llnl.dat* is replaced by its opposite (negative) value. It is possible that the minus sign was omitted when compiling the *llnl.dat* data. [f] Marion *et al.* (2008). [g] Marion *et al.* (2003).

Table 18: Thermodynamic data for dissolution reactions of gases added to the expanded database

Species	log $K_s = a_1 + a_2\ T + a_3/T + a_6\ T^2$, T in K				T range	T_c	P_c
	a_1	a_2 (K^{-1})	a_3 (K)	a_6 (K^{-2})	(K)	(K)	(bar)
C_2H_6 [a]	5.35	-0.0456	0	6.00×10^{-5}	273–448	305	48.6
C_2H_4 [b]	4.46	-0.037	0	4.715×10^{-5}	273–448	283	50.53

These data were added to the *llnl.dat* database to create the expanded *core5.dat* database. Data from [a] Helgeson *et al.* (1998) and [b] Shock (1993), respectively.

ideal solute portion of the equations of Appelo *et al.* (2014) were added for as many solutes as possible. These parameters were taken either from the *phreeqc.dat* database (Appelo *et al.*, 2014) or, if unavailable there, from the *OBIGT* database (primary data from Shock and Helgeson (1988a, 1990), Shock *et al.* (1989), Shock and Koretsky (1993), Shock and McKinnon (1993), Haas *et al.* (1995), Shock (1995), McCollom and Shock (1997), Shock *et al.* (1997a,b), Sverjensky *et al.* (1997), Sassani and Shock (1998), Stefánsson (2001), and Schulte *et al.* (2001)). Most molar volumes of solids were taken from the *OBIGT* database (primary data from Helgeson (1978), Robie *et al.* (1979), Jackson and Helgeson (1985), Clodic and Meike (1997), and Shock *et al.* (1997a)), from Marion *et al.* (2005, 2008, 2009, 2012), or if unavailable from these references, from the online databases *Mincryst* at http://database.iem.ac.ru/mincryst (Chichagov *et al.*, 2001), *WebElements* (for elemental species) at http://www.webelements.com/periodicity/molar_volume, and *WebMineral* at http://webmineral.com.

5.2.4 Limitations of our Equilibrium Simulations

Our calculations suffered from several limitations. First, while most conditions resulted in solutions dilute enough for the extended Debye-Hückel model to apply

(ionic strength $\mu < 0.1$), the few conditions under which brucite formed involved concentrated solutions ($\mu \approx 10$) beyond the range of application of the model. Second, we assumed that trace elements formed their own pure minerals, rather than replacing major elements at the crystallographic sites of more common minerals (Allen and Mason, 1973; Lodders, 2003). However, owing to their low abundances, any assumption on trace species likely seldom influences calculation outcomes. Third, the calculations involved thermodynamic data assembled from many sources. This compilation, albeit comprehensive, may contain inconsistencies between datasets. Fourth, our simulations did not account for kinetic effects, which may arise from low T, slow fluid transport, or limited water-rock contact area (Skelton *et al.*, 2005). Finally, some thermodynamic data are undetermined or invalid over part of the T and P ranges spanned by our calculations. While all database species were included in every calculation, care was taken during the interpretation of simulation results to account for this limitation. This was especially true for salt species, whose data are often determined only at $T < 50°C$.

5.3 Modeling Results

The results of all simulations are provided in tab-separated .txt files supplementary to this article. Below, we highlight key outcomes. Simulations which did not converge to a stable equilibrium (see above) are shown by black squares in the figures below.

5.3.1 Dependency on Initial Conditions

Before investigating simulation outputs, we performed several checks of the validity of the *PHREEQC* simulations. First, we checked whether simulations were carried out at ionic strengths within the range of validity of the extended Debye-Hückel electrolyte theory ($\mu < 0.1$). This was the case for most runs at *W:R* ≥ 1 by mass, but never the case at *W:R*=0.1. Results reported for *W:R*=0.1 are still provided, only for qualitative comparison with outcomes at higher *W:R*.

Second, we checked the dependency of equilibrium *W:R*, pH, and redox, the key inputs allowed to vary during a run (T and P being fixed), on their input values. Equilibrium *W:R* tended to match the input values; however, simulations starting with ordinary chondrite at *W:R*=0.1 tended to yield equilibrium *W:R* of 0.01 or lower, consistent with high μ at these conditions. Generally, final pH and redox conditions depended on those initially specified (lower initial pH and log fO_2 yielding lower final pH and log fO_2), rather than being buffered by a specific set of chemical reactions. This was especially true at *W:R* of 1 and 10 by mass, independently of T and P.

Therefore, we checked the dependency of final mineral, gas, and solution compositions on starting pH and redox. Equilibrium mineral and fluid compositions at a given T and P seem to depend little on initial redox conditions (Fig. 29). However, at 100°C and above, different equilibrium solution compositions and mineral assemblages were obtained for high-pH simulations compared to those run at lower initial pH. Because high-pH simulations tended to produce concentrated solutions ($\mu \approx 10$, far above the validity threshold of the extended Debye-Hückel model), we did not lend credence to these outcomes. The relative production of gas species was insensitive

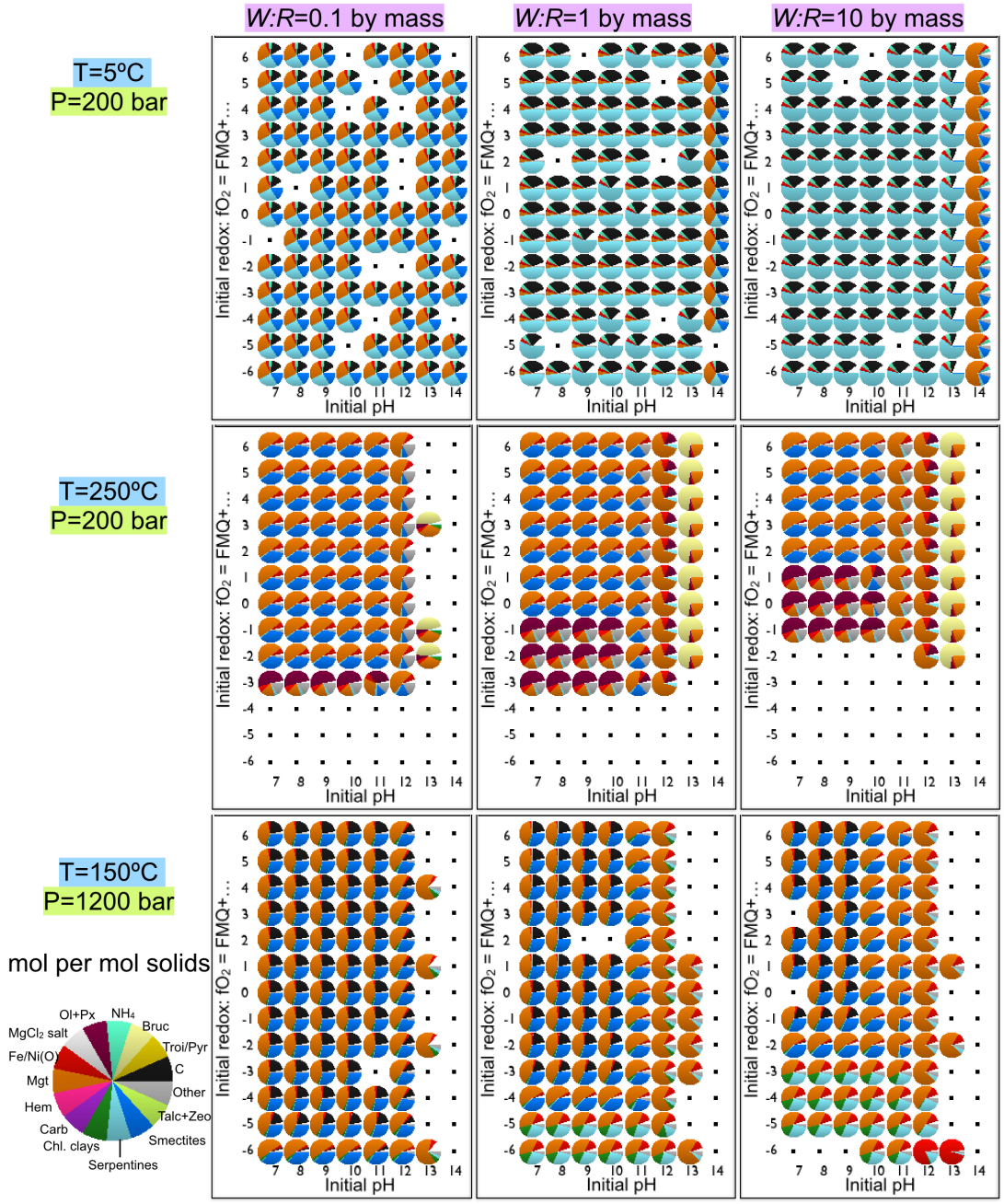

Figure 29: Sensitivity of equilibrium mineral assemblages to starting pH and redox

The sensitivity is explored for a variety of $W{:}R$, P, and T, for CM chondrite rock reacting with pure water. See Fig. 30 for detailed mineral key. Black dots represent cases where the code did not readily converge (see text).

to starting pH and redox, except for H_2 gas, whose production was higher for more reduced initial conditions, especially at high T and $W{:}R \geq 1$.

5.3.2 Equilibrium Assemblages

5.3.2.1 Simulation Products

Equilibrium solid, solution, and gas compositions are shown in Fig. 30, 31, and 32, respectively, for a variety of T, P, $W{:}R$, and initial fluid and rock compositions. Solution and gas compositions are reported by mole, whereas mineral distributions are reported by mass. As only major minerals are shown, mineral distributions do not quite add up to 100%.

Solid assemblages are dominated by serpentines, chiefly antigorite which contains most Mg and Si; chlorite and smectite clays are also common (Fig. 30). Fe is primarily present as magnetite if the initial rock composition is that of CM chondrites, and otherwise as the serpentine cronstedtite, olivines and pyroxenes (if $T \geq 200$°C), or reduced Fe, FeO, or Fe-Ni oxides.

Such mineral compositions commonly result from the serpentinization of mafic (Fe- and Mg-rich) rocks (e.g., Vance *et al.*, 2007). However, anhydrous olivines and pyroxenes are expected to predominate over clays only for $T \geq 400$°C (Wunder *et al.*, 2001; Fortes *et al.*, 2007; Vance *et al.*, 2007) at the range of pressures simulated ($P < 10^4$ bar). Their occurrence in our simulation outcomes, in lesser or equal amounts to clays, may arise from a gradual transition in the degree of hydration of mafic silicates from low to high T, incompletely captured in our numerical models which include only mineral end-members.

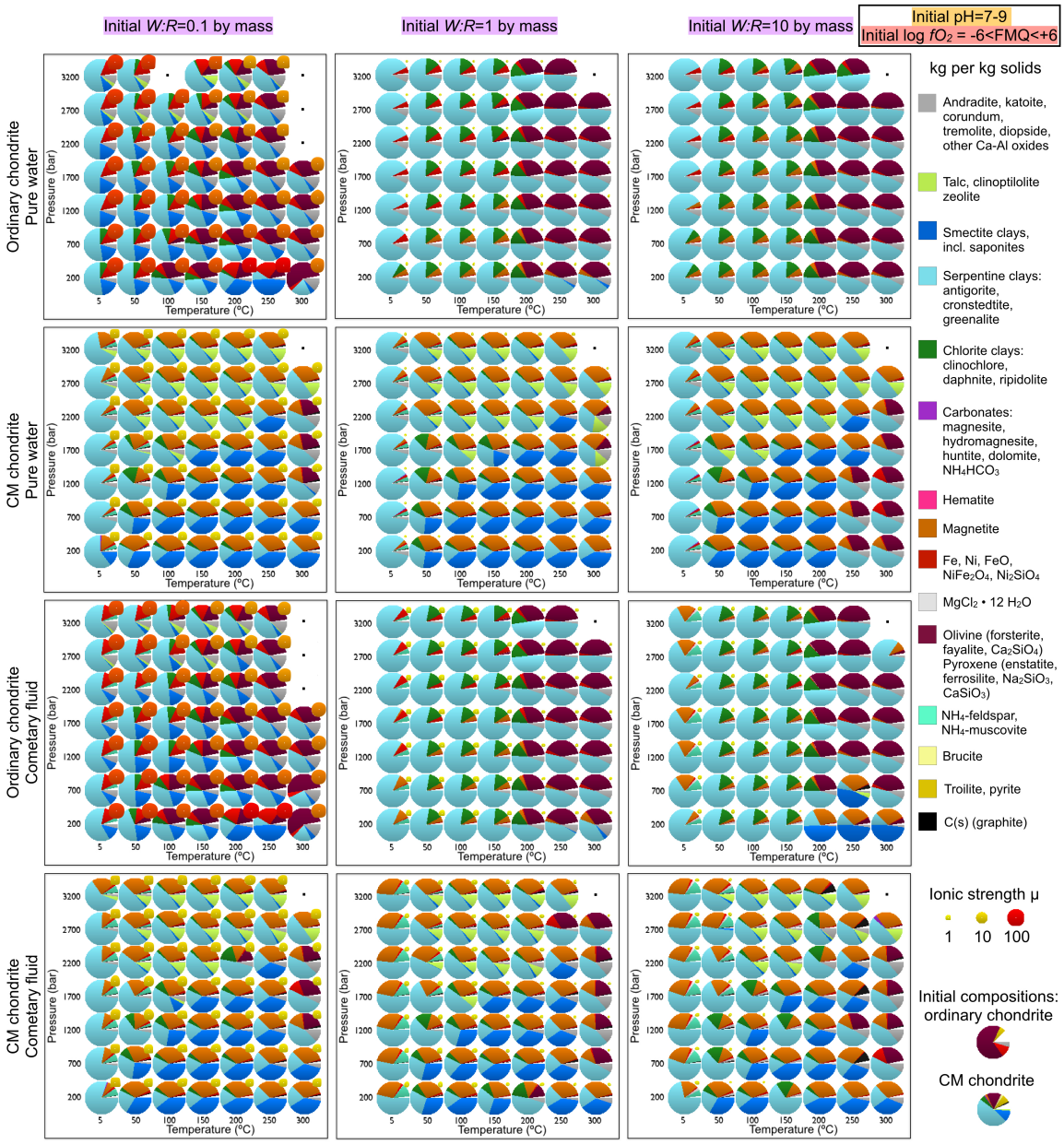

Figure 30: Equilibrium mineral assemblages

Inset for each pie chart: ionic strength of the solution in equilibrium with the assemblage. Equilibrium $W{:}R$ are similar to initial values except for runs starting with ordinary chondrite at $W{:}R = 0.1$, in which case equilibrium $W{:}R \sim 0.01$.

Notably, these assemblages are devoid of C- and especially S-bearing species. Indeed, C and S are mostly present in solution, of which they often dominate the composition (Fig. 31). C is mostly reduced, present mainly as dissolved CH_4 with some C_2H_6. However, in about 17% of all successful runs, carbonate is present above 10^{-3} mol kg^{-1} H_2O and can exceed CH_4, even though CH_4 is never negligible ($> 10^{-3}$ mol kg^{-1} H_2O). In all runs, formate $HCOO^-$ is the most common organic solute (up to $\sim 10^{-2}$ mol kg^{-1} H_2O), followed by acetate CH_3COO^-. S is mildly oxidized, present chiefly as pentathionate $S_5O_6^{2-}$ in all runs. H_2 dominates the composition of solutions resulting from the reaction between ordinary chondrite rock and pure water if $W{:}R \geq 1$, whereas N species (NH_3 and NH_4^+) predominate if the starting fluid is cometary and $W{:}R \geq 1$. Finally, Ca and Na make up to 30 mol% of solutes. Cl, not shown, is present above 10^{-3} mol kg^{-1} H_2O in 28% of all successful simulations and makes up to ∼1% of solutes. The elemental composition of all solution compositions seems independent of pH and redox.

Gas compositions are dominated by the reduced species H_2 and, if substantial C is initially present in the system, CH_4 (with some C_2H_6 if $T < 50°C$, but negligible C_3H_8 and no C_2H_4). Major gas production occurs at high cometary fluid:rock ratios due to the larger volatile supply. H_2 is a typical serpentinization product (Abrajano *et al.*, 1990; Sherwood Lollar *et al.*, 1993; Sleep *et al.*, 2004), resulting from the reduction of H_2O as reduced mafic rock is oxidized. CH_4 gas is a common product of hydrothermal reactions, its abiotic production stemming either from degradation of organic matter or reduction of CO_2 by H_2 (Gunter, 1978; Sherwood Lollar *et al.*, 1993; Darling, 1998; Oze and Sharma, 2005); both processes likely occur in our simulations since C is supplied both as chondritic organics and in cometary fluid. Comparatively, production of CO_2 and N gases is negligible, and no S gases are produced.

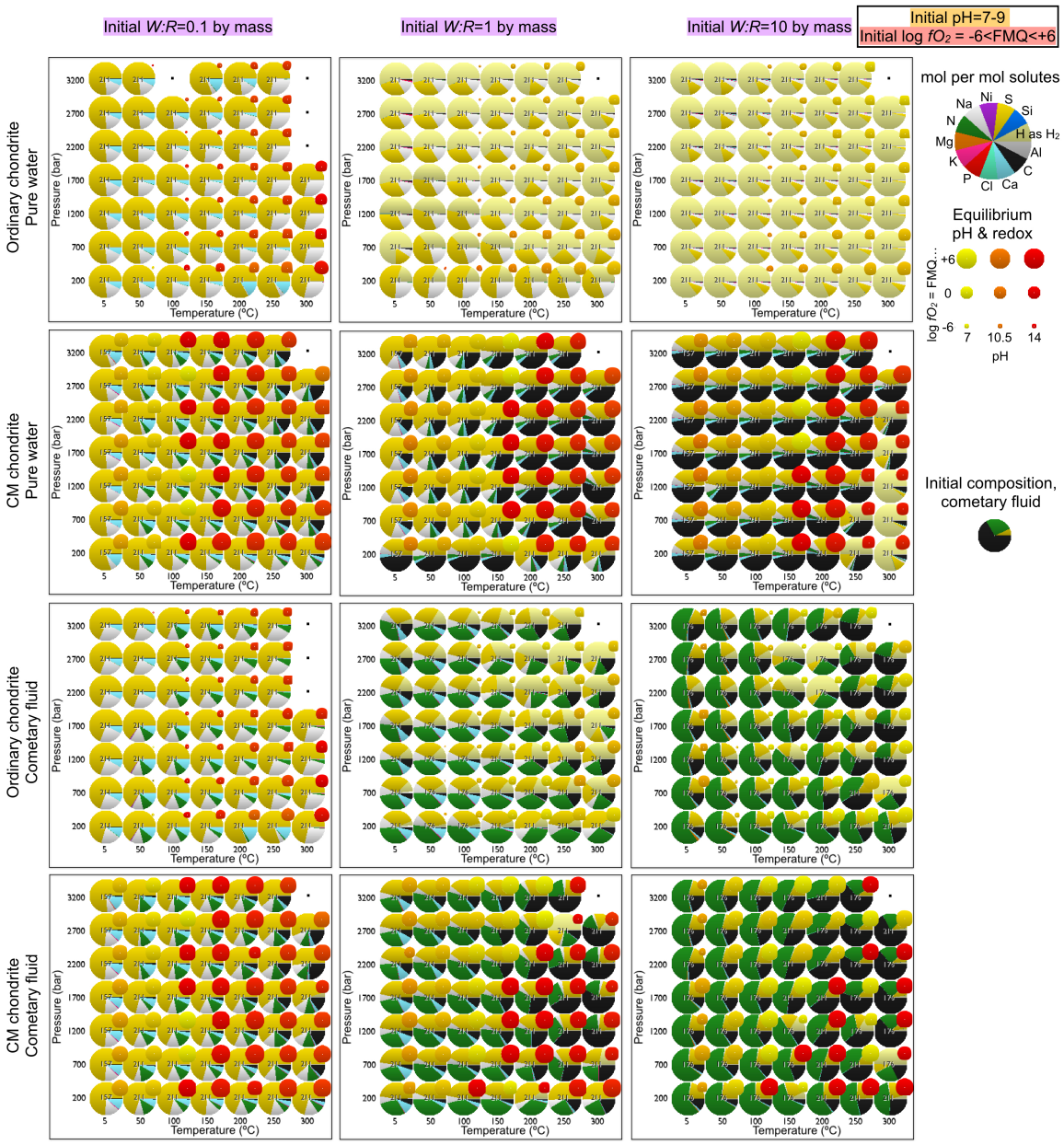

Figure 31: Relative elemental composition of equilibrium solutions

These solutions are in equilibrium with the assemblages shown in Fig. 30. The solution freezing temperature is indicated, assuming fractional precipitation the species listed in Table 12 as T decreases below 273 K. The inset for each pie chart indicates equilibrium pH (color) and redox (size) conditions. Equilibrium $W{:}R$ are similar to initial values except for runs starting with ordinary chondrite at $W{:}R = 0.1$, in which case equilibrium $W{:}R \sim 0.01$.

5.3.2.2 Comparison with Carbonaceous Chondrite Mineralogies

CI chondrites, the most aqueously altered chondrites in the meteorite collection (Brearley, 2006), provide a useful benchmark for our modeling results. Our simulations encompass the presumed physico-chemical conditions of alteration that yielded CI material (Table 3 from Brearley, 2006; Zolensky *et al.*, 1993). Our equilibrium assemblages (Fig. 30) are similar to CI chondrite mineralogies, which are rich in Fe- and Mg-serpentines, saponite (smectite), and contain about 10% magnetite by mass (Hyman and Rowe, 1983; McSween, 1987; Tomeoka and Buseck, 1988; Zolensky *et al.*, 1993; Brearley, 2006). Sulfates might also precipitate from our equilibrium solutions should the water activity decrease (Fig. 31); this is consistent with observations of sulfate salts in CIs, whether indigenous or remobilized and re-precipitated after falling on Earth (Fredriksson and Kerridge, 1988; Zolensky *et al.*, 1993; Gounelle and Zolensky, 2001; Airieau *et al.*, 2005; Brearley, 2006). Above 200°C, the persistence of olivine and pyroxene (Fig. 30) is consistent with the conditions of aqueous alteration (metasomatism) previously inferred from observations of largely anhydrous mineral assemblages in carbonaceous chondrites (Brearley, 2006, and references therein).

However, other CI mineral groups are notably absent from our assemblages: carbonates (Fredriksson and Kerridge, 1988; Tomeoka and Buseck, 1988; Johnson and Prinz, 1993; Zolensky *et al.*, 1993; Endreß and Bischoff, 1996) and sulfides (Kerridge *et al.*, 1979; McSween, 1987; Tomeoka and Buseck, 1988; Zolensky *et al.*, 1993). Both mineral groups are also present in CM, CR, and CV chondrites. Why, then, do our simulations yield oxidized S and reduced C rather than the contrary?

A clue may come from the C isotopic composition of CI carbonates, heavier than that of CI organics. For this reason, carbonates on CIs are believed to result from

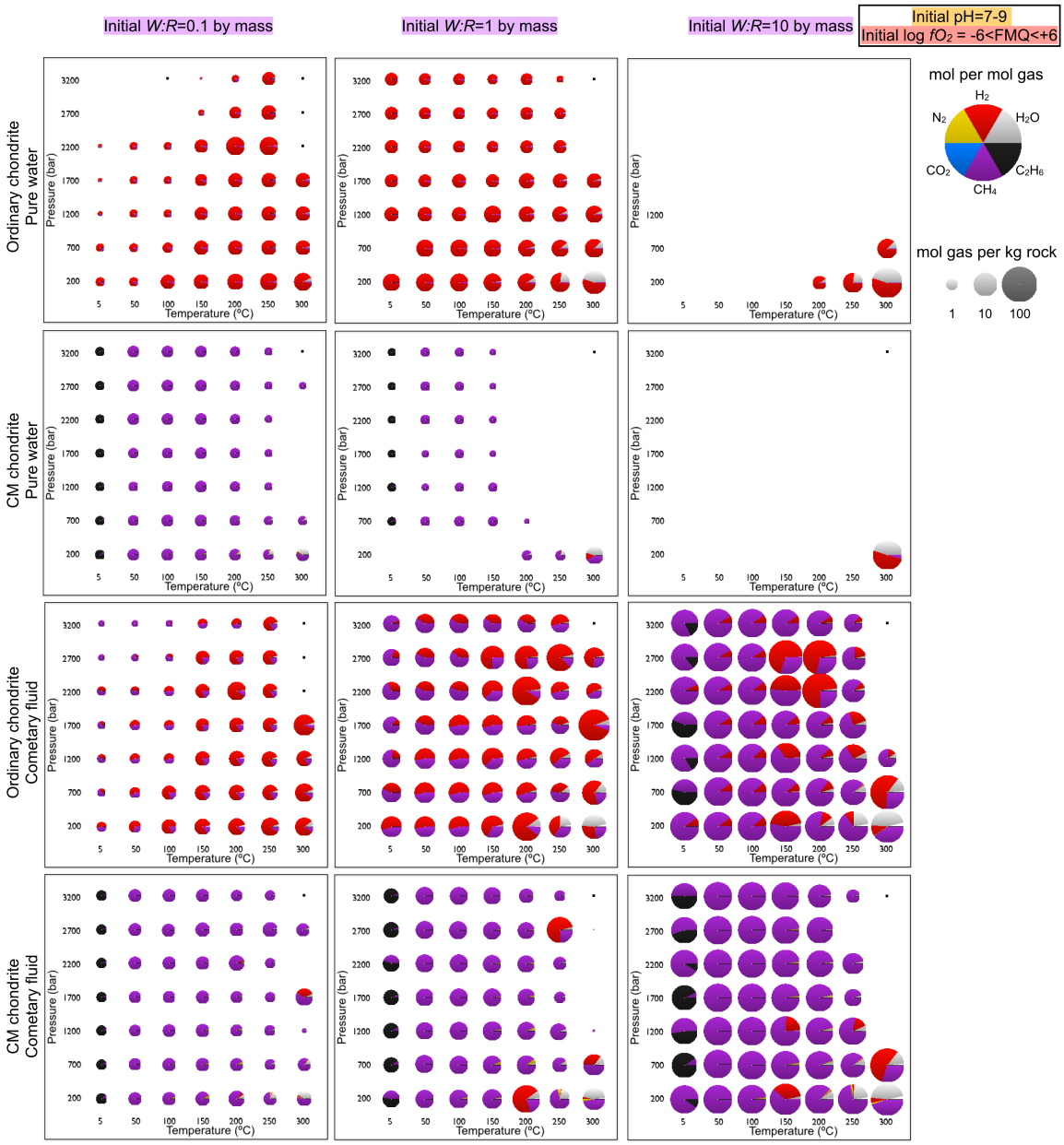

Figure 32: Equilibrium gas compositions

The pie chart size indicates the amount of gas produced; the relative molar species distribution is color-coded according to the legend in the right margin. Equilibrium $W{:}R$ are similar to initial values except for runs starting with ordinary chondrite at $W{:}R = 0.1$, in which case equilibrium $W{:}R \sim 0.01$.

selective aqueous alteration of presolar grains of heavy C isotopic composition on a parent body (Brearley, 2006, and references therein). This postulated localized alteration is different from the global chemical equilibrium we simulated. Moreover, nearly all the initial solid carbon in our simulations is supplied as organics rather than carbides (Tables 14 and 15). Finally, it may be that H_2 and (maybe) CH_4 gas products were outgassed (Fig. 32), leaving the chemical system before parent-body alteration ceased, and driving it toward more oxidizing conditions that led the remaining carbon to remain as carbonates in CIs. If so, most of the H_2 outgassing would have had to occur before much C reduction took place, because carbonates make up enough of CIs ($\sim$ 5 vol%) to contain most of the presumed C in the fluid-rock system (Fredriksson and Kerridge, 1988; Endreß and Bischoff, 1996). The major influence of redox conditions on C and S speciation was also noted by Zolotov (2007).

The absence of S as sulfides in our simulation results suggests that S becomes oxidized by aqueous fluids if reactions proceed to equilibrium. S oxidation may have been only partial on carbonaceous chondrite parent bodies: the higher solubility (mobility) of sulfate in aqueous fluids compared to other alteration products may have resulted in S oxidation at a different time and place than the formation of most other secondary species (Airieau *et al.*, 2005).

5.3.2.3 Comparison with Icy World Ocean Chemistries

The equilibrium solutions resulting from our geochemical simulations have high S/Cl ratio, similar to bulk chondritic (input) values, because both elements are largely in solution. This composition reflects the scarcity of Cl compared to S, both in chondrites (Wasson and Kallemeyn, 1988; Lodders, 2003) and in comets (Mumma

and Charnley, 2011; Bockelée-Morvan *et al.*, 2014). Previous geochemical models assuming similar starting chondritic compositions have also yielded sulfur-rich oceans on icy worlds (Kargel *et al.*, 2000; Zolotov and Shock, 2001; Zolotov and Kargel, 2009). In stark contrast, icy world oceans seem rich in chlorine. In Enceladus' plume, NaCl constitutes about 1% of plume icy grains (Postberg *et al.*, 2009, 2011), whereas S is present as H_2S gas only at about 20 ppmv (Waite *et al.*, 2009). Europa's surface salts were initially interpreted to be a mixture of sulfates with some sulfuric acid and carbonates (McCord *et al.*, 1998, 1999, 2002; Orlando *et al.*, 2005), but recent experiments suggest they may be $> 0.1\%$ by mass of irradiated chlorides instead (Hand and Carlson, 2015). Although Ganymede's surface seems to bear surface salts (McCord *et al.*, 2001), this interpretation might be subject to revision in light of the results of Hand and Carlson (2015).

Sulfate salts are predicted chondritic alteration products (Kargel *et al.*, 2000; Zolotov and Kargel, 2009, this work). Conversely, a scarcity of S salts may be due to sulfide mineral formation under equilibrium conditions (Zolotov, 2007). Chlorine-dominated oceans may result from the unique hydrophilic behavior of Cl (Zolotov, 2007; Glein and Shock, 2010; Sharp and Draper, 2013). It is also possible that Cl was delivered to carbonaceous chondrite parent bodies via HCl ices (Zolotov and Mironenko, 2007); we made this assumption implicitly by assuming CI levels of chlorine in simulations involving cometary fluid. Most chlorine, remaining in volatile components, might then have escaped during parent body evolution, following impacts (Sharp and Draper, 2013) including the event leading to parent body disruption. On the (larger) icy worlds that did not get disrupted, Cl would still be abundant. To date, HCl gas sublimated from ice has not been observed on comets (upper limits around 0.01 mol% with respect to water vapor), even though it is seen in interstellar

molecular clouds (Bockelée-Morvan *et al.*, 2014). A final complication, at least in icy worlds with thick, convecting ice shells, is the possibility for compositional evolution of brine during transport, e.g. from S-dominated at the shell bottom to Cl-dominated at the top (Zolotov *et al.*, 2004).

We further explored the effects of increased chlorine abundances by performing runs with 6800 ppm initial Cl by mass with respect to water, i.e., ten times its abundance in CIs if the water:rock ratio is 1. These simulations resulted in a greater proportion of Cl either in mineral assemblages ($T \leq 150$°C, as $MgCl_2{\cdot}12H_2O$) or in solution ($T > 150$°C). The effects were most noticeable at $W{:}R$=10 since this extra Cl is supplied as ices: under these conditions and below 150°C, $MgCl_2{\cdot}12H_2O$ makes up 25% of the solids by mass. Above 150°C, the molar Cl:S ratio in solution reaches values of ≈3. Unsurprisingly, adding more Cl had no effect on the chemical system at $W{:}R$=0.1. Thus, an abundant initial supply of Cl in ices might result in Cl-dominated oceans even in the absence of sulfide formation.

5.3.3 Fate of Antifreezes

The goal of this study is to determine the effects of water-rock interaction on the fate of antifreezes and radionuclides. We first focus on the antifreezes listed in Table 12.

Volatile antifreezes (CH_3OH, NH_3, CH_2O) in aqueous solution have the lowest eutectic T (Table 12), to the exception of CH_2O whose antifreeze capabilities are hindered by its exothermic reactivity in water (polymerization) or with ammonia to form $(CH_2)_6N_4$ (Kargel, 1992). Our simulations of chemical equilibrium result in neither CH_3OH nor CH_2O being present in solution in substantial amounts: their

concentrations are always below 10^{-6} and 10^{-11} mol kg^{-1} H_2O, respectively, even under conditions for which oxidized and reduced C-solutes (carbonate and methane) coexist. This is consistent with organic compounds being only metastable in the C-H-O-N system: only kinetic barriers could prevent loss of primordial or synthesized CH_3OH and CH_2O in aqueous solution (Shock, 1990). Kinetic aspects were not considered in our simulations.

Conversely, NH_3 is a stable equilibrium product in the C-H-O-N system (Shock, 1990). Thus, at equilibrium, NH_3 can only be lost by conversion to inorganic forms: oxidation to N_2, exsolution as NH_3 gas, and protonation to NH_4^+ possibly followed by incorporation in NH_4-bearing minerals and salts. The partitioning of N between solid, aqueous, and gas phases is shown in Fig. 33, under the same physico-chemical conditions leading to the mineral, solution, and gas compositions described above. Generally, NH_3 is at least partially conserved. Crucially however, the stable form of N in the lowest-T (5°C) fluid-chondritic systems simulated is often NH_4-minerals, especially at low *W:R*. Protonation to NH_4^+ commonly occurs, to a greater extent at lower values of T, *W:R*, and (generally) pH, and to a lesser extent if the supply of Cl is greater (assuming supply as ices; see above; data not shown). Unsurprisingly, N_2 production depends on redox conditions. Although oxidation to N_2 occurs only where shown on Fig. 33, it is higher than shown (but not by much) at $fO_2 >$ FMQ and can become zero for FMQ $>$ log $fO_2 >$ FMQ-6. The lack of strong NH_3 oxidation to N_2 is somewhat at odds with the analytical speciation calculations in the CH_4-CO_2-NH_3-N_2 system of Glein *et al.* (2008), for Enceladus' ocean at similar N molalities and redox conditions. A possible cause for this mismatch is that Glein *et al.* (2008) did not account for NH_4^+ or other N aqueous and gas species, such as N_2 gas. However, the

persistence of NH_3 together with CH_4 is consistent with equilibrium conditions at $T < 300°C$ and $fO_2 \gtrapprox$ FMQ (Glein *et al.*, 2009).

The antifreeze role of NH_3 is complemented by that of salts. On Fig. 31, we have indicated the freezing point of equilibrium solutions, should they cool below 273 K and the brine antifreezes shown in Table 12 fully freeze out, sequentially, once their binary eutectic T with H_2O is reached. These calculations are approximative in two ways: first, solutes may also be removed if supersaturated species precipitate, following an equilibrium (rather than fractional) pathway, if freezing occurs more slowly than speciation. This is likely the case for freezing driven by a decline in radiogenic heating rates, which occurs over geological timescales (e.g. Desch *et al.*, 2009; Castillo-Rogez and McCord, 2010; Neveu *et al.*, 2015a). In these calculations, equilibrium speciation is ignored. Second, ternary and higher-order salt systems, which tend to have lower eutectic T than binary salt-H_2O systems, are not considered. Usually, eutectic T for such systems are within a few K of the lower eutectic T of the constituting binary systems (Kargel, 1992).

Because most solutions are rich in mildly oxidized S, we assumed sulfate salts may be allowed to form. If so, while $CaSO_4$ and Na_2SO_4 brine freezing at $T \approx 272$ K would remove part of S solutes, there seems to be enough oxidized S in solution to maintain liquid brine down to 211 K, the H_2SO_4-H_2O eutectic point (Carlson *et al.*, 1999; Marion *et al.*, 2005). This would require acidification of the solution during partial freezing between 273 and 211 K. Assuming all the initial S goes into solution and not accounting for H_2O loss to mineral hydration, about 20% of the initial liquid H_2O remains at 211 K. Alternatively, N-dominated solutions can remain partially liquid down to 176 K, the eutectic T of the NH_3-H_2O system (Croft *et al.*, 1988; Kargel, 1992; Leliwa-Kopystynski *et al.*, 2002; Yatsenko and Chudotvortsev,

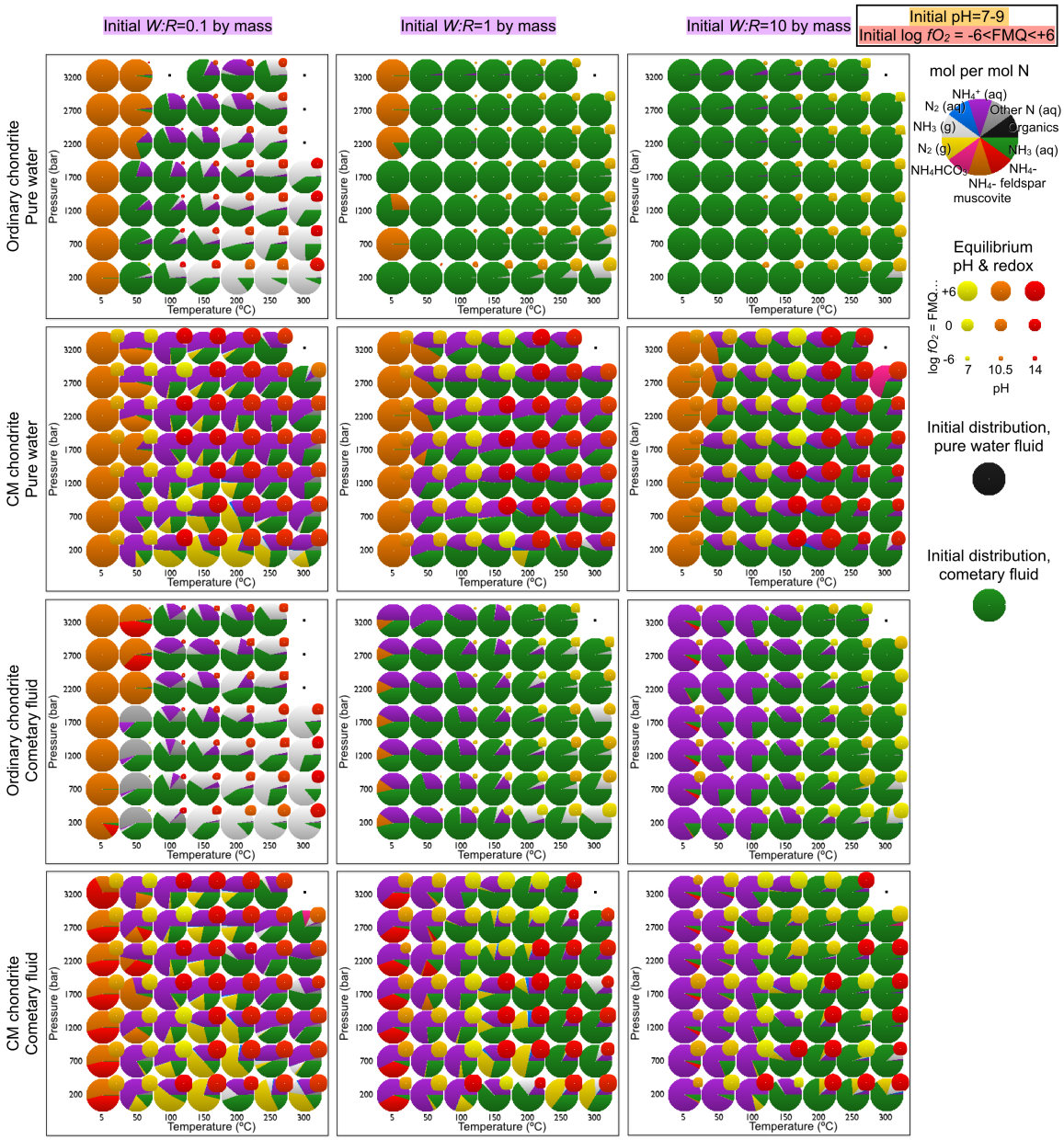

Figure 33: Fate of N species

Equilibrium $W{:}R$ are similar to initial values except for runs starting with ordinary chondrite at $W{:}R = 0.1$, in which case equilibrium $W{:}R \sim 0.01$. Equilibrium pH and redox conditions (inset for each pie chart) are indicated in the key. “Other N (aq)" primarily refers to metal:NH_3 complexes.

2002). This occurs only if there remains enough reduced N after freezing of NH_4ClO_4, NH_4HCO_3, NH_4Cl, NH_4NO_3, and $(NH_4)_2SO_4$ brines. If the initial NH_3 (2 mol% or 1.11 mol kg^{-1} H_2O) is conserved, and neglecting mineral hydration, about 4% of the initial liquid H_2O remains at 176 K. In Fig. 31, some solutions are shown to remain partially liquid down to 157 K, the CH_3OH-H_2O eutectic temperature (Miller and Carpenter, 1964); in this case only a tiny fraction ($< 10^{-8}$) of the initial liquid H_2O remains, given that the methanol molality must increase from $< 10^{-6}$ mol kg^{-1} H_2O before any freezing occurs to 127 mol kg^{-1} H_2O at the eutectic composition.

Thus, while water-rock interaction results in negligible CH_3OH and CH_2O abundances at chemical equilibrium, NH_3 tends to be a non-negligible N species in warm and hot solutions ($T \geq 50°C$) where incorporation into NH_4-bearing minerals is prevented. Therefore, NH_3 may be the prominent volatile antifreeze, provided that as circulating fluids cool, kinetic barriers (such as low T or dilution to high *W:R*) prevent its incorporation into minerals, or that water-rock interaction has ceased. While water-rock reactions can partially consume some initial NH_3, they also leach S and other elements, whose precipitation as salts can lower the freezing point of equilibrium solutions down to 211 K.

5.3.4 Fate of Radionuclides

The distribution of potassium K between feldspar, clays, and solutes is shown in Fig. 34. At chemical equilibrium, K is either locked up in clays or leached. Leaching seems favored at high pH and/or high *W:R*, with no obvious dependence on T, P, and redox conditions. The lack of constraints on pH in icy world oceans (Glein *et al.*, 2015), makes it difficult to robustly predict the extent to which the distribution of

^{40}K radionuclide could shift from that of rock to that of liquid or ice. However, hints from observations or geophysical models that water-rock interaction occurred under a variety of water:rock ratios, including values above 1 by mass, may be taken as an indication that a substantial fraction of ^{40}K may have been leached.

Contrasting strongly with K, only a tiny fraction of thorium Th (<0.01%) is leached in all runs, and no Th-bearing solid species form aside from the thorianite (ThO_2) specified initially. (Admittedly, the thermodynamic database contained only a few Th solids: Th, $Th(NO_3)_4 \cdot 5\ H_2O$, $Th(OH)_4$, $Th(SO_4)_2$, ThS, ThS_2, Th_2S_3, Th_7S_{12}, and $ThCl_4$.) Thus, water-rock interaction does not seem to affect the distribution of the radionuclide ^{232}Th, which remains associated with rock.

At equilibrium, all uranium U is present either as the primary mineral UO_2 or as leached solutes (data not shown). U partitioning between UO_2 and solutes seems to depend solely on *W:R* and temperature: the fate of radionuclides ^{235}U and ^{238}U hinges on these two geophysical parameters. At *W:R*=10, the fraction of dissolved U is 100% for $T \geq 150$°C and 10-70% at lower T. At *W:R*=1, this fraction is 100% for $T \geq 200$°C, 10-30% at 150°C, and 1-5% at lower T. At *W:R*=0.1 (beyond the range of applicability of the Debye-Hückel model), it is 100% if $T \geq 250$°C, ≈10% at 200°C, and negligible at lower T.

Th and U may be less likely present as pure ThO_2 or UO_2 than as trace impurities in more abundant minerals. If so, their fate (preservation, dissolution, or hydration) may be linked to that of the host mineral. The above results provide a useful indication of their fate as isolated species, should they become concentrated, e.g., by fluid intrusions in the host matrix.

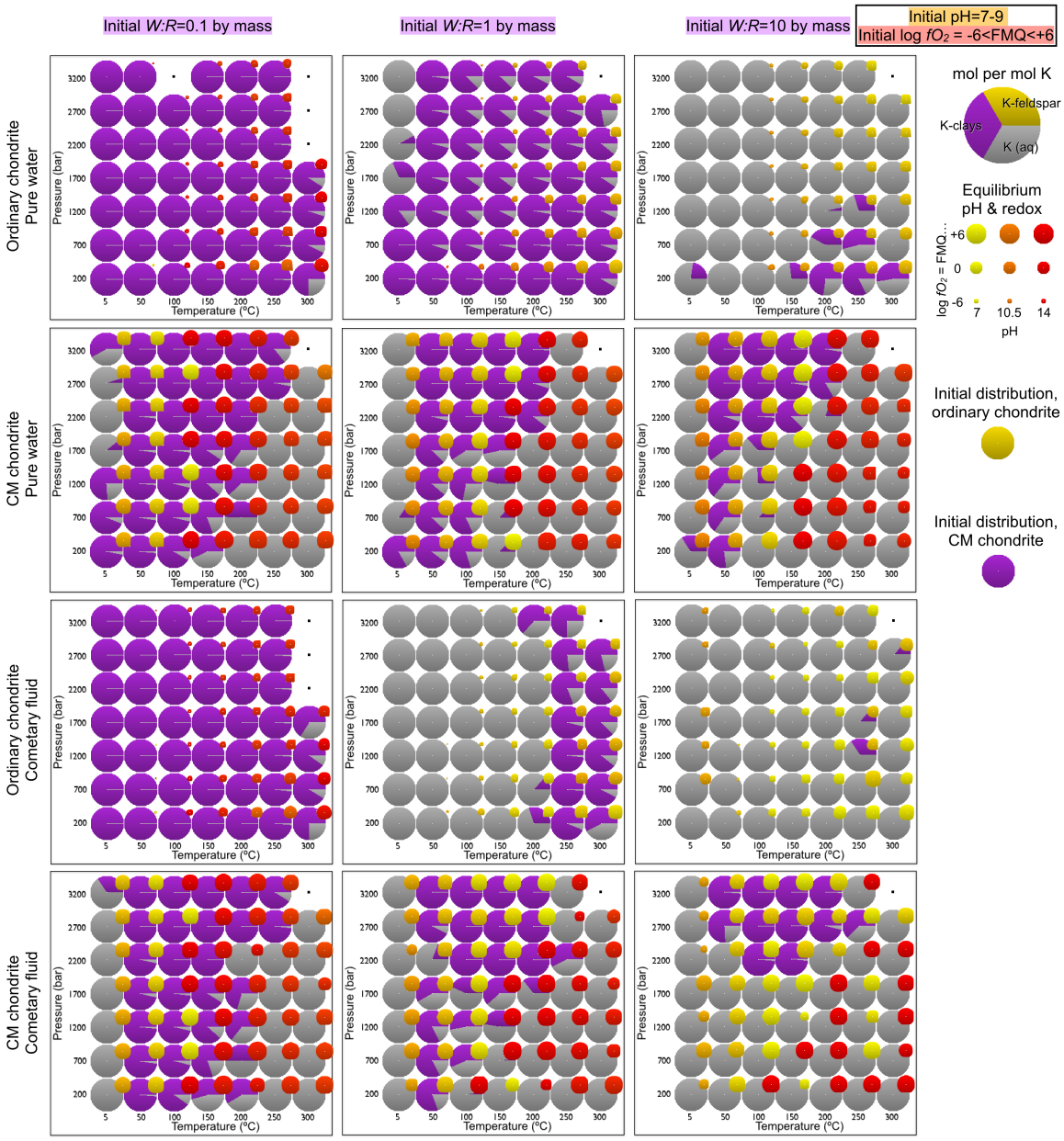

Figure 34: Fate of K

Equilibrium $W{:}R$ are similar to initial values except for runs starting with ordinary chondrite at $W{:}R = 0.1$, in which case equilibrium $W{:}R \sim 0.01$. Equilibrium pH and redox conditions (inset for each pie chart) are indicated in the key.

5.4 Effects on Geophysical Evolution

5.4.1 Suggestions for Geophysical Models

The above results suggest that the effects of water-rock interaction on antifreezes and radionuclides vary greatly between species. This is not surprising for antifreezes, which are chemically diverse, but perhaps more so for radionuclides, which are traditionally clumped by geophysical modelers as a single, total radiogenic heat source. These results are intended to help modelers incorporate the feedbacks of water-rock interaction on geophysical evolution (Fig. 28). To this end, we suggest the following guidelines:

1. **Antifreezes**: Depending on initial fluid and rock compositions modeled, the properties of pure water (such as phase diagram, viscosity, density, or heat capacity) can be replaced by those of sulfate-bearing or water-ammonia fluid.
2. ^{40}**K**: Of all antifreezes and radionuclides studies here, the behavior of ^{40}K is arguably the hardest to predict. We suggest simulating end-member cases of total leaching (initial ^{40}K all in liquid and ice) or no leaching at all (^{40}K all in rock).
3. ^{232}**Th** always remains associated with rock, even if water-rock reactions proceed to chemical equilibrium.
4. ^{235}**U and** ^{238}**U**: The behavior of these radionuclides hinges solely on temperature and water:rock ratio, two common parameters in models of geophysical evolution. Total or partial U leaching occurs if T and $W{:}R$ exceed the thresholds specified above.

5.4.2 Implications for Exsolution-Driven Cryovolcanism

The compositional outcomes of our simulations can also be used to constrain existing models and inform interpretations of ongoing icy world observations. For example, there are hints in data recently returned by the *Dawn* and *New Horizons* spacecrafts that fluids may have been cryovolcanically emplaced on the surfaces of Ceres and Pluto, respectively. Fluids can reach the surface more easily if buoyant with respect to the subsurface material (likely primarily water ice). Neveu *et al.* (2015b) explored a mechanism, first suggested by Crawford and Stevenson (1988), to overcome the negative buoyancy of liquid water in water ice. They assumed any liquid would bear volatiles similar to those seen in comets and disks. Should pressurization of the liquid reservoir trigger fluid ascent, decreasing confining pressures would drive volatile exsolution, thereby increasing fluid buoyancy. Neveu *et al.* (2015b) found CO to be the strongest driving volatile for this mechanism, followed by N_2 and CH_4. H_2 would play a minor role due to its low assumed abundance, and NH_3 would remain in solution.

In contrast, the present simulations suggest that should water-rock reactions proceed to equilibrium, primordial volatiles would be converted to CH_4 (up to 9.4 mol% with respect to H_2O) and H_2 (up to 8.6 mol% w.r.t. H_2O), with negligible CO and N_2. This may suggest that the ubiquitous N_2 outgassed on Titan, Triton, and Pluto, as well as the CO concentrated in the seemingly recently emplaced Tombaugh Regio on Pluto, may both be of primordial origin with no (or kinetically-limited) aqueous interaction with rock. Conversely, significant amounts of CH_4 in Titan and Pluto's atmospheres and Enceladus' plume are compatible with a hydrothermal origin (Mousis *et al.*, 2009), even though measurements of the atmospheric D/H ratio on Titan

suggest otherwise (Glein *et al.*, 2009). (Any H_2 outgassed along with CH_4 would escape to space, preventing its atmospheric accumulation.) Similarly, low CO abundances on Triton (0.1%) compared to comets ($\lesssim$20%; Mumma and Charnley, 2011), could be due to CO consumption in water-rock reactions driven towards equilibrium (Shock and McKinnon, 1993). Thus, our results do not preclude water-rock interaction from having processed the initial volatile inventory of these worlds.

5.4.3 Application to Ceres

Ceres, currently being explored by the *Dawn* spacecraft, has a hydrated, rocky surface that seems to be resulting from water-rock interaction (Lebofsky *et al.*, 1981). The identification of specific surface minerals, specifically those responsible for a hydration band in the near-infrared (IR) at 3.05 μm, has been debated: brucite $Mg(OH)_2$, suggested by Milliken and Rivkin (2009), is now contested (Beck *et al.*, 2015). Absorption at 3.05 μm, together with a 0.4 μm cutoff, broad 1.2 μm band, and broad reflectance near 9.5 μm, may also be partially contributed by the Fe-serpentine cronstedtite (Rivkin *et al.*, 2006; Milliken and Rivkin, 2009); though near-IR colors suggest low surface coverage for this mineral (Carry *et al.*, 2008). The 0.4 and 1.2 μm features have also been attributed to magnetite Fe_3O_4 (Larson *et al.*, 1979; Rivkin *et al.*, 2012). Previously, the 3.05 μm band had been attributed to NH_4-phyllosilicates such as saponites (King *et al.*, 1992), but this interpretation was invalidated based on poor matches with mid-IR spectra (5.5-14 μm) of Ceres (Cohen *et al.*, 1998; Rivkin *et al.*, 2006; Milliken and Rivkin, 2009). However, Beck *et al.* (2015) revisited this hypothesis, arguing that the spectral features of NH_4-minerals had not been studied under Ceres surface conditions. Recent data from *Dawn*'s visible and near-IR

spectrometer seem indeed to suggest the presence of NH_4 species after all (DeSanctis *et al.*, 2015). Additionally, strong evidence for carbonates arises from IR spectral features near 3.3 μm, 3.8-4.0 μm, 6.5-7 μm, 9 μm, 10 μm, and 11.3 μm (Rivkin *et al.*, 2006; Milliken and Rivkin, 2009; Rivkin *et al.*, 2012; Beck *et al.*, 2015). Finally, a contribution from dark organics is possible (Cohen *et al.*, 1998; Vernazza *et al.*, 2005; Milliken and Rivkin, 2009; Rivkin *et al.*, 2012). Endo- versus exogenic contributions are unknown at this time. Presumably, minerals rarely observed in meteorites such as carbonates, brucite, and NH_4-phyllosilicates would be endogenic.

Our simulations suggest that alteration of CM-type material by either pure water or N-bearing fluid, or alteration of ordinary chondrite material by N-bearing fluid, can produce together saponite, cronstedtite, and magnetite, even though antigorite is the prime phyllosilicate (Fig. 30). Short of thermodynamic data, NH_4-saponite was absent form our simulations; however these included NH_4-muscovite, a reasonable proxy for NH_4-phyllosilicates. NH_4-muscovite, cronstedtite, and magnetite occurred together at $T \leq 50$°C, pH=7-10, and within 6 log units of the FMQ redox buffer (Fig. 30). Such alteration could have taken place over a P range spanning Ceres' interior from near-surface to center, and water:rock ratios from <1 to 10. Water-rock interaction under such conditions was likely prevalent over Ceres' history (Neveu *et al.*, 2015a, view).

However, the simulations shown in Fig. 30 produced neither carbonate minerals nor brucite. NH_4HCO_3 is made in one simulation at 300°C and 2700 bar, well outside the range for which its thermodynamic properties were derived (Appendix C, Table 23); therefore this result is not reliable. However, oxidized C species (bicarbonate and carbonate, with some aqueous CO_2) are often present in solution, as mentioned above. Curiously, the abundance of oxidized C is somewhat sensitive to the pH

initially specified: only starting pH values of 9 and above result in oxidized C making up >10% of the solutes, largely as bicarbonate and carbonate. This dependence on input pH may be due to simulated fluid-rock interactions being slightly dependent on initial solution speciation as a function of input pH and pe, making our calculations path-dependent in this regard.

As Zolotov (2014) pointed out, any pathway to brucite production must include a sink for the excess Si and Fe. A few runs starting with pure water at pH $\geq$ 12 produced solid assemblages of roughly 40% brucite, 40% magnetite, 10% olivines and pyroxenes, and 10% other minerals (Fig. 29), in equilibrium with silica-rich solutions. However, high silica concentrations yielded ionic strengths of $\sim$10, far above the validity threshold of the aqueous model.

Tochilinite, 6 $Fe_{0.9}S \cdot 5$ $(Mg,Fe)(OH)_2$, was suggested by McSween and the *Dawn* Science Team (2015) as another possible source for the 3.05 μm absorption, on the basis of its near-IR spectrum being similar to that of brucite. Synthetic tochilinite, at room temperature, absorbs at 2.7 and 2.8 μm and has a broad absorption feature around 6.5 μm (Moroz *et al.*, 1997). Though Ceres displays a similar 6.5 μm feature, it is unclear whether the 2.7-2.8 μm absorption can be shifted to 3.05 μm at Ceres surface conditions. We did not explicitly include tochilinite in our simulations short of thermodynamic data, but instead resorted to an ideal mixture of brucite and troilite (FeS) for the initial CM composition (Browning and Bourcier, 1996, see also Table 15). [The molar volume of tochilinite at 298.15 K is 270.29 cm^3 mol^{-1} for a hydroxide layer content of 29 mol% Fe (*Mincryst* database; Chichagov *et al.*, 2001). At a minimum, one would need to also measure its enthalpy of formation at 298.15 K and 1 bar by drop calorimetry, and its heat capacity from near 0 K to $\geq$298.15 K by cryogenic calorimetry (Anderson, 2005). Gooding and Zolensky (1987) attempted to

measure its heat capacity above 298.15 K. From their differential scanning calorimetry measurements, we derive a heat capacity $C_p(T) = a + b\ T + c/T^2$ with $a = 9425$ J mol^{-1} K^{-1}, $b = -11.687$ J mol^{-1} K^{-2}, and $c = -1.264 \times 10^8$ J mol^{-1} K, for 328 K $< T <$ 658 K.]

Out of 61152 simulations, 159 come closest to reproducing current best estimates of Ceres' surface mineralogy: they produce together antigorite or cronstedtite, magnetite, NH_4-clay, and >10% of C solutes as carbonate or bicarbonate. While Ceres' surface minerals need not have been produced together (Zolotov, 2014), these simulations suggest that they could have if alteration took place at $T < 100$°C, equilibrium pH ≥ 11, equilibrium fO_2 0.5 to 3.5 log units above the FMQ buffer, and with *W:R*$\leq$1 although a few of these simulations were run for *W:R*=10. We note that all simulations in this subset resulted in equilibrium ionic strengths above 2, beyond the range of applicability of the extended Debye-Hückel equations (ionic strengths $\leq$0.1) used in the model. In these runs, 0 to 90% of the initial NH_3 remains in solution, the rest being converted to NH_4 solutes and minerals. Equilibrium solutions, assuming fractional freezing and neglecting methanol, would freeze at 176 K if there is any NH_3 left, or 211 K (the H_2SO_4-H_2O eutectic temperature) otherwise. ^{40}K radionuclides would seldom be leached, and ^{232}Th, ^{235}U, and ^{238}U would not. Crucially, most of these "Ceres-like" simulations start out with CM-like material: only four do not. This suggests that Ceres could have formed from chondritic planetesimals after they had undergone aqueous alteration, as postulated by Zolotov (2009). If so, Ceres would have had to accrete late enough for aqueous alteration to take place on planetesimals (i.e., several Myr to tens of Myr after planetesimal formation). A late-accretion scenario may be consistent with Ceres having formed further out compared to its current $a \approx 2.8$ AU

orbit (Kenyon *et al.*, 2008), perhaps in the Kuiper belt forming region, as suggested by McKinnon (2008, 2012).

5.5 Conclusions

Prompted by widespread evidence for water-rock interaction on icy worlds, we have investigated through equilibrium geochemical simulations how such interaction can affect antifreezes and radionuclides, which in some instances may allow liquid water in the first place. We have found that water-rock interaction can strongly alter the nature and amount of antifreeze in fluids, resulting in solutions rich in reduced N, mildly oxidized S, and (sometimes) reduced C that can remain partially liquid down to around 211 K or even 176 K, the respective eutectic temperatures of the H_2SO_4-H_2O and NH_3-H_2O systems. If any gas is produced, its composition is dominated by CH_4 and H_2. Equilibrium mineral assemblages are rich in serpentine and saponite clays. They retain ^{232}Th and, at low temperatures and water:rock ratios, ^{235}U and ^{238}U radionuclides. The radionuclide ^{40}K can be leached at high pH and/or high *W:R*. We recommend the inclusion of these effects in future models of the geophysical evolution of ocean-bearing icy worlds.

Applied to Ceres, these geochemical simulations suggest that if the hydrated minerals on Ceres' surface are NH_4-phyllosilicates, they may result from low-T alteration of chondritic material by N-bearing fluids. Although Ceres' surface species need not have formed together, a subset of our simulations (mostly starting with CM-like chondritic material) can produce them under single sets of physicochemical conditions ($T < 100$°C; pH $\geq$11; FMQ + 0.5 < log fO_2 < FMQ + 3.5; *W:R* generally $\leq$1; independently of P).

Chapter 6

PREREQUISITES FOR EXPLOSIVE CRYOVOLCANISM ON DWARF PLANET-CLASS KUIPER BELT OBJECTS

In the previous two chapters, I characterized hydrothermal feedbacks between geophysical and geochemical processes in dwarf planet evolution. As these processes presumably take place deep in the interiors of icy worlds, any evidence for their occurrence requires a mechanism to transport material from subsurface hydrothermal systems to the surface where this evidence can be observed. As mentioned in Chapter 1 and detailed in Chapter 4 and 5 and below, many icy worlds in the solar system do display not only surface expressions of deep hydrothermal processes, but also evidence that the transport mechanism may, at least in part, involve aqueous volcanic activity, or cryovolcanism.

In this chapter, I investigate physical and chemical mechanisms that might drive explosive cryovolcanism on dwarf planets, with particular focus on the Pluto-Charon couple. This chapter was published in *Icarus* with co-authors Steve Desch, Everett Shock, and Chris Glein (Neveu *et al.*, 2015b) before images of Pluto-Charon and Ceres were returned by *New Horizons* and *Dawn*, respectively. Therefore, it is interesting to ponder these results in light of evidence of recent, localized, possibly cryovolcanic activity on all three of these worlds (Fig. 2 and Chapter 8), even though this activity does not seem to be explosive. A brief summary of the paper is given below, followed by the paper text.

Explosive extrusion of cold material from the interior of icy bodies, or cryovolcanism, has been observed on Enceladus and, perhaps, Europa, Triton, and Ceres. It may

explain the observed evidence for a young surface on Charon (Pluto's surface is masked by frosts). Here, we evaluate prerequisites for cryovolcanism on dwarf planet-class Kuiper belt objects (KBOs). We first review the likely spatial and temporal extent of subsurface liquid, proposed mechanisms to overcome the negative buoyancy of liquid water in ice, and the volatile inventory of KBOs. We then present a new geochemical equilibrium model for volatile exsolution and its ability to drive upward crack propagation. This novel approach bridges geophysics and geochemistry, and extends geochemical modeling to the seldom-explored realm of liquid water at subzero temperatures. We show that carbon monoxide (CO) is a key volatile for gas-driven fluid ascent; whereas CO_2 and sulfur gases only play a minor role. N_2, CH_4, and H_2 exsolution may also drive explosive cryovolcanism if hydrothermal activity produces these species in large amounts (a few percent with respect to water). Another important control on crack propagation is the internal structure: a hydrated core makes explosive cryovolcanism easier, but an undifferentiated crust does not. We briefly discuss other controls on ascent such as fluid freezing on crack walls, and outline theoretical advances necessary to better understand cryovolcanic processes. Finally, we make testable predictions for the 2015 *New Horizons* flyby of the Pluto-Charon system.

6.1 Introduction

Cryovolcanism is *"the eruption of liquid or vapor phases (with or without entrained solids) of water or other volatiles that would be frozen solid at the normal temperature of the icy satellite's surface"* (Geissler, 2000). It is a clear marker of extant geological activity, and planetary bodies that show evidence for or suggestive of cryovolcanism,

such as Europa, Titan, Enceladus, and Triton are the foci of many planetary science and astrobiology investigations. Cryovolcanism could occur by either effusive or explosive processes (e.g. Fagents, 2003). Evidence for past or recent effusive activity has remained inconclusive, because of the difficulty to distinguish cryovolcanic from diapiric surface morphologies (Fagents, 2003; Lopes *et al.*, 2007). Gas-driven activity, on the other hand, has been unmistakably identified in the form of plumes on Triton, Enceladus, and perhaps Europa and Ceres (Kirk *et al.*, 1995; Porco *et al.*, 2006; Roth *et al.*, 2014; Küppers *et al.*, 2014). The upcoming flyby of the Pluto-Charon system by the *New Horizons* spacecraft brings a new opportunity to look for plumes on Pluto and Charon that would imply extensive geophysical and geochemical activity on these icy dwarf planets. The scope of this chapter is to evaluate the likelihood of extant cryovolcanism on dwarf planet-class Kuiper belt objects (KBOs) from our current knowledge of explosive cryovolcanic processes, the volatile inventory in the Kuiper belt, and the thermal evolution of KBOs. To this end, we use a novel approach that couples geophysics and geochemistry, and extends predictive geochemical modeling to the domain of liquid water at subzero temperatures. We begin in this introduction by briefly reviewing evidence for explosive cryovolcanism in the outer solar system. In the following section, we review previous theoretical results on gas-driven cryovolcanism, as well as current knowledge of the volatile inventory of KBOs. Building on these results, we then present a new geochemical model for gas exsolution to drive the propagation of fluid-filled cracks to the surface. Next, we discuss other controls on fluid ascent, such as the presence of a primordial ice-rock crust or fluid freezing in the cracks. We conclude by making predictions on the possibility of cryovolcanism on Pluto, Charon, and KBOs of similar size.

6.1.1 Explosive Volcanism and Outgassing

Outgassing of volatiles by a planetary body may occur by sublimation of ices close to the surface, as this surface is heated by a source external to the body, such as the Sun or an impact. Alternatively, the volatiles may originate much deeper inside the body, and the cause of their outgassing be rooted in endogenic heating processes. Here, we call the former phenomenon "sublimation" and the latter "explosive cryovolcanism", and we use "outgassing" as a generic term. These processes can all result in observable plumes, and only more detailed analyses (e.g. of their chemical composition or thermal emission) can conclusively determine the cause of outgassing.

For KBOs, the semantics are complicated because two communities have investigated their origins, evolution, and present state. The "large icy satellites" community sees KBOs as mini-worlds with possible geophysical evolution over geological timescales; their viewpoint applies to bodies large enough to be differentiated, with little porosity, and which may have sustained subsurface liquid water. Such bodies may have enough endogenic energy to drive explosive cryovolcanism as understood in the viewpoint of icy satellites (Crawford and Stevenson, 1988; Fagents, 2003; Hansen *et al.*, 2006), although sublimation may also occur. On the other hand, the "small primitive bodies" community sees the Kuiper belt as a reservoir of comet nuclei that have undergone little or no evolution since their formation; their viewpoint applies to smaller (<100 km), undifferentiated bodies, with significant porosity, and no liquid. For these bodies, as for comets, surface manifestations of outgassing are necessarily due to sublimation, except perhaps early in their history (De Sanctis *et al.*, 2001; Choi *et al.*, 2002). Here, we focus on KBOs for which the "large icy satellite" viewpoint applies. These may be

referred to as dwarf planet-class KBOs; we call them KBOs for short in the rest of this chapter.

6.1.2 Evidence for Cryovolcanism in the Outer Solar System

Extant outgassing has been so far conclusively observed in the form of N_2 gas plumes on Triton, assumed to be a KBO captured by Neptune (Smith *et al.*, 1989; Soderblom *et al.*, 1990; Kirk *et al.*, 1995) and H_2O plumes on Enceladus (Hansen *et al.*, 2006; Porco *et al.*, 2006; Matson *et al.*, 2007; Postberg *et al.*, 2009; Waite *et al.*, 2009). An observation of plumes on Europa has also been recently reported (Roth *et al.*, 2014), as well as water emission from Ceres localized in space and time (Küppers *et al.*, 2014). For Triton, although both exogenic and endogenic sources have been suggested to drive the N_2 eruptions, the N_2 may originate in a layer close to the surface (Brown *et al.*, 1990; Ingersoll and Tryka, 1990), but may nonetheless reveal a regime of convection in Triton's icy mantle (Duxbury and Brown, 1997). Triton also experienced an early phase of heating by tidal dissipation during its capture by Neptune (Shock and McKinnon, 1993). On Enceladus, the cryovolcanic interpretation is favored because the plume ejects species such as NaCl and silica; this suggests that the source of the plume contains material leached from Enceladus' rocky core (Postberg *et al.*, 2009, Hsu et al., in preparation, Sekine et al., in preparation). Moreover, the plume activity is synchronized to Enceladus' orbit, with a surge when Enceladus is farthest from Saturn such that South Pole fractures experience tensile tidal stresses (Hedman *et al.*, 2013). *Cassini* observations of Titan suggest that it too is undergoing cryovolcanism, although this remains uncertain (Sotin *et al.*, 2005; Nelson *et al.*, 2009); cryovolcanism could explain the presence of argon-40 and methane in Titan's atmosphere (Tobie

et al., 2006). Recently, ground-based observations of an aurora near the south pole of Europa have strongly suggested that it too is experiencing explosive cryovolcanism (Roth *et al.*, 2014). As for Enceladus, plume activity occurs when Europa is farthest from Jupiter, and seems to depend on tidal stresses (Roth *et al.*, 2014). The radii (250 to 2575 km) and densities of these moons (1.6 to 3.0 g cm^{-3}) bracket those of the Kuiper Belt Objects (KBOs) Pluto and Charon [1150 and 600 km; 2.0 and 1.6 g cm^3; Buie *et al.* (2006)]. This suggests bulk compositions, internal structures, and thermal histories similar to those of the icy satellites, with the notable exception that Pluto and Charon may have experienced little or no tidal heating.

Several observations of KBO surfaces are suggestive of recent cryovolcanic eruptions, whether effusive or explosive. First, short-lived ammonia hydrates have been detected on the surfaces of Charon and, likely, Orcus (Brown and Calvin, 2000; Cook *et al.*, 2007; Merlin *et al.*, 2010; Delsanti *et al.*, 2010). These compounds should be destroyed by solar ultraviolet radiation and galactic cosmic rays on timescales shorter than 1 to 50 Myr (Jewitt and Luu, 2004; Cook *et al.*, 2007), and no mechanism other than recent localized resurfacing by cryovolcanism has conclusively explained their presence on Charon's surface (Jewitt and Luu, 2004; Cook *et al.*, 2007; McKinnon *et al.*, 2008; Desch *et al.*, 2009; Brown, 2012). The presence of abundant crystalline ice has also been suggested as evidence for resurfacing, because it too should be amorphized on short timescales; however, its presence on KBOs much too small to be geologically active (Brown, 2012) suggests that another process must be at play, such as annealing of amorphous ice by dust impacts (Porter *et al.*, 2010). More generally, cryovolcanism has been invoked to explain the observation of volatile ices other than water (mainly N_2, CH_4, CH_3OH, and NH_3) on KBO surfaces [see recent reviews by McKinnon *et al.* (2008) and Brown (2012)].

Evidence and mechanisms for effusive volcanism have previously been investigated. For example, Fagents (2003) reviewed a dozen studies that proposed past effusive cryovolcanism to explain morphologies on satellites of Jupiter (Europa and Ganymede), Saturn (Enceladus, Dione, Tethys, and Iapetus), and Uranus (Miranda and Ariel). These morphologies include *"smooth and/or sparsely cratered surfaces, infilled craters and graben, domes, lobate features, ridges, caldera-like features, and low-albedo surfaces"* (Fagents, 2003). Recently, similar morphologies have been studied on Titan using *Cassini* radar and infrared imagery (Lopes *et al.*, 2007; Wall *et al.*, 2009; Le Corre *et al.*, 2009; Soderblom *et al.*, 2009). To assess the possible cryovolcanic origin of these observed morphologies, laboratory experiments and modeling studies have investigated the rheological properties of cryolavas of water-volatile compositions (Schenk, 1991; Kargel *et al.*, 1991; Zhong *et al.*, 2009). Similar effusive morphologies may certainly also occur on KBOs and may well be observed by *New Horizons* at Pluto and Charon. However, as for the icy satellites, it is unlikely that a clear distinction between a cryovolcanic versus diapiric origin of such features will be made. Therefore, for the remainder of this chapter, we focus exclusively on predicting the likelihood of *explosive* cryovolcanism on KBOs, which results in outgassing plumes that should be unambiguously detected by *New Horizons* if presently occurring on Pluto or Charon.

6.2 Ingredients for Explosive Cryovolcanism

6.2.1 Liquid Persistence

Extant explosive cryovolcanism requires the persistence of fluid to the present day, either as a subsurface ocean layer, as a localized pocket of liquid in the icy mantle

(Fagents, 2003; Schmidt *et al.*, 2011), or as volatile molecules trapped in clathrate hydrates which may outgas upon heating. Liquid persistence depends strongly on body size and melting point depression by antifreezes (McKinnon *et al.*, 2008; Desch *et al.*, 2009).

Larger bodies have a lower surface area:volume ratio, which scales as the inverse of the radius of the body. Because radiogenic heat production scales with volume and heat transport fluxes scale with surface area, larger bodies evacuate heat less effectively. Therefore, their internal temperatures are higher and they are better able to maintain liquid.

Antifreezes are dissolved volatile or salt impurities that prevent water molecules from getting organized in a solid phase. Volatile antifreezes of relevance to icy bodies are ammonia NH_3 and methanol CH_3OH, two abundant compounds in comets (Mumma and Charnley, 2011, and references therein) that were likely accreted by Kuiper belt objects. The eutectic point of a water-ammonia mixture at 1 bar is depressed to about 176 K (Croft *et al.*, 1988) and that of a water-methanol mixture is about 157 K (Miller and Carpenter, 1964). Relevant salt antifreezes are chlorides, carbonates, and especially sulfates (Kargel, 1991). These salts are components of chondrites (Kargel, 1991), the primitive rocky material likely accreted by KBOs, but they could also be leached from interactions between rock and liquid water.

The persistence of a liquid water layer for several Gyr, possibly to the present day, is a common outcome of geophysical evolution models of Pluto (Robuchon and Nimmo, 2011), Charon (Desch *et al.*, 2009), and KBOs of similar dwarf-planet size. Pluto-sized bodies are more likely to retain liquid (even pure water at 273 K) in the absence of heat transfer by solid-state convection in the overlying ice shell, which transports heat outward more effectively than conduction (Robuchon and Nimmo, 2011). Smaller,

Charon-sized bodies retain a liquid layer only if water contains dissolved antifreezes, or if an insulating undifferentiated crust mitigates heat loss over geologic time (Desch *et al.*, 2009). Undifferentiated ice-rock crusts are insulating because the thermal conductivity of hydrated or chondritic rock, 0.5 to 2.5 W m^{-1} K^{-1} (Yomogida and Matsui, 1983; Clauser and Huenges, 1995; Opeil *et al.*, 2010) is much lower than that of crystalline ice, 5.67 (100 K / T) W m^{-1} K^{-1} (Klinger, 1980). Such crusts are unstable gravitationally, but should not overturn over the age of the solar system due to the frigid temperatures and resulting high viscosity of ice near the surface of KBOs (Rubin *et al.*, 2014).

Therefore, the existence of subsurface liquid in KBOs for most of the age of the solar system, and possibly until the present day, is well motivated. If (a) heat transfer through ice shells is conductive rather than convective, (b) antifreezes are concentrated in water, and (c) Charon-sized KBOs retained crusts, the total amount of liquid water retained collectively by KBOs today may equal that of Earth's oceans (Desch *et al.*, 2009).

6.2.2 Bringing Cryolavas to the Surface

6.2.2.1 Pressurization and Crack Opening

Cryovolcanism requires liquid to be lifted to the surface by overpressurization. This can be accomplished by freezing a small volume of water, raising the pressure in the remaining liquid. Freezing occurs because Pluto and Charon-sized KBOs cool after about 2 Gyr, when energy becomes transported to the surface and radiated to space faster than it is generated by long-lived radionuclides in the core (Desch *et al.*,

2009; Robuchon and Nimmo, 2011). The overpressure ΔP generated by freezing a volume of liquid water is given by (Fagents, 2003):

$$\Delta P = \frac{f}{\beta_w (1-f)} \left(\frac{\rho_w}{\rho_i} - 1 \right) \tag{6.1}$$

where $\beta_w = -(1/V)(\partial V/\partial P)_T$ is the isothermal compressibility of water and f the fraction of water that freezes. This phenomenon causes the ice spikes one can sometimes see in ice cube trays in kitchen freezers. A large fluid-ice density contrast yields a higher overpressure, which is highest for pure liquid water freezing as pure ice, but becomes negligible for a eutectic mixture of H_2O-NH_3 freezing to ammonia dihydrate ice of similar density (Desch *et al.*, 2009).

Equation (6.1) assumes a fixed volume of water. In reality, water exerts pressure on the walls of its container. In a global sense, water can raise the height of the ice shell. In a local sense, ice on the pocket walls can be compressed. Ice Ih at low pressure has a compressibility $\beta_i = 1.3 \times 10^{-10}$ Pa^{-1}, not too different from that of liquid water ($\beta_w = 5 \times 10^{-10}$ Pa^{-1}). Therefore, ice will also move or be compressed to some extent to accommodate the volume change due to freezing, and the overpressure in liquid water will not be quite as high as given by equation (6.1).

Regardless of this caveat, pressurization due to freezing is potent. Freezing just 1% of the ice overpressurizes a water pocket by $\Delta P = 2.0 \times 10^6$ Pa. At the top of a liquid water pocket, the overpressure (above the pressure of surrounding ice) is:

$$dP = \Delta P - (\rho_w - \rho_i) g (h - z) \tag{6.2}$$

where g is the gravitational acceleration (assumed constant), z the depth of the top of the pocket, and h the depth of the base of the pocket. Even for at the surface (z

$= 0$), the overpressure is $dP = \Delta P - (\rho_w - \rho_i)gh = 2.0 \times 10^6$ Pa -1.2×10^6 Pa $= 0.8 \times 10^6$ Pa. This aids in the opening of cracks.

6.2.2.2 Crack Propagation

Once a crack is open, can it keep propagating? Crawford and Stevenson (1988) investigated analytically a possible propagation mechanism using linear elastic fracture mechanics theory. If the normal stress intensity K_I in Pa m$^{1/2}$ exceeds a critical value K_{Ic}, the fracture toughness of the material, the crack propagates. In water ice, $K_{Ic} =$ 0.10 to 0.12 MPa m$^{1/2}$ (Liu and Miller, 1979; Andrews, 1985; Bentley *et al.*, 1989). K_I is given by:

$$K_I = \sqrt{\pi\ l}\ [\Delta P - 2\ g\ (\rho_w - \rho_i)\ l/\pi] \tag{6.3}$$

where the stress intensity decreases with crack length l due to the positive liquid-ice density contrast $(\rho_w - \rho_i)$ for water. Cracks propagate upward through the ice shell if either external stresses T overcome both the negative buoyancy and the fracture toughness of the ice: $T > 2g(\rho_w - \rho_i)l/\pi + K_{Ic}/\sqrt{\pi l}$, or if the cryovolcanic fluid is sufficiently less dense than ice $(\rho_w < \rho_i)$ that $K_I > K_{Ic}$.

External stress can originate from tides, as on Europa or Enceladus. Overpressures from freezing also generate stress. From our analysis above, $T = dP$ of order 10^6 Pa (for f=1%), is sufficient to drive a crack with length $l > 60$ km. Therefore, pressurization alone can initiate kilometer-sized cracks during freezing of either the entire ocean (Manga and Wang, 2007) or, more easily, water pockets in the ice (Fagents, 2003).

Propagation can occur by positive buoyancy if cracks ascend through a shell denser

than pure liquid water. Such a shell can be a clathrate-containing or CO_2 ("dry ice") icy mantle (Lunine and Stevenson, 1985; Crawford and Stevenson, 1988), or even an undifferentiated ice-rock crust (Desch *et al.*, 2009). Positive buoyancy can also occur if the fluid is not pure water, but rather an aqueous solution of volatile species that can decrease fluid density by exsolving during ascent, due to the decreasing confining pressure (Crawford and Stevenson, 1988; Matson *et al.*, 2012). Whether volatile exsolution occurs depends on the volatile composition of cryolavas and on the solubility of these volatiles in water at the temperatures and pressures relevant to KBOs. We focus on these aspects in the following sections.

6.2.3 Volatile Inventory of KBOs

Volatiles are better retained by large bodies (higher gravities) that are distant from the Sun (cold). Dynamical models predict that KBOs formed between 15 and 30 AU away from the Sun (Levison *et al.*, 2008; McKinnon *et al.*, 2008); a simple energy balance calculation reveals that this corresponds to temperatures between 45 and 65 K. Direct comparison between these temperatures and equilibrium condensation temperatures in the solar nebula (Lodders, 2003) to determine which volatiles were accreted is tricky, because the condensation chemistry was likely governed by kinetic processes. In Table 19, the condensation temperatures are provided only for the species that should have condensed under equilibrium. Condensation of the other species in Table 19 was likely kinetically allowed, because they are observed today in comets that should have undergone little endogenic processing, as well as in extrasolar disks. McKinnon *et al.* (2008) cautioned that any direct extrapolation from present-day comets to volatiles accreted by KBOs overlooks evolutionary effects on

cometary volatile-to-water ratios (e.g., Shock and McKinnon, 1993). Interstellar cloud abundances and direct observation of inner extrasolar disk compositions are also biased, because the bulk compositions of extrasolar systems may be widely different from that of the solar system (Young *et al.*, 2014). However, Table 19 reports abundances of CO, H_2O, HCN, and C_2H_6 from a variety of observations of comets (Mumma and Charnley, 2011) that are of same order of magnitude as those observed in extrasolar disks (Maret *et al.*, 2006; Carr and Najita, 2008), although the CO_2 abundances differ significantly. The general consistency between these values provides guidance to estimate primordial volatile abundances in the solar system. Species too volatile to condense at 45 to 65 K, such as primordial Ar, were presumably initially trapped in amorphous ice or as clathrate hydrates. Spectroscopic observations have not revealed any compositional gradient across the inner regions of the Kuiper belt today up to 50 AU (McKinnon *et al.*, 2008), which suggests that significant shuffling of the KBO orbits occurred. Extensive orbital migration is also suggested by dynamical models (Levison *et al.*, 2008).

Early heating on cold bodies may have sublimated the most volatile species, which would have recondensed closer to the surface at colder regions, resulting in a redistribution of volatiles with depth and stratification (Choi *et al.*, 2002; McKinnon, 2002; Prialnik *et al.*, 2008). Past outgassing would have partially depleted the smaller KBOs in volatiles (Choi *et al.*, 2002). However, most volatiles should have been retained in dwarf planets such as Pluto and Charon (McKinnon *et al.*, 2008): H_2 may have been lost (but later produced in water-rock reactions), but N_2 and CH_4 are seen today in the atmospheres of Pluto and Triton (Buratti *et al.*, 1999; Sicardy *et al.*, 2003), and comets of much smaller size than KBOs have retained CO today in large quantities (Mumma and Charnley, 2011). Subsequent softening or melting of ice due

Table 19: Condensation temperatures and typical cometary and disk abundances of volatiles

				Bulk abundance A_i (mol/mol, % w.r.t. H_2O)			
			Condensation	Primordial		Endogenic	Canonical model
	Volatile species	Formula	Temperature (K)[a]	Comets[b]	Disk		
O	Water ice	H_2O	121 to 182	100	100		
C	Carbon monoxide	CO		0.4-30	50-100 [c]		20
	Carbon dioxide	CO_2		2-30	0.002-0.26 [c]		10
	Methane	CH_4	78 (hydrate), 41 (pure)	0.4-1.6		Some?	1
	Ethane	C_2H_6		0.01-2	0.008-0.016 [c]		
	Methanol	CH_3OH		0.2-7			3
	Formaldehyde	H_2CO		0.1-1			
	Formic acid	HCOOH		0.06-0.14			
N	Molecular nitrogen	N_2	58 (hydrate)			Some?	1
	Ammonia	NH_3	131 (hydrate)	0.2-1.4	7-14.5 [a,d]		1
	Isocyanic acid	HNCO		0.02-0.1			
	Hydrogen cyanide	HCN		0.01-0.05	0.13-0.26 [c]		
S	Hydrogen sulfide	H_2S		0.12-1.4		Some?	0.5
	Carbonyl sulfide	OCS		0.1-0.4			
	Sulfur dioxide	SO_2		0.002		Some?	0.002
H	Molecular hydrogen	H_2				Most	0.001
Ar	Argon	Ar	48 (clathrate hydrate)	1? [e,f]			0.1

Abundances were determined by molecular spectroscopy, which explains why abundances of diatomic molecules and noble gases have not been measured. After [a]Lodders (2003), [b]Mumma and Charnley (2011, and references therein), [c]Carr and Najita (2008), [d]Maret *et al.* (2006), [e]Stern *et al.* (2000), [f]Bockelee-Morvan *et al.* (2003). The values from Lodders (2003) represent equilibrium at 10^{-4} bar, but the condensation chemistry of ices was likely governed by kinetic effects.

to heating by short- and long-lived radionuclides, tidal interactions, differentiation, crystallization of amorphous ice, or exothermic water-rock reactions would have further processed this volatile inventory, potentially concentrating volatile impurities into the aqueous melt (McKinnon *et al.*, 2008). Thus, the icy mantle may be purer water than the liquid layer, whose dissolved volatiles and salts would act as antifreezes to preserve liquid on geological time scales (Desch *et al.*, 2009; Robuchon and Nimmo, 2011). If not dissolved, volatiles could have escaped or could still be outgassing today even on Charon-sized bodies (Choi *et al.*, 2002); this is the process that we investigate in this chapter. We review in further detail the current knowledge of primordial abundances and fate of volatile species below.

6.2.3.1 Carbon Species

Carbon in the protoplanetary disk should have been in the form of CO, CO_2, CH_3OH, and CH_4, as well as condensed in refractory C-rich organics. Refractory organics could have taken up to 80% of the total carbon, as suggested by measurements on cometary particles both in-situ at Halley (Fomenkova, 2000) and returned from Wild-2 by the *Stardust* mission (Sandford *et al.*, 2006), as well as by observations of the dark surface of Phoebe, a likely captured KBO (McKinnon, 2002; Castillo-Rogez *et al.*, 2012, and references therein), and by models of the chemical evolution of protoplanetary disks (Kress *et al.*, 2010). This material could make up to 25% of the mass of KBOs (McKinnon *et al.*, 2008).

Of the remaining 20% of the gas-phase C, the values in Table 19 suggest that up to 50-80% was CO (not in equilibrium) at low temperature past Saturn. If much CO and CO_2 were accreted, less oxygen would have been available to form H_2O, yielding denser bodies in regions where rock and ice condensed, but not CO. Conversely, if most of the carbon accreted was refractory, then the initial ice/rock ratio should have been higher than today, implying loss of ices (McKinnon, 2002). CO abundances are observed to be around 20% in comets (Mumma and Charnley, 2011), but only 0.1% on Triton's surface (McKinnon *et al.*, 2008). CO depletion could be due to its consumption in hydrothermal processes (Shock and McKinnon, 1993). CO_2 is absent in KBO spectra; however, it has been observed on the surface of Triton (McKinnon *et al.*, 2008).

Methanol CH_3OH has been suggested to be in pristine material in planetesimals; it should have been accreted at one to several percent with respect to H_2O on Centaurs (Cruikshank *et al.*, 1998) and KBOs (Barucci *et al.*, 2008). Its irradiation products

would explain the red colors of both classes of objects (Brown, 2012). However, surface methanol could also be exogenic, resulting from the ultraviolet photolysis of carbon-bearing ices (Castillo-Rogez *et al.*, 2012, and references therein). Methanol is an antifreeze, depressing the melting point of water down to 157 K (Miller and Carpenter, 1964) at 1 bar, or slightly lower temperatures if other antifreezes are present as well (Kargel, 1992).

Finally, methane has been observed on the surfaces of the largest KBOs (Pluto, Quaoar, Eris, Sedna, and Makemake) and Triton (McKinnon *et al.*, 2008). Methane can be produced in water-rock reactions; this process was investigated for Enceladus (Glein *et al.*, 2008). Ethane ice, resulting from the radiative processing of methane, has been observed on Makemake, and perhaps on Orcus and Quaoar (Brown, 2012). Methane could also be the product of hydrothermal alteration of refractory organic matter in heated rocky cores, possibly with a high D/H ratio (Glein *et al.*, 2009).

6.2.3.2 Nitrogen Species

The dominant nitrogen volatiles accreted are ammonia (NH_3) and N_2, and nitrogen was likely also accreted in condensed carbonaceous matter (McKinnon *et al.*, 2008); although which of these three forms dominates is unknown. The previously mentioned analyses of cometary particles revealed C:N ratios of 5 to 50 (Fomenkova, 2000; Sandford *et al.*, 2006). These ratios translate to 0.5 to 5% of the total KBO mass consisting of nitrogen in the form of refractory organics.

NH_3 could have been accreted at one to several percent with respect to H_2O on Centaurs (Cruikshank *et al.*, 1998) and KBOs (Barucci *et al.*, 2008), perhaps as high as 14.5% assuming all N condensed into NH_3 (Lodders, 2003). These estimates are

in agreement with observations of extrasolar disks (Maret *et al.*, 2006), although in solar system comets, the ratio NH_3/H_2O is less than 2% (Mumma and Charnley, 2011). NH_3 has been observed on Orcus (de Bergh *et al.*, 2005; Barucci *et al.*, 2008; Carry *et al.*, 2011) and Charon (Brown and Calvin, 2000; Dumas *et al.*, 2001; Cook *et al.*, 2007; Merlin *et al.*, 2010) in amounts relative to water similar to comets. These measurements used the absorption band of ammonia hydrate ices at 2.2 μm. Because this signature is easily masked by the presence of methane, ammonia may be present on other KBOs that display the spectral signature of methane, such as Pluto, Quaoar (Jewitt and Luu, 2004), and Makemake. A similar ammonia-to-water ratio has also been measured in the plume of Enceladus (Waite *et al.*, 2009), and flows of cryolava with this ratio would display morphologies comparable to those observed on Miranda and Ariel (Thomas *et al.*, 1987; Schenk, 1991); ammonia may have been observed on Miranda (Bauer *et al.*, 2002). Like methanol, ammonia is also an antifreeze and depresses the melting point of water down to 176 K (Leliwa-Kopystynski *et al.*, 2002).

N_2 lacks an electric dipole, therefore its spectral signature is hard to detect and hampers the quantification of its abundance. It is also difficult to distinguish N_2 from CO by mass spectrometry. Bockelee-Morvan *et al.* (2003) reported upper limits on reliable N_2 measurements of $< 0.2\%$ in comets. N_2 ice is a major surface component on Pluto and Triton, and contributes substantially to their tenuous, seasonal atmosphere. N_2 has also been observed on Sedna and perhaps Eris (McKinnon *et al.*, 2008). N_2 could also be generated by hydrothermal processes on icy bodies (Glein *et al.*, 2008; Mousis *et al.*, 2009). Here, we assume that roughly half of the N accreted by KBOs was in the form of N_2, so that $A_{N_2} \approx A_{NH_3}$ in Table 19.

The sources and abundances of N in the solar nebula, and the extent to which N

compounds may have been accreted by outer solar system bodies, have been reviewed in further detail by Desch *et al.* (2009).

6.2.3.3 Sulfur Species, Hydrogen, and Noble Gases

Sulfur volatiles of relevance are H_2S and SO_2; both have been observed in comets in small amounts with respect to water (Table 19). Hydrothermal processing of sulfur-bearing minerals also generates these gases. Crawford and Stevenson (1988) pointed out that SO_2 may not concentrate in the aqueous melt, because it is readily trapped in the ice as a clathrate hydrate. SO_2 can also react with water to form sulfurous acid and sulfite species.

It is difficult to envision how dwarf planets could have accreted H_2, unless a small amount was trapped in mixed clathrates or in amorphous ice. However, H_2 is an abundant product of hydrothermal reactions between water and reduced rock. One can estimate an upper limit on the amount of H_2 produced by hydrothermal alteration of the core from the reaction $3\ Fe_2SiO_{4\ (s)} + 9\ Mg_2SiO_{4\ (s)} + 14\ H_2O_{\ (l)} \rightarrow 2\ Fe_3O_{4\ (s)} + 6\ Mg_3Si_2O_5(OH)_{4\ (s)} + 2\ H_{2\ (g)}$ (i.e., fayalite + forsterite + water $\rightarrow$ magnetite + serpentine + hydrogen gas). This assumes that the silicate component of KBOs is dry olivine at the time of KBO formation. For Charon (bulk density 1.6 g cm^{-3}), a dry olivine core (density 3.25 g cm^{-3}, accounting for macroporosity) would extend to a radius of about 350 km, with a mass 5.8×10^{20} kg, about half the mass of the icy shell (assuming rock fully differentiates from ice). Since fayalite and forsterite have molar masses of 204 g mol^{-1} and 140 g mol^{-1}, this corresponds to a bulk olivine content of 3.7×10^{21} mol inside Charon. If all of it is serpentinized, 6.2×10^{20} mol of H_2 are produced. The molar H_2/H_2O ratio is then about 1%. Thus, considerable

quantities of H_2 can in principle be produced. For our canonical simulations, we assume a much smaller amount of 0.001% relative to H_2O, which may correspond to a balance between production and outgassing.

Finally, noble gas observations are sparse for comets. In principle, Ar can be sequestered in amorphous ice to be later accreted during planet formation (Desch and Monga, 2014). Ar was observed in Hale-Bopp at a level of about 1% with respect to water vapor (Stern *et al.*, 2000), but this detection was from a low-resolution spectrum and the spectral line observed may have been due to another species (Bockelee-Morvan *et al.*, 2003). Since Ar has not otherwise been observed on relevant icy bodies, we estimate an Ar abundance from the bulk solar ratio N/Ar $\approx$ 20 estimated by Lodders (2003).

6.3 Geochemical Model

6.3.1 Modeling Geochemical Equilibrium

The purpose of modeling the volatile geochemistry of cryolavas is twofold. First, volatiles can exsolve to make cryolavas positively buoyant, and therefore able to rise spontaneously in ice. Second, geochemical models help constrain the volatile composition of cryolavas. To investigate the propensity of the various volatiles considered in the previous section to exsolve and drive cryovolcanism, we developed a simple chemical model. This model only considers the aqueous and gaseous forms of the volatiles, neglecting volatile speciation into salts or clathrates. It also considers only thermodynamic equilibrium, neglecting kinetic aspects. At chemical equilibrium,

the number of moles of a given dissolved volatile per kilogram of water, or molality m, is given by:

$$\log\ K(T,P) = \log\frac{\gamma_{\text{volatile (aq)}} m_{\text{volatile (aq)}}}{\phi_{\text{volatile (g)}} P_i} \tag{6.4}$$

where K is the equilibrium (Henry's law) constant for the reaction Volatile (g) $\rightarrow$ Volatile (aq) at given temperature T and pressure P, γ is the activity coefficient of the solute, and ϕ and P_i are the fugacity coefficient and partial pressure (in bar) of the volatile gas. To evaluate the propensity of volatiles to exsolve as fluid rises, we consider the ideal case of a single volatile dissolved in pure water ($\gamma = 1$). The exsolved gas is assumed to be ideal and composed of the pure volatile ($\phi = 1$ and $P = P_{\text{volatile}}$). The assumption of ideality is reasonable at the low pressures inside KBOs: using the program REFPROP (Lemmon *et al.*, 2010), we calculate a fugacity coefficient $\phi = 1.7$ for N_2 at 240 K and 1000 bar, the upper end of the pressure range encountered in the icy shells of Pluto and Charon.

Each species has a bulk abundance A_i relative to water, determined from Table 19. Provided a crack is open, fluids will spontaneously rise to the level of neutral buoyancy of water ice in liquid water (Crawford and Stevenson, 1988; Matson *et al.*, 2012), such that $z/h = 1 - \rho_i/\rho_w$. Assuming gas absorbs overpressures in the crack, $P_{\text{gas}} = dP$. Let us consider the case where pressurization at the crack tip is just high enough to bring fluid from the neutral buoyancy level (NBL) to the surface: $\Delta P = \rho_i g z$. It follows from equation (6.2) that $P_{\text{gas}} = dP = \rho_i g h - \rho_w g(h-z)$. We should not assume g to be constant if z or h are not negligible compared to the dwarf planet radius R_p, so $P_{\text{gas}} = \left(\rho_i \int_{Rp-h}^{Rp} g(r)dr\right) - \left(\rho_w \int_{Rp-h}^{Rp-z} g(r)dr\right)$. P_{gas} decreases from the base of the crack and becomes zero at the NBL. Any gas mixture has total pressure P_{gas}, which is

the sum of the partial pressures of all mixture components. The partitioning of each species i between the liquid (m_i) and gas (P_i) is therefore determined by:

$$K_i(T, P) \approx m_i / P_i \tag{6.5}$$

$$m_i \ \rho_w V_{\rm liq} + P_i V_{\rm gas}/(RT) = A_{i,w} \tag{6.6}$$

$$\sum_{i=1}^{n_{\rm species}} P_i = P_{\rm gas} \tag{6.7}$$

In equation (6.5), we assumed no salinity effect ($\gamma_i = 1$ and $\phi_i = 1$). If all volatiles are transferred into the liquid as ice melts and refreezes, $A_{i,w} = A_i(1 + M_{\rm ice}/M_{\rm liq})(\rho_w V_{\rm liq}/M_{\rm H2O})$ moles, where $M_{\rm ice}/M_{\rm liq}$ is the ratio of the bulk masses of ice and liquid and $M_{\rm H2O}$ is the molecular mass of water. If not, we just have $A_{i,w} = A_i(\rho_w V_{\rm liq}/M_{\rm H2O})$ moles of volatile i. We use $M_{\rm H2O}$ as the mean molecular mass of the liquid assuming it is mostly water; this no longer holds if the liquid approaches eutectic with an antifreeze. Knowing A_i, T, and $P_{\rm gas}$, and fixing the volumic vapor fraction $x_{\rm vap} = V_{\rm liq}/V_{\rm gas}$, we can solve for all m_i and P_i.

6.3.2 Implementation of the Geochemical Model

In our models, we fixed $V_{\rm liq}$ as the total volume of liquid water inside the planet, not taking into account other possible liquid species such as ammonia. We conservatively assumed $A_{i,w} = A_i$. The volumic vapor fraction $x_{\rm vap}$ was solved for using equation (6.7), and the molalities m_i and partial pressures P_i were then calculated using equations (6.5) and (6.6). Our C routine, “Cryolava", can be freely accessed at https://github.com/MarcNeveu/IcyDwarf.

Equation (6.6) translates into:

$$m_i M_{\text{liq}} + \frac{P_i x_{\text{vap}} M_{\text{liq}}}{\rho_{\text{liq}} RT} = A_{i,w} \tag{6.8}$$

where all terms are abundances in mol. $M_{\text{liq}} = \rho_{\text{liq}} V_{\text{liq}}$ is the total mass of liquid in the body and $x_{\text{vap}} = V_{\text{gas}}/V_{\text{liq}}$ is the overall volumic vapor fraction. Using equation (6.5), this becomes:

$$m_i M_{\text{liq}} \left(1 + \frac{x_{\text{vap}}}{K_i \rho_{\text{liq}} RT}\right) = A_{i,w} \tag{6.9}$$

Equivalently:

$$P_i = \frac{A_{i,w}}{K_i M_{\text{liq}} \left(1 + \frac{x_{\text{vap}}}{K_i \rho_{\text{liq}} RT}\right)} \tag{6.10}$$

Therefore, equation (6.7) becomes:

$$\sum_{i=1}^{n_{\text{species}}} \frac{A_{i,w}}{M_{\text{liq}} \left(K_i + \frac{x_{\text{vap}}}{\rho_{\text{liq}} RT}\right)} = P_{\text{gas}} \tag{6.11}$$

where P is the local pressure. Solving equation (6.11) requires finding the root of a polynomial of degree n_{species} in $X = x_{\text{vap}}/(\rho_{\text{liq}} RT)$,

$$P_{\text{gas}} M_{\text{liq}} \prod_{i=1}^{n_{\text{species}}} (K_i + X) - \sum_{i=1}^{n_{\text{species}}} A_{i,w} \prod_{\substack{j=1 \\ j \neq i}}^{n_{\text{species}}} (K_j + X) = 0 \tag{6.12}$$

The variable X has same units as K_i: mol kg^{-1} bar^{-1} in our assumption of negligible salinity. In principle, this polynomial has n_{species} complex roots. In practice, the coefficients in front of the positive terms ($P_{\text{gas}} M_{\text{liq}} \approx 10^{26}$ Pa kg), whose largest degree is n_{species}, are much larger than those in front of the negative terms ($A_{i,w} \approx 10^{18}$ mol), whose largest degree is only $n_{\text{species}} - 1$. This causes the polynomial to increase

monotonically in the range of physically plausible X ($X > 0$), except at small X ($X \ll \min[K_i]$). When X is very small, the K_i terms dominate X. The sum term with the largest $K_i \approx 10^3$ (here taken as a dimensionless equilibrium constant) likely dominates the polynomial if its $A_{i,w}$ is not exceptionally low, since the product of all K_i is only about 10^{-8} for the ten species accounted for in this chapter. At $P_{\rm gas}$ less or equal than a typical value at the seafloor of dwarf planets (30 MPa), this is enough for the polynomial to become negative at small X, which guarantees that equation (6.12) has a single real positive root. (At higher $P \gtrsim 150$ MPa with our choice of species and bulk abundances, the polynomial is positive for all $X > 0$ and only has negative roots: physically, exsolution does not occur.) This root was found using a combined bisection/Newton-Raphson algorithm.

Knowing X, the molalities and partial pressures of all species are obtained from equation (6.9):

$$m_i = \frac{A_{i,w}/M_{\rm liq}}{1 + X/K_i} \tag{6.13}$$

$$P_i = m_i/K_i \tag{6.14}$$

Throughout the algorithm, one needs to pay special attention to the pressure units, because P_i are in bar in equation (6.5), but in Pa in equations (6.6) and (6.7).

6.3.3 Modeling at Low Temperature and High Pressure

An idea of the pressure ranges involved can be obtained from the radial pressure profile for a spherical, homogeneous KBO of density ρ and radius R, given by McKinnon *et al.* (2008):

$$P(r) \approx 2000 \text{ bar} \left(\frac{\rho}{2\text{g cm}^{-3}} \right)^2 \left(\frac{R}{600\text{km}} \right)^2 \left(1 - \frac{r^2}{R^2} \right) \quad (6.15)$$

Here, we use units of bar (1 bar = 0.1 MPa), in which geochemical data are referenced. Differentiated bodies will experience slightly higher pressures.

T and P range between about 50 K, 0 bar at the surface and 273 K, $\gtrsim$1 kbar at the base of the ice shell (Desch *et al.*, 2009; Robuchon and Nimmo, 2011). Geochemical codes provide $K(T, P)$ from thermodynamic datasets referenced at 298.15 K and 1 bar, using an equation of state for solutes. The Pitzer (Pitzer, 1973) and HKF (Helgeson *et al.*, 1981, and references therein) equations are commonly used. The former equation has been used down to 173 K in the FREZCHEM code (Marion *et al.*, 2012), but is derived from polynomial fits to experimental data. Thus, it has little predictive power and is restricted to species for which data are available at given T and P. The semi-empirical HKF equation models interactions between solute molecules in water, and does have predictive capabilities. However, it was developed using data above 273 K. We used the software package CHNOSZ (Dick, 2008) to test the accuracy of the HKF equation down to 253.15 K (the minimum temperature achievable with CHNOSZ) to predict solute properties in supercooled water, and found close agreement with experimental data (Figure 35). Temperatures down to 235 K could be reached using the most up to date equation of state for water, IAPWS-95 (Wagner and Prüß, 2002), in CHNOSZ calculations. Using the IAPWS-95 formulation along with the HKF equation of state makes the model less consistent, because the HKF solute parameters were determined with a previous thermodynamic formulation for water (Haar *et al.*, 1984). However, the CHNOSZ calculations in the temperature range (T>254 K) where both the Haar et al. and IAPWS-95 formulations could be used showed no significant difference in solute properties (Figure 36); therefore we

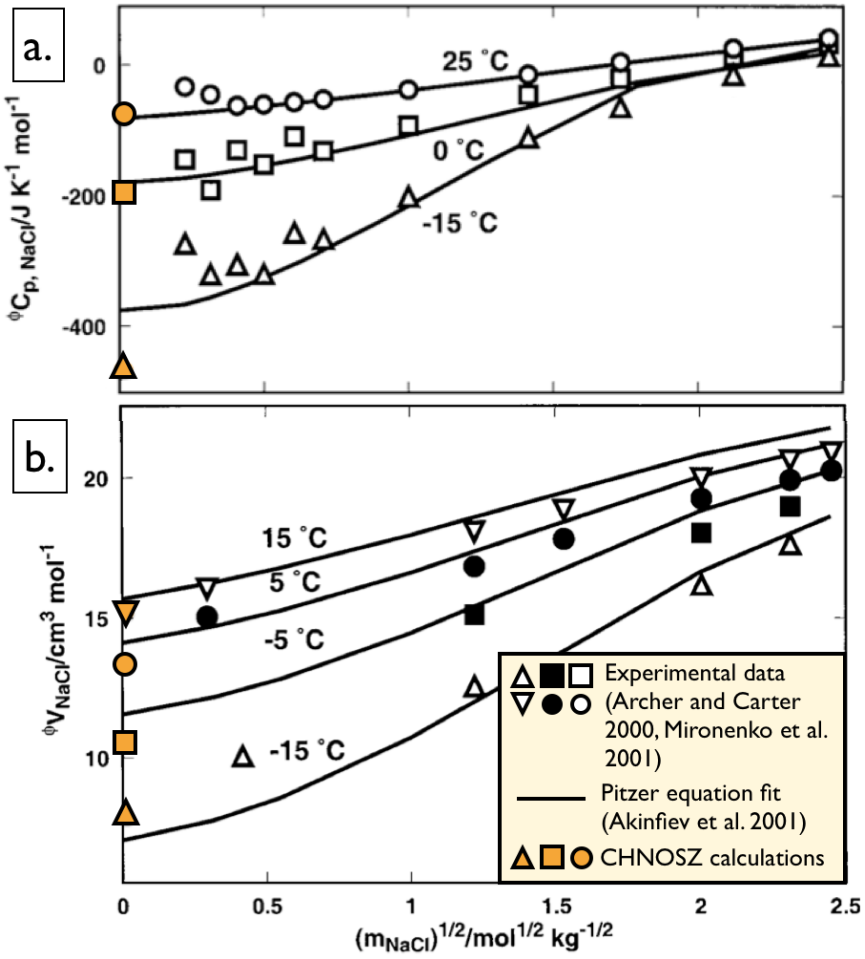

Figure 35: Apparent molar heat capacity (A) and volume (B) of NaCl at subzero temperatures as a function of the square root of the NaCl molality

CHNOSZ predictions at infinite dilution are as accurate as the Pitzer fits (Akinfiev *et al.*, 2001) to experimental data (Archer and Carter, 2000; Mironenko *et al.*, 2001) at low temperature. Modified from Akinfiev *et al.* (2001).

confidently extrapolated our calculations down to 235 K. In the CHNOSZ calculations, we used thermodynamic data from Kelley (1960) and Wagman *et al.* (1982) for gaseous CH_4, CO_2, Ar, SO_2, N_2, H_2S, H_2, and NH_3; Shock *et al.* (1989) for aqueous SO_2, N_2, H_2S, H_2, and NH_3; Plyasunov and Shock (2001) for aqueous Ar, CH_4, and CO_2; and Shock (1993) and Shock and McKinnon (1993) for CO.

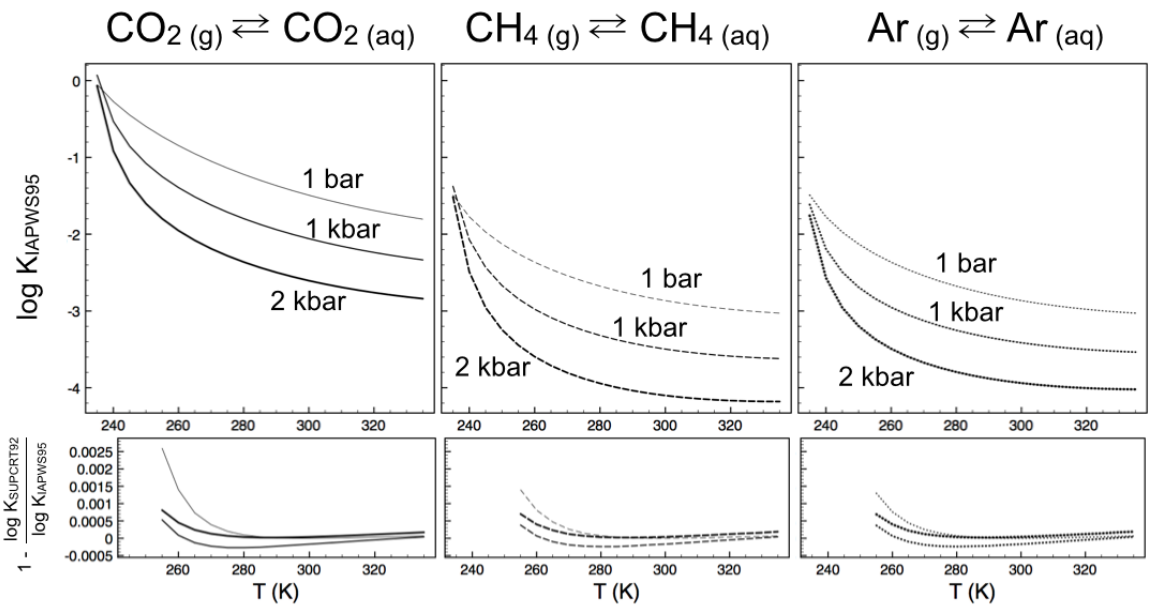

Figure 36: Equilibrium constants for the dissolution of carbon dioxide, methane, and argon gases

Top panels: Logarithm of the equilibrium (Henry's law) constant for the solution of CO_2 (g), CH_4 (g), and Ar (g) as a function of temperature (range 235 K to 335 K) at 1, 1000, and 2000 bar. These predictive curves match experimental data where they exist (above 273 K; Shock *et al.*, 1989). The log K for the other seven species investigated follow similar trends. Note that K, the intrinsic solubility, decreases both with increasing temperature *and* pressure. This linear variation of the logarithm of Henry's law's "constant" with pressure is made explicit in the Krichevsky-Kasarnovsky equation (Krichevsky and Kasarnovsky, 1935). Decreasing pressure causes exsolution mainly because the denominator term in equation (6.4) decreases, even though log $K(T, P)$ increases. *Bottom panels:* Relative difference in log K estimated using the formulations of water adopted for SUPCRT92 (Haar *et al.*, 1984) and from IAPWS-95 (Wagner and Prüß, 2002). The relative difference is negligible compared to the value of log K, although it increases towards lower temperatures. If log K_{SUPCRT92} versus T curves were plotted on the top panels, they would be indistinguishable from the log K_{IAPWS95} versus T curves.

6.3.4 Condition for Crack Propagation

Assuming cracks of length l were initiated by freezing pressurization, exsolution allows further propagation if $K_I > K_{Ic}$. In equation (6.3), ρ_w is replaced with

$\rho_{\text{fluid}} = \rho_w/(1 + x_{\text{vap}})$; the fluid is therefore positively buoyant in ice for $x_{\text{vap}} > 0.07$. Cryovolcanism is considered to occur if (a) exsolution occurs in cracks of length reasonably permitted by freezing pressurization, and (b) cracks propagate all the way to the surface. Therefore, exsolution serves two purposes in this model: it makes cryolavas buoyant in ice (as suggested by Crawford and Stevenson (1988) and Matson *et al.* (2012)), but also creates a buoyancy force able to disrupt ice and propagate cracks.

6.4 Results

6.4.1 Application to Charon

The analytical solution of equations (6.5-6.7) enables both the determination of x_{vap} as a function of total gas pressure P_{gas}, which provides the crack propagation condition, as well as the identification of the species that exsolve. We first ran the geophysical code of Desch *et al.* (2009) for three cases: (a) a "warm Charon" where rock and ice fully differentiate into a mantle of ice and a core of dry rock (density $\rho_{\text{core}} = 3250$ kg m^{-3}, accounting for about 30% macroporosity), perhaps because of a short-lived radionuclide or amorphous ice crystallization heat peak in the first few Myr of Charon's evolution; (b) a colder case in which Charon only partially differentiates, but where the core still warms up enough to be dehydrated; and (c) a scenario where Charon partially differentiates and its core never dehydrates (density $\rho_{\text{core}} = 2350$ kg m^{-3}, including 30% macroporosity). The putative interior structures of dwarf planets have been discussed in further detail elsewhere (Desch *et al.*, 2009; Castillo-Rogez and

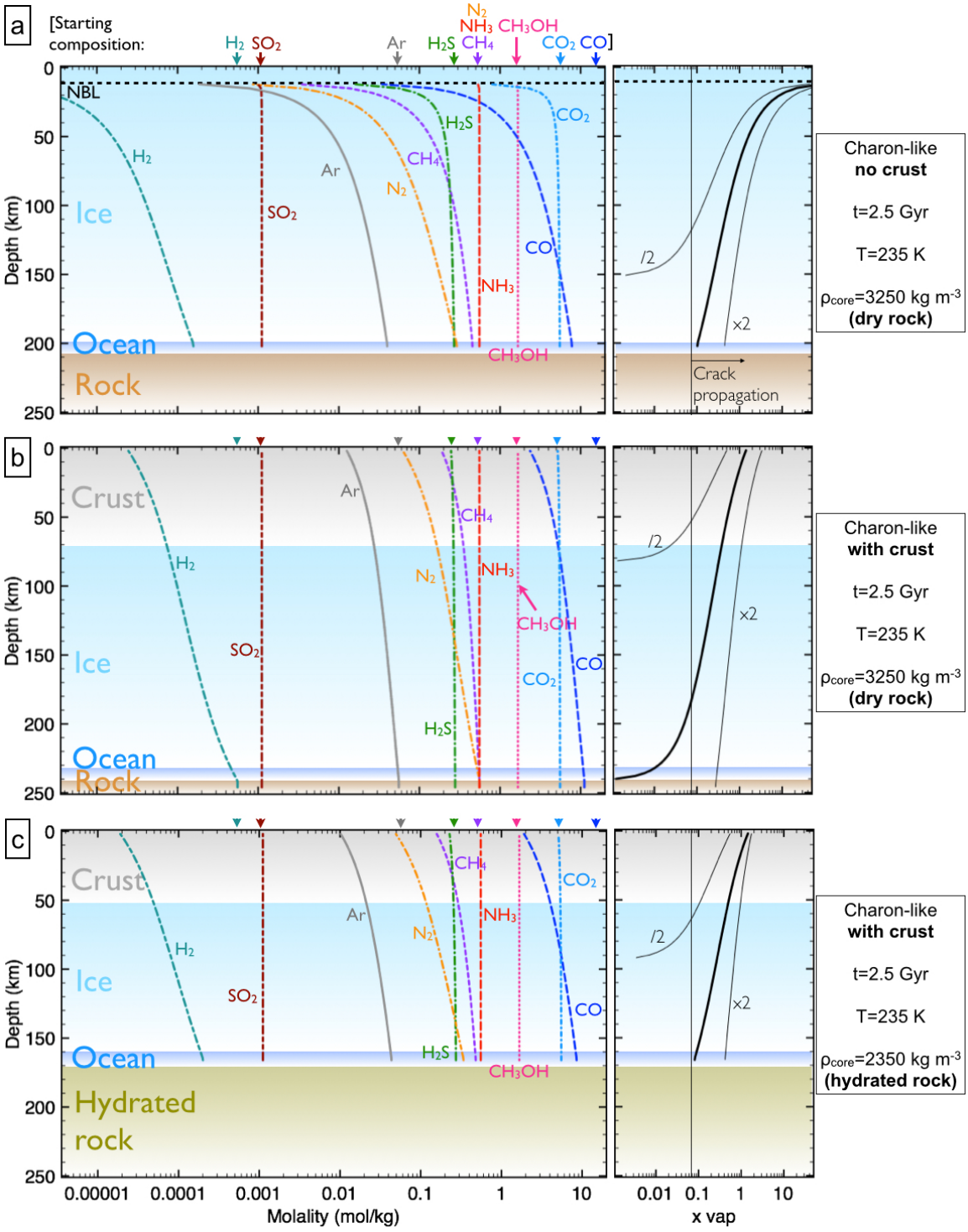

Figure 37: Molality of key volatiles with canonical starting abundances (left panels) and volumic vapor fraction (right panels) as a function of depth for a Charon-like KBO

Figure 37: (Continued from previous page.) Three scenarios are considered: (a) no crust, dry core; (b) crust, dry core; (c) crust, hydrated core. *Left panels*: The degree to which a species exsolves at a given depth can be estimated by comparing its saturation molality (curve) to its starting concentration, indicated by an arrow at the top of each panel. Low discrepancies indicate that the species is mostly in solution, high discrepancies indicate exsolution. In case (a) where the neutral buoyancy level of water in ice is defined, it is indicated by a dashed line marked "NBL" beyond which calculations were not attempted since $P_{\rm gas} = 0$. *Right panels*: $x_{\rm vap}$ is plotted for the canonical run (thick line), as well as runs with half and twice the abundances (marked "/2" and "x2", respectively). The volumic vapor fraction $x_{\rm vap}$ determines the fluid density $\rho_{\rm fluid} = \rho_w/(1 + x_{\rm vap})$. For $x_{\rm vap} > 0.07$, $\rho_{\rm fluid} < \rho_i$ and $K_I > K_{Ic}$ in cracks of length $l > [\sqrt{\pi} K_{Ic}/(2\Delta\rho g)]^{2/3} \approx 100$ m to 1 km. This limit for crack propagation in ice is indicated as a thin vertical line.

McCord, 2010; Robuchon and Nimmo, 2011). Despite an assumed ammonia antifreeze content of 1% with respect to water, liquid is not preserved until the present day in scenarios (a) and (c). Therefore, to allow comparisons between all three cases, we ran the geochemical model after 2.5 Gyr of geophysical evolution, when liquid is still present in all cases in the form of an ocean layer 5 to 10 km thick at a depth dependent on the geophysical structure.

The left panels on Figure 37 show the equilibrium molality m of relevant volatiles as a function of depth (or, equivalently, gas pressure $P_{\rm gas}$) at 235 K, a temperature typical of a Charon subsurface ocean in the geophysical runs. The most apolar species such as H_2, N_2, and Ar, as well as CH_4 and CO, exsolve most easily. CO_2 and H_2S exsolve only in the crust-less scenario (a), and the miscible species SO_2, CH_3OH, and NH_3 do not exsolve at all. These results are not sensitive to the values for the input abundances of these compounds.

On the right panels of Figure 37, the volumic vapor fraction $x_{\rm vap}$ is plotted as a function of depth. The case of canonical abundances is represented by a thick line; other lines indicate half and double volatile concentrations, to outline uncertainties in

volatile accretion and possible concentration by melting and refreezing. A polynomial approximation for $x_{\rm vap}$ as a function of depth d for the cases with a crust (b and c) is $x_{\rm vap} \approx -4 \times 10^{-7} d^3 + 1 \times 10^{-4} d^2 - 0.02d + 1.3$. For case (a), a power law provides a better fit: $x_{\rm vap} \approx 2400 d^{-1.85}$. The fluid density is then $\rho_{\rm fluid} = \rho_w/(1+x_{\rm vap})$, neglecting the density of gases. The vertical line on these plots indicates the threshold $x_{\rm vap} > 0.07$ at which fluid becomes positively buoyant in ice. Crack propagation occurs as soon as the fluid is buoyant if cracks are longer than:

$$l > \left(\frac{\sqrt{\pi}\ K_{Ic}}{2\ \Delta\rho\ g} \right)^{2/3} \approx 1 \text{ km} \left(\frac{10 \text{ kg m}^{-3}}{\Delta\rho} \right)^{2/3} \tag{6.16}$$

Therefore, assuming canonical abundances, cracks of $l \approx 200$ m, 40 km, and 400 m are needed in cases (a), (b), and (c), respectively. Exsolution is easier without a crust, which acts like a pressure seal to keep the volatiles in solution. It is also easier if the core is hydrated, because the larger volume taken up by the core yields a seafloor closer to the surface. However, the right panels also show that initial abundances, not internal structure, are the main control over crack propagation. In particular, carbon monoxide (CO) plays a major role, because of its combined high abundance and low solubility. Figure 38 shows how sensitive crack propagation is to the initial abundance of CO with respect to water, for each of the three scenarios. With less than 10% CO with respect to water and all other volatile abundances as in Table 19, cracks tens to hundreds of kilometers need to be initiated (presumably by freezing pressurization) for exsolution to drive their propagation further. However, above 15% to 25% CO depending on internal structure, cracks only a few hundred meters high can be propagated by CO exsolution.

6.4.2 Uncertainty on Gas Solubilities

The dominant sources of uncertainty for these results are (a) the pressure, temperature, and structure inside Charon, (b) the starting dissolved volatile abundances, (c) the fracture toughness of ice, and (d) the solubility of gases in supercooled water.

We have discussed above the first two sources of uncertainty. Regarding the third one, equation (6.16) shows that the crack length l scales with the ice fracture toughness as $l \propto K_{Ic}^{2/3}$: varying K_{Ic} over a plausible range of one order of magnitude changes l by less than an order of magnitude. This is less than the dependence of l on internal structure, as shown in Figure 37.

Uncertainties on the solubility of gases obtained by regressions of experimental data above 273 K were estimated by Shock *et al.* (1989), whose results we used for our extrapolations in the supercooled regime. Shock *et al.* (1989) estimated a typical uncertainty in standard molar Gibbs energy for neutral species of $\Delta G^{\circ} \approx 1400$ J/mol at 1000 bar and 500°C. This uncertainty decreases as P and T shift away from the critical point of pure water: at 1000 bar and 25°C, Shock *et al.* (1989) estimated an uncertainty of only 11 J/mol. When considering a solubility reaction, $\Delta_r G^{\circ} = G^{\circ}_{\text{product}} - G^{\circ}_{\text{reactant}} = 2.3\ R\ T\ \log\ (K)$, so the relative uncertainty in K is $\Delta K/K = \Delta[\log K] = 2\ \Delta G^{\circ}/(2.3\ R\ T)$. Using the worst-case typical uncertainty $\Delta G^{\circ} \approx 1400$ J/mol and T=235 K, we find $\Delta K \approx 0.6\ K$. Summing the relative uncertainties on K over the ten species considered implies that X, and therefore x_{vap}, are determined within one order of magnitude. This is comparable to changing the volatile abundances by a factor of two in Figure 37, and does not significantly impact the results.

6.5 Discussion

6.5.1 Comparing the Explosiveness of Gases

Non-polar species are those that most easily outgas. However, these species are not necessarily abundant and therefore not necessarily the best drivers of explosive cryovolcanism. In order to easily evaluate the capacity of a given species to drive cryovolcanism given its solubility and abundance, we evaluate its contribution to x_{vap}, i.e., its mole fraction $X_{i(\mathrm{g})} = P_i/P_{\mathrm{gas}}$ in the gas phase. From equation (6.11):

$$X_{i(\mathrm{g})} = \frac{A_{i,w}/M_{\mathrm{liq}}}{K_i + x_{\mathrm{vap}}/(\rho_w RT)} \frac{1}{P_{\mathrm{gas}}} \tag{6.17}$$

where $A_{i,w}$ is the starting abundance of volatiles in liquid water (in mol), M_{liq} is the mass of liquid, and K_i is the equilibrium constant (which depends on temperature and pressure) for the dissolution of each volatile species i. As expected, X_i decreases with the ratio $K_i = m_i/P_i$. Moreover, X_i is directly proportional to $A_{i,w}$: comparing X_i for two different species allows to solve for an abundance ratio for which these species have the same explosiveness. Because x_{vap} and $K_i(T, P_{\mathrm{gas}})$ vary with depth, it is most useful to evaluate both at the threshold depth where positive buoyancy is first reached, even though the composition of the gas does not change significantly with depth. The comparative explosiveness for the ten gases considered in this study is shown in Table 20.

CO is the best driver of cryovolcanism, assuming it is present in KBOs in cometary abundances. Its contribution to the gas exceeds that of CO_2 by nearly two orders of magnitude. N_2, CH_4, and H_2 also exsolve easily, but H_2 plays only a minor role in the runs described above because of its low starting abundance. However, most H_2

Table 20: Composition of the gas driving explosive volcanism at the depth where positive buoyancy is reached

Volatile species	Model abundance	Mole fraction $X_{i(g)}$ at highest depth of positive buoyancy		
	A_i (% w.r.t. H_2O)	(a) No crust, dry core	(b) Crust, dry core	(c) Crust, hydrated core
CO	20	8.8×10^{-1}	7.6×10^{-1}	7.6×10^{-1}
N_2	1	7.0×10^{-2}	7.3×10^{-2}	6.1×10^{-2}
CH_4	1	2.7×10^{-2}	2.1×10^{-2}	2.2×10^{-2}
CO_2	10	1.2×10^{-2}	7.8×10^{-3}	9.2×10^{-3}
Ar	0.1	4.2×10^{-3}	3.5×10^{-3}	3.6×10^{-3}
H_2S	0.5	2.3×10^{-3}	1.3×10^{-3}	1.4×10^{-3}
H_2	0.001	1.0×10^{-4}	1.5×10^{-4}	1.0×10^{-4}
CH_3OH	3	5.0×10^{-5}	2.0×10^{-5}	1.8×10^{-5}
NH_3	1	1.4×10^{-5}	7.0×10^{-6}	7.2×10^{-6}
SO_2	0.002	4.3×10^{-8}	2.8×10^{-8}	3.4×10^{-8}

The three cases correspond to cases (a), (b), and (c) of Figure 37, for canonical initial abundances.

is likely to arise from hydrothermal reactions at or below the seafloor, the extent of which is currently unconstrained. Such reactions could result in starting abundances of up to 30%. Charlou *et al.* (2002) measured abundances of hydrothermal H_2, CH_4, and CO near a seafloor hydrothermal field. The abundances of CH_4 and CO were negligible compared to those inferred from comets. However, Charlou *et al.* (2002) measured an H_2 abundance of 16 mmol kg^{-1}, or roughly 0.03% by mole with respect to water. Although this is 30 times the abundance we considered, it would bring the explosiveness of H_2 on par with that of H_2S, which only contributes to the exsolved gas in a minor way. CO_2 and N_2 abundances highly depend on the redox state of the ocean (Shock and McKinnon, 1993; Glein *et al.*, 2008). CO_2, even at a high abundance, does not exsolve much. However, assuming that temperatures are high enough to convert all of NH_3 to N_2 (Glein *et al.*, 2008), molecular nitrogen may help drive cryovolcanism (although, in that case, there would be no NH_3 antifreeze and another solute would be required to maintain liquid). The contribution of N_2 to the exsolved gas may also be higher than estimated in Table 20 if we underestimated the unconstrained bulk N abundances of KBOs. Ar potentially has a significant role, but

as a noble gas its abundance is difficult to constrain. Sulfur gases only play a minor role. However, Crawford and Stevenson (1988) suggested that SO_2 would stay trapped in clathrates rather than being concentrated in the aqueous melt. These clathrates would not only increase the ice density and favor positive buoyancy (see below), but also provide an extra source of gas along the way.

Ultimately, all gas abundances depend on how these volatiles speciate among solid (clathrates, amorphous carbon), solute (dissolved volatiles, carbonates, etc.), and gas phases. For example, clathrates and carbonates potentially represent a large volatile sink. Future work will address the speciation issue, but will first require the extension of predictive speciation models to low temperatures. Regardless of the speciation caveat, this analysis of volatile efficiency in driving cryovolcanism ("explosiveness") is useful to identify the species that matter most.

6.5.2 Fate of CO in a Subsurface Ocean

CO seems to be a key species that can drive explosive cryovolcanic activity because of its expected high abundance and predicted high solubility in water under conditions relevant to KBOs. Therefore, one aspect worth investigating is the geochemical stability of CO in a subsurface ocean. High concentrations of CO are not stable in liquid water: Shock (1993) found a thermodynamic drive at high temperatures (473 K) and pressures (3500 bar) to either hydrolyze CO to formic acid or formate, or to oxidize CO to CO_2 (presumably via formic acid). Figure 39 shows a similar outcome at 235 K and 1000 bar, at relevant redox conditions. The thermodynamic data on the aqueous species used to make Figure 39 were obtained from Shock *et al.* (1989) for NH_3 and N_2; Plyasunov and Shock (2001) for methanol, ethanol, and CO_2; Shock and

McKinnon (1993) for CO, urea, and HCN; Shock (1995) for formic acid and acetic acid; Dick *et al.* (2006) for glycine; and Shock (1993) for acetaldehyde. The data on minerals were taken from Helgeson (1978). Whether CO accreted by KBOs is destroyed over the geologic history of these bodies depends on the rate at which CO is consumed to form one of these species.

Trump and Miller (1973) determined the kinetics of the formation of formate ($HCOO^-$) from CO according to the reaction:

$$CO_{(aq)} + OH^-_{(aq)} = HCOO^-_{(aq)} \tag{6.18}$$

from 20°C to 60°C. They found the rate data to fit the following equation:

$$\frac{d[CO]}{dt} = -k_{hyd}[OH^-][CO] \tag{6.19}$$

with $\log(k_{hyd}) = 15.83\text{-}4886/T(K)$ M^{-1} h^{-1}, where k_{hyd} represents the second-order rate constant for the alkaline hydrolysis of CO. It appears that Trump and Miller (1973) determined this experimental rate under the assumption of second-order kinetics; reproducing their experiments by adding in turn each of the reactants in excess and confirming the rates to be proportional to each of the reactants would confirm this. However, it seems plausible, mechanistically, that OH^- base would catalyze the reaction by reacting with the electrophilic carbon atom of CO.

Given this rate of CO consumption, the time needed for the concentration of CO to decrease to 10% of its initial value is given by:

$$t_{10\%} = \frac{\ln(10)}{k_{hyd}[OH^-]} \approx \frac{2.3a_{H+}}{k_{hyd}K_w} \tag{6.20}$$

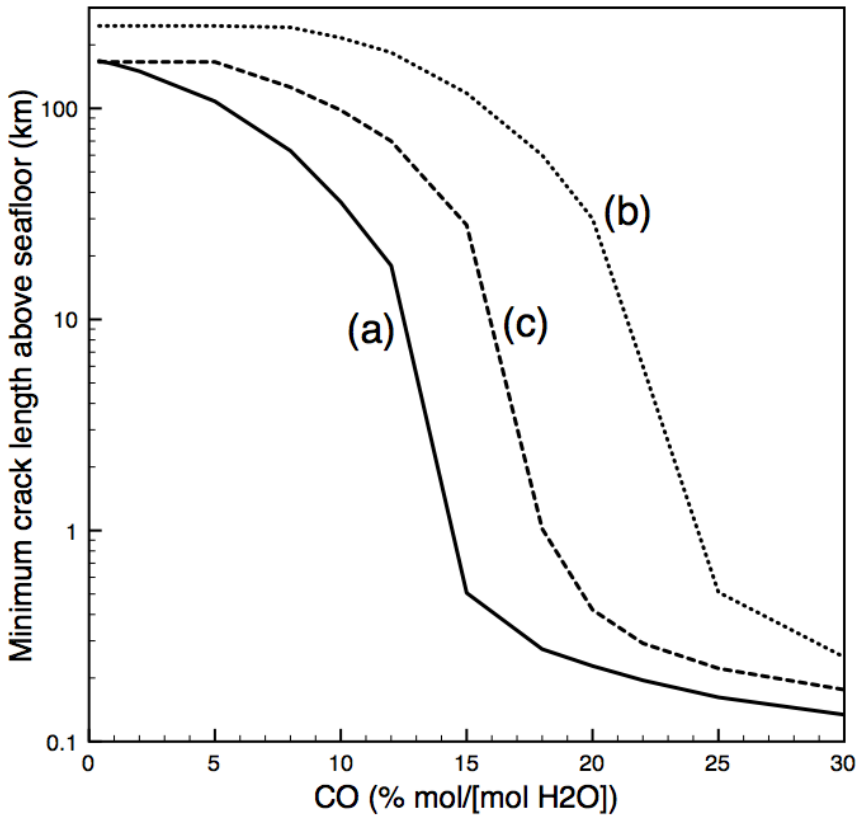

Figure 38: Minimum crack length necessary so that exsolution drives crack propagation, as a function of the initial abundance of carbon monoxide

The scenarios (a), (b), and (c) are the same as in Figure 37.

where a_{H+} corresponds to the activity of H^+, which is equivalent to pH = – log (a_{H+}), and K_w designates the ionization constant of water (for the reaction $H_2O = H^+ + OH^-$). K_w in supercooled water at 1 kbar can be estimated by extrapolating data from SUPCRT92 (Johnson *et al.*, 1992):

$$\log(K_w) = 44.27 - 4921/T(\mathrm{K}) - 7.266\ \ln(T) \tag{6.21}$$

The thermodynamic data used to make this extrapolation are from Haar *et al.* (1984) for H_2O and Shock and Helgeson (1988b) for the ions. The neutral pH is $pH_{Neu} = -\log(K_w^{0.5})$, and the activity of H^+ at pH relative to neutrality ($pH = pH_{Neu} + x$) can be

expressed as $a_{H^+} = K_w^{0.5} \times 10^{-x}$. Therefore, the characteristic timescale for conversion of CO to formate can be written as:

$$t_{10\%} \approx \frac{2.3 \times 10^{-x}}{k_{hyd} K_w^{0.5}} \tag{6.22}$$

Figure 40 shows the analytical solution of equation (6.22), $t_{10\%}$, as a function of pH relative to neutral (x). These results should be viewed as having order-of-magnitude quality because of the extrapolation to low temperatures. CO is hydrolyzed faster at higher temperatures and higher pH. If even slightly warm (323 K) hydrothermal systems arose on Pluto or Charon, CO would have been destroyed extremely quickly. Lower pH would allow CO to survive longer. Zolotov (2012) modeled chemical equilibrium between cometary volatiles and CI chondrite solids down to 0°C, and found that the predicted equilibrium pH is about two units above neutrality. The relatively high pH in these systems is dictated by reactions between ultramafic silicate minerals and the aqueous solution. Therefore, supercooled oceans inside KBOs may also have a pH greater than neutrality. However, production of formic acid would decrease the pH. Figure 40 shows that CO should be destroyed rapidly (in terms of geologic time) in such mildly alkaline solutions. Very low temperatures (below 200 K) are required to prevent significant hydrolysis of CO over the age of the solar system. However, exceptionally cold NH_3-H_2O oceans may not preserve CO, as they could be highly alkaline (Marion *et al.*, 2012).

CO is present in the surface reflectance spectra of Pluto-sized KBOs, but not in those of Charon-sized bodies (Brown, 2012, and references therein). Schaller and Brown (2007) argued that this was because a minimum dwarf planet radius of 500 to 700 km was necessary to prevent Jeans escape of CO at KBO surface equivalent temperatures of 30 to 40 K. Surface CO could either never have been in contact with

liquid water (and therefore not been hydrolyzed to formate), or could have originated from formate that dissociated into CO and H_2O at the very cold surface temperatures or under irradiation. Therefore, there may be appreciable amounts of CO in the ocean from recent melting of CO-bearing ice. In this case, however, the concentration of CO in the ocean would presumably be much lower than the primordial abundance, so the potential for CO to drive cryovolcanism from an ocean may be diminished.

6.5.3 Effect of Internal Structure

Comparing results between scenarios (a) and (b) yields insights into the influence of a crust on gas-driven crack propagation. Undifferentiated crusts are a surprising outcome of thermal evolution models of KBOs (Desch *et al.*, 2009), because these crusts are denser than the underlying ice mantle. Detailed modeling of the rheology of silicate-ice mixtures has shown that KBOs with a size up to that of Charon remain too cold near the surface for a crust dozens of kilometers thick to founder by Rayleigh-Taylor instabilities over timescales comparable to the age of the solar system (Rubin *et al.*, 2014).

In principle, undifferentiated crusts dozens of kilometers thick should *favor* the ascent of fluid-filled cracks, because of the favorable density contrast even when the fluid is pure liquid water. Percolation of methanol- and ammonia-rich cryolavas upward through undifferentiated ice-rock mixtures has indeed been invoked as a mechanism to extrude material that, once irradiated, resembles the red surfaces of many 100 km-class Centaurs and KBOs (McKinnon *et al.*, 2008). However, Charon-sized bodies are still large enough that they experienced partial differentiation into a rocky core

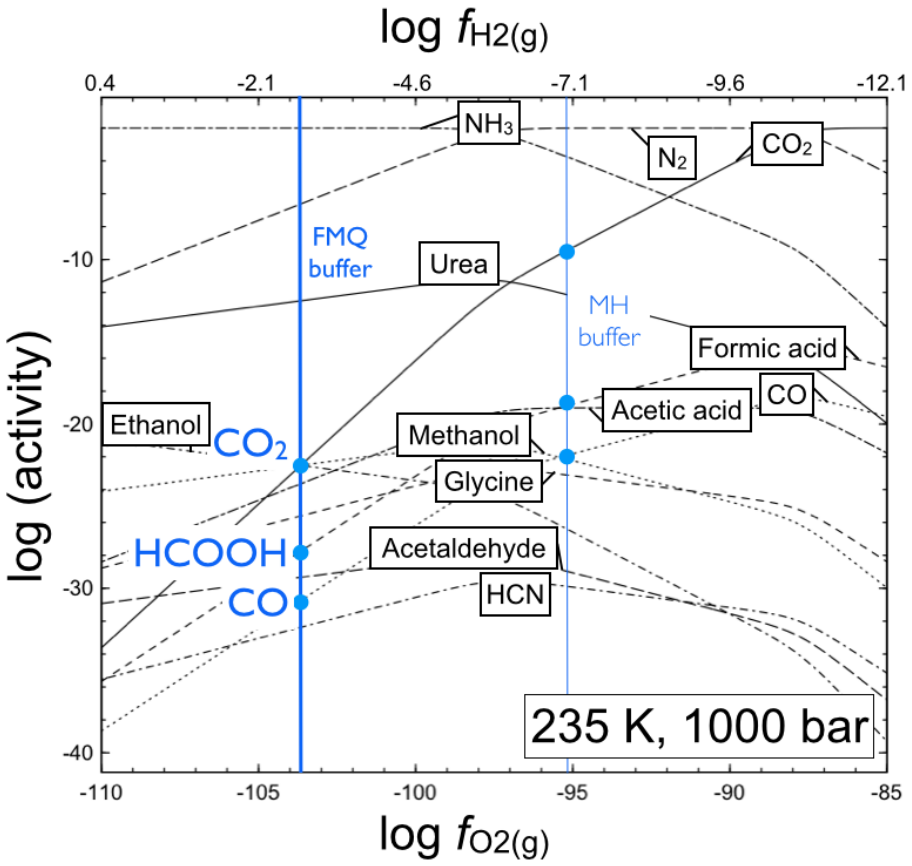

Figure 39: Logarithm of the activities of cometary volatiles, likely to have been accreted by KBOs, as a function of redox conditions in a subsurface ocean at 235 K and 1000 bar

Possible redox conditions are shown by two buffers: the equilibrium between fayalite, magnetite, and quartz ("FMQ"), and that between magnetite and hematite ("MH"). The equilibria between CO and CO_2 and between CO and HCOOH are strongly shifted to the latter species in both cases. Methane is not included in these calculations based on the argument of metastable equilibrium given by Shock and McKinnon (1993).

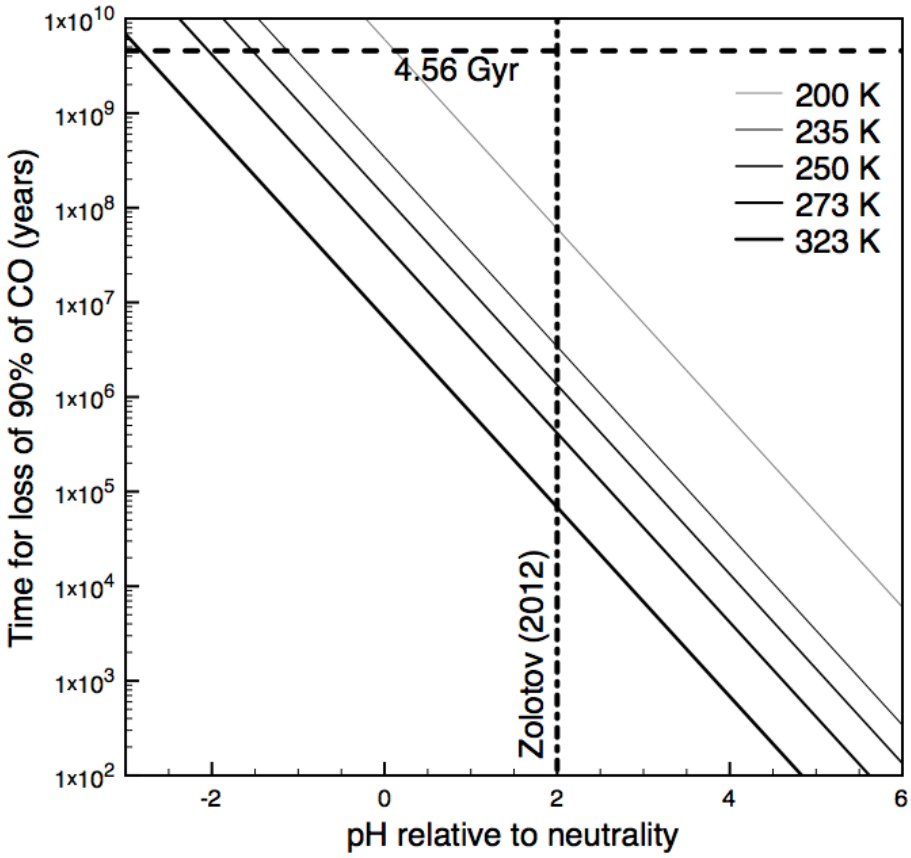

Figure 40: Time after which 90% of aqueous CO is consumed to make formate, as a function of pH relative to neutrality, for temperatures between 200 K and 323 K

Overlain are the age of the solar system (4.56 Gyr) and a plausible pH of KBO subsurface oceans, two units above neutrality, suggested by Zolotov (2012).

and an icy mantle, through which fluid-filled cracks must propagate before reaching the base of the crust. Therefore, fluid pressurization by volatile exsolution or partial freezing remains necessary in the ice mantle.

An outcome of the present study is that undifferentiated crusts *inhibit* exsolution by raising the confining pressure in the icy mantle and the ocean. Higher confining pressures require either longer fluid-filled cracks or higher volatile (CO) abundances for exsolution-driven ascent to occur. Another inhibiting feature of crusts is that their fracture toughness K_{Ic} should be higher than that of ice, given that a crust is an

undifferentiated mixture of icy and rocky grains (F. Nimmo, personal communication). How much higher K_{Ic} becomes is difficult to predict, but it could not be higher than its value for hydrated, loosely consolidated rock, about 0.5 MPa $m^{1/2}$ (Chen *et al.*, 2000; Backers, 2005; Tromans and Meech, 2002; Wang *et al.*, 2007), which is higher by a factor of about 5 than the value for pure ice. Finally, near-surface porosity could decrease the crustal density enough to impede ascent through the last kilometers of crust. However, at these shallow depths, gas-dominated fluid should still be buoyant.

Comparing results between scenarios (b) and (c) allows us to investigate the influence of hydration in the core on cryovolcanism. A hydrated core (density similar to that of serpentine rock with a few percent porosity) takes up a larger volume than a dry core (density similar to that of olivine rock with a few percent porosity). A larger, hydrated core results in the ocean being closer to the surface, at lower pressures than in scenario (b). Thus, exsolution is favored in case (c) compared to case (b), although it is not as easy as in case (a) despite the fact that the seafloor is shallower.

6.5.4 Freezing During Ascent

Another issue of fluid ascent is that it needs to be faster than the timescale of its freezing on the channel walls (Desch *et al.*, 2009). This timescale is increased if the liquid contains antifreezes. Stevenson (1982) estimated upward propagation velocities of 1 to 10 cm s^{-1} and 10% of fluid freezing on icy Saturnian satellites of sizes and densities comparable to those of dwarf planets and for crack diameters D of order 10^2 to 10^3 m. From his estimations, we infer a propagation timescale through a 100 km thick ice shell of 10^6 to 10^7 s and a freezing timescale of 10^7 to 10^8 s. However,

antifreezes also increase the viscosity of the liquid, which slows it down near the walls. The maximum propagation velocity of a viscous fluid through a pipe is given by:

$$v_{\max} = \frac{D^2}{4\eta}\frac{\partial P}{\partial z} \tag{6.23}$$

where D is the pipe (crack) diameter, η the fluid viscosity, and $\partial P/\partial z = (\rho_w - \rho_i)\ g$ the hydrostatic pressure gradient. For cracks originating at the base of an ice shell of thickness d overlying a liquid layer, the ascent time scale $\tau_{\text{asc.}} = d/v_{\max}$ is therefore:

$$\tau_{\text{asc.}} = \frac{4\ d\ \eta}{\Delta\rho\ g\ D^2} \tag{6.24}$$

Kargel (1991, 1992) and Kargel *et al.* (1991, 2000) studied the composition, rheology, and ascent of cryolavas composed of H_2O, NH_3, CH_3OH, and N_2 that may be liquid down to 155 K. Kargel *et al.* (1991) determined experimentally that the viscosity of H_2O-NH_3 mixtures is between 10 and 100 Pa s at T=175 to 235 K and X_{NH3} of a few percent up to eutectic composition (32.1%). Adding methanol increases the viscosity up to 10^4 Pa s near the peritectic. These viscosities are much higher than those of water or ammonia alone, mostly because of hydrogen bonding and partial crystallization in the mixtures. For a water-ammonia liquid of viscosity 100 Pa s, g = 0.3 m s^{-2}, d = 100km, and a cylindrical channel width D of 1 m, we calculate an ascent time scale of 2.7×10^5 (500 kg m$^{-3}/\Delta\rho$) s.

When ascent is driven by pressurization of freezing water, the pressure gradient can be approximated by $\partial P/\partial z \approx (\beta_w h)^{-1}(\Delta V/V)$, where β_w is the compressibility of pure water, h is the depth of the pocket in the ice shell, and $\Delta V/V$ is the relative shrinkage in volume of the water pocket. With $\beta_w \approx 5 \times 10^{-10}$ Pa^{-1}, h = 10 km, and

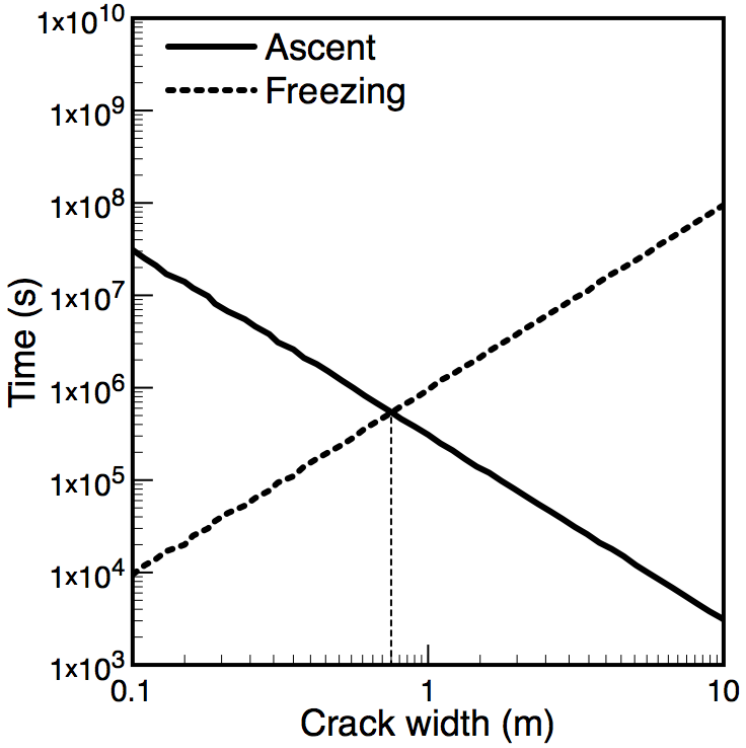

Figure 41: Comparison of timescales for ascent and freezing

The thin dashed line indicates the minimum crack width (diameter) above which propagation through an ice shell is possible before liquid freezes.

$\Delta V/V = 0.1$, $\partial P/\partial z \approx 200$ Pa m^{-1}; this is comparable to the buoyancy arising from gas exsolution: $\Delta\rho\ g \approx 150$ Pa m^{-1}.

The timescale of freezing a 1 m column of pure water can be estimated as follows. The specific heat to be conducted away is $H = C_p(T)\ \Delta T + L_{\text{freeze}}$, where $C_p(T)$ is the heat capacity and L_{freeze} is the latent heat of freezing. The timescale of freezing τ_{freeze} is then given by:

$$\tau_{\text{freeze}} \approx \rho_{\text{liq}} \times 1 \times \pi D^2\ H \left(\frac{\partial H}{\partial t}\right)^{-1} = \rho_{\text{liq}} \times 1 \times \pi D^2 \frac{H}{k_{\text{ice}}} \left(\frac{\partial^2 T}{\partial r^2}\right)^{-1} \tag{6.25}$$

Here, r indicates the horizontal distance away from the center of the crack in cylindrical coordinates. We (crudely) approximate the second derivative term as

$\partial^2 T/\partial r^2 \approx [(\Delta T/\Delta r)_{\text{crack-wall}} - (\Delta T/\Delta r)_{\text{wall-ice}}]/\Delta r$. We assume a temperature of 235 K at the center of the column and 100 K at the walls, as well as 1 m into the ice: $\Delta r = D = 1$ m, $\Delta_{\text{crack-wall}} T = 135$ K, and $\Delta_{\text{wall-ice}} T = 0$ K. Taking $k_{\text{ice}} = 5 * (100K/T) \approx 5$ W K^{-1} m^{-1} (crystalline ice), $C_p \approx 5000$ J K^{-1} kg^{-1} [increases from 4188 to 7000 J/K/kg between 273 K and 230 K, diverges at 228 K for pure water; Archer and Carter (2000)], $L_{\text{freeze}} = 334$ kJ kg^{-1}, and $\Delta T = 235 - 176$ K in the $C_p \Delta T$ term, we estimate $\tau_{\text{freeze}} \approx 1.5$ (ρ_{liq}/500 kg m^{-3}) $\times 10^6$ s. For pure ammonia, C_p is 4700 J K^{-1} kg^{-1} (Desch *et al.*, 2009), and L_{freeze} for eutectic H_2O-NH_3 is 131.9 kJ kg^{-1}, which yields $\tau_{\text{freeze}} \approx 0.95$ (ρ_{liq}/500 kg m^{-3}) $\times 10^6$ s. In addition to freezing because of temperature decrease, there is also the possibility of decompression freezing for pure water ice Ih, which has a negative slope in the P-T phase diagram.

Thus, ascent times are of order 10^5 for both non viscous water (Crawford and Stevenson, 1988) and viscous water-ammonia liquids. This is shorter than the minimum 10^6 s time scale needed for water-ammonia to cool down to 176 K and the latent heat of freezing to be conducted away in crystalline ice. Given the uncertainties in crack geometry, temperatures, material properties, and that we did not consider freezing of the gas component of the fluid, these rough estimates do little more than provide some intuition about the relevant time scales when comparing competing effects on ascent. Figure 41 compares these timescales for various crack widths D. Despite the roughness and uncertainties of the above analysis, the large range of ascent and freezing timescales involved entail a specific threshold crack width, of order 1 m, for successful ascent. It is worth noting that the width of a fracture on Enceladus has recently been estimated at 9 m (Goguen *et al.*, 2013).

Note that ascent happens far too quickly for cracks to heal by solid-state creep

of ice. Assuming a crack with $l = 1$m has opened, it would close on a timescale $\tau_{\rm heal}$ given by:

$$\tau_{\rm heal} = \frac{1}{\dot{\epsilon}} = \frac{2\eta}{\sigma} \approx \frac{2\eta\sqrt{\pi l}}{K_{Ic}} = 6 \text{ Myr} \left(\frac{\eta}{5 \times 10^{18} \text{Pa s}} \right) \tag{6.26}$$

where η is the viscosity of ice, taken from Goldsby and Kohlstedt (2001); $\dot{\epsilon}$ is the strain rate, and σ is the stress. The indicative value of 5×10^{18} Pa s for the ice viscosity is valid for a Pluto- or Charon-sized body at $T \approx 176$ K. This temperature is the eutectic point of a water-ammonia mixture and a likely temperature at the base of the ice shell if volatile antifreezes play any role in maintaining liquid. Near subsurface liquid at 176 K, cracks can remain open for several Myr. At 273 K, the viscosity falls to about 10^{12} Pa s and relaxation occurs in only about one year. Closer to the surface where temperatures are lower and viscosities higher, cracks could remain open over much longer time scales.

6.5.5 Other Model Considerations

Several other loosely constrained considerations influence the likelihood of explosive cryovolcanism. First, gas solubility increases with decreasing temperature; this should hamper exsolution during ascent to some extent. Here, we considered the ascent of fluid to be quick enough ($\tau_{\rm asc.} \approx 0.1\ \tau_{\rm freeze}$) that the fluid does not have time to cool significantly. In principle, including the temperature effect on solubility should be straightforward, because this effect translates into higher values of $K_i(T, P_{\rm gas})$ as T decreases. In practice, a predictive geochemical model has yet to be devised for temperatures below that used here, 235 K.

In addition to equilibrium chemical speciation, one should also consider kinetic

effects on exsolution. At frigid ocean temperatures, it is possible that speciation and exsolution are inhibited kinetically. To address this uncertainty, experiments in the relevant temperature and pressure regime are necessary, as in the case of explosive silicate volcanism (Mangan and Sisson, 2000). Further insight could be gained from models of nucleation and bubble growth (Yund and McCallister, 1970; Rosner and Epstein, 1972; Sparks, 1978; Proussevitch and Sahagian, 1998) applied to the case of volatiles in aqueous solutions. Exsolution kinetics slower than freezing time scales would keep volatiles trapped into the ice.

Scarce experimental data on supercooled solutes make equilibrium calculations below 235 K speculative. The HKF model for determining solute properties becomes singular at 228 K, where supercooled water seems to have a liquid-liquid critical point near 1 bar (Speedy and Angell, 1976). However, this diverging behavior was not observed at higher pressures, where measurements of supercooled water properties have recently been made possible down to 200 K and up to 4000 bar thanks to improvements in experimental setups (Mishima, 2010). This progress in the experimental determination of supercooled water properties is in turn driving efforts to extend the equation of state of supercooled water in this temperature and pressure regime (Holten *et al.*, 2012). A next logical step would be to update the HKF equation for aqueous solutes, which depends on the equation of state for water, to account for these improvements, and fit solute properties to existing experimental solute data. This would enable HKF-based codes such as CHNOSZ to compute predictions for properties of species that have not been experimentally characterized (Figure 42).

Extension to a higher pressure regime would enable studies of larger icy bodies. McKinnon *et al.* (2008) noted that there are no dynamical arguments against larger KBOs the size of Mars or the Earth further away from the Sun. Their study is

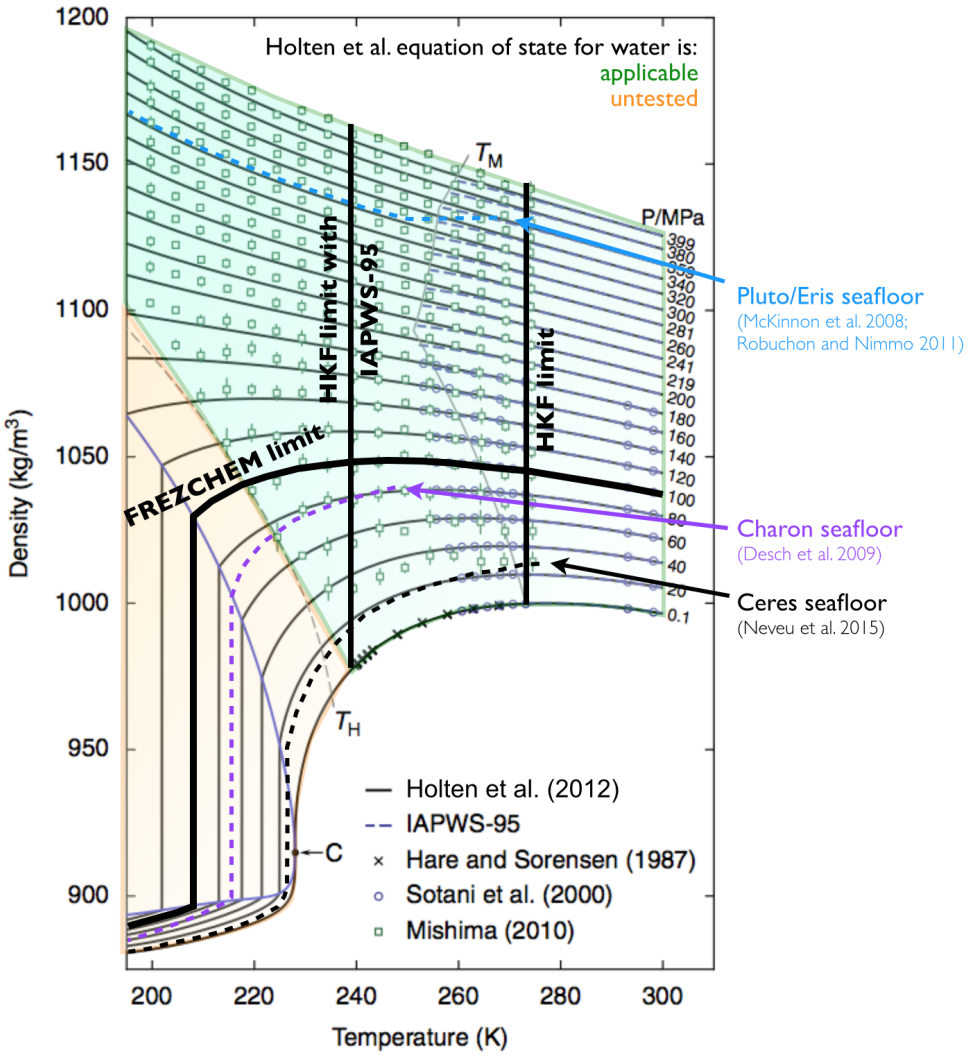

Figure 42: Applicability of current geochemical codes in the pressure-temperature-density space of relevance to icy dwarf planets

This space is delimited by the ammonia-water eutectic point at 176 K (Leliwa-Kopystynski *et al.*, 2002) and the seafloor pressure for Pluto-sized bodies (4000 bar or 400 MPa). The thin solid black curves are predictions of an improved equation of state for water (Holten *et al.*, 2012) that accurately describes measurements from Mishima (2010) and others. Overlain are the geotherms of Ceres- to Pluto-sized dwarf planets (dashed curves), starting at the seafloor and moving through lower T and P to the surface. Seafloor conditions are at the limit of current geochemical codes, such as FREZCHEM and HKF-based CHNOSZ, but theoretical improvements are needed in order to push models to lower T and higher P. Figure modified from Holten *et al.* (2012).

hampered because current geochemical models are capped at pressures of several thousand bars, the pressures reached near the center of Pluto-sized bodies. A recent model (Facq *et al.*, 2014) has extended the predictive HKF framework to explore the solubility and speciation of carbonate species up to 80 kbar; however, this model cannot currently be used at subzero temperatures. Exoplanets, likely icy, of super-Earth size have also been discovered (Beaulieu *et al.*, 2006). The extension of aqueous geochemical models to higher pressures than present would provide a valuable tool to model the interior of such bodies. When modeling gas exsolution at higher pressures, one should keep in mind that the assumption of ideality is no longer valid: using the program REFROP, we calculate fugacity coefficients for N_2 at 240 K of 1.7 at 1 kbar, 6.1 at 2 kbar, 22 at 3 kbar, 81 at 4 kbar, and 284 at 5 kbar. Large fugacity coefficients make real gases more soluble (less likely to outgas) than ideal gases.

Finally, we have neglected any speciation of dissolved gases (e.g., CO_2 to bicarbonate and carbonate), clathration, and volatile condensation (e.g., CO_2 has a critical point at 304 K). These three phenomena are volatile sinks, decreasing the amount of gas available to form a buoyant fluid. For example, calculations using REFROP show that the fugacity of CO_2 $f_{CO2} = (\phi_{CO2} P_{CO2})$ is only 70 bars at 1 kbar and 240 K. The fugacity of CO_2 cannot keep increasing up to the total pressure; instead, it condenses during ascent once the system pressure approaches this fugacity, preventing further increases in the fugacity. On the other hand, pickup of condensed volatile pockets or clathrates by cryovolcanic fluids during ascent could increase their gas content (Battaglia et al., in preparation).

6.5.6 Predictions for Pluto and Charon

The time scale of cryovolcanic activity on Pluto and Charon-sized KBOs depends on the time at which last freezing occurs, if freezing of water pockets indeed initiates cracks (Fagents, 2003; Manga and Wang, 2007). In the Kuiper belt, dwarf planet oceans are predicted to freeze entirely after a few billion years (Desch *et al.*, 2009; Robuchon and Nimmo, 2011), perhaps about 1 Gyr ago for Charon (Rubin *et al.*, 2014; Desch, 2015). Cryovolcanic activity could be sustained over the time needed to freeze a given liquid volume. Assuming a liquid layer several kilometers thick, which corresponds to a eutectic H_2O-NH_3 ocean on Charon if the bulk NH_3 content of the ice was initially 1%, this time could be a few hundred million years (Desch *et al.*, 2009; Rubin *et al.*, 2014). Additional activity is expected from freezing of localized water pockets closer to the surface. If such pockets occur, their presumed volume, much smaller than that of a global ocean layer, would sustain cryovolcanism for a correspondingly shorter time: roughly 50 years for a spherical pocket 1 km in radius. If freezing pressurization drives a cryovolcanic outflow, no more than 7% of the freezing volume (i.e., $\rho_w/\rho_i - 1$) may be erupted. With the same assumptions as above, cryovolcanism resulting from global ocean freezing could in principle emplace a global layer up to a kilometer thick on Charon's surface. In practice, one can expect the efficiency of cryovolcanism as a resurfacing process to be orders of magnitude lower.

Plumes arising from explosive cryovolcanism may be observed on Pluto or Charon by the *New Horizons* probe. These plumes may be rich in CO, since this volatile could make up 80% of the exsolved gas and a few percent to tens of percent of the water- and antifreeze-rich material ejected. However, the calculated short lifetime

of CO in a subsurface ocean implies that the gas may be generated by near-surface sublimation of CO ice, vaporization of subsurface liquid CO, or eruption of a recent cryovolcanic aqueous melt that is disconnected from the ocean.

Plumes rich in the reduced gases CH_4, H_2, and perhaps N_2 would be evidence for hydrothermal activity inside Pluto or Charon. H_2 does not have a spectral signature in the visible and near-infrared regions covered by the *Ralph* package, *New Horizons*'s visible and near-infrared spectrometers (Reuter *et al.*, 2008). However, lines resulting from the dissociation of H_2 molecules could be seen in *Alice* ultraviolet spectra (Stern *et al.*, 2008). More generally, each of the ten gases investigated in this study, if abundant enough, can be detected by least one of these instruments.

N_2 plumes could also be evidence that Pluto and Charon accreted rich in N. However, because Pluto's surface and atmosphere are rich in N_2, it will be difficult to assess the origin of such plumes, which could also arise from frost sublimation on the surface as observed on Triton. The co-detection of other gases along with N_2 could be an argument in favor of a deep origin; conversely, plumes of frost composition would likely originate in surface layers. Hydrothermally produced H_2, CH_4, and N_2 may be distinguished from primordial species by their isotopically heavy makeup (Glein *et al.*, 2009; Rousselot *et al.*, 2014).

In addition, evidence for recent explosive cryovolcanism may be gathered from the detailed composition of the surfaces, atmospheres, or exospheres of Pluto and Charon. The fate of cryovolcanic products (condensation or escape) depends on equilibrium and kinetic constraints similar to those during primordial accretion. Species such as CO, CO_2, CH_4, or N_2 could condense back on the surface depending on surface temperature and gravity (Schaller and Brown, 2007), whereas H_2 would certainly escape. The extent to which a given volatile may condense back to the surface could be more

precisely estimated if *New Horizons* measurements constrain the rate of processes such as Jeans escape, hydrodynamic escape, and ultraviolet photolysis (Schaller and Brown, 2007). Such measurements include atmospheric thermal profiles (to constrain heating from extreme ultraviolet radiation) and structure (in particular, the exobase altitude from which escape may take place), as well as ejection velocity in potential plumes. *New Horizons* is well equipped to perform such measurements: ultraviolet spectra and atmospheric maps will be acquired by the *Alice* instrument (Stern *et al.*, 2008); atmospheric temperature and structure profiles will be inferred from radio occultations using *REX* (Tyler *et al.*, 2008); and *SWAP* (McComas *et al.*, 2008) and *PEPSSI* (McNutt *et al.*, 2008) will be used to perform solar wind measurements and energetic particle spectrometry to determine *in situ* escape rates (Stern and Spencer, 2003).

Past cryovolcanism may have been the source of methane for Pluto's atmosphere and frosts; this would mean that its past or current ocean had a very reduced composition. On the other hand, mild heating of subsurface clathrate hydrates may suffice to concentrate guest species at the surface. Miscible species such as CH_3OH or NH_3 are not expected to exsolve, but they play a key role in maintaining liquid as antifreezes, and would be entrained by the gas onto the surface during an eruption. Local concentrations of these species would be evidence for extrusion of material from the interior; however, their cryovolcanic origin (i.e., surface deposition as a fluid) would likely be as ambiguous as previous interpretations of similar features on other icy bodies.

6.6 Conclusions

In this study, we investigated gas exsolution as a mechanism to drive cryovolcanism. We used a novel approach that couples geophysics and geochemistry, and extended geochemical modeling to the seldom-explored realm of liquid water at subzero temperatures. We showed that, provided liquid and crack initiation (e.g. by freezing pressurization), cryovolcanism can occur on dwarf planet-sized KBOs.

CO seems to be an excellent driver for explosive venting, whereas species such as CO_2 and sulfur gases are not. Primordial N accreted as N_2 could also drive cryovolcanism if its abundance, currently unconstrained, is above a few percent with respect to water. CH_4 and H_2 resulting from hydrothermal activity at the putative seafloors of KBOs may also trigger cryovolcanism if they are present in substantial amounts (a few percent with respect to water). The miscible antifreezes CH_3OH and NH_3 remain in solution; this allows persistence of liquid at temperatures well below 200 K.

Therefore, the onset of explosive cryovolcanism hinges mainly on the abundances of CO, N_2, CH_4, and H_2: abundances of a few percent in solution for at least one of these seem necessary to initiate exsolution even in the most favorable settings. This requires at least one of the following scenarios: (a) CO does not get destroyed in an ocean, (b) the quantity of N accreted is at the high end of current estimates, or (c) large amounts of reduced gases are produced by vigorous hydrothermal activity.

Undifferentiated crust that never overturned inhibits exsolution and cryovolcanism by acting as a pressure seal. This finding contradicts previous predictions that crusts provide a favorable medium for fluid-filled crack propagation because of the positive fluid buoyancy. Cryovolcanism is favored if the rocky core is hydrated, because the

core then takes up a larger volume and places the seafloor closer to the surface; this reduces the pressure solubilization of volatiles. Other considerations, such as ice relaxation of cracks and fluid freezing during ascent, may hamper cryovolcanism, but rough calculations showed that they do not prevent it if crack propagation happens quickly enough. Therefore, current or recent explosive cryovolcanism is expected on Pluto and Charon if either currently has a subsurface liquid layer, a plausible outcome of thermal evolution models. If this is the case, the icy dwarf planets of the Kuiper belt may well join the list of potentially habitable bodies in the solar system.

Chapter 7

GEOCHEMISTRY, THERMAL EVOLUTION, AND CRYOVOLCANISM ON CERES WITH A MUDDY ICE MANTLE

In this chapter, I combine results on hydrothermal couplings between geophysical and geochemical processes and their surface expression (Chapters 4 through 6) to interpret preliminary data returned by the *Dawn* spacecraft and make predictions to be tested by upcoming *Dawn* measurements. Using results of combined geophysical evolution and geochemical simulations, I paint a picture of Ceres' evolution consistent with all recent available data gathered on Ceres.

This chapter, co-authored by Steve Desch, has been submitted for publication in *Geophysical Research Letters*. Below is a brief summary of the results, followed by the text of the paper.

We present a model of the internal evolution of Ceres consistent with pre-*Dawn* observations and preliminary data returned by *Dawn*. We assume that Ceres accreted ice and both micron- and millimeter-sized rock particles, and that micron-sized fines stayed suspended in liquid during differentiation. We conclude that aqueously altered grains were emplaced on Ceres' surface during the first tens of Myr of its evolution. Our geochemical simulations suggest Ceres' unusual surface mineralogy is consistent with aqueous alteration of CM material, possibly by NH_3-bearing fluid. Thermal evolution simulations including insulating fines yield present-day liquid at depth if Ceres has a small core or no core at all; otherwise they yield temperatures at the core-mantle boundary of 240–250 K, just warm enough for chloride brines to persist and be freezing today. We hypothesize that ongoing freezing may over-pressurize

liquid or briny reservoirs, driving cryovolcanic outflow whose surface expression may have been observed by *Dawn* at Ceres' 'bright spots'. These outflows may contribute to the water vapor being produced at Ceres.

7.1 Introduction

Of all the solar system worlds known to possess a substantial ($>$ 10wt%) ice fraction, none is as close to the Sun as Ceres. Ceres potentially harbors subsurface liquid water like Europa and Enceladus (Neveu *et al.*, 2015a); confirmation of subsurface liquid would hold great implications for habitability in the Solar System. The *Dawn* spacecraft now orbiting Ceres may provide evidence of subsurface liquid delivery to the surface. Interpretation of *Dawn* data demands a model for the evolution of Ceres' structure to date. Here we describe such a model, constrained by observations, that hypothesizes the presence in Ceres' ice of micron-sized, aqueously-altered silicate fines. We explore the effect of this 'muddy ice' on Ceres' thermal evolution, and its surface expression.

Constraints on Ceres' density and structure come from its mass, $9.395 \pm 0.0125 \times 10^{20}$ kg (Thomas *et al.*, 2005) and its shape and size. From telescopic observations, two oblate spheroid shape models have been determined: equatorial radius $a = 487.3 \pm 1.8$ km, polar radius $c = 454.7 \pm 1.6$ km, yielding mean radius $R = 476.2$ km and mean density $\bar{\rho} = 2077 \pm 36$ kg m^{-3} (Thomas *et al.*, 2005); and $a = 483.5 \pm 5$ km, $c = 446 \pm 5$ km (Drummond *et al.*, 2014), yielding $R = 470.7$ km and $\bar{\rho} = 2151 \pm 40$ kg m^{-3}. Combined with its 9.074 hour rotation period (Carry *et al.*, 2008), we derive normalized moments of inertia (NMOI) for the Thomas *et al.* (2005) shape of 0.347 using the equations of Bourda and Capitaine (2004), or 0.326 using those of Zolotov (2009)

(calculating the rotational parameter q using the equatorial radius). The Drummond *et al.* (2014) shape yields NMOI of 0.400 and 0.380, respectively. The *Dawn* team has recently reported preliminary axes of $a = 482.6 \pm 1.0$ km, $b = 480.6 \pm 1.0$ km, and $c = 445.6 \pm 1.0$ km, yielding (assuming $b = a$) mean radius $R = 469.3$ km and NMOI of 0.400 and 0.378 (Russell *et al.*, 2015). The Thomas *et al.* (2005) shape is consistent with models in which Ceres has a core of radius R_c and density ρ_c, overlain by a mantle of density ρ_m, whereas the other two shapes could be consistent with a small core or completely homogenous body such as Zolotov (2009) suggested.

Several authors (McCord and Sotin, 2005; Castillo-Rogez and McCord, 2010; Castillo-Rogez, 2011; Neveu *et al.*, 2015a) have modeled Ceres as having a rocky core and pure ice mantle ($\rho_m = 918$ kg m^{-3}), or ice containing solutes or clathrates (Castillo-Rogez and McCord, 2010), as expected if rock (refractory silicates and organics) and ice fully differentiated within Ceres. Some lines of evidence indeed support an ice mantle. Ceres exhibits little (< 8 km) topography (Thomas *et al.*, 2005). It also lacks a collisional family, possibly because fragments derive from an icy mantle and sublimate after ejection (Rivkin *et al.*, 2014).

Other lines of evidence argue against a pure ice mantle. Ceres' surface is dark and uniform (albedo 0.04 to 0.09; Li *et al.* (2006)), with spectra consistent with minerals resulting from aqueous alteration (Lebofsky *et al.*, 1981; Rivkin *et al.*, 2006), possibly brucite, magnetite, carbonates (magnesite), and phyllosilicates (cronstedtite or saponites) (King *et al.*, 1992; Milliken and Rivkin, 2009; Rivkin *et al.*, 2012; Beck *et al.*, 2015). Ceres' unique surface composition argues against exogenous sources such as meteoritic infall, or formation from the observed surface material (as Zolotov (2009) suggests), unless the observed minerals formed out of fluid-rock equilibrium in transient near-surface fluids generated by chondritic impactors (Zolotov, 2014).

Otherwise, endogenous processes must have emplaced hydrated minerals onto Ceres' surface. Ice within a few meters of Ceres' surface (at latitudes $< 60°$) will sublimate (Fanale and Salvail, 1989; Schorghofer, 2015; Titus, 2015), so the surface is widely interpreted as a lag deposit. This implies a mantle of ice with embedded minerals.

These apparently conflicting observations may be reconciled if Ceres has a mixed mantle of ice containing a substantial mass fraction of fines. This idea was first suggested by Bland *et al.* (2013), who noted that chondritic parent bodies likely accreted a mixture of chondritic material (micron-sized fines 'matrix' and millimeter-sized 'chondrules') and ices. In bodies large enough to melt ice, they assumed chondrules would settle to form a rocky core, but that fines would remain suspended by convection in a muddy melt. They recently applied their 'mudball convection' models to Ceres (Bland and Travis, 2014), assuming a rock density $\rho_c = 2700$ kg m^{-3}, core radius $R_c \approx 300$ km, and a mantle 'mud' density $\rho_m = 1870$ kg m^{-3} (Travis *et al.*, 2015). These parameters yield an NMOI of 0.376, intermediate between those derived for the shapes of Thomas *et al.* (2005) and Drummond *et al.* (2014).

Ceres' mass and NMOI can also be matched by a family of solutions with different ρ_m reflecting different mass fractions of fines. For the shape of Thomas *et al.* (2005), one end member is a pure ice mantle, $\rho_m = 918$ kg m^{-3}, requiring Ceres to be 86wt% rock with low density $\rho_c = 2628$ kg m^{-3}, consistent with hydrated silicates but unrealistically metal-free. The other end member assumes Ceres is 74wt% rock with the highest plausible density, $\rho_c = 3700$ kg m^{-3}, consistent with Fe-rich olivine, yielding $\rho_m = 1676$ kg m^{-3}. Below, we explore a plausible intermediate case with $\rho_m = 1468$ kg m^{-3}, requiring Ceres to be 18wt% ice and 82wt% rock with density $\rho_c = 2900$ kg m^{-3}, the density of grains in the heavily hydrated CM chondrites (McKinnon, 1997) and that determined by Desch and Neveu (2015b) to represent

aqueously altered chondritic material. Three quarters of the rock would reside in a core with radius 358 km, one quarter of it mixed in the mantle, which matches the 3:1 ratio of millimeter-sized chondrules (which would sink to a core) to micron-sized matrix grains (which, we assume, stay suspended), as reported by Scott and Krot (2005) for enstatite, ordinary, and some carbonaceous chondrites. For the Drummond *et al.* (2014) and Russell *et al.* (2015) shapes, Ceres can be assumed to be undifferentiated or to have a minimal core (radius 85 km if Ceres is 1wt% rock and 99wt% muddy ice). This chondrule-free case is compatible with accretion of CI chondrite-type material (Tomeoka and Buseck, 1988). For $\bar{\rho} = 2151$ kg m^{-3} and again assuming a rock density of 2900 kg m^{-3}, the mixture contains 62vol% fines.

This paper is organized as follows. In §2 we consider Ceres' differentiation, early surface emplacement, and muddy mantle formation. In §3 we explore the effects of this muddy ice mantle on Ceres' thermal evolution. This evolution scenario yields several opportunities for aqueous alteration (§4) and may allow present-day cryovolcanism (§5). In §6, we list predictions testable by *Dawn* measurements.

7.2 Differentiation and Origin of a Muddy Ice Mantle

Following Travis *et al.* (2015), we assume Ceres accreted a homogeneous mixture of ice and rock grains of chondritic composition and size distribution (micron-sized fines 'matrix' and millimeter-sized 'chondrules'). Ice can melt solely from long-lived radionuclide heating (§3), but decay of ^{26}Al can generate liquid in the first few Myr. Chondrules quickly settle via Stokes flow through the liquid, falling distances $\Delta R \sim 100$ km due to gravity ($g \approx 0.28$ m s^{-2} near the surface) on short timescales:

$$t_{\rm settle} = \frac{18\,(\Delta R)\,\eta}{(\rho_{\rm r} - \rho_{\rm l})\;g\,D^2} \approx 50\left(\frac{\rho_{\rm r} - \rho_{\rm l}}{800\,{\rm kg\,m^{-3}}}\right)^{-1}\left(\frac{\eta}{0.18\,{\rm Pa\,s}}\right)\left(\frac{\Delta R}{100\,{\rm km}}\right)\left(\frac{D}{1\,{\rm mm}}\right)^{-2}{\rm yr}. \tag{7.1}$$

We assume that fines and chondrules, if accreted dry, become quickly hydrated, reaching density $\rho_{\rm r} = 2900$ kg m^{-3}. In the first melt, the volume fraction of solids is $\phi = 0.57$, so the viscosity of the fluid exceeds that of water (0.0018 Pa s) by a factor $(1 - \phi/\phi_{\rm m})^{-2} \approx 100$, where $\phi_{\rm m} = 0.63$ (Mueller *et al.*, 2009). Within decades chondrules settle, leaving the liquid with density $\rho_{\rm l} = 1526$ kg m^{-3}, solids volume fraction $\phi \approx 0.26$, and viscosity 0.005 Pa s. In such liquid, micron-sized fines take $\approx$ 0.8 Myr to settle out. If all rock is in fines, as required by the Drummond *et al.* (2014) and Russell *et al.* (2015) shapes, then $\phi \approx 0.62$ and $t_{\rm settle} \approx 1$ Gyr.

Whether liquid and fines unmix is uncertain, and not addressed by Travis *et al.* (2015, and references therein) from first principles. The Shields diagram commonly used in sedimentology predicts suspension of micron-sized fines on Earth if flow speeds exceed the small threshold ~ 3 km yr^{-1} (Shields, 1936), or a much lower threshold on Ceres due to its lower gravity. Because of its fast rotation, Ceres' ocean may experience geostrophic currents with velocities ~ 1 km yr^{-1} (Melosh *et al.*, 2004; Boubnov and Golitsyn, 1990, their equation 4.2) if the seafloor heat flux exceeds 100 mW m^{-2}, a value measured in hydrothermal areas on Earth (Elderfield and Schultz, 1996), but 15- to 150-fold higher than those typically reached throughout our thermal evolution simulations (§3). In addition, fines may settle rapidly if they coagulate into larger aggregates. Other authors (McCord and Sotin, 2005; Castillo-Rogez and McCord, 2010; Neveu *et al.*, 2015a) have explored the case in which fines settle. In light of evidence that Ceres' subsurface is not pure ice (§1), we explore the possibility that fines remain suspended in the liquid, and its implications for surface emplacement,

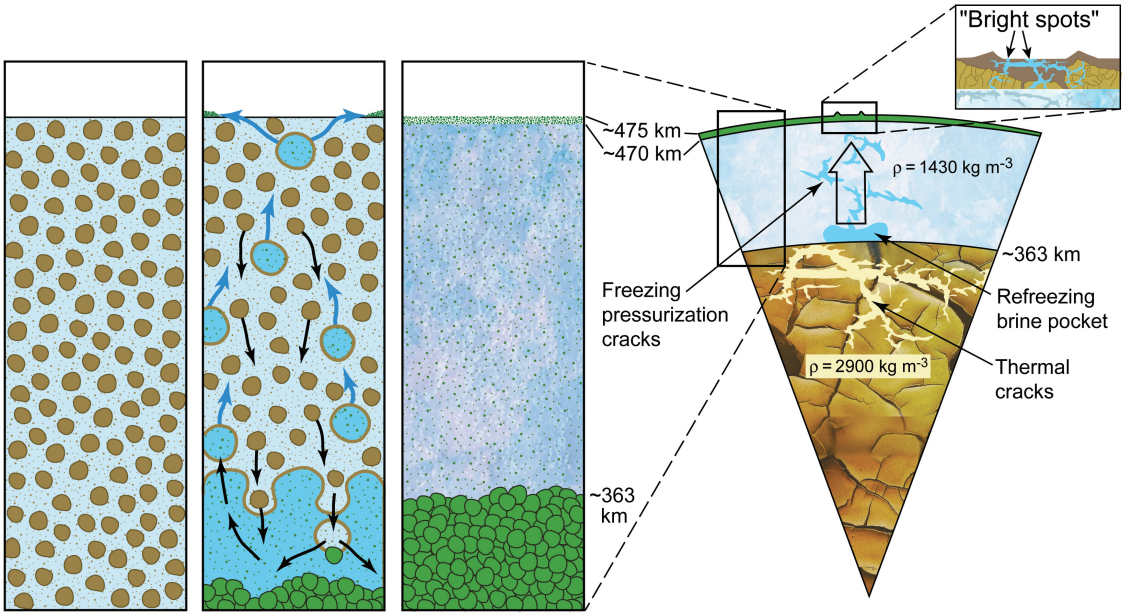

Figure 43: Differentiation if Ceres formed 4-7 Myr after CAIs

Left: Ceres begins as a homogeneous, frozen mix of ice, 'chondrules', and fines. Radiogenic heat melts ice; chondrules and fines are aqueously altered (green); chondrules sink, forming a core; and Rayleigh-Taylor instabilities at the ice-liquid interface generate diapirs tens of km in size containing liquid bearing fines; diapirs rise and emplace fines on the surface. The entire mantle overturns in this way. Ice sublimation leaves a lag deposit at the surface. If Ceres formed < 4 Myr after CAIs, overturn proceeds via rapid melting and foundering of the thin (< 4 km) crust, but results in the same structure. *Right*: Ceres' structure today: a cracked core of hydrated 'chondrules' (possibly smaller or nonexistent if Ceres accreted less or no chondrules), under a mantle of ice and fines, with pockets of cold (≈ 250 K), briny liquid in between. This liquid may ascend to the surface due to freezing pressurization. Effusion is likely through pre-existing cracks, e.g., in large craters.

under two scenarios. (Fines are assumed hydrated, but we neglect the effect of salts in the liquid.)

In the first scenario, Ceres forms 4 to 7 Myr after calcium, aluminum-rich inclusions (CAIs). Our thermal evolution simulations (§3) show ^{26}Al decay heat quickly melts water in central layers.

The case of the Thomas *et al.* (2005) shape is shown in Fig. 43. In melted layers, chondrules sink to the core within 10^2 yr (Equation 7.1), creating a density inversion at the top of a subsurface ocean ($\rho_l = 1526$ kg m^{-3} underlying $\rho = 2077$ kg m^{-3}), triggering Rayleigh-Taylor (RT) instabilities. An important scale is $L =$

$(nRT_0/E_a)(T_0/|dT/dr|)$, the lengthscale over which the viscosity changes significantly. The fastest growing wavelengths of the RT instability are $\lambda \approx 7L$ (Conrad and Molnar, 1997), generating diapirs $\sim \lambda/2$ in diameter. Assuming basal slip is the relevant ice rheology, $n = 1.8$ and $E_a = 49$ kJ mol^{-1} ($R = 8.31$ J mol^{-1} K^{-1}); we assume $T_0 = 273$ K at the ice-liquid interface. Our thermal evolution simulations suggest $dT/dr \sim 2$ K km^{-1} in the ice above the subsurface ocean in the first 60 Myr. Thus, $L \sim 11$ km, yielding diapirs with diameters ~ 40 km. These diapirs, which trap liquid and suspended, hydrated fines, are generated by RT instabilities growing on timescales $t_{RT} \approx 5.4\,\eta\,(L/Z_0)^{0.44}\,(\Delta\rho\,g\,L)^{-1} \approx 6000$ yr (Rubin *et al.*, 2014). Here, $\eta \sim 10^{14}\,(1-\phi/\phi_m)^{-2} \sim 10^{16}$ Pa s is the viscosity of primordial, solids-laden ice at the liquid-ice interface, and $Z_0 \sim 1$ km is the size of the perturbation initiating the RT instability. From Equation 7.1, the timescale for a diapir of diameter 40 km and density ≈ 1500 kg m^{-3} to buoyantly rise 10 km by Stokes flow, assuming an ice viscosity $\eta = 10^{16}\,\exp[20\,(273\,\mathrm{K}/T - 1)]$ Pa s (Shoji and Kurita, 2014), is about 250 yr for ice at 273 K near the liquid-ice interface, increasing to 50 Myr in ice at 170 K. While diapirs ascend to the surface, fingers of ice bearing fines and chondrules sink into the liquid layer where they melt, delivering more chondrules to the core and fines to the ocean (Fig. 43). RT instabilities keep generating diapirs containing liquid and fines until the entire crust has overturned, yielding a mantle of refrozen ice mixed with aqueously altered fines, all within the first ≈ 60 Myr of Ceres' evolution. If Ceres is nearly homogeneous (Drummond *et al.* (2014) and Russell *et al.* (2015) shapes), material from the central ice layers — which after <70 Myr periodically melts, circulates through the tiny core, and refreezes — is transported to shallow depths by thermally-driven subsolidus convection, where it can be subsequently exposed by impacts.

In the second scenario, applicable to either shape, Ceres forms < 3 Myr after CAIs. The ^{26}Al-driven heat flux is much greater, and in < 10 Myr near-surface temperature gradients approach $dT/dr \sim 30$ K km^{-1}, yielding a crust only ≈ 4 km thick overlying a >100-km deep ocean. As before, chondrules settle out rapidly, but we assume fines remain well mixed. The crust can easily overturn by diapirism (if denser than the underlying ocean) or melting by impacts. It is replaced by liquid bearing aqueously altered fines.

In either scenario, ice sublimates from the surface, leaving a lag deposit of hydrated fines. As long as fines do not unmix from the liquid on $\sim 10^7$ yr timescales, and assuming Ceres formed within about 7 Myr of CAIs, this model robustly results in Ceres being globally resurfaced during its first few tens of Myr, leaving a lag deposit of micron-sized particles that experienced aqueous alteration during residence in subsurface liquid.

7.3 Thermal Evolution

Previous models of Ceres' geophysical and thermal structure have either assumed no differentiation at all (Zolotov, 2009), or complete ice-rock differentiation (McCord and Sotin, 2005; Castillo-Rogez and McCord, 2010; Neveu *et al.*, 2015a). The latter models assume Ceres' mantle has the rheological and thermal properties of pure water ice, in apparent conflict with the assumption that the surface represents a lag deposit of minerals. In their recent thermal evolution model, Travis *et al.* (2015) assume ice and rock fines remain well mixed, affecting shell rheological and thermal properties; they conclude thermal convection is vigorous within Ceres. Here we model the thermal evolution of Ceres, including the effects of a muddy ice mantle with fines, thermal

convection, and hydrothermal circulation, using the 1-D code of Desch *et al.* (2009), modified by Neveu *et al.* (2015a).

In the following runs, we assume Ceres' radius is 470.7 km, its bulk density 2151 kg m^{-3}, that it accreted 'cold' with uniform temperature 168 K, from a homogeneous mixture of ice (density 918 kg m^{-3}) and chondritic rock (which quickly hydrated to have density 2900 kg m^{-3}), either 1/4 in fines and 3/4 in chondrules or 99% in fines. The code, described in detail by Desch *et al.* (2009) and Neveu *et al.* (2015a), calculates heating by differentiation and by radioactive decay of both long-lived (^{40}K, ^{232}Th, ^{235}U, ^{238}U) and short-lived (^{26}Al) radionuclides present in the rock at CI abundances (Lodders, 2003). Temperatures are found by balancing the flow of heat to the surface (at fixed temperature 168 K) by conduction, thermal convection in the mantle if the Rayleigh criterion is satisfied, or hydrothermal circulation in the core if it is cracked and the Rayleigh criterion is satisfied. Differentiation of chondrules and ice into a lithified silicate core and a muddy ice mantle is allowed by redistribution of components within fixed volumes, first by Stokes settling in layers warmer than 273 K, then immediately by RT instabilities (§2) once the radius of the outward-moving differentiation front exceeds half of Ceres' radius (Neveu *et al.*, 2015a). The assumption that fines and ice are well mixed (§2), even as liquid freezes into a muddy mantle, is implemented by forcing differentiated layers to retain either 25% or 99% (homogeneous case) of their initial rock mass. Rocky fines have lower thermal conductivity ($\sim$ 1 W m^{-1} K^{-1}) than ice ($\sim$ 3 W m^{-1} K^{-1}), making the mantle more insulating according to the formalism of Desch *et al.* (2009); they also increase its viscosity by a factor $(1 - \phi/\phi_{\rm m})^{-2} \approx 3$ or 4000 for volume fractions $\phi = 0.26$ and 0.62, respectively (Mueller *et al.*, 2009). Other assumed parameters (e.g., densities, heat capacities, thermal conductivities) and formalisms are those of Desch *et al.* (2009) and Neveu *et al.* (2015a).

The simulated thermal evolution of Ceres under the second scenario above (formation 3 Myr after CAIs with substantial ^{26}Al decay heating) is shown in Fig. 44. Results for the differentiated case (Fig. 44a) are similar to those obtained by Neveu *et al.* (2015a). Differentiation occurs within 1 Myr after formation, yielding a rocky core of radius 363 km overlain by a 112 km-thick muddy hydrosphere that for the first 60 Myr is fully melted and vigorously convecting. Liquid also circulates through the thermally fractured core, efficiently transferring heat from the core to the hydrosphere. Convective heat transport within the hydrosphere leads it to cool and partially freeze around 0.75 Gyr. Through the frozen outer layers, heat flows slowly by conduction rather than convection, causing radiogenic heat buildup, until more liquid is again produced around 1 Gyr to within 30 km of the surface. The hydrosphere again partially refreezes around 1.5 Gyr, then remelts up to 60 km below the surface before fully freezing at 2.5 Gyr, stopping hydrothermal circulation in the core. Subsequently, sluggish conductive heat transfer in the core keeps the center above 600 K, but outer core regions remain below 273 K, preventing a global ocean above. Today, core-mantle boundary temperatures of $\approx$ 250 K (Fig. 44) could allow liquid brine pockets. For the small core case, the same processes lead to a similar thermal evolution (Fig. 44b), although at the present day the muddy hydrosphere remains liquid and convective at radii up to 360 km (110 km depth).

If Ceres forms later, $\approx$ 7 Myr after CAIs, our calculations show a similar evolution. Early on, the crust is much thicker and the temperature gradient much lower, $|dT/dr| \approx$ 2 K km^{-1}, but evolution past 100 Myr is unchanged.

We have assumed a CI composition for Ceres, yielding the highest radiogenic heating rate among chondrites. Using CO chondrite abundances (Wasson and Kallemeyn, 1988), which yield the lowest radiogenic heating rate among non-enstatite chondrites,

we find a similar evolution. In the large core case, freezing episodes occur earlier (0.25 and 1.25 Gyr, full freezing at 1.5 Gyr), with present-day temperatures ≈ 240 K at the core-mantle boundary. In the small core case, the present-day hydrosphere remains liquid at radii up to 300 km only.

7.4 Geochemistry

The above scenarios provide three opportunities for water-rock interaction: in the first few tens of Myr, as most of the current surface is emplaced and vigorous hydrothermal circulation occurs (temperature T up to 300°C, pressure P between 20 and 140 MPa, bulk water:rock mass ratio $W{:}R = 0.15$); in the subsequent ocean ($T \approx 0-30$°C, $P \approx 20-140$ MPa, $W{:}R \geq 0.15$); and in impact-generated hydrothermal systems at the surface ($T < 10$°C assuming the heat of impact melts ice but does not heat the liquid, $P < 0.1$ MPa, $W{:}R < 0.6$). We investigated equilibrium fluid and rock compositions as a function of T, P, and $W{:}R$, using the geochemical modeling software *PHREEQC* (Parkhurst and Appelo, 2013), implementing an extended Debye-Hückel equation to compute solute activity coefficients (Pitzer and Brewer, 1961; Helgeson, 1969; Anderson, 2005), a Peng-Robinson equation to compute gas fugacity coefficients (Peng and Robinson, 1976), and thermodynamic data compiled in the *llnl.dat* database (Parkhurst and Appelo, 2013) with solute and mineral molar volumes compiled in the *OBIGT* database (Dick, 2008). Initial rock minerals and abundances were chosen to match representative elemental (Wasson and Kallemeyn, 1988) and mineralogical (Howard *et al.*, 2009, 2011) compositions of CM chondrites to within a few percent for each element and mineral group, including all elements more abundant than 500 ppm (Al, C, Ca, Co, Cr, Fe, H, K, Mg, Mn, Na, Ni, O, P, S, Si and Ti), plus N

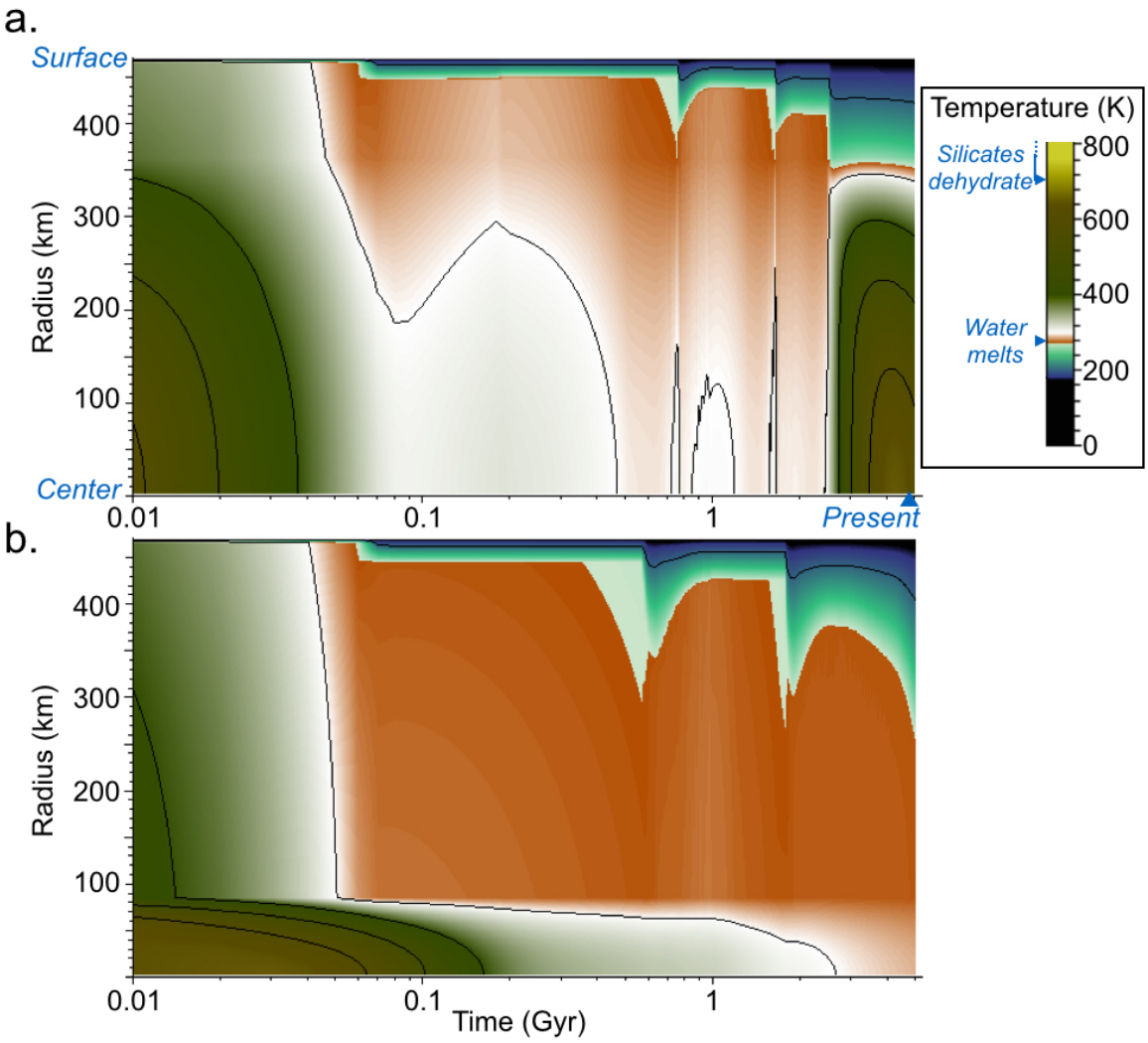

Figure 44: Temperatures inside Ceres, versus depth and time since formation (logarithmic scale)

Colors denote temperature, not composition. a. Shape model of Thomas *et al.* (2005), with 363 km radius chondrule core. Ceres' mantle is usually frozen past 2.5 Gyr. b. Shape models of Drummond *et al.* (2014) and Russell *et al.* (2015), with a very small core (<1% of all rock mass, radius 85 km). At the present day, ice below 360 km is melted.

and additional trace elements. Two initial fluid compositions were simulated: pure water, and water with 5 mol% C, 2 mol% N, 0.5 mol% S, and 520 mol ppm of Cl to approximate the volatile (C, N, S) content of comets (Mumma and Charnley, 2011) and the chlorine content of CI chondrites (Wasson and Kallemeyn, 1988). The initial pH varied between 7 and 14. The initial oxygen fugacity fO_2 varied from 6 log units below to 6 log units above the fayalite-magnetite-quartz (FMQ) buffer. Calculations were run at *W:R* of 0.1, 1, and 10, but only the latter two values yielded solutions dilute enough for the geochemical model to be valid. These values are higher than the bulk *W:R* mentioned above, but may be appropriate under the assumption that not all the rock is altered. Further details on these calculations and illustrations of their results are provided in supplementary material.

Water-rock interactions generally yield fluids dominated by S (pentathionate $S_5O_6^{2-}$), C (methane) solutes, and (for starting cometary fluid) N as NH_3 or NH_4^+, with $< 25\%$ of the solutes being Na and Ca. At high T the fluid can be rich in H_2. The dominant mineralogies are magnetite and clays (saponite smectite; some antigorite, cronstedtite, and greenalite serpentines; chlorites; NH_4-clays). A few simulations yield brucite (above 200°C, initial pH $\geq$13), but they involve concentrated solutions with ionic strength ≈ 10, beyond the range of applicability of the Debye-Hückel model (ionic strength < 0.1).

The clays produced by our model tend to be richer in Mg than Fe, although Fe-rich cronstedtite replaces magnetite as the dominant Fe-mineral at low T in simulations with initial pure water. The presence of saponite and NH_4-clays rather than brucite may be consistent with recent (and previous) interpretations of Ceres' 3.06 μm feature (Beck *et al.*, 2015; King *et al.*, 1992). Carbonates, which seem prominent on Ceres (Rivkin *et al.*, 2012), are absent from our simulation results, suggesting Ceres may

have undergone alteration at conditions more oxidizing than those simulated here. Nevertheless, the clays and magnetite identified on Ceres' surface could be equilibrium products of aqueous alteration of CM material. Because these products seem to form independently of T and P, we cannot discriminate between early, hot alteration or cold interaction occurring later on. If confirmed, abundant NH_4-clays at Ceres' surface would suggest that Ceres accreted N-rich cometary ices.

Under conditions producing methane-rich solutions, methane clathrates could form, as most of the subsurface liquid colder than 300 K lies in their stability field (Mousis *et al.*, 2015). As thermodynamic data for methane clathrates were not included in our geochemical calculations, we cannot predict at this time whether clathration occurs.

7.5 Possible Ongoing Cryovolcanism

Ceres' surface displays hints of exposed subsurface liquid, especially at several 'bright spots' of albedo >0.4 located in the 92 km-diameter crater Occator (latitude 20°N, longitude 239°, http://photojournal.jpl.nasa.gov/catalog/PIA19889). Increased brightness at this longitude was observed by Li *et al.* (2006), and determined from near-infrared J, H, and K reflectance to be more consistent with salts or clays than water ice (Carry *et al.*, 2008). Surface water ice is not stable at these latitudes (Fanale and Salvail, 1989; Schorghofer, 2015). Notably, water vapor is produced at these longitudes (Küppers *et al.*, 2014). The brightest spot or group of spots, at the crater center, appears circular with diameter $\sim$ 9 km. It is surrounded by smaller spots. A sparser group of circular spots is located a few dozen km to the east. The spots lack the ejecta rays observed around other bright areas such as crater Haulani (latitude 5°N, longitude 11°); arguing against an impact origin. That the Occator spots are located

in topographically low areas (http://photojournal.jpl.nasa.gov/catalog/PIA19891) may suggest pooling of fluids created during or after the Occator impact. The spots could also be a lag deposit of solutes and entrained particles brought to the surface cryovolcanically. Another potential cryovolcanic feature is an isolated mountain 15 km wide and 5 km high (latitude 19°S, longitude 315°) with bright streaks that seem to run downslope (http://photojournal.jpl.nasa.gov/catalog/PIA19578 and /PIA19631).

Cryovolcanism is remarkably plausible in the context of our evolution models. Widespread extant subsurface liquid is expected in the small core scenario (§3), bearing solutes leached from its interaction with rock. Even in the large core scenario, for which the deepest ice is at 250 K, a thin global layer (or isolated pockets) of briny or NH_3-rich liquid could persist to the present day. A eutectic mixture of water and 23.3wt% NaCl, of density ≈ 1200 kg m^{-3}, melts at -21°C = 252 K (Barduhn and Manudhane, 1979), and the eutectic temperature of the H_2O–NH_3 system is 176 K (Leliwa-Kopystynski *et al.*, 2002). Our geochemical calculations suggest that Na, C, S, and perhaps N are major solutes in subsurface liquid, and that some Cl remains in solution. This situation is analogous to that studied by Zolotov and Shock (2001) for Europa. As that ocean cools, sulfate hydrates first freeze out of solution, concentrating chlorides into a reduced volume of liquid (1% the original volume). The solution remains liquid until KCl (sylvite), $NaCl{\cdot}2H_2O$ (hydrohalite), and $MgCl_2{\cdot}12H_2O$ freeze out at temperatures between -29°C and -36°C. Thus, at the core-mantle boundary, temperatures seem warm enough for $\sim 1\%$ of the original ocean to persist as briny liquid.

In either scenario, liquid is undergoing freezing at the present day. As just $\approx 2\%$ of a liquid reservoir freezes, it compresses the liquid, over-pressurizing it by the $\sim$ 10 MPa needed for it to ascend $\sim$ 100 km (Fagents, 2003; Manga and Wang, 2007;

Neveu *et al.*, 2015b; O'Brien *et al.*, 2015). In the large core case (Thomas *et al.*, 2005), the liquid density $\rho_l = 1526$ kg m^{-3} and fines volume fraction $\Phi = 0.26$ (§2) yield a hydrosphere volume increase of 4.1% if it freezes entirely. If the volume increase takes place solely by effusion of material, a global layer 77 m-thick (20 m once the ice has sublimated away) is effused atop the 107 km-thick hydrosphere. In the small core case (Drummond *et al.*, 2014; Russell *et al.*, 2015), the liquid density $\rho_l = 2151$ kg m^{-3} and fines volume fraction $\Phi = 0.62$ (§2) yield a volume increase upon freezing of 1.4%. Our simulations suggest that only the upper 110 km have refrozen so far (Fig. 44b), corresponding to a global layer 29 m thick, or 18 m thick after ice sublimation. Liquid is likely to effuse to the surface through preexisting fractures, such as those in the basements of craters, as postulated for the Moon and Mercury (Thomas *et al.*, 2015). Perhaps basement fractures formed during the Occator impact intersect the large NW-SE oriented fracture network in the Ebisu and Palo mapping quadrants, favoring ongoing effusion in this particular region of Ceres. Thus, evidence of slow effusion over geological timescales might be restricted to large craters; without sufficient material erupted (<20 m equivalent global layer) to significantly erase impact morphologies at the hundred-meter scales observed so far by *Dawn*'s Framing Camera.

We hypothesize that the bright spots on Ceres are active manifestations of effusion of solute-bearing liquid, possibly containing fines of aqueously altered minerals, brought to the surface by over-pressurization due to freezing of a subsurface liquid reservoir. Ice sublimates from the outpouring, possibly contributing to the observed 6 kg s^{-1} of water vapor production (Küppers *et al.*, 2014), leaving behind a growing lag deposit of salts and perhaps fines. Assuming water is effused as fast as it is sublimated, salts and fines would be emplaced at a rate 11 kg s^{-1}. The bright spots, with total inferred

volume ~ 100 km^3 and mass $\sim 1 \times 10^{14}$ kg, would have been emplaced over 0.3 Myr by effusion of ~ 150 km^3 of material.

7.6 Conclusions

We have presented a model for Ceres' evolution, informed by analysis of how differentiation would proceed, numerical geophysical modeling of its thermal history, and geochemical calculations. We have attempted to explain pre-*Dawn* observations and preliminary data returned by *Dawn*, and to make predictions testable by *Dawn* at Ceres. We assume Ceres is made of ice, millimeter-sized particles ('chondrules'), and micron-sized fines that remain mixed in liquid. We predict Ceres' mantle is a mix of ice and fines that suffered aqueous alteration, with the following implications.

1. **Internal Structure**: We predict that Ceres has a rocky core, made of whatever chondrules Ceres accreted, overlain by a mantle of ice and micron-sized hydrated fines. The core size must be constrained by observations, but our model is consistent with both end-member shape models. For the Thomas *et al.* (2005) shape model, we predict a core of density $\rho_c \approx 2900$ kg m^{-3} and radius ≈ 363 km, under a mantle of ice and hydrated fines with density $\rho_m \approx 1430$ kg m^{-3}, yielding a NMOI ≈ 0.347. For the Drummond *et al.* (2014) and Russell *et al.* (2015) shape models, we predict a very small or absent core (no chondrules), surrounded by a uniform mixture of ice and hydrated fines, with density $\bar{\rho} \approx 2151$ kg m^{-3}, yielding a NMOI ≈ 0.4.
2. **Surface Morphology**: We predict Ceres' surface was globally overturned in its first few tens of Myr, replaced by ice bearing fines of minerals that suffered aqueous alteration while residing in subsurface liquid. Overturn was

accomplished by compositional diapirism from a small subsurface ocean if Ceres formed 4-7 Myr after CAIs; if Ceres formed with more ^{26}Al, < 4 Myr after CAIs, then overturn was accomplished by foundering of a thin (~ 4 km) crust over a deep ocean. In contrast, Travis *et al.* (2015) predict overturn by convection throughout Ceres' history, and Shoji and Kurita (2014) predict overturn by diapirism over Ceres' history, but only near its equator. Crater counts to derive Ceres' surface age can test these predictions. We predict Ceres' surface is a lag deposit of micron-sized fines, lacking millimeter-sized particles. Surface particle size may be determined by fits to Ceres' reflectance spectrum. Below the lag deposit should be a mixture of ice and rock fines, whose rheology may be intermediate between pure rock and pure ice. This may be tested by modeling crater relaxation and determining the simple-to-complex crater transition diameter.

3. **Surface Mineralogy**: We predict the fines on Ceres' surface and throughout its ice mantle were aqueously altered. We reproduce the observed surface clays (cronstedtite, saponite, NH_4-clays, though always with Mg-serpentine) and magnetite, but not carbonates and likely not brucite (Rivkin *et al.*, 2012) by simulating the aqueous alteration of rock with CM chondritic elemental abundances by pure or cometary water. Chloride salts may be concentrated in areas of cryovolcanic effusions.
4. **Cryovolcanism**: We hypothesize that the bright spots are salts, and possibly fines of aqueously altered minerals, left after sublimation of cryovolcanically-emplaced water ice. Our evolution models suggest cryovolcanism can be driven by pressurization of freezing liquid reservoirs. If so, since it should have started operating only in the recent geologic past, cryovolcanic heat transport should

have made a negligible contribution to cooling Ceres. Effusion into the cracked basement of craters would seem common.

Chapter 8

CONCLUSIONS AND FUTURE WORK

8.1 How Far Have We Gotten?

Among the results presented in the previous chapters are three major findings. First, life in a wide variety of hydrothermal settings on Earth, although taxonomically diverse, displays a remarkable uniformity in its use of major and trace chemical elements (Chapter 3). Second, hydrothermal systems may be widespread in the solar system, even at the present day, under the surfaces of not only Mars and some icy moons, but perhaps a few dozen dwarf planets as well (Chapter 4). Third, those solar system worlds that harbor hydrothermal systems may have been profoundly affected physically and chemically by water-rock interaction, in ways that can now be quantified (Chapters 5 through 7).

These findings bode well for the search for microbial life in the solar system: they suggest that we look for life, with mechanisms in place to preserve a relatively constrained extended elemental composition that can be used as a biosignature, in hydrothermal material transported to or above the surface of water-bearing worlds. Such material has likely already been sampled at Mars (Ruff *et al.*, 2011) and Enceladus (Hsu *et al.*, 2015), and ongoing and planned Mars rovers are equipped to determine compositions of element suites similar to those of Chapter 3 (Wiens *et al.*, 2012; Allwood *et al.*, 2014). Upcoming and proposed missions may return hydrothermal samples to Earth, where elemental analyses can be complemented to ascertain the

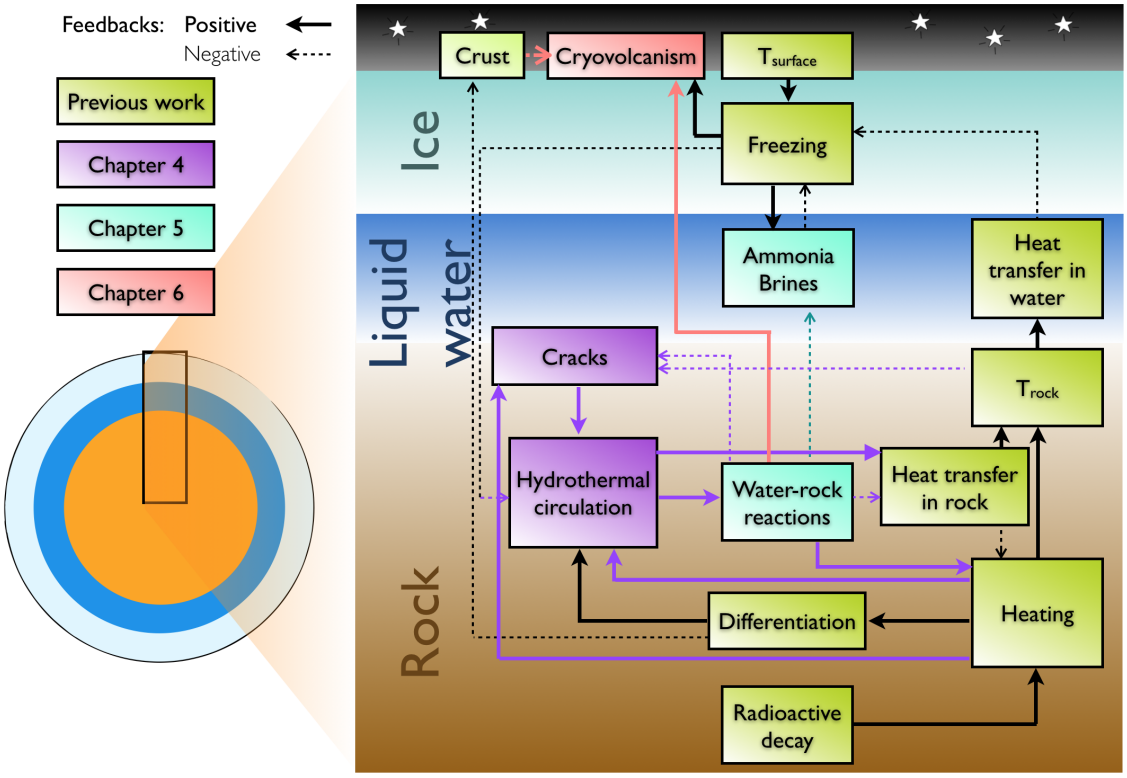

Figure 45: Unveiling the complexity of internal processes governing the evolution of icy dwarf planets

Radioactive decay (bottom) drives endogenic evolution. Subsequent geophysical processes were modeled in previous codes (Desch *et al.*, 2009; Castillo-Rogez and McCord, 2010) in fair detail (green boxes), but neglected key geochemical inputs. Geochemical models of static bodies ("water-rock interactions"; Glein *et al.*, 2009; Zolotov, 2009; Marion *et al.*, 2012) likewise lacked major thermal evolution effects (Castillo-Rogez, 2011). This work links the two, improving our understanding of how dwarf planet interiors function.

presence of life in these samples (Tsou *et al.*, 2012; Mustard *et al.*, 2013; Sherwood, 2015).

These findings also reveal the complexity of internal processes governing the evolution of icy dwarf planets (Fig. 45). Prior models focused either on physical or chemical aspects, but results from Chapters 4 through 7 suggest strong couplings between the two which can no longer be ignored. The models developed as part of this dissertation will inform the interpretation of data returned by *Dawn* at Ceres and *New Horizons* at Pluto, enhancing their science return; in turn, matching the predictions made in previous chapters to close-up observations will provide useful tests for these models.

8.2 Ground Truth: Preliminary Results from *Dawn* and *New Horizons*

Ongoing exploration of Ceres and the Pluto system has confirmed the suggestions of Chapters 4 through 7 that dwarf planets have been geologically active worlds, and likely still are at the present day. Ceres' surface features conspicuous "bright spots", described in Chapter 7 (Fig. 46). These spots seem to have been emplaced by an ongoing aqueous process rather than by exogenic impact. Favored hypotheses include pooling of hydrothermal fluids generated by the Occator impact, or cryovolcanic effusion through fractures in the crater basement (Chapter 7; Le Corre *et al.*, 2015). The composition of the bright spots is unknown at the time of writing, but will be a key test of the Chapter 7 predictions on Ceres' geophysical and geochemical evolution.

Preliminary measurements of Ceres' surface composition hint at the presence of ammoniated phyllosilicates (DeSanctis *et al.*, 2015). If confirmed, these observations would suggest that aqueous NH_3 did play a key role in fluids on dwarf planets,

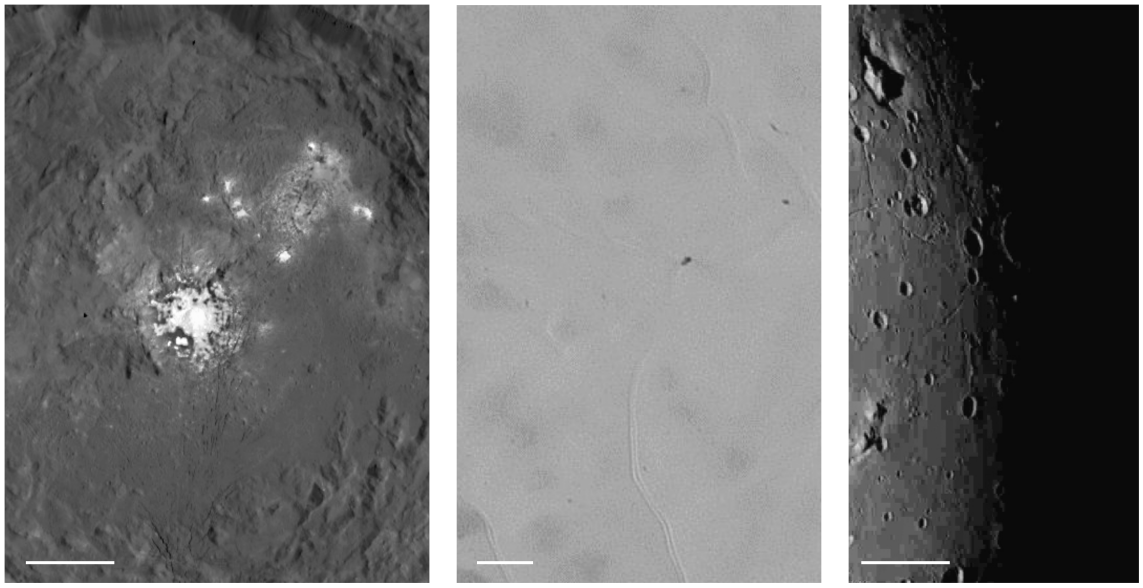

Figure 46: Geologically active dwarf planets

Left: Bright spots located in Occator crater, Ceres. Scale bar: ≈10 km, image PIA19889. *Center*: Frozen plains of Tombaugh Regio, Pluto. Scale bar: ≈20 km, image PIA19936. *Right*: Charon's "mountain in a moat" (top left). Scale bar: ≈50 km, image PIA19713. In all three images, the dearth of impact craters bears witness to the youth of these dwarf planet terrains.

Source: NASA Planetary Photojournal, http://photojournal.jpl.nasa.gov.

strengthening the relevance of the models described in Chapter 5 and the assumption (which permeates Chapters 4 through 7) that NH_3 is a key chemical species. It is interesting to note that even though some models of planetary accretion predict the condensation of ammonia ices at Ceres' current orbit (Dodson-Robinson *et al.*, 2009), others may require formation of Ceres farther from the Sun (McKinnon, 2008) for it to accrete NH_3, possibly in the same region where Kuiper belt objects are thought to have formed (Levison *et al.*, 2008).

Even in the Kuiper belt, the dwarf planets Pluto and Charon display surprising geological activity. On Pluto, the informally-named Tombaugh Regio seems nearly devoid of impact craters even at the smallest scales imaged (Fig. 46), sug-

gesting very recent emplacement of ice. The ice is assumed to be composed of mainly N_2, with diluted methane (http://photojournal.jpl.nasa.gov/catalog/PIA19712) and the strongest CO signal of Pluto's hemisphere imaged at closest approcah (http://photojournal.jpl.nasa.gov/catalog/PIA19718). The discussion in Chapter 6 regarding the chemical conversion of CO in water to more thermodynamically stable species (such as formate HCOOH) suggests that if the emplacement of Tombaugh Regio results from aqueous activity, conversion to HCOOH may have been kinetically inhibited. At this time, the origin of Tombaugh Regio remains unknown, and it may be that its emplacement results from solid-state convection in subsurface ice rather than aqueous processes (Robuchon and Nimmo, 2011). Although Pluto's North polar terrain also seems young, the apparent lack of craters may result from seasonal condensation of frosts (Spencer *et al.*, 1997). Interestingly, Pluto's three most abundant surface and atmospheric compounds, N_2, CH_4, and CO, are also the exsolving species found most likely to drive explosive cryovolcanism in Chapter 6. Future work will be needed to constrain the endogenic origin of these species, and whether (and to what extent) accreted ices may have been processed hydrothermally.

At this time, only a handful of images of Charon have been downlinked from the *New Horizons* spacecraft. These images have unveiled a world which, although more cratered than Pluto, has experienced geological activity (as evidence by planetary-scale canyons; http://photojournal.jpl.nasa.gov/catalog/PIA19932). One of the highest-resolution images features a $\sim$ 50-km structure, nicknamed "mountain in a moat", and resembling a mountain sinking into Charon's crust (Fig. 46). Isostatic adjustment would require a low crustal viscosity, achievable only if ices near their melting point are brought near the surface (Desch and Neveu, 2015a). Is Charon experiencing intrusion

of antifreeze-bearing ices? This hypothesis could be tested by interpreting upcoming *New Horizons* data using the models described in Chapters 4 through 7.

8.3 Future Steps

The research results presented in this dissertation are immediately applicable to the ongoing exploration of dwarf planets. They imply that these objects are of astrobiological significance. To conclude this work, I suggest avenues for research in the longer term.

Characterizing microbial elemental chemistries in hydrothermal systems helps not only improve our understanding of life in what seems to be a common solar system habitat, but also provides a chemical indicator of life which, despite being inconclusive as a biosignature, can be routinely measured by spacecraft (Wiens *et al.*, 2012; Allwood *et al.*, 2014). However, the microbial elemental abundances measured in Chapter 3 were averages over taxonomically diverse communities. The robustness of the Chapter 3 results could be tested by performing elemental analyses of single cells from these communities, following the methods of Steenbergh *et al.* (2013).

Numerical codes of dwarf planet evolution that couple geophysics and geochemistry at each time step are just one step away. Here, although I have identified the couplings and quantified the feedbacks between geophysics and geochemistry, these feedbacks remain to be fully integrated at each time step into a single evolution code. This will be a key objective of my upcoming postdoctoral work.

Finally, the current evolution codes of Chapters 4 through 7 do not simulate tidal processes, which can dominate the internal evolution of icy moons such as Europa and Enceladus. As these objects are prime targets of astrobiology missions being

developed or proposed (e.g. National Research Council, 2011; Tsou *et al.*, 2012; McKay *et al.*, 2014; Pappalardo *et al.*, 2015; Sherwood, 2015), understanding their workings is essential to enhancing the science return of such missions. This will be another major goal of my postdoctoral work.

Abrajano, T. A., N. C. Sturchio, B. M. Kennedy, G. L. Lyon, K. Muehlenbachs and J. K. Bohlke, "Geochemistry of reduced gas related to serpentinization of the Zambales ophiolite, Philippines", Applied Geochemistry **5**, 5, 625–630 (1990).

Abramov, O. and D. A. Kring, "Impact-induced hydrothermal activity on early Mars", Journal of Geophysical Research: Planets (1991–2012) **110**, E12 (2005).

Abramov, O. and S. J. Mojzsis, "Abodes for life in carbonaceous asteroids?", Icarus **213**, 1, 273–279 (2011).

Adams, M. M., M. R. Gómez-García, A. R. Grossman and D. Bhaya, "Phosphorus deprivation responses and phosphonate utilization in a thermophilic *Synechococcus* sp. from microbial mats", Journal of Bacteriology **190**, 24, 8171–8184 (2008).

Agee, C. B., J. Li, M. C. Shannon and S. Circone, "Pressure-temperature phase diagram for the Allende meteorite", Journal of Geophysical Research: Solid Earth (1978–2012) **100**, B9, 17725–17740 (1995).

Airieau, S. A., J. Farquhar, M. H. Thiemens, L. A. Leshin, H. Bao and E. Young, "Planetesimal sulfate and aqueous alteration in CM and CI carbonaceous chondrites", Geochimica et Cosmochimica Acta **69**, 16, 4167–4172 (2005).

Akinfiev, N. N., M. V. Mironenko and S. A. Grant, "Thermodynamic properties of NaCl solutions at subzero temperatures", Journal of Solution Chemistry **30**, 12, 1065–1080 (2001).

Alexander, C. M. O. D., M. Fogel, H. Yabuta and G. D. Cody, "The origin and evolution of chondrites recorded in the elemental and isotopic compositions of their macromolecular organic matter", Geochimica et Cosmochimica Acta **71**, 17, 4380–4403 (2007).

Alexander, C. M. O. D., S. S. Russell, J. W. Arden, R. D. Ash, M. M. Grady and C. T. Pillinger, "The origin of chondritic macromolecular organic matter: A carbon and nitrogen isotope study", Meteoritics & Planetary Science **33**, 4, 603–622 (1998).

Allen, C. C., F. G. Albert, H. S. Chafetz, J. Combie, C. R. Graham, T. L. Kieft, S. J. Kivett, D. S. McKay, A. Steele, A. E. Taunton, M. R. Taylor, K. L. Thomas-Keprta and F. Westall, "Microscopic physical biomarkers in carbonate hot springs: Implications in the search for life on Mars", Icarus **147**, 1, 49–67 (2000).

Allen, C. C. and D. Z. Oehler, "A case for ancient springs in Arabia Terra, Mars", Astrobiology **8**, 6, 1093–1112 (2008).

Allen, R. O. and B. Mason, "Minor and trace elements in some meteoritic minerals", Geochimica et Cosmochimica Acta **37**, 6, 1435–1456 (1973).

Allwood, A., J. Hurowitz, L. W. A. Wade, R. P. Hodyss and D. Flannery, "Seeking ancient microbial biosignatures with PIXL on Mars 2020", in "AGU Fall Meeting Abstracts", pp. P24A–07 (2014).

Amalfitano, S. and S. Fazi, "Recovery and quantification of bacterial cells associated with streambed sediments", Journal of Microbiological Methods **75**, 2, 237–243 (2008).

Amalfitano, S., S. Fazi and A. Puddu, "Flow cytometric analysis of benthic prokaryotes attached to sediment particles", Journal of Microbiological Methods **79**, 2, 246–249 (2009).

Amend, J. P. and E. L. Shock, "Energetics of amino acid synthesis in hydrothermal ecosystems", Science **281**, 5383, 1659–1662 (1998).

Anbar, A. D., "Elements and evolution", Science **322**, 5907, 1481–1483 (2008).

Anbar, A. D. and A. Knoll, "Proterozoic ocean chemistry and evolution: a bioinorganic bridge?", Science **297**, 5584, 1137–1142 (2002).

Anderson, G. M., *Thermodynamics of Natural Systems* (Cambridge University Press, 2005).

Andrews, R. M., "Measurement of the fracture toughness of glacier ice", Journal of Glaciology **31**, 108, 171–176 (1985).

Andrews, S., "FastQC – A quality control tool for high throughput sequence data", http://www.bioinformatics.babraham.ac.uk/projects/fastqc, retrieved Feb. 26, 2015 (2010).

Appelo, C. A. J., D. L. Parkhurst and V. E. A. Post, "Equations for calculating hydrogeochemical reactions of minerals and gases such as CO_2 at high pressures and temperatures", Geochimica et Cosmochimica Acta **125**, 49–67 (2014).

Archer, D. G. and R. W. Carter, "Thermodynamic properties of the NaCl+H_2O system. 4. Heat capacities of H_2O and NaCl (aq) in cold-stable and supercooled states", The Journal of Physical Chemistry B **104**, 35, 8563–8584 (2000).

Auzende, A.-L., R.-M. Pellenq, B. Devouard, A. Baronnet and O. Grauby, "Atomistic calculations of structural and elastic properties of serpentine minerals: the case of lizardite", Physics and Chemistry of Minerals **33**, 4, 266–275 (2006).

Backers, T., *Fracture toughness determination and micromechanics of rock under mode I and mode II loading*, Ph.D. thesis, University of Potsdam (2005).

Bales, R. C. and J. J. Morgan, "Dissolution kinetics of chrysotile at pH 7 to 10", Geochimica et Cosmochimica Acta **49**, 11, 2281–2288 (1985).

Ballhaus, C., R. F. Berry and D. H. Green, "Oxygen fugacity controls in the Earth's upper mantle", Nature **348**, 437–440 (1990).

Balme, M., V. Rocchi, C. Jones, P. Sammonds, P. Meredith and S. Boon, "Fracture toughness measurements on igneous rocks using a high-pressure, high-temperature rock fracture mechanics cell", Journal of Volcanology and Geothermal Research **132**, 2, 159–172 (2004).

Barber, D. J., "Matrix phyllosilicates and associated minerals in C2M carbonaceous chondrites", Geochimica et Cosmochimica Acta **45**, 6, 945–970 (1981).

Barduhn, A. J. and A. Manudhane, "Temperatures required for eutectic freezing of natural waters", Desalination **28**, 3, 233–241 (1979).

Barnhart, C., F. Nimmo and B. Travis, "Martian post-impact hydrothermal systems incorporating freezing", Icarus **208**, 1, 101–117 (2010).

Barucci, M., F. Merlin, A. Guilbert, C. De Bergh, A. Alvarez-Candal, O. Hainaut, A. Doressoundiram, C. Dumas, T. Owen and A. Coradini, "Surface composition and temperature of the tno orcus", Astronomy and Astrophysics **479**, 1, L13–L16 (2008).

Baudouin-Cornu, P., Y. Surdin-Kerjan, P. Marliere and D. Thomas, "Molecular evolution of protein atomic composition", Science **293**, 5528, 297–300 (2001).

Bauer, J. M., T. L. Roush, T. R. Geballe, K. J. Meech, T. C. Owen, W. D. Vacca, J. T. Rayner and K. T. Jim, "The near infrared spectrum of Miranda: Evidence of crystalline water ice", Icarus **158**, 1, 178–190 (2002).

Beaulieu, J.-P., D. P. Bennett, P. Fouqué, A. Williams, M. Dominik, U. G. Jørgensen, D. Kubas, A. Cassan, C. Coutures, J. Greenhill, K. Hill, J. Menzies, P. D. Sackett, M. Albrow, S. Brillant, J. A. R. Caldwell, J. J. Calitz, K. H. Cook, E. Corrales, M. Desort, S. Dieters, D. Dominis, J. Donatowicz, M. Hoffman, S. Kane, J.-B. Marquette, R. Martin, P. Meintjes, K. Pollard, K. Sahu, C. Vinter, J. Wambsganss, K. Woller, K. Horne, I. Steele, D. M. Bramich, M. Burgdorf, C. Snodgrass, M. Bode, A. Udalski, M. K. Szymański, M. Kubiak, T. Więckowski, G. Pietrzyński, I. Soszyński, O. Szewczyk, Ł. Wyrzykowski, B. Paczyński, F. Abe, I. A. Bond, T. R. Britton, A. C. Gilmore, J. B. Hearnshaw, Y. Itow, K. Kamiya, P. M. Kilmartin, A. V. Korpela, K. Masuda, Y. Matsubara, M. Motomura, Y. Muraki, S. Nakamura, C. Okada, K. Ohnishi, N. J. Rattenbury, T. Sako, S. Sato, M. Sasaki, T. Sekiguchi, D. J. Sullivan, P. J. Tristram, P. C. M. Yock and T. Yoshioka, "Discovery of a cool planet of 5.5 Earth masses through gravitational microlensing", Nature **439**, 7075, 437–440 (2006).

Beck, P., B. Schmitt, E. A. Cloutis and P. Vernazza, "Low-temperature reflectance spectra of brucite and the primitive surface of 1-Ceres?", Icarus **257**, 471–476 (2015).

Becker, L., D. P. Glavin and J. L. Bada, "Polycyclic aromatic hydrocarbons (PAHs) in Antarctic Martian meteorites, carbonaceous chondrites, and polar ice", Geochimica et Cosmochimica Acta **61**, 2, 475–481 (1997).

Bentley, D. L., J. P. Dempsey, D. S. Sodhi and Y. Wei, "Fracture toughness of columnar freshwater ice from large scale DCB tests", Cold regions science and technology **17**, 1, 7–20 (1989).

Bibring, J.-P., Y. Langevin, J. F. Mustard, F. Poulet, R. Arvidson, A. Gendrin, B. Gondet, N. Mangold, P. Pinet, F. Forget, the OMEGA team, M. Berthé, J.-P. Bibring, A. Gendrin, C. Gomez, B. Gondet, D. Jouglet, F. Poulet, A. Soufflot, M. Vincendon, M. Combes, P. Drossart, T. Encrenaz, T. Fouchet, R. Merchiorri, G. Belluci, F. Altieri, V. Formisano, F. Capaccioni, P. Cerroni, A. Coradini, S. Fonti, O. Korablev, V. Kottsov, N. Ignatiev, V. Moroz, D. Titov, L. Zasova, D. Loiseau, N. Mangold, P. Pinet, S. Douté, B. Schmitt, C. Sotin, E. Hauber, H. Hoffmann, R. Jaumann, U. Keller, R. Arvidson, J. F. Mustard, T. Duxbury, F. Forget and G. Neukum, "Global mineralogical and aqueous Mars history derived from OMEGA/Mars Express data", Science **312**, 5772, 400–404 (2006).

Birch, F., "Finite elastic strain of cubic crystals", Physical Review **71**, 11, 809 (1947).

Bizzarri, A. and M. Cocco, "A thermal pressurization model for the spontaneous dynamic rupture propagation on a three-dimensional fault: 1. methodological approach", Journal of Geophysical Research: Solid Earth (1978–2012) **111**, B5 (2006).

Bland, M. T., "Predicted crater morphologies on Ceres: Probing internal structure and evolution", Icarus **226**, 1, 510–521 (2013).

Bland, P. A. and B. J. Travis, "More mudballs: Simulating primordial planetesimals as unconsolidated mixtures of mud and chondrules", in "77th Annual Meeting of the Meteoritical Society Abstracts", p. 5295 (The Meteoritical Society, 2014).

Bland, P. A., B. J. Travis, K. A. Dyl and G. Schubert, "Giant convecting mudballs of the early solar system", in "44th Lunar and Planetary Science Conference Abstracts", p. 1447 (Lunar and Planetary Institute, 2013).

Bockelée-Morvan, D., N. Biver, J. Crovisier, D. C. Lis, P. Hartogh, R. Moreno, M. de Val-Borro, G. A. Blake, S. Szutowicz, J. Boissier, J. Cernicharo, S. B. Charnley, M. Combi, M. A. Cordiner, T. de Graauw, P. Encrenaz, C. Jarchow, M. Kidger, M. Küppers, S. N. Milam, H. S. P. Müller, T. G. Phillips and M. Rengel, "Searches for HCl and HF in comets 103P/Hartley 2 and C/2009 P1 (Garradd) with the Herschel Space Observatory", Astronomy & Astrophysics **562**, A5 (2014).

Bockelee-Morvan, D., J. Crovisier, M. J. Mumma and H. A. Weaver, "The composition of cometary volatiles", in "Comets II", edited by M. Festou, H. U. Keller and H. A. Weaver, pp. 391–423 (University of Arizona Press, 2003).

Bolton, E. W., A. C. Lasaga and D. M. Rye, "Dissolution and precipitation via forced-flux injection in a porous medium with spatially variable permeability: Kinetic control in two dimensions", Journal of Geophysical Research: Solid Earth (1978–2012) **102**, B6, 12159–12171 (1997).

Bolton, E. W., A. C. Lasaga and D. M. Rye, "Long-term flow/chemistry feedback in a porous medium with heterogenous permeability; kinetic control of dissolution and precipitation", American Journal of Science **299**, 1, 1–68 (1999).

Borcard, D., F. Gillet and P. Legendre, *Numerical Ecology with* R (Springer Science & Business Media, 2011).

Boston, P. J., M. V. Ivanov and C. P. McKay, "On the possibility of chemosynthetic ecosystems in subsurface habitats on Mars", Icarus **95**, 2, 300–308 (1992).

Boubnov, B. M. and G. S. Golitsyn, "Temperature and velocity field regimes of convective motions in a rotating plane fluid layer", Journal of Fluid Mechanics **219**, 215–239 (1990).

Boudier, F., A. Baronnet and D. Mainprice, "Serpentine mineral replacements of natural olivine and their seismic implications: oceanic lizardite versus subduction-related antigorite", Journal of Petrology **51**, 1-2, 495–512 (2010).

Bouhifd, M., D. Andrault, G. Fiquet and P. Richet, "Thermal expansion of forsterite up to the melting point", Geophysical Research Letters **23**, 10, 1143–1146 (1996).

Bourda, G. and N. Capitaine, "Precession, nutation, and space geodetic determination of the Earth's variable gravity field", Astronomy & Astrophysics **428**, 2, 691–702 (2004).

Bowen, H. J. M., *Environmental Chemistry of the Elements* (Academic Press, London, 1979).

Bowler, C., M. van Montagu and D. Inze, "Superoxide dismutase and stress tolerance", Annual Review of Plant Physiology and Plant Molecular Biology **43**, 1, 83–116 (1992).

Bowling, T. J., B. C. Johnson, D. M. Blair and J. Melosh, "Large impact basins on Ceres: Probing beneath the icy mantle", in "AGU Fall Meeting Abstracts", pp. P41E–03 (2014).

Brace, W. F. and D. L. Kohlstedt, "Limits on lithospheric stress imposed by laboratory experiments", Journal of Geophysical Research: Solid Earth (1978–2012) **85**, B11, 6248–6252 (1980).

Brearley, A. J., "The action of water", in "Meteorites and the Early Solar System II", edited by D. S. Lauretta and H. Y. McSween, pp. 584–624 (University of Arizona Press, 2006).

Bridges, J. C., D. C. Catling, J. M. Saxton, T. D. Swindle, I. C. Lyon and M. M. Grady, "Alteration assemblages in Martian meteorites: Implications for near-surface processes", Space Science Reviews **96**, 365–392 (2001).

Brinza, L., L. G. Benning and P. J. Statham, "Adsorption studies of Mo and V onto ferrihydrite", Mineralogical Magazine **72**, 1, 385–388 (2008).

Britt, D. T. and G. J. Consolmagno, "Stony meteorite porosities and densities: A review of the data through 2001", Meteoritics and Planetary Science **38**, 1161–1180 (2003).

Britten, R. J. and F. T. McClure, "The amino acid pool in *Escherichia coli*", Bacteriological Reviews **26**, 3, 292 (1962).

Broecker, W. S., "Glacial to interglacial changes in ocean chemistry", Progress in Oceanography **11**, 2, 151–197 (1982).

Brown, A. J., S. J. Hook, A. M. Baldridge, J. K. Crowley, N. T. Bridges, B. J. Thomson, G. M. Marion, C. R. de Souza Filho and J. L. Bishop, "Hydrothermal formation of clay-carbonate alteration assemblages in the Nili Fossae region of Mars", Earth and Planetary Science Letters **297**, 174–182 (2010).

Brown, M. E., "The compositions of Kuiper belt objects", Annual Review of Earth and Planetary Sciences **40**, 1, 467–494 (2012).

Brown, M. E. and W. M. Calvin, "Evidence for crystalline water and ammonia ices on Pluto's satellite Charon", Science **287**, 5450, 107–109 (2000).

Brown, R. H., R. L. Kirk, T. V. Johnson and L. A. Soderblom, "Energy sources for Triton's geyser-like plumes", Science **250**, 4979, 431–435 (1990).

Browning, L. B. and W. L. Bourcier, "Tochilinite: a sensitive indicator of alteration conditions on the CM asteroidal parent body", in "27th Lunar and Planetary Science Conference Abstracts", p. 171 (1996).

Bruland, K. W., J. R. Donat and D. A. Hutchins, "Interactive influences of bioactive trace metals on biological production in oceanic waters", Limnology and Oceanography **36**, 8, 1555–1577 (1991).

Buie, M. W., W. M. Grundy, E. F. Young, L. A. Young and S. A. Stern, "Orbits and photometry of Pluto's satellites: Charon, S/2005 P1, and S/2005 P2", The Astronomical Journal **132**, 1, 290–298 (2006).

Buratti, B. J., M. D. Hicks and R. L. Newburn Jr, "Does global warming make Triton blush?", Nature **397**, 6716, 219–219 (1999).

Burchell, M. J., S. A. Bowden, M. Cole, M. C. Price and J. Parnell, "Survival of organic materials in hypervelocity impacts of ice on sand, ice, and water in the laboratory", Astrobiology **14**, 6, 473–485 (2014).

Busemann, H., A. F. Young, C. M. Alexander, P. Hoppe, S. Mukhopadhyay and L. R. Nittler, "Interstellar chemistry recorded in organic matter from primitive meteorites", Science **312**, 5774, 727–730 (2006).

Buttigieg, P. L. and A. Ramette, "A guide to statistical analysis in microbial ecology: a community-focused, living review of multivariate data analyses", FEMS Microbiology Ecology **90**, 3, 543–550 (2014).

Byerlee, J., "Friction of rocks", Pure and applied Geophysics **116**, 4-5, 615–626 (1978).

Cabello, P., M. D. Roldán, F. Castillo and C. Moreno-Vivián, "Nitrogen cycle", in "Encyclopedia of Microbiology, 3rd Edition", vol. 2, pp. 299–321 (Academic Press Oxford, 2009).

Cady, S. L. and J. D. Farmer, "Fossilization processes in siliceous thermal springs: trends in preservation along thermal gradients", in "Evolution of hydrothermal ecosystems on Earth (and Mars?)", pp. 150–173 (1996).

Cady, S. L., J. D. Farmer, J. P. Grotzinger, J. W. Schopf and A. Steele, "Morphological biosignatures and the search for life on Mars", Astrobiology **3**, 2, 351–368 (2003).

Cameron, V., C. H. House and S. L. Brantley, "A first analysis of metallome biosignatures of hyperthermophilic archaea", Archaea **2012**, 789278 (2012).

Caporaso, J. G., C. L. Lauber, W. A. Walters, D. Berg-Lyons, J. Huntley, N. Fierer, S. M. Owens, J. Betley, L. Fraser, M. Bauer, N. Gormley, J. A. Gilbert, G. Smith and R. Knight, "Ultra-high-throughput microbial community analysis on the Illumina HiSeq and MiSeq platforms", The ISME Journal **6**, 8, 1621–1624 (2012).

Carlson, R. W., R. E. Johnson and M. S. Anderson, "Sulfuric acid on Europa and the radiolytic sulfur cycle", Science **286**, 5437, 97–99 (1999).

Carr, J. S. and J. R. Najita, "Organic molecules and water in the planet formation region of young circumstellar disks", Science **319**, 5869, 1504–1506 (2008).

Carry, B., C. Dumas, M. Fulchignoni, W. J. Merline, J. Berthier, D. Hestroffer, T. Fusco and P. Tamblyn, "Near-infrared mapping and physical properties of the dwarf-planet Ceres", Astronomy & Astrophysics **478**, 1, 235–244 (2008).

Carry, B., Hestroffer, D., DeMeo, F. E., Thirouin, A., Berthier, J., Lacerda, P., Sicardy, B., Doressoundiram, A., Dumas, C., Farrelly, D. and Müller, T. G., "Integral-field spectroscopy of (90482) Orcus-Vanth", Astronomy & Astrophysics **534**, A115, 9 pp. (2011).

Castillo-Rogez, J. C., "Ceres: Neither a porous nor salty ball", Icarus **215**, 2, 599–602 (2011).

Castillo-Rogez, J. C., T. Johnson, P. Thomas, M. Choukroun, D. Matson and J. Lunine, "Geophysical evolution of Saturn's satellite Phoebe, a large planetesimal in the outer Solar System", Icarus **219**, 1, 86–109 (2012).

Castillo-Rogez, J. C. and J. I. Lunine, "Evolution of Titan's rocky core constrained by *Cassini* observations", Geophysical Research Letters **37**, 20, L20205 (2010).

Castillo-Rogez, J. C., D. L. Matson, C. Sotin, T. V. Johnson, J. I. Lunine and P. C. Thomas, "Iapetus' geophysics: Rotation rate, shape, and equatorial ridge", Icarus **190**, 1, 179–202 (2007).

Castillo-Rogez, J. C. and T. B. McCord, "Ceres' evolution and present state constrained by shape data", Icarus **205**, 2, 443–459 (2010).

Cavosie, A. J., "Reconciling early impacts and the rise of life", Geology **42**, 5, 463–464 (2014).

Charlou, J. L., J. P. Donval, Y. Fouquet, P. Jean-Baptiste and N. Holm, "Geochemistry of high H_2 and CH_4 vent fluids issuing from ultramafic rocks at the Rainbow hydrothermal field (36° 14" N, MAR)", Chemical Geology **191**, 4, 345–359 (2002).

Charlton, S. R. and D. L. Parkhurst, "Modules based on the geochemical model *PHREEQC* for use in scripting and programming languages", Computers & Geosciences **37**, 10, 1653–1663 (2011).

Chen, C. Y., G. S. Lan and W. H. Tuan, "Preparation of mullite by the reaction sintering of kaolinite and alumina", Journal of the European Ceramic Society **20**, 14, 2519–2525 (2000).

Cherkaoui, A. S. and W. S. Wilcock, "Laboratory studies of high Rayleigh number circulation in an open-top Hele-Shaw cell: An analog to mid-ocean ridge hydrothermal systems", Journal of Geophysical Research: Solid Earth (1978–2012) **106**, B6, 10983–11000 (2001).

Chichagov, A. V., D. A. Varlamov, R. A. Dilanyan, T. N. Dokina, N. A. Drozhzhina, O. L. Samokhvalova and T. V. Ushakovskaya, "Mincryst: a crystallographic database for minerals, local and network (www) versions", Crystallography Reports **46**, 5, 876–879 (2001).

Choi, Y.-J., M. Cohen, R. Merk and D. Prialnik, "Long-term evolution of objects in the Kuiper belt zone: Effects of insolation and radiogenic heating", Icarus **160**, 2, 300–312 (2002).

Choukroun, M. and O. Grasset, "Thermodynamic data and modeling of the water and ammonia-water phase diagrams up to 2.2 GPa for planetary geophysics", Journal of Chemical Physics **133**, 14, 144502 (2010).

Christensen, N. I., "Elasticity of ultrabasic rocks", Journal of Geophysical Research **71**, 24, 5921–5931 (1966).

Christensen, N. I., "Poisson's ratio and crustal seismology", Journal of Geophysical Research: Solid Earth (1978–2012) **101**, B2, 3139–3156 (1996).

Christov, C., "Thermodynamic study of quaternary systems with participation of ammonium and sodium alums and chromium alums", Calphad **26**, 3, 341–352 (2002a).

Christov, C., "Thermodynamics of formation of ammonium, sodium and potassium alums and chromium alums", Calphad **26**, 1, 85–94 (2002b).

Chung, D. H., "Elasticity and equations of state of olivines in the Mg_2SiO_4–Fe_2SiO_4 system", Geophysical Journal International **25**, 5, 511–538 (1971).

Clauser, C. and E. Huenges, "Thermal conductivity of rocks and minerals", AGU reference shelf **3**, 105–126 (1995).

Clegg, S. L., P. Brimblecombe and A. S. Wexler, "Thermodynamic model of the system H^+–NH_4^+–Na^+–SO_4^{2-}–NO_3^-–Cl^-–H_2O at 298.15 K", Journal of Physical Chemistry A **102**, 12, 2155–2171 (1998a).

Clegg, S. L., P. Brimblecombe and A. S. Wexler, "Thermodynamic model of the system H^+–NH_4^+–SO_4^{2-}–NO_3^-–H_2O at tropospheric temperatures", Journal of Physical Chemistry A **102**, 12, 2137–2154 (1998b).

Cleveland, C. C. and D. Liptzin, "C: N: P stoichiometry in soil: is there a "Redfield ratio" for the microbial biomass?", Biogeochemistry **85**, 3, 235–252 (2007).

Clodic, L. and A. Meike, "Thermodynamics of calcium silicate hydrates – development of a database to model concrete dissolution at 25°C using the *EQ3/6* geochemical modeling code", Tech. rep., Lawrence Livermore National Laboratory (1997).

Cohen, B. A. and R. F. Coker, "Modeling of liquid water on CM meteorite parent bodies and implications for amino acid racemization", Icarus **145**, 2, 369–381 (2000).

Cohen, M., F. C. Witteborn, T. Roush, J. Bregman and D. Wooden, "Spectral irradiance calibration in the infrared. VIII. 5-14 micron spectroscopy of the asteroids Ceres, Vesta, and Pallas", The Astronomical Journal **115**, 4, 1671 (1998).

Collier, R. and J. Edmond, "The trace element geochemistry of marine biogenic particulate matter", Progress in Oceanography **13**, 2, 113–199 (1984).

Conrad, C. P. and P. Molnar, "The growth of Rayleigh–Taylor-type instabilities in the lithosphere for various rheological and density structures", Geophysical Journal International **129**, 1, 95–112 (1997).

Consolmagno, G. J. and J. S. Lewis, "The evolution of icy satellite interiors and surfaces", Icarus **34**, 2, 280–293 (1978).

Cook, J. C., S. J. Desch, T. L. Roush, C. A. Trujillo and T. R. Geballe, "Near-infrared spectroscopy of Charon: Possible evidence for cryovolcanism on Kuiper belt objects", The Astrophysical Journal **663**, 2, 1406–1419 (2007).

Corliss, J. B., "Hot springs and the origin of life", Nature **347**, 624 (1990).

Coughlin, R. T., S. Tonsager and E. J. McGroarty, "Quantitation of metal cations bound to membranes and extracted lipopolysaccharide of *Escherichia coli*", Biochemistry **22**, 8, 2002–2007 (1983).

Cox, A., E. L. Shock and J. R. Havig, "The transition to microbial photosynthesis in hot spring ecosystems", Chemical Geology **280**, 3, 344–351 (2011).

Crawford, G. D. and D. J. Stevenson, "Gas-driven water volcanism and the resurfacing of Europa", Icarus **73**, 1, 66–79 (1988).

Croft, S. K., J. S. Kargel, R. L. Kirk, J. M. Moore, P. M. Schenk and R. G. Strom, *The Geology of Triton*, pp. 879–947 (University of Arizona Press, 1995).

Croft, S. K., J. I. Lunine and J. Kargel, "Equation of state of ammonia-water liquid: Derivation and planetological applications", Icarus **73**, 2, 279–293 (1988).

Cruikshank, D. P., T. L. Roush, M. J. Bartholomew, T. R. Geballe, Y. J. Pendleton, S. M. White, J. F. Bell, J. K. Davies, T. C. Owen, C. De Bergh, D. J. Tholen, M. P. Bernstein, R. H. Brown, K. A. Trykak and C. Dalle Ore, "The composition of centaur 5145 Pholus", Icarus **135**, 2, 389–407 (1998).

Czechowski, L. and J. Leliwa-Kopystynski, "Convection driven by tidal and radiogenic heating in medium size icy satellites", Planetary and Space Science **53**, 7, 749–769 (2005).

Darling, W. G., "Hydrothermal hydrocarbon gases: 1, Genesis and geothermometry", Applied Geochemistry **13**, 7, 815–824 (1998).

de Baar, H. J. W. and J. La Roche, "Trace metals in the oceans: Evolution, biology and global change", in "Marine Science Frontiers for Europe", pp. 79–105 (Springer, 2003).

de Bergh, C., A. Delsanti, G. P. Tozzi, E. Dotto, A. Doressoundiram and M. A. Barucci, "The surface of the transneptunian object 90482 Orcus", Astronomy & Astrophysics **437**, 3, 1115–1120 (2005).

De Sanctis, M. C., M. T. Capria and A. Coradini, "Thermal Evolution and Differentiation of Edgeworth-Kuiper Belt Objects", Astronomical Journal **121**, 2792–2799 (2001).

De Sanctis, M. C., J.-P. Combe, E. Ammannito, E. Palomba, A. Longobardo, T. B. McCord, S. Marchi, F. Capaccioni, M. T. Capria, D. W. Mittlefehldt, C. M. Pieters, J. Sunshine, F. Tosi, F. Zambon, F. Carraro, S. Fonte, A. Frigeri, G. Magni, C. A. Raymond, C. T. Russell and D. Turrini, "Detection of widespread hydrated materials on Vesta by the VIR imaging spectrometer on board the *Dawn* mission", The Astrophysical Journal Letters **758**, 2, L36 (2012).

De Sanctis, M. C., A. Coradini, E. Ammannito, G. Filacchione, M. T. Capria, S. Fonte, G. Magni, A. Barbis, A. Bini, M. Dami, I. Ficai-Veltroni, G. Preti and the VIR team, "The VIR spectrometer", Space Science Reviews **163**, 329–369 (2011).

Delsanti, A., Merlin, F., Guilbert-Lepoutre, A., Bauer, J., Yang, B. and Meech, K. J., "Methane, ammonia, and their irradiation products at the surface of an intermediate-size KBO?", Astronomy & Astrophysics **520**, A40, 15 pp. (2010).

DeMartin, B., G. Hirth and B. Evans, "Experimental constraints on thermal cracking of peridotite at oceanic spreading centers", Mid-Ocean Ridges pp. 167–185 (2004).

DeSanctis, M. C. *et al.*, "Ammonia bearing species on Ceres: Implication on origin and evolution", in "AGU Fall Meeting Abstracts", (2015).

DeSantis, T. Z., P. Hugenholtz, N. Larsen, M. Rojas, E. L. Brodie, K. Keller, T. Huber, D. Dalevi, P. Hu and G. L. Andersen, "*Greengenes*, a chimera-checked 16S rRNA gene database and workbench compatible with ARB", Applied and Environmental Microbiology **72**, 7, 5069–5072 (2006).

Desch, S. J., "Density of Charon formed from a disk generated by the impact of partially differentiated bodies", Icarus **246**, 37–47 (2015).

Desch, S. J., J. C. Cook, T. Doggett and S. B. Porter, "Thermal evolution of Kuiper belt objects, with implications for cryovolcanism", Icarus **202**, 2, 694–714 (2009).

Desch, S. J. and N. Monga, "Jupiter's noble gas abundances may require external UV irradiation of the solar nebula", in "45th Lunar and Planetary Institute Science Conference Abstracts", p. 1725 (2014).

Desch, S. J. and M. Neveu, "Charon quandaries", in "DPS Meeting Abstracts", (2015a).

Desch, S. J. and M. Neveu, "On the origin of Haumea", in "46th Lunar and Planetary Science Conference Abstracts", vol. 46, p. 2082 (Lunar and Planetary Institute, 2015b).

Dick, J. M., "Calculation of the relative metastabilities of proteins using the *CHNOSZ* software package", Geochemical Transactions **9**, 10, 17 pp. (2008).

Dick, J. M., D. E. LaRowe and H. C. Helgeson, "Temperature, pressure, and electrochemical constraints on protein speciation: Group additivity calculation of the standard molal thermodynamic properties of ionized unfolded proteins", Biogeosciences **3**, 3, 311–336 (2006).

Dodson-Robinson, S. E., K. Willacy, P. Bodenheimer, N. J. Turner and C. A. Beichman, "Ice lines, planetesimal composition and solid surface density in the solar nebula", Icarus **200**, 2, 672–693 (2009).

Dombard, A. J. and P. M. Schenk, "The giant cue ball: Efficient relaxation of Ceres' craters", in "44th Lunar and Planetary Institute Science Conference Abstracts", p. 1798 (2013).

Drummond, J. D., B. Carry, W. J. Merline, C. Dumas, H. Hammel, S. Erard, A. Conrad, P. Tamblyn and C. R. Chapman, "Dwarf planet Ceres: Ellipsoid dimensions and rotational pole from Keck and VLT adaptive optics images", Icarus **236**, 28–37 (2014).

Drummond, J. D. and J. Christou, "Triaxial ellipsoid dimensions and rotational poles of seven asteroids from Lick Observatory adaptive optics images, and of Ceres", Icarus **197**, 2, 480–496 (2008).

Dumas, C., R. J. Terrile, R. H. Brown, G. Schneider and B. A. Smith, "Hubble space telescope NICMOS spectroscopy of Charon's leading and trailing hemispheres", The Astronomical Journal **121**, 2, 1163–1170 (2001).

Dupont, C. L., A. Butcher, R. E. Valas, P. E. Bourne and G. Caetano-Anollés, "History of biological metal utilization inferred through phylogenomic analysis of protein structures", Proceedings of the National Academy of Sciences **107**, 23, 10567–10572 (2010).

Dutrow, B. and D. Norton, "Evolution of fluid pressure and fracture propagation during contact metamorphism", Journal of Metamorphic Geology **13**, 6, 677–686 (1995).

Duxbury, N. S. and R. H. Brown, "The role of an internal heat source for the eruptive plumes on Triton", Icarus **125**, 1, 83–93 (1997).

Ehlmann, B. L., J. F. Mustard and S. L. Murchie, "Geologic setting of serpentine deposits on Mars", Geophysical Research Letters **37**, L06201, 5 pp. (2010).

Elderfield, H. and A. Schultz, "Mid-ocean ridge hydrothermal fluxes and the chemical composition of the ocean", Annual Review of Earth and Planetary Sciences **24**, 191–224 (1996).

Ellsworth, K. and G. Schubert, "Saturn's icy satellites: Thermal and structural models", Icarus **54**, 3, 490–510 (1983).

Elser, J. J., C. Acquisti and S. Kumar, "Stoichiogenomics: the evolutionary ecology of macromolecular elemental composition", Trends in Ecology & Evolution **26**, 1, 38–44 (2011).

Elser, J. J., W. F. Fagan, R. F. Denno, D. R. Dobberfuhl, A. Folarin, A. Huberty, S. Interlandi, S. S. Kilham, E. McCauley, K. L. Schulz, E. H. Siemann and R. W. Sterner, "Nutritional constraints in terrestrial and freshwater food webs", Nature **408**, 6812, 578–580 (2000).

Elser, J. J. and R. P. Hassett, "A stoichiometric analysis of the zooplankton–phytoplankton interaction in marine and freshwater ecosystems", Nature **370**, 211–213 (1994).

Endreß, M. and A. Bischoff, "Carbonates in CI chondrites: Clues to parent body evolution", Geochimica et Cosmochimica Acta **60**, 3, 489–507 (1996).

Engel, S., J. I. Lunine and D. L. Norton, "Silicate interactions with ammonia-water fluids on early Titan", Journal of Geophysical Research: Planets (1991–2012) **99**, E2, 3745–3752 (1994).

Epstein, W. and S. G. Schultz, "Cation transport in *Escherichia coli*. V. regulation of cation content", Journal of General Physiology **49**, 2, 221–234 (1965).

Escartin, J., G. Hirth and B. Evans, "Effects of serpentinization on the lithospheric strength and the style of normal faulting at slow-spreading ridges", Earth and Planetary Science Letters **151**, 3, 181–189 (1997a).

Escartin, J., G. Hirth and B. Evans, "Nondilatant brittle deformation of serpentinites: Implications for Mohr-Coulomb theory and the strength of faults", Journal of Geophysical Research **102**, B2, 2897–2913 (1997b).

Escartin, J., G. Hirth and B. Evans, "Strength of slightly serpentinized peridotites: Implications for the tectonics of oceanic lithosphere", Geology **29**, 11, 1023–1026 (2001).

Evans, A. G. and D. R. Clarke, "Residual stresses and microcracking induced by thermal contraction inhomogeneity", in "Thermal Stresses in Severe Environments", pp. 629–648 (Springer, 1980).

Evans, B. W., K. Hattori and A. Baronnet, "Serpentinite: What, why, where?", Elements **9**, 2, 99–106 (2013).

Facq, S., I. Daniel, G. Montagnac, H. Cardon and D. A. Sverjensky, "In situ Raman study and thermodynamic model of aqueous carbonate speciation in equilibrium with aragonite under subduction zone conditions", Geochimica et Cosmochimica Acta **132**, 375–390 (2014).

Fagents, S. A., "Considerations for effusive cryovolcanism on Europa: The post-*Galileo* perspective", Journal of Geophysical Research **108**, E12, 5139 (2003).

Fagerbakke, K. M., M. Heldal and S. Norland, "Content of carbon, nitrogen, oxygen, sulfur and phosphorus in native aquatic and cultured bacteria", Aquatic Microbial Ecology **10**, 1, 15–27 (1996).

Falkowski, P. G., "Evolution of the nitrogen cycle and its influence on the biological sequestration of CO_2 in the ocean", Nature **387**, 6630, 272–275 (1997).

Fanale, F. P. and J. R. Salvail, "The water regime of asteroid (1) Ceres", Icarus **82**, 1, 97–110 (1989).

Farmer, J. D., "Hydrothermal systems on Mars: an assessment of present evidence", in "Evolution of hydrothermal Earth (and Mars?)", pp. 273–299 (1996).

Farmer, J. D., "Hydrothermal systems: Doorways to early biosphere evolution", GSA Today **10**, 7, 1–9 (2000).

Farmer, J. D. and D. J. Des Marais, "Exploring for a record of ancient Martian life", Journal of Geophysical Research **104**, E11, 26977–26995 (1999).

Fisher, A. T., "Permeability within basaltic oceanic crust", Reviews of Geophysics **36**, 143–182 (1998).

Fomenkova, M. N., "On the organic refractory component of cometary dust", in "Composition and Origin of Cometary Materials", pp. 109–114 (Springer, 2000).

Fortes, A. D., P. M. Grindrod, S. K. Trickett and L. Vočadlo, "Ammonium sulfate on Titan: Possible origin and role in cryovolcanism", Icarus **188**, 1, 139–153 (2007).

Fortes, A. D., I. G. Wood, J. P. Brodholt and L. Vočadlo, "The structure, ordering and equation of state of ammonia dihydrate (NH_3 $2H_2O$)", Icarus **162**, 1, 59–73 (2003).

Fourqurean, J. W., J. C. Zieman and G. V. Powell, "Phosphorus limitation of primary production in Florida Bay: evidence from C: N: P ratios of the dominant seagrass *Thalassia testudinum*", Limnology and Oceanography **37**, 1, 162–171 (1992).

Fraústo da Silva, J. and R. J. P. Williams, *The Biological Chemistry of the Elements: the Inorganic Chemistry of Life, 2nd Edition* (Oxford University Press, 2001).

Fredrich, J. T. and T.-F. Wong, "Micromechanics of thermally induced cracking in three crustal rocks", Journal of Geophysical Research **91**, B12, 12743–12 (1986).

Fredriksson, K. and J. F. Kerridge, "Carbonates and sulfates in CI chondrites: Formation by aqueous activity on the parent body", Meteoritics **23**, 35–44 (1988).

Frew, R. D., D. A. Hutchins, S. Nodder, S. Sanudo-Wilhelmy, A. Tovar-Sanchez, K. Leblanc, C. E. Hare and P. W. Boyd, "Particulate iron dynamics during FeCycle in subantarctic waters southeast of New Zealand", Global Biogeochemical Cycles **20**, 1 (2006).

Frigstad, H., T. Andersen, R. G. J. Bellerby, A. Silyakova and D. O. Hessen, "Variation in the seston C: N ratio of the Arctic Ocean and pan-Arctic shelves", Journal of Marine Systems **129**, 214–223 (2014).

Funatsu, T., M. Seto, H. Shimada, K. Matsui and M. Kuruppu, "Combined effects of increasing temperature and confining pressure on the fracture toughness of clay bearing rocks", International Journal of Rock Mechanics and Mining Sciences **41**, 6, 927–938 (2004).

Geissler, P. E., "Cryovolcanism in the outer solar system", in "Encyclopedia of Volcanoes", edited by H. Sigurdsson, pp. 785–800 (Academic, 2000).

Gellert, R., J. L. Campbell, P. L. King, L. A. Leshin, G. W. Lugmair, J. G. Spray, S. W. Squyres and A. S. Yen, "The Alpha-Particle-X-Ray Spectrometer (APXS) for the Mars Science Laboratory (MSL) rover mission", in "40th Lunar and Planetary Science Conference Abstracts", p. 2364 (Lunar and Planetary Institute, 2009).

Germanovich, L. N., R. P. Lowell and D. K. Astakhov, "Temperature-dependent permeability and bifurcations in hydrothermal flow", Journal of Geophysical Research: Solid Earth (1978–2012) **106**, B1, 473–495 (2001).

Glass, J. B., F. Wolfe-Simon and A. D. Anbar, "Coevolution of metal availability and nitrogen assimilation in cyanobacteria and algae", Geobiology **7**, 2, 100–123 (2009).

Glein, C. R., "Noble gases, nitrogen, and methane from the deep interior to the atmosphere of Titan", Icarus **250**, 570–586 (2015).

Glein, C. R., J. A. Baross and J. H. Waite, "The pH of Enceladus' ocean", Geochimica et Cosmochimica Acta **162**, 202–219 (2015).

Glein, C. R., S. J. Desch and E. L. Shock, "The absence of endogenic methane on Titan and its implications for the origin of atmospheric nitrogen", Icarus **204**, 2, 637–644 (2009).

Glein, C. R. and E. L. Shock, "Sodium chloride as a geophysical probe of a subsurface ocean on Enceladus", Geophysical Research Letters **37**, 9, L09204 (2010).

Glein, C. R., M. Y. Zolotov and E. L. Shock, "The oxidation state of hydrothermal systems on early Enceladus", Icarus **197**, 1, 157–163 (2008).

Goguen, J. D., B. J. Buratti, R. H. Brown, R. N. Clark, P. D. Nicholson, M. M. Hedman, R. R. Howell, C. Sotin, D. P. Cruikshank, K. H. Baines, K. J. Lawrence, J. R. Spencer and D. G. Blackburn, "The temperature and width of an active fissure on Enceladus measured with *Cassini* VIMS during the 14 April 2012 South Pole flyover", Icarus **226**, 1, 1128–1137 (2013).

Goldfarb, M. S. and J. R. Delaney, "Response of two-phase fluids to fracture configurations within submarine hydrothermal systems", Journal of Geophysical Research **93**, B5, 4585–4594 (1988).

Goldman, J. C., J. J. McCarthy and D. G. Peavey, "Growth rate influence on the chemical composition of phytoplankton in oceanic waters", Nature **279**, 210–215 (1979).

Goldsby, D. L. and D. L. Kohlstedt, "Superplastic deformation of ice: Experimental observations", Journal of Geophysical Research **106**, B6, 11017–11030 (2001).

Goldspiel, J. M. and S. W. Squyres, "Groundwater sapping and valley formation on Mars", Icarus **148**, 1, 176–192 (2000).

Gooding, J. L. and M. E. Zolensky, "Thermal stability of tochilinite", in "18th Lunar and Planetary Science Conference Abstracts", p. 343 (1987).

Goodman, J. C. and E. Lenferink, "Numerical simulations of marine hydrothermal plumes for Europa and other icy worlds", Icarus **221**, 2, 970–983 (2012).

Goryniuk, M. C., B. A. Rivard and B. Jones, "The reflectance spectra of opal-A (0.5–25 μm) from the taupo volcanic zone: Spectra that may identify hydrothermal systems on planetary surfaces", Geophysical Research Letters **31**, 24, L24701 (2004).

Gounelle, M. and M. E. Zolensky, "A terrestrial origin for sulfate veins in CI1 chondrites", Meteoritics & Planetary Science **36**, 10, 1321–1329 (2001).

Gregorkiewitz, M., B. Lebech, M. Mellini and C. Viti, "Hydrogen positions and thermal expansion in lizardite-1 T from Elba: a low-temperature study using Rietveld refinement of neutron diffraction data", American Mineralogist **81**, 9, 1111–1116 (1996).

Griffith, A. A., "The phenomena of rupture and flow in solids", Philosophical Transactions of the Royal Society of London A **221**, 163–198 (1921).

Griffith, L. L. and E. L. Shock, "A geochemical model for the formation of hydrothermal carbonates on Mars", Nature **377**, 6548, 406–408 (1995).

Grimm, R. E. and H. Y. McSween, "Water and the thermal evolution of carbonaceous chondrite parent bodies", Icarus **82**, 2, 244–280 (1989).

Gu, C., Á. Somogyi, V. H. Wysocki and K. F. Medzihradszky, "Fragmentation of protonated oligopeptides XLDVLQ (X= L, H, K or R) by surface induced dissociation: additional evidence for the 'mobile proton' model", Analytica Chimica Acta **397**, 1, 247–256 (1999).

Guilbert-Lepoutre, A., Lasue, J., Federico, C., Coradini, A., Orosei, R. and Rosenberg, E. D., "New 3D thermal evolution model for icy bodies – application to transneptunian objects", Astronomy & Astrophysics **529**, A71 (2011).

Gulick, V. C., "Magmatic intrusions and a hydrothermal origin for fluvial valleys on Mars", Journal of Geophysical Research **103**, E8, 19365–19387 (1998).

Gunter, B. D., "C_1-C_4 hydrocarbons in hydrothermal gases", Geochimica et Cosmochimica Acta **42**, 1, 137–139 (1978).

Haar, L., J. S. Gallagher and G. S. Kell, *NBS-NRC Steam Tables: Thermodynamics And Transport Properties and Computer Programs for Vapor and Liquid States of Water in SI Units* (Taylor & Francis Group, 1984).

Haas, J. R., E. L. Shock and D. C. Sassani, "Rare earth elements in hydrothermal systems: Estimates of standard partial molal thermodynamic properties of aqueous complexes of the rare earth elements at high pressures and temperatures", Geochimica et Cosmochimica Acta **59**, 21, 4329–4350 (1995).

Han, L., R. P. Lowell and K. C. Lewis, "The dynamics of two-phase hydrothermal systems at a seafloor pressure of 25 MPa", Journal of Geophysical Research: Solid Earth (2013).

Hand, K. P. and R. W. Carlson, "Europa's surface color suggests an ocean rich with sodium chloride", Geophysical Research Letters **42**, 9, 3174–3178 (2015).

Hanowski, N. P. and A. J. Brearley, "Aqueous alteration of chondrules in the CM carbonaceous chondrite, Allan Hills 81002: Implications for parent body alteration", Geochimica et Cosmochimica Acta **65**, 3, 495–518 (2001).

Hansen, C. J., L. Esposito, A. Stewart, J. Colwell, A. Hendrix, W. Pryor, D. Shemansky and R. West, "Enceladus' water vapor plume", Science **311**, 5766, 1422–1425 (2006).

Haraguchi, H., "Metallomics as integrated biometal science", Journal of Analytical Atomic Spectrometry **19**, 1, 5–14 (2004).

Havig, J. R., *Geochemistry of Hydrothermal Biofilms: Composition of Biofilms in a Siliceous Sinter-Deposition Hot Spring*, Ph.D. thesis, Arizona State University (2009).

Havig, J. R., J. Raymond, D. R. Meyer-Dombard, N. Zolotova and E. L. Shock, "Merging isotopes and community genomics in a siliceous sinter-depositing hot spring", Journal of Geophysical Research: Biogeosciences (2005–2012) **116**, G1 (2011).

Hayba, D. O. and S. E. Ingebritsen, "The computer model *Hydrotherm*, a three-dimensional finite-difference model to simulate ground-water flow and heat transport in the temperature range of 0 to 1,200 degrees C", Tech. rep., USGS (1994).

Hecky, R. E., P. Campbell and L. L. Hendzel, "The stoichiometry of carbon, nitrogen, and phosphorus in particulate matter of lakes and oceans", Limnology and Oceanography **38**, 4, 709–724 (1993).

Hedman, M. M., C. M. Gosmeyer, P. D. Nicholson, C. Sotin, R. H. Brown, R. N. Clark, K. H. Baines, B. J. Buratti and M. R. Showalter, "An observed correlation between plume activity and tidal stresses on Enceladus", Nature **500**, 7461, 182–184 (2013).

Heldal, M., D. Scanlan, S. Norland, F. Thingstad and N. Mann, "Elemental composition of single cells of various strains of marine *Prochlorococcus* and *Synechococcus* using X-ray microanalysis", Limnology and Oceanography **48**, 5, 1732–1743 (2003).

Helgeson, H. C., "Thermodynamics of hydrothermal systems at elevated temperatures and pressures", American Journal of Science **267**, 7, 729–804 (1969).

Helgeson, H. C., "Summary and critique of the thermodynamic properties of rock-forming minerals", American Journal of Science **278**, 1–229 (1978).

Helgeson, H. C., D. H. Kirkham and G. C. Flowers, "Theoretical prediction of the thermodynamic behavior of aqueous electrolytes by high pressures and temperatures; IV, Calculation of activity coefficients, osmotic coefficients, and apparent molal and standard and relative partial molal properties to 600 degrees C and 5kb", American Journal of Science **281**, 10, 1249–1516 (1981).

Helgeson, H. C., C. E. Owens, A. M. Knox and L. Richard, "Calculation of the standard molal thermodynamic properties of crystalline, liquid, and gas organic molecules at high temperatures and pressures", Geochimica et Cosmochimica Acta **62**, 6, 985–1081 (1998).

Helgeson, H. C., L. Richard, W. F. McKenzie, D. L. Norton and A. Schmitt, "A chemical and thermodynamic model of oil generation in hydrocarbon source rocks", Geochimica et Cosmochimica Acta **73**, 3, 594–695 (2009).

Hezel, D. C., S. S. Russell, A. J. Ross and A. T. Kearsley, "Modal abundances of CAIs: Implications for bulk chondrite element abundances and fractionations", Meteoritics & Planetary Science **43**, 11, 1879–1894 (2008).

Hilairet, N., I. Daniel and B. Reynard, "P–V equations of state and the relative stabilities of serpentine varieties", Physics and Chemistry of Minerals **33**, 8-9, 629–637 (2006).

Hillebrand, H. and U. Sommer, "The nutrient stoichiometry of benthic microalgal growth: Redfield proportions are optimal", Limnology and Oceanography **44**, 2, 440–446 (1999).

Hirth, G. and S. Guillot, "Rheology and tectonic significance of serpentinite", Elements **9**, 2, 107–113 (2013).

Hirth, G. and D. L. Kohlstedt, "Experimental constraints on the dynamics of the partially molten upper mantle: Deformation in the diffusion creep regime", Journal of Geophysical Research: Solid Earth (1978–2012) **100**, B2, 1981–2001 (1995).

Ho, T.-Y., A. Quigg, Z. V. Finkel, A. J. Milligan, K. Wyman, P. G. Falkowski and F. M. M. Morel, "The elemental composition of some marine phytoplankton", Journal of Phycology **39**, 6, 1145–1159 (2003).

Holm, N. G. and E. Andersson, "Hydrothermal simulation experiments as a tool for studies of the origin of life on Earth and other terrestrial planets: A review", Astrobiology **5**, 4, 444–460 (2005).

Holm, N. G., C. Oze, O. Mousis, J. Waite and A. Guilbert-Lepoutre, "Serpentinization and the formation of H_2 and CH_4 on celestial bodies (planets, moons, comets)", Astrobiology **15**, 7, 587–600 (2015).

Holmsgaard, P. N., A. Norman, S. C. Hede, P. H. B. Poulsen, W. A. Al-Soud, L. H. Hansen and S. J. Sørensen, "Bias in bacterial diversity as a result of Nycodenz extraction from bulk soil", Soil Biology and Biochemistry **43**, 10, 2152–2159 (2011).

Holten, V., C. E. Bertrand, M. A. Anisimov and J. V. Sengers, "Thermodynamics of supercooled water", Journal of Chemical Physics **136**, 094507, 18 pp. (2012).

Horai, K.-I., "Thermal conductivity of rock-forming minerals", Journal of Geophysical Research **76**, 5, 1278–1308 (1971).

Howard, K. T., G. K. Benedix, P. A. Bland and G. Cressey, "Modal mineralogy of CM2 chondrites by X-ray diffraction (PSD-XRD). Part 1: Total phyllosilicate abundance and the degree of aqueous alteration", Geochimica et Cosmochimica Acta **73**, 15, 4576–4589 (2009).

Howard, K. T., G. K. Benedix, P. A. Bland and G. Cressey, "Modal mineralogy of CM chondrites by X-ray diffraction (PSD-XRD): Part 2. degree, nature and settings of aqueous alteration", Geochimica et Cosmochimica Acta **75**, 10, 2735–2751 (2011).

Hsu, H.-W., F. Postberg, Y. Sekine, T. Shibuya, S. Kempf, M. Horányi, A. Juhász, N. Altobelli, K. Suzuki, Y. Masaki, T. Kuwatani, S. Tachibana, S.-i. Sirono, G. Moragas-Klostermeyer and R. Srama, "Ongoing hydrothermal activities within Enceladus", Nature **519**, 7542, 207–210 (2015).

Hudson, R. J. M. and F. M. M. Morel, "Trace metal transport by marine microorganisms: implications of metal coordination kinetics", Deep Sea Research Part I: Oceanographic Research Papers **40**, 1, 129–150 (1993).

Hussmann, H., F. Sohl and T. Spohn, "Subsurface oceans and deep interiors of medium-sized outer planet satellites and large trans-neptunian objects", Icarus **185**, 1, 258–273 (2006).

Hyman, M. and M. W. Rowe, "Magnetite in CI chondrites", Journal of Geophysical Research: Solid Earth (1978–2012) **88**, S02, A736–A740 (1983).

Iess, L., R. A. Jacobson, M. Ducci, D. J. Stevenson, J. I. Lunine, J. W. Armstrong, S. W. Asmar, P. Racioppa, N. J. Rappaport and P. Tortora, "The tides of Titan", Science **337**, 6093, 457–459 (2012).

Iess, L., D. J. Stevenson, M. Parisi, D. Hemingway, R. A. Jacobson, J. I. Lunine, F. Nimmo, J. W. Armstrong, S. W. Asmar, M. Ducci and P. Tortora, "The gravity field and interior structure of Enceladus", Science **344**, 6179, 78–80 (2014).

Ingebritsen, S. E. and M. S. Appold, "The physical hydrogeology of ore deposits", Economic Geology **107**, 4, 559–584 (2012).

Ingebritsen, S. E., S. Geiger, S. Hurwitz and T. Driesner, "Numerical simulation of magmatic hydrothermal systems", Reviews of Geophysics **48**, 1 (2010).

Ingersoll, A. P. and K. A. Tryka, "Triton's plumes: The dust devil hypothesis", Science **250**, 4979, 435–437 (1990).

Jackson, K. J. and H. C. Helgeson, "Chemical and thermodynamic constraints on the hydrothermal transport and deposition of tin; II, Interpretation of phase relations in the Southeast Asian tin belt", Economic Geology **80**, 5, 1365–1378 (1985).

Jewitt, D. C. and J. Luu, "Crystalline water ice on the Kuiper belt object (50000) Quaoar", Nature **432**, 7018, 731–733 (2004).

Johnson, C. A. and M. Prinz, "Carbonate compositions in CM and CI chondrites and implications for aqueous alteration", Geochimica et Cosmochimica Acta **57**, 12, 2843–2852 (1993).

Johnson, J. W., E. H. Oelkers and H. C. Helgeson, "*SUPCRT92*: A software package for calculating the standard molal thermodynamic properties of minerals, gases, aqueous species, and reactions from 1 to 5000 bar and 0 to 1000 C", Computers & Geosciences **18**, 7, 899–947 (1992).

Jones, G. D., F. F. Whitaker, P. L. Smart and W. E. Sanford, "Numerical analysis of seawater circulation in carbonate platforms: II. The dynamic interaction between geothermal and brine reflux circulation", American Journal of Science **304**, 3, 250–284 (2004).

Jones, G. E., L. G. Royle and L. Murray, "Cationic composition of 22 species of bacteria grown in seawater medium", Applied and Environmental Microbiology **38**, 5, 800–805 (1979).

Kallmeyer, J., D. C. Smith, A. J. Spivack and S. D'Hondt, "New cell extraction procedure applied to deep subsurface sediments", Limnology and Oceanography: Methods **6**, 6, 236–245 (2008).

Kargel, J. S., "Brine volcanism and the interior structures of asteroids and icy satellites", Icarus **94**, 2, 368–390 (1991).

Kargel, J. S., "Ammonia-water volcanism on icy satellites: Phase relations at 1 atmosphere", Icarus **100**, 2, 556–574 (1992).

Kargel, J. S., S. K. Croft, J. I. Lunine and J. S. Lewis, "Rheological properties of ammonia-water liquids and crystal-liquid slurries: Planetological applications", Icarus **89**, 1, 93–112 (1991).

Kargel, J. S., J. Z. Kaye, J. W. Head, G. M. Marion, R. Sassen, J. K. Crowley, O. P. Ballesteros, S. A. Grant and D. L. Hogenboom, "Europa's crust and ocean: Origin, composition, and the prospects for life", Icarus **148**, 1, 226–265 (2000).

Kasting, J. F., "Earth's early atmosphere", Science **259**, 5097, 920–926 (1993).

Kelemen, P. B. and G. Hirth, "Reaction-driven cracking during retrograde metamorphism: Olivine hydration and carbonation", Earth and Planetary Science Letters **345**, 81–89 (2012).

Kelley, D. S. and J. R. Delaney, "Two-phase separation and fracturing in mid-ocean ridge gabbros at temperatures greater than 700 C", Earth and Planetary Science Letters **83**, 1, 53–66 (1987).

Kelley, D. S., K. M. Gillis and G. Thompson, "Fluid evolution in submarine magma-hydrothermal systems at the mid-Atlantic ridge", Journal of Geophysical Research: Solid Earth (1978–2012) **98**, B11, 19579–19596 (1993).

Kelley, D. S., J. A. Karson, G. L. Früh-Green, D. R. Yoerger, T. M. Shank, D. A. Butterfield, J. M. Hayes, M. O. Schrenk, E. J. Olson, G. Proskurowski, M. Jakuba, A. Bradley, B. Larson, K. Ludwig, D. Glickson, K. Buckman, A. S. Bradley, W. J. Brazelton, K. Roe, M. J. Elend, A. Delacour, S. M. Bernasconi, M. D. Lilley, J. A. Baross, R. E. Summons and S. P. Sylva, "A serpentinite-hosted ecosystem: The Lost City hydrothermal field", Science **307**, 5714, 1428–1434 (2005).

Kelley, K. K., *High-temperature heat-content, heat-capacity, and entropy data for the elements and inorganic compounds* (US Government Printing Office, 1960).

Kenyon, S. J. and B. C. Bromley, "Coagulation calculations of icy planet formation at 15-150 AU: A correlation between the maximum radius and the slope of the size distribution for trans-neptunian objects", The Astronomical Journal **143**, 3, 63 (2012).

Kenyon, S. J., B. C. Bromley, D. P. O'Brien and D. R. Davis, "Formation and collisional evolution of Kuiper belt objects", in "The Solar System Beyond Neptune", pp. 293–314 (University of Arizona Press, 2008).

Kerridge, J. F., J. D. Macdougall and K. Marti, "Clues to the origin of sulfide minerals in CI chondrites", Earth and Planetary Science Letters **43**, 3, 359–367 (1979).

Khurana, K. K., M. G. Kivelson, D. J. Stevenson, G. Schubert, C. T. Russell, R. J. Walker and C. Polanskey, "Induced magnetic fields as evidence for subsurface oceans in Europa and Callisto", Nature **395**, 6704, 777–780 (1998).

King, T. V., R. N. Clark, W. M. Calvin, D. M. Sherman and R. H. Brown, "Evidence for ammonium-bearing minerals on Ceres", Science **255**, 5051, 1551–1553 (1992).

Kirk, R. L., L. A. Soderblom, R. H. Brown, S. W. Kieffer and J. S. Kargel, "Triton's plumes: discovery, characteristics, and models", in "Neptune and Triton", vol. 1, pp. 949–989 (University of Arizona Press, 1995).

Kirk, R. L. and D. J. Stevenson, "Thermal evolution of a differentiated Ganymede and implications for surface features", Icarus **69**, 1, 91–134 (1987).

Kivelson, M. G., K. K. Khurana, C. T. Russell, M. Volwerk, R. J. Walker and C. Zimmer, "*Galileo* magnetometer measurements: A stronger case for a subsurface ocean at Europa", Science **289**, 5483, 1340–1343 (2000).

Kivelson, M. G., K. K. Khurana and M. Volwerk, "The permanent and inductive magnetic moments of Ganymede", Icarus **157**, 2, 507–522 (2002).

Klausmeier, C. A., E. Litchman, T. Daufresne and S. A. Levin, "Optimal nitrogen-to-phosphorus stoichiometry of phytoplankton", Nature **429**, 6988, 171–174 (2004).

Klinger, J., "Influence of a phase transition of ice on the heat and mass balance of comets", Science **209**, 271 (1980).

Koerselman, W. and A. F. M. Meuleman, "The vegetation N: P ratio: a new tool to detect the nature of nutrient limitation", Journal of Applied Ecology **33**, 6, 1441–1450 (1996).

Kohlstedt, D. L., B. Evans and S. J. Mackwell, "Strength of the lithosphere: Constraints imposed by laboratory experiments", Journal of Geophysical Research **100**, B9, 17587–17602 (1995).

Konhauser, K. O., E. Pecoits, S. V. Lalonde, D. Papineau, E. G. Nisbet, M. E. Barley, N. T. Arndt, K. Zahnle and B. S. Kamber, "Oceanic nickel depletion and a methanogen famine before the Great Oxidation Event", Nature **458**, 7239, 750–753 (2009).

Korenaga, J. and S.-I. Karato, "A new analysis of experimental data on olivine rheology", Journal of Geophysical Research: Solid Earth (1978–2012) **113**, B2 (2008).

Kozich, J. J., S. L. Westcott, N. T. Baxter, S. K. Highlander and P. D. Schloss, "Development of a dual-index sequencing strategy and curation pipeline for analyzing amplicon sequence data on the MiSeq Illumina sequencing platform", Applied and Environmental Microbiology **79**, 17, 5112–5120 (2013).

Kress, M. E., A. G. G. M. Tielens and M. Frenklach, "The 'soot line': Destruction of presolar polycyclic aromatic hydrocarbons in the terrestrial planet-forming region of disks", Advances in Space Research **46**, 1, 44–49 (2010).

Krichevsky, I. R. and J. S. Kasarnovsky, "Thermodynamical calculations of solubilities of nitrogen and hydrogen in water at high pressures", Journal of the American Chemical Society **57**, 11, 2168–2171 (1935).

Kumazawa, M. and O. L. Anderson, "Elastic moduli, pressure derivatives, and temperature derivatives of single-crystal olivine and single-crystal forsterite", Journal of Geophysical Research **74**, 25, 5961–5972 (1969).

Küppers, M., L. O'Rourke, D. Bockelée-Morvan, V. Zakharov, S. Lee, P. von Allmen, B. Carry, D. Teyssier, A. Marston, T. Müller, J. Crovisier, M. A. Barucci and R. Moreno, "Localized sources of water vapour on the dwarf planet (1) Ceres", Nature **505**, 7484, 525–527 (2014).

Lane, T. W., M. A. Saito, G. N. George, I. J. Pickering, R. C. Prince and F. M. M. Morel, "Biochemistry: a cadmium enzyme from a marine diatom", Nature **435**, 7038, 42 (2005).

Lapwood, E. R., "Convection of a fluid in a porous medium", Mathematical Proceedings of the Cambridge Philosophical Society **44**, 508–521 (1948).

Larson, H. P., M. A. Feierberg, U. Fink and H. A. Smith, "Remote spectroscopic identification of carbonaceous chondrite mineralogies: Applications to Ceres and Pallas", Icarus **39**, 2, 257–271 (1979).

Lauretta, D. S. and K. Lodders, "The cosmochemical behavior of beryllium and boron", Earth and Planetary Science Letters **146**, 1, 315–327 (1997).

Le Corre, L., S. Le Mouélic, C. Sotin, J.-P. Combe, S. Rodriguez, J. W. Barnes, R. H. Brown, B. J. Buratti, R. Jaumann, J. Soderblom, L. A. Soderblom, R. Clark, K. H. Baines and P. D. Nicholson, "Analysis of a cryolava flow-like feature on Titan", Planetary and Space Science **57**, 7, 870–879 (2009).

Le Corre, L., A. Nathues, V. Reddy, M. Neveu, S. J. Desch, J. C. Castillo-Rogez, B. E. Schmidt, J.-Y. Li, M. V. Sykes, T. Platz, M. Hoffman, M. Schaefer, C. T. Russel and C. A. Raymond, "Are there cryovolcanoes on Ceres?", in "AGU Fall Meeting Abstracts", (2015).

Le Ravalec, M. and Y. Guéguen, "Permeability models for heated saturated igneous rocks", Journal of Geophysical Research: Solid Earth (1978–2012) **99**, B12, 24251–24261 (1994).

Lebofsky, L. A., M. A. Feierberg, A. T. Tokunaga, H. P. Larson and J. R. Johnson, "The 1.7-to 4.2-μm spectrum of asteroid 1 Ceres: evidence for structural water in clay minerals", Icarus **48**, 3, 453–459 (1981).

Lee, Z. M. P., L. Steger, J. R. Corman, M. Neveu, A. T. Poret-Peterson, V. Souza and J. J. Elser, "Response of a stoichiometrically imbalanced ecosystem to manipulation of nutrient supplies and ratios", PLoS ONE **10**, 4 (2015).

Leliwa-Kopystynski, J., M. Maruyama and T. Nakajima, "The water-ammonia phase diagram up to 300 MPa: Application to icy satellites", Icarus **159**, 2, 518–528 (2002).

Lemmon, E. W., M. L. Huber and M. O. McLinden, *NIST Reference Fluid Thermodynamic and Transport Properties - REFPROP* (NIST, 2010).

Levison, H. F., A. Morbidelli, C. VanLaerhoven, R. Gomes and K. Tsiganis, "Origin of the structure of the Kuiper belt during a dynamical instability in the orbits of Uranus and Neptune", Icarus **196**, 1, 258–273 (2008).

Levitus, S., M. E. Conkright, J. L. Reid, R. G. Najjar and A. Mantyla, "Distribution of nitrate, phosphate and silicate in the world oceans", Progress in Oceanography **31**, 3, 245–273 (1993).

Lewis, J. S., "Satellites of the outer planets: Their physical and chemical nature", Icarus **15**, 2, 174–185 (1971).

Li, J.-Y., L. A. McFadden, J. W. Parker, E. F. Young, S. A. Stern, P. C. Thomas, C. T. Russell and M. V. Sykes, "Photometric analysis of 1 Ceres and surface mapping from HST observations", Icarus **182**, 1, 143–160 (2006).

Lindahl, V. and L. R. Bakken, "Evaluation of methods for extraction of bacteria from soil", FEMS Microbiology Ecology **16**, 2, 135–142 (1995).

Liu, H. W. and K. J. Miller, "Fracture toughness of fresh-water ice", Journal of Glaciology **22**, 135–143 (1979).

Lodders, K., "Solar system abundances and condensation temperatures of the elements", The Astrophysical Journal **591**, 2, 1220–1247 (2003).

Lopes, R. M. C., K. L. Mitchell, E. R. Stofan, J. I. Lunine, R. Lorenz, F. Paganelli, R. L. Kirk, C. A. Wood, S. D. Wall, L. E. Robshaw, A. D. Fortes, C. D. Neish, J. Radebaugh, E. Reffet, S. J. Ostro, C. Elachi, M. D. Allison, Y. Anderson, R. Boehmer, G. Boubin, P. Callahan, P. Encrenaz, E. Flamini, G. Francescetti, Y. Gim, G. Hamilton, S. Hensley, M. A. Janssen, W. T. K. Johnson, K. Kelleher, D. O. Muhleman, G. Ori, R. Orosei, G. Picardi, F. Posa, L. E. Roth, R. Seu, S. Shaffer, L. A. Soderblom, B. Stiles, S. Vetrella, R. D. West, L. Wye and H. A. Zebker, "Cryovolcanic features on Titan's surface as revealed by the *Cassini* Titan Radar Mapper", Icarus **186**, 2, 395–412 (2007).

Lunine, J. I. and D. J. Stevenson, "Thermodynamics of clathrate hydrate at low and high pressures with application to the outer solar system", The Astrophysical Journal **58**, 493–531 (1985).

Lutz, R. A., T. M. Shank, D. J. Fornari, R. M. Haymon, M. D. Lilley, K. L. Vondamm and D. Desbruyeres, "Rapid growth at deep-sea vents", Nature **371**, 6499, 663–664 (1994).

MacDonald, A. and W. Fyfe, "Rate of serpentinization in seafloor environments", Tectonophysics **116**, 1, 123–135 (1985).

Madigan, M. T., J. M. Martinko, D. A. Stahl and D. P. Clark, "Phototrophy, chemolithotrophy, and major biosyntheses", in "Brock Biology of Microorganisms, 13th Edition", pp. 340–371 (Pearson Education, 2012).

Malamud, U. and D. Prialnik, "Modeling serpentinization: Applied to the early evolution of Enceladus and Mimas", Icarus **225**, 1, 763–774 (2013).

Malamud, U. and D. Prialnik, "Modeling Kuiper belt objects Charon, Orcus and Salacia by means of a new equation of state for porous icy bodies", Icarus **246**, 21–36 (2015).

Manga, M. and C.-Y. Wang, "Pressurized oceans and the eruption of liquid water on europa and enceladus", Geophysical Research Letters **34**, 7, L07202 (2007).

Mangan, M. and T. Sisson, "Delayed, disequilibrium degassing in rhyolite magma: decompression experiments and implications for explosive volcanism", Earth and Planetary Science Letters **183**, 3, 441–455 (2000).

Maret, S., E. Bergin and C. Lada, "A low fraction of nitrogen in molecular form in a dark cloud", Nature **442**, 7101, 425–427 (2006).

Marion, G. M., "Carbonate mineral solubility at low temperatures in the Na–K–Mg–Ca–H–Cl–SO_4–OH–HCO_3–CO_3–CO_2–H_2O system", Geochimica et Cosmochimica Acta **65**, 12, 1883–1896 (2001).

Marion, G. M., "A molal-based model for strong acid chemistry at low temperatures ($<$ 200 to 298 K)", Geochimica et Cosmochimica Acta **66**, 14, 2499–2516 (2002).

Marion, G. M., D. C. Catling and J. S. Kargel, "Modeling aqueous ferrous iron chemistry at low temperatures with application to Mars", Geochimica et Cosmochimica Acta **67**, 22, 4251–4266 (2003).

Marion, G. M., D. C. Catling, K. J. Zahnle and M. W. Claire, "Modeling aqueous perchlorate chemistries with applications to Mars", Icarus **207**, 2, 675–685 (2010).

Marion, G. M., J. K. Crowley, B. J. Thomson, J. S. Kargel, N. T. Bridges, S. J. Hook, A. Baldridge, A. J. Brown, B. R. da Luz and C. de Souza Filho, "Modeling aluminum–silicon chemistries and application to Australian acidic playa lakes as analogues for Mars", Geochimica et Cosmochimica Acta **73**, 11, 3493–3511 (2009).

Marion, G. M. and R. E. Farren, "Mineral solubilities in the Na–K–Mg–Ca–Cl–SO_4–H_2O system: A re-evaluation of the sulfate chemistry in the Spencer-Møller-Weare model", Geochimica et Cosmochimica Acta **63**, 9, 1305–1318 (1999).

Marion, G. M., J. S. Kargel and D. C. Catling, "Modeling ferrous–ferric iron chemistry with application to martian surface geochemistry", Geochimica et Cosmochimica Acta **72**, 1, 242–266 (2008).

Marion, G. M., J. S. Kargel, D. C. Catling and S. D. Jakubowski, "Effects of pressure on aqueous chemical equilibria at subzero temperatures with applications to Europa", Geochimica et Cosmochimica Acta **69**, 2, 259–274 (2005).

Marion, G. M., J. S. Kargel, D. C. Catling and J. I. Lunine, "Modeling ammonia–ammonium aqueous chemistries in the solar system's icy bodies", Icarus **220**, 2, 932–946 (2012).

Marion, G. M., J. S. Kargel, D. C. Catling and J. I. Lunine, "Modeling nitrogen-gas,-liquid,-solid chemistries at low temperatures (173–298K) with applications to Titan", Icarus **236**, 1–8 (2014).

Maron, P.-A., H. Schimann, L. Ranjard, E. Brothier, A.-M. Domenach, R. Lensi and S. Nazaret, "Evaluation of quantitative and qualitative recovery of bacterial communities from different soil types by density gradient centrifugation", European Journal of Soil Biology **42**, 2, 65–73 (2006).

Martin, J. H. and G. A. Knauer, "The elemental composition of plankton", Geochimica et Cosmochimica Acta **37**, 7, 1639–1653 (1973).

Martin, J. T. and R. P. Lowell, "Precipitation of quartz during high-temperature, fracture-controlled hydrothermal upflow at ocean ridges: Equilibrium versus linear kinetics", Journal of Geophysical Research: Solid Earth (1978–2012) **105**, B1, 869–882 (2000).

Martiny, A. C., C. T. A. Pham, F. W. Primeau, J. A. Vrugt, J. K. Moore, S. A. Levin and M. W. Lomas, "Strong latitudinal patterns in the elemental ratios of marine plankton and organic matter", Nature Geoscience **6**, 4, 279–283 (2013).

Masella, A. P., A. K. Bartram, J. M. Truszkowski, D. G. Brown and J. D. Neufeld, "*PANDAseq*: paired-end assembler for illumina sequences", BMC Bioinformatics **13**, 1, 31 (2012).

Matear, R. J. and A. C. Hirst, "Long-term changes in dissolved oxygen concentrations in the ocean caused by protracted global warming", Global Biogeochemical Cycles **17**, 4 (2003).

Matson, D. L., J. C. Castillo, J. Lunine and T. V. Johnson, "Enceladus' plume: Compositional evidence for a hot interior", Icarus **187**, 2, 569–573 (2007).

Matson, D. L., J. C. Castillo-Rogez, A. G. Davies and T. V. Johnson, "Enceladus: A hypothesis for bringing both heat and chemicals to the surface", Icarus **221**, 1, 53–62 (2012).

McCollom, T. M. and E. L. Shock, "Geochemical constraints on chemolithoautotrophic metabolism by microorganisms in seafloor hydrothermal systems", Geochimica et Cosmochimica Acta **61**, 20, 4375–4391 (1997).

McComas, D., F. Allegrini, F. Bagenal, P. Casey, P. Delamere, D. Demkee, G. Dunn, H. Elliott, J. Hanley, K. Johnson, J. Langle, G. Miller, S. Pope, M. Reno, B. Rodriguez, N. Schwadron, P. Valek and S. Weidner, "The solar wind around Pluto (SWAP) instrument aboard *New Horizons*", Space Science Reviews **140**, 261–313 (2008).

McCord, T. B., J. C. Castillo-Rogez and A. S. Rivkin, "Ceres: its origin, evolution and structure and *Dawn*'s potential contribution", in "The *Dawn* Mission to Minor Planets 4 Vesta and 1 Ceres", pp. 63–76 (Springer, 2012).

McCord, T. B., G. B. Hansen, F. P. Fanale, R. W. Carlson, D. L. Matson, T. V. Johnson, W. D. Smythe, J. K. Crowley, P. D. Martin, A. Ocampo, C. A. Hibbitts, J. C. Granahan and the NIMS Team, "Salts on Europa's surface detected by *Galileo*'s Near Infrared Mapping Spectrometer", Science **280**, 5367, 1242–1245 (1998).

McCord, T. B., G. B. Hansen and C. A. Hibbitts, "Hydrated salt minerals on Ganymede's surface: Evidence of an ocean below", Science **292**, 5521, 1523–1525 (2001).

McCord, T. B., G. B. Hansen, D. L. Matson, T. V. Johnson, J. K. Crowley, F. P. Fanale, R. W. Carlson, W. D. Smythe, P. D. Martin, C. A. Hibbitts, J. C. Granahan and A. Ocampo, "Hydrated salt minerals on Europa's surface from the *Galileo* near-infrared mapping spectrometer (NIMS) investigation", Journal of Geophysical Research **104**, E5, 11827–11851 (1999).

McCord, T. B. and C. Sotin, "Ceres: Evolution and current state", Journal of Geophysical Research (Planets) **110**, 5009 (2005).

McCord, T. B., G. Teeter, G. B. Hansen, M. T. Sieger and T. M. Orlando, "Brines exposed to Europa surface conditions", Journal of Geophysical Research **107**, E1, 5004 (2002).

McKay, C. P., A. D. Anbar, C. Porco and P. Tsou, "Follow the plume: The habitability of Enceladus", Astrobiology **14**, 4, 352–355 (2014).

McKinnon, W., "Where did ceres accrete?", LPI Contributions **1667**, 6475 (2012).

McKinnon, W. B., "Mystery of Callisto: Is it undifferentiated?", Icarus **130**, 2, 540–543 (1997).

McKinnon, W. B., "On the initial thermal evolution of Kuiper belt objects", in "Asteroids, Comets, and Meteors: ACM 2002", vol. 500, pp. 29–38 (2002).

McKinnon, W. B., "Could Ceres be a refugee from the Kuiper belt?", in "Asteroids, Comets, Meteors", p. 8389 (2008).

McKinnon, W. B., D. Prialnik, S. A. Stern and A. Coradini, "Structure and evolution of Kuiper belt objects and dwarf planets", in "The Solar System Beyond Neptune", pp. 213–241 (University of Arizona Press, 2008).

McKinnon, W. B. and M. E. Zolensky, "Sulfate content of Europa's ocean and shell: Evolutionary considerations and some geological and astrobiological implications", Astrobiology **3**, 4, 879–897 (2003).

McMurdie, P. J. and S. Holmes, "*phyloseq*: an *R* package for reproducible interactive analysis and graphics of microbiome census data", PLoS ONE **8**, 4, e61217 (2013).

McNutt, R. L., S. A. Livi, R. S. Gurnee, M. E. Hill, K. A. Cooper, G. B. Andrews, E. P. Keath, S. M. Krimigis, D. G. Mitchell, B. Tossman, F. Bagenal, J. D. Boldt, W. Bradley, W. S. Devereux, G. C. Ho, S. E. Jaskulek, T. W. Lefevere, H. Malcom, G. A. Marcus, J. R. Hayes, G. T. Moore, M. E. Perry, B. D. Williams, P. Wilson, L. E. Brown, M. B. Kusterer and J. D. Vandegriff, "The Pluto energetic particle spectrometer science investigation (PEPSSI) on the *New Horizons* mission", Space Science Reviews **140**, 1-4, 315–385 (2008).

McSween, H. Y., "Aqueous alteration in carbonaceous chondrites: Mass balance constraints on matrix mineralogy", Geochimica et Cosmochimica Acta **51**, 9, 2469–2477 (1987).

McSween, H. Y., M. E. Bennett and E. Jarosewich, "The mineralogy of ordinary chondrites and implications for asteroid spectrophotometry", Icarus **90**, 1, 107–116 (1991).

McSween, H. Y. and the *Dawn* Science Team, "The reflectance spectrum of synthetic tochilinite", in "78th Annual Meeting of the Meteoritical Society Abstracts", p. 5049 (The Meteoritical Society, 2015).

Melosh, H. J., A. G. Ekholm, A. P. Showman and R. D. Lorenz, "The temperature of Europa's subsurface water ocean", Icarus **168**, 2, 498–502 (2004).

Merlin, F., M. A. Barucci, C. de Bergh, F. E. DeMeo, A. Alvarez-Candal, C. Dumas and D. P. Cruikshank, "Chemical and physical properties of the variegated Pluto and Charon surfaces", Icarus **210**, 2, 930–943 (2010).

Meslin, P.-Y., O. Gasnault, O. Forni, S. Schröder, A. Cousin, G. Berger, S. M. Clegg, J. Lasue, S. Maurice, V. Sautter, S. Le Mouélic, R. C. Wiens, C. Fabre, W. Goetz, D. Bish, N. Mangold, B. Ehlmann, N. Lanza, A.-M. Harri, R. Anderson, E. Rampe, T. H. McConnochie, P. Pinet, D. Blaney, R. Léveillé, D. Archer, B. Barraclough, S. Bender, D. Blake, J. G. Blank, N. Bridges, B. C. Clark, L. DeFlores, D. Delapp, G. Dromart, M. D. Dyar, M. Fisk, B. Gondet, J. Grotzinger, K. Herkenhoff, J. Johnson, J.-L. Lacour, Y. Langevin, L. Leshin, E. Lewin, M. B. Madsen, N. Melikechi, A. Mezzacappa, M. A. Mischna, J. E. Moores, H. Newsom, A. Ollila, R. Perez, N. Renno, J.-B. Sirven, R. Tokar, M. de la Torre, L. d'Uston, D. Vaniman, A. Yingst and the MSL Science Team, "Soil diversity and hydration as observed by ChemCam at Gale Crater, Mars", Science **341**, 6153, 1238670 (2013).

Metzler, K., A. Bischoff and D. Stöffler, "Accretionary dust mantles in CM chondrites: Evidence for solar nebula processes", Geochimica et Cosmochimica Acta **56**, 7, 2873–2897 (1992).

Meyer-Dombard, D. R., E. L. Shock and J. P. Amend, "Archaeal and bacterial communities in geochemically diverse hot springs of Yellowstone National Park, USA", Geobiology **3**, 3, 211–227 (2005).

Miller, G. A. and D. K. Carpenter, "Solid-liquid phase diagram of the system methanol-water.", Journal of Chemical & Engineering Data **9**, 3, 371–373 (1964).

Miller, S. L. and A. Lazcano, "The origin of life–did it occur at high temperatures?", Journal of Molecular Evolution **41**, 6, 689–692 (1995).

Milliken, R. E. and A. S. Rivkin, "Brucite and carbonate assemblages from altered olivine-rich materials on Ceres", Nature Geoscience **2**, 4, 258–261 (2009).

Millington, R. J. and J. P. Quirk, "Permeability of porous solids", Transactions of the Faraday Society **57**, 1200–1207 (1961).

Mironenko, M. V., G. E. Boitnott, S. A. Grant and R. S. Sletten, "Experimental determination of the volumetric properties of NaCl solutions to 253 K", Journal of Physical Chemistry B **105**, 41, 9909–9912 (2001).

Mishima, O., "Volume of supercooled water under pressure and the liquid-liquid critical point", Journal of Chemical Physics **133**, 144503, 6 pp. (2010).

Moore, D. E., D. A. Lockner, M. Shengli, R. Summers and J. D. Byerlee, "Strengths of serpentinite gouges at elevated temperatures", Journal of Geophysical Research **102**, B7, 14787–14 (1997).

Morel, F. M. M., "The co-evolution of phytoplankton and trace element cycles in the oceans", Geobiology **6**, 3, 318–324 (2008).

Morel, F. M. M., R. J. M. Hudson and N. M. Price, "Limitation of productivity by trace metals in the sea.", Limnology and Oceanography **36**, 8, 1742–1755 (1991).

Morel, F. M. M. and N. M. Price, "The biogeochemical cycles of trace metals in the oceans", Science **300**, 5621, 944–947 (2003).

Morono, Y., T. Terada, J. Kallmeyer and F. Inagaki, "An improved cell separation technique for marine subsurface sediments: Applications for high-throughput analysis using flow cytometry and cell sorting", Environmental Microbiology **15**, 10, 2841–2849 (2013).

Moroz, L. V., S. V. Kozerenko and V. V. Fadeev, "The reflectance spectrum of synthetic tochilinite", in "28th Lunar and Planetary Science Conference Abstracts", p. 1288 (Lunar and Planetary Institute, 1997).

Mousis, O., E. Chassefière, N. G. Holm, A. Bouquet, J. H. Waite, W. D. Geppert, S. Picaud, Y. Aikawa, M. Ali-Dib, J.-L. Charlou and P. Rousselot, "Methane clathrates in the solar system", Astrobiology **15**, 4, 308–326 (2015).

Mousis, O., J. I. Lunine, J. H. Waite, B. Magee, W. S. Lewis, K. E. Mandt, D. Marquer and D. Cordier, "Formation conditions of Enceladus and origin of its methane reservoir", The Astrophysical Journal Letters **701**, 1, L39–L42 (2009).

Mueller, S., E. W. Llewellin and H. M. Mader, "The rheology of suspensions of solid particles", Proceedings of the Royal Society of London A pp. rspa20090445, 28 pp. (2009).

Mumma, M. J. and S. B. Charnley, "The chemical composition of comets – Emerging taxonomies and natal heritage", Annual Reviews of Astronomy and Astrophysics **49**, 1, 471–524 (2011).

Mustard, J. F., M. Adler, A. Allwood, D. S. Bass, D. W. Beaty, J. F. Bell, W. B. Brinckerhoff, M. Carr, D. J. Des Marais, B. Drake, K. S. Edgett, J. Eigenbrode, L. T. Elkins-Tanton, J. A. Grant, S. M. Milkovich, D. Ming, C. Moore, S. Murchie, T. C. Onstott, S. W. Ruff, M. A. Sephton, A. Steele and A. Treiman, "Report of the Mars 2020 science definition team", Tech. rep., Mars 2020 Science Definition Team (2013).

National Research Council, *Vision and Voyages for Planetary Science in the Decade 2013-2022* (NRC, 2011).

Nealson, K. H. and D. Saffarini, "Iron and manganese in anaerobic respiration: environmental significance, physiology, and regulation", Annual Reviews in Microbiology **48**, 1, 311–343 (1994).

Nelson, R. M., L. W. Kamp, R. M. C. Lopes, D. L. Matson, R. L. Kirk, B. W. Hapke, S. D. Wall, M. D. Boryta, F. E. Leader, W. D. Smythe, K. L. Mitchell, K. H. Baines, R. Jaumann, C. Sotin, R. N. Clark, D. P. Cruikshank, P. Drossart, J. I. Lunine, M. Combes, G. Bellucci, J.-P. Bibring, F. Capaccioni, P. Cerroni, A. Coradini, V. Formisano, G. Filacchione, Y. Langevin, T. B. McCord, V. Mennella, P. D. Nicholson, B. Sicardy, P. G. J. Irwin and J. C. Pearl, "Photometric changes on Saturn's Titan: Evidence for active cryovolcanism", Geophysical Research Letters **36**, 4, L04202 (2009).

Nestola, F., R. J. Angel, J. Zhao, C. J. Garrido, V. L. Sánchez-Vizcaíno, G. Capitani and M. Mellini, "Antigorite equation of state and anomalous softening at 6 GPa: an in situ single-crystal X-ray diffraction study", Contributions to Mineralogy and Petrology **160**, 1, 33–43 (2010).

Neveu, M., S. J. Desch and J. C. Castillo-Rogez, "Core cracking and hydrothermal circulation can profoundly affect Ceres' geophysical evolution", Journal of Geophysical Research: Planets **120**, 2, 123–154 (2015a).

Neveu, M., S. J. Desch and J. C. Castillo-Rogez, "Geochemistry, thermal evolution, and cryovolcanism on Ceres with a muddy ice mantle", Geophysical Research Letters (in review).

Neveu, M., S. J. Desch, E. L. Shock and C. R. Glein, "Prerequisites for explosive cryovolcanism on dwarf planet-class Kuiper belt objects", Icarus **246**, 48–64 (2015b).

Neveu, M., A. T. Poret-Peterson, A. D. Anbar and J. J. Elser, "Ordinary stoichiometry of extraordinary microorganisms", Geobiology (2015c).

Neveu, M., A. T. Poret-Peterson, Z. M. P. Lee, A. D. Anbar and J. J. Elser, "Prokaryotic cells separated from sediments are suitable for elemental composition analysis", Limnology and Oceanography: Methods **12**, 7, 519–529 (2014).

Newsom, H. E., "Hydrothermal alteration of impact melt sheets with implications for Mars", Icarus **44**, 1, 207–216 (1980).

Newsom, H. E., J. J. Hagerty and I. E. Thorsos, "Location and sampling of aqueous and hydrothermal deposits in Martian impact craters", Astrobiology **1**, 1, 71–88 (2001).

Nimmo, F. and D. McKenzie, "Volcanism and tectonics on Venus", Annual Review of Earth and Planetary Sciences **26**, 1, 23–51 (1998).

Norton, D. L., "Theory of hydrothermal systems", Annual Review of Earth and Planetary Sciences **12**, 1, 155–177 (1984).

Norton, D. L. and B. L. Dutrow, "Complex behavior of magma-hydrothermal processes: role of supercritical fluid", Geochimica et Cosmochimica Acta **65**, 21, 4009–4017 (2001).

Novoselov, A. A., P. Serrano, M. L. A. Forancelli Pacheco, M. S. Chaffin, J. T. O'Malley-James, S. C. Moreno and F. B. Ribeiro, "From cytoplasm to environment: The inorganic ingredients for the origin of life", Astrobiology **13**, 3, 294–302 (2013).

Nuester, J., S. Vogt, M. Newville, A. B. Kustka and B. S. Twining, "The unique biogeochemical signature of the marine diazotroph *Trichodesmium*", Frontiers in Microbiology **3**, 150, 10.3389/fmicb.2012.00150 (2012).

O'Brien, D. P., B. J. Travis, W. C. Feldman, M. V. Sykes, P. M. Schenk, S. Marchi, C. T. Russell and C. A. Raymond, "The potential for volcanism on Ceres due to crustal thickening and pressurization of a subsurface ocean", in "46th Lunar and Planetary Science Conference Abstracts", p. 2831 (Lunar and Planetary Institute, 2015).

Ojha, L., M. B. Wilhelm, S. L. Murchie, A. S. McEwen, J. J. Wray, J. Hanley, M. Massé and M. Chojnacki, "Spectral evidence for hydrated salts in recurring slope lineae on Mars", Nature Geoscience **Advance online publication**, 10.1038/ngeo2546, 5 pp (2015).

Oksanen, J., R. Kindt, P. Legendre, B. O'Hara, M. H. H. Stevens and H. Wagner, "The *vegan* package", https://cran.r-project.org/web/packages/vegan, retrieved Sept. 12, 2015 (2007).

Opeil, C. P., G. J. Consolmagno and D. T. Britt, "The thermal conductivity of meteorites: New measurements and analysis", Icarus **208**, 1, 449–454 (2010).

Ord, A., B. E. Hobbs and D. R. Lester, "The mechanics of hydrothermal systems: I. Ore systems as chemical reactors", Ore Geology Reviews (2012).

Orlando, T. M., T. B. McCord and G. A. Grieves, "The chemical nature of Europa surface material and the relation to a subsurface ocean", Icarus **177**, 2, 528–533 (2005).

Osako, M., A. Yoneda and E. Ito, "Thermal diffusivity, thermal conductivity and heat capacity of serpentine (antigorite) under high pressure", Physics of the Earth and Planetary Interiors **183**, 1, 229–233 (2010).

Outten, C. E. and T. V. O'Halloran, "Femtomolar sensitivity of metalloregulatory proteins controlling zinc homeostasis", Science **292**, 5526, 2488–2492 (2001).

Oze, C. and M. Sharma, "Have olivine, will gas: Serpentinization and the abiogenic production of methane on Mars", Geophysical Research Letters **32**, 10 (2005).

Pace, N. R., "A molecular view of microbial diversity and the biosphere", Science **276**, 5313, 734–740 (1997).

Palguta, J., G. Schubert and B. J. Travis, "Fluid flow and chemical alteration in carbonaceous chondrite parent bodies", Earth and Planetary Science Letters **296**, 3, 235–243 (2010).

Papineau, D., R. Purohit, T. Goldberg, D. Pi, G. A. Shields, H. Bhu, A. Steele and M. L. Fogel, "High primary productivity and nitrogen cycling after the Paleoproterozoic phosphogenic event in the Aravalli Supergroup, India", Precambrian Research **171**, 1, 37–56 (2009).

Pappalardo, R. T., M. J. S. Belton, H. H. Breneman, M. H. Carr, C. R. Chapman, G. C. Collins, T. Denk, S. Fagents, P. E. Geissler, B. Giese, R. Greeley, R. Greenberg, J. W. Head, P. Helfenstein, G. Hoppa, S. D. Kadel, K. P. Klaasen, J. E. Klemaszewski, K. Magee, A. S. McEwen, J. M. Moore, W. B. Moore, G. Neukum, C. B. Phillips, L. M. Prockter, G. Schubert, D. A. Senske, R. J. Sullivan, B. R. Tufts, E. P. Turtle, R. Wagner and K. K. Williams, "Does Europa have a subsurface ocean? Evaluation of the geological evidence", Journal of Geophysical Research **104**, E10, 24015–24055 (1999).

Pappalardo, R. T., D. Senske, L. Prockter, B. Paczkowski, S. Vance, B. Goldstein, T. Magner and B. Cooke, "Science and reconnaissance from the Europa Clipper mission concept: Exploring Europa's habitability", in "46th Lunar and Planetary Science Conference Abstracts", p. 2673 (Lunar and Planetary Institute, 2015).

Parkhurst, D. L. and C. A. J. Appelo, "Description of input and examples for *PHREEQC* version 3: A computer program for speciation, batch-reaction, one-dimensional transport, and inverse geochemical calculations", Tech. rep., US Geological Survey (2013).

Parks, D. H., G. W. Tyson, P. Hugenholtz and R. G. Beiko, "*STAMP*: statistical analysis of taxonomic and functional profiles", Bioinformatics **30**, 21, 3123–3124 (2014).

Parmentier, E. M., J. F. Mustard, B. L. Ehlmann and L. H. Roach, "Deep hydrothermal circulation and implications for the early crustal compositional and thermal evolution of Mars", in "39th Lunar and Planetary Science Conference Abstracts", (2008).

Paterson, M. S. and T.-F. Wong, *Experimental rock deformation – The brittle field* (Springer, 2005).

Paytan, A. and K. McLaughlin, "The oceanic phosphorus cycle", Chemical Reviews **107**, 2, 563–576 (2007).

Peng, D.-Y. and D. B. Robinson, "A new two-constant equation of state", Industrial & Engineering Chemistry Fundamentals **15**, 1, 59–64 (1976).

Pernthaler, J., F.-O. GIöckner, W. Schönhuber and R. Amann, "Fluorescence *in situ* Hybridization (FISH) with rRNA-targeted oligonucleotide probes", Marine Microbiology **30**, 207 (2001).

Perrillat, J.-P., I. Daniel, K. T. Koga, B. Reynard, H. Cardon and W. A. Crichton, "Kinetics of antigorite dehydration: a real-time X-ray diffraction study", Earth and Planetary Science Letters **236**, 3, 899–913 (2005).

Person, M., A. Hofstra, D. Sweetkind, W. Stone, D. Cohen, C. W. Gable and A. Banerjee, "Analytical and numerical models of hydrothermal fluid flow at fault intersections", Geofluids **12**, 4, 312–326 (2012).

Phillips, O. M., *Flow and reactions in permeable rocks* (Cambridge University Press, 1991).

Pilson, M. E. Q., *An Introduction to the Chemistry of the Sea* (Cambridge University Press, 2012).

Pinneker, E. V., *General Hydrogeology* (Cambridge University Press, 2010).

Pirajno, F., *Hydrothermal Processes and Mineral Systems* (Springer, 2009).

Pitzer, K. S., "Thermodynamics of electrolytes. I. Theoretical basis and general equations", The Journal of Physical Chemistry **77**, 2, 268–277 (1973).

Pitzer, K. S. and L. Brewer, *Revised edition of Thermodynamics by G. N. Lewis and M. Randall* (McGraw-Hill, 1961).

Plescia, J. B., "Geological terrains and crater frequencies on Ariel", Nature **327**, 6119, 201–204 (1987).

Plyasunov, A. V. and E. L. Shock, "Correlation strategy for determining the parameters of the revised Helgeson-Kirkham-Flowers model for aqueous nonelectrolytes", Geochimica et Cosmochimica Acta **65**, 21, 3879–3900 (2001).

Pokrovsky, O. S., S. V. Golubev, J. Schott and A. Castillo, "Calcite, dolomite and magnesite dissolution kinetics in aqueous solutions at acid to circumneutral pH, 25 to 150°C and 1 to 55 atm pCO_2: New constraints on CO_2 sequestration in sedimentary basins", Chemical Geology **265**, 1, 20–32 (2009).

Pokrovsky, O. S. and J. Schott, "Processes at the magnesium-bearing carbonates/solution interface. II. Kinetics and mechanism of magnesite dissolution.", Geochimica et Cosmochimica Acta **63**, 6, 881–897 (1999).

Pope, K. O., S. W. Kieffer and D. E. Ames, "Impact melt sheet formation on Mars and its implication for hydrothermal systems and exobiology", Icarus **183**, 1, 1–9 (2006).

Porco, C. C., P. Helfenstein, P. C. Thomas, A. P. Ingersoll, J. Wisdom, R. West, G. Neukum, T. Denk, R. Wagner, T. Roatsch, S. Kieffer, E. Turtle, A. McEwen, T. V. Johnson, J. Rathbun, J. Veverka, D. Wilson, J. Perry, J. Spitale, A. Brahic, J. A. Burns, A. D. DelGenio, L. Dones, C. D. Murray and S. Squyres, "*Cassini* observes the active south pole of Enceladus", Science **311**, 5766, 1393–1401 (2006).

Porter, S. B., S. J. Desch and J. C. Cook, "Micrometeorite impact annealing of ice in the outer solar system", Icarus **208**, 1, 492–498 (2010).

Portillo, M. C., J. W. Leff, C. L. Lauber and N. Fierer, "Cell size distributions of soil bacterial and archaeal taxa", Applied and Environmental Microbiology **79**, 24, 7610–7617 (2013).

Postberg, F., S. Kempf, J. Schmidt, N. Brilliantov, A. Beinsen, B. Abel, U. Buck and R. Srama, "Sodium salts in E-ring ice grains from an ocean below the surface of Enceladus", Nature **459**, 7250, 1098–1101 (2009).

Postberg, F., J. Schmidt, J. Hillier, S. Kempf and R. Srama, "A salt-water reservoir as the source of a compositionally stratified plume on Enceladus", Nature **474**, 7353, 620–622 (2011).

Poté, J., A. G. Bravo, P. Mavingui, D. Ariztegui and W. Wildi, "Evaluation of quantitative recovery of bacterial cells and DNA from different lake sediments by Nycodenz density gradient centrifugation", Ecological Indicators **10**, 2, 234–240 (2010).

Poulton, S. W. and D. E. Canfield, "Ferruginous conditions: a dominant feature of the ocean through Earth's history", Elements **7**, 2, 107–112 (2011).

Prettyman, T., W. Feldman, H. McSween, R. Dingler, D. Enemark, D. Patrick, S. Storms, J. Hendricks, J. Morgenthaler, K. Pitman and R. Reedy, "*Dawn*'s Gamma Ray and Neutron Detector", Space Science Reviews **163**, 371–459 (2011).

Prialnik, D., G. Sarid, E. D. Rosenberg and R. Merk, "Thermal and chemical evolution of comet nuclei and Kuiper belt objects", Space Science Reviews **138**, 1-4, 147–164 (2008).

Price, N. M., G. I. Harrison, J. G. Hering, R. J. Hudson, P. M. V. Nirel, B. Palenik and F. M. M. Morel, "Preparation and chemistry of the artificial algal culture medium Aquil", Biological Oceanography **6**, 5-6, 443–461 (1989).

Proussevitch, A. A. and D. L. Sahagian, "Dynamics and energetics of bubble growth in magmas: analytical formulation and numerical modeling", Journal of Geophysical Research: Solid Earth (1978–2012) **103**, B8, 18223–18251 (1998).

Quast, C., E. Pruesse, P. Yilmaz, J. Gerken, T. Schweer, P. Yarza, J. Peplies and F. O. Glöckner, "The *SILVA* ribosomal RNA gene database project: improved data processing and web-based tools", Nucleic Acids Research **41**, D590–D596 (2012).

Quigg, A., Z. V. Finkel, A. J. Irwin, Y. Rosenthal, T.-Y. Ho, J. R. Reinfelder, O. Schofield, F. M. M. Morel and P. G. Falkowski, "The evolutionary inheritance of elemental stoichiometry in marine phytoplankton", Nature **425**, 6955, 291–294 (2003).

Ransford, G. A., A. A. Finnerty and K. D. Collerson, "Europa's petrological thermal history", Nature **289**, 21–24 (1981).

Rathbun, J. A. and S. W. Squyres, "Hydrothermal systems associated with Martian impact craters", Icarus **157**, 2, 362–372 (2002).

Raven, J. A., "Predictions of Mn and Fe use efficiencies of phototrophic growth as a function of light availability for growth and of C assimilation pathway", New Phytologist **116**, 1, 1–18 (1990).

R Core Team, "*R*: A language and environment for statistical computing", http://www.R-project.org, retrieved Feb. 26, 2015 (2014).

Redfield, A. C., "On the proportions of organic derivatives in sea water and their relation to the composition of plankton", in "James Johnstone Memorial Volume", (University Press of Liverpool, 1934).

Redfield, A. C., "The biological control of chemical factors in the environment", American Scientist **46**, 3, 230A, 205–221 (1958).

Redfield, A. C., "The influence of organisms on the composition of sea-water", in "The Sea, Volume 2: The Composition of Sea-Water Comparative and Descriptive Oceanography", pp. 26–77 (Interscience, 1963).

Reuter, D., S. Stern, J. Scherrer, D. Jennings, J. Baer, J. Hanley, L. Hardaway, A. Lunsford, S. McMuldroch, J. Moore, C. Olkin, R. Parizek, H. Reitsma, D. Sabatke, J. Spencer, J. Stone, H. Throop, J. Van Cleve, G. Weigle and L. Young, "Ralph: A Visible/Infrared Imager for the *New Horizons* Pluto/Kuiper Belt Mission", Space Science Reviews **140**, 129–154 (2008).

Rhee, G.-Y., "Effects of N: P atomic ratios and nitrate limitation on algal growth, cell composition, and nitrate uptake", Limnology and Oceanography **23**, 1, 10–25 (1978).

Rhoads, D. B. and W. Epstein, "Cation transport in *Escherichia coli*. IX. Regulation of K transport", The Journal of General Physiology **72**, 3, 283–295 (1978).

Ribando, R. J., K. E. Torrance and D. L. Turcotte, "Numerical models for hydrothermal circulation in the oceanic crust", Journal of Geophysical Research **81**, 17, 3007–3012 (1976).

Richard, L., "Calculation of the standard molal thermodynamic properties as a function of temperature and pressure of some geochemically important organic sulfur compounds", Geochimica et Cosmochimica Acta **65**, 21, 3827–3877 (2001).

Richard, L. and H. C. Helgeson, "Calculation of the thermodynamic properties at elevated temperatures and pressures of saturated and aromatic high molecular weight solid and liquid hydrocarbons in kerogen, bitumen, petroleum, and other organic matter of biogeochemical interest", Geochimica et Cosmochimica Acta **62**, 23, 3591–3636 (1998).

Rickwood, D., T. Ford and J. Graham, "Nycodenz: a new nonionic iodinated gradient medium", Analytical Biochemistry **123**, 1, 23–31 (1982).

Rimstidt, J. D. and H. Barnes, "The kinetics of silica-water reactions", Geochimica et Cosmochimica Acta **44**, 11, 1683–1699 (1980).

Rivkin, A. S., E. Asphaug and W. F. Bottke, "The case of the missing Ceres family", Icarus **243**, 429–439 (2014).

Rivkin, A. S., J.-Y. Li, R. E. Milliken, L. F. Lim, A. Lovell, B. E. Schmidt, L. A. McFadden and B. A. Cohen, "The surface composition of Ceres", Space Science Reviews **163**, 95–116 (2012).

Rivkin, A. S., E. L. Volquardsen and B. E. Clark, "The surface composition of Ceres: Discovery of carbonates and iron-rich clays", Icarus **185**, 2, 563–567 (2006).

Roberts, J. H., "The fluffy core of Enceladus", Icarus **258**, 54–66 (2015).

Robie, R. A., B. S. Hemingway and J. R. Fisher, "Thermodynamic properties of minerals and related substances at 298.15 K and 1 bar (10^5 Pascals) pressure and at higher temperatures", Tech. rep., US Geological Survey Bulletin 1452 (1979).

Robuchon, G. and F. Nimmo, "Thermal evolution of Pluto and implications for surface tectonics and a subsurface ocean", Icarus **216**, 2, 426–439 (2011).

Rosner, D. E. and M. Epstein, "Effects of interface kinetics, capillarity and solute diffusion on bubble growth rates in highly supersaturated liquids", Chemical Engineering Science **27**, 1, 69–88 (1972).

Roth, L., J. Saur, K. D. Retherford, D. F. Strobel, P. D. Feldman, M. A. McGrath and F. Nimmo, "Transient water vapor at Europa's south pole", Science **343**, 171–174 (2014).

Rouf, M. A., "Spectrochemical analysis of inorganic elements in bacteria", Journal of Bacteriology **88**, 6, 1545–1549 (1964).

Rousselot, P., E. Jehin, J. Manfroid, O. Mousis, C. Dumas, B. Carry, U. Marboeuf and J.-M. Zucconi, "A search for water vaporization on Ceres", The Astronomical Journal **142**, 125 (2011).

Rousselot, P., O. Pirali, E. Jehin, M. Vervloet, D. Hutsemékers, J. Manfroid, D. Cordier, M.-A. Martin-Drumel, S. Gruet, C. Arpigny, A. Decock and O. Mousis, "Toward a unique nitrogen isotopic ratio in cometary ices", The Astrophysical Journal Letters **780**, 2, L17, 5 pp. (2014).

Rubin, M. E., S. J. Desch and M. Neveu, "The effect of Rayleigh-Taylor instabilities on the thickness of undifferentiated crust on Kuiper belt objects", Icarus **236**, 122–135 (2014).

Ruff, S. W., J. D. Farmer, W. M. Calvin, K. E. Herkenhoff, J. R. Johnson, R. V. Morris, M. S. Rice, R. E. Arvidson, J. F. Bell, P. R. Christensen and S. W. Squyres, "Characteristics, distribution, origin, and significance of opaline silica observed by the *Spirit* rover in Gusev crater, Mars", Journal of Geophysical Research **116**, E00F23 (2011).

Russell, C. and C. Raymond, "The *Dawn* mission to Vesta and Ceres", Space Science Reviews **163**, 3–23 (2011).

Russell, C. T., C. A. Raymond, A. Coradini, H. Y. McSween, M. T. Zuber, A. Nathues, M. C. De Sanctis, R. Jaumann, A. S. Konopliv, F. Preusker, S. W. Asmar, R. S. Park, R. Gaskell, H. U. Keller, S. Mottola, T. Roatsch, J. E. C. Scully, D. E. Smith, P. Tricarico, M. J. Toplis, U. R. Christensen, W. C. Feldman, D. J. Lawrence, T. J. McCoy, T. H. Prettyman, R. C. Reedy, M. E. Sykes and T. N. Titus, "*Dawn* at Vesta: Testing the protoplanetary paradigm", Science **336**, 6082, 684–686 (2012).

Russell, C. T., C. A. Raymond, A. Nathues, P. Gutierrez-Marquez, M. C. DeSanctis, E. Ammannito, T. H. Prettyman, A. Konopliv, R. Park, H. Y. McSween, R. Jaumann, S. Joy, C. A. Polanskey, M. D. Rayman and the Dawn Science Team, "Dawn explores Ceres: Results from the survey orbit", http://nesf2015.arc.nasa.gov/sites/default/files/downloads/pdf/05.pdf, 2nd NASA Exploration Science Forum, July 21, 2015; retrieved Sept. 22, 2015 (2015).

Russell, M. J., L. M. Barge, R. Bhartia, D. Bocanegra, P. J. Bracher, E. Branscomb, R. Kidd, S. McGlynn, D. H. Meier, W. Nitschke, T. Shibuya, S. Vance, L. White and I. Kanik, "The drive to life on wet and icy worlds", Astrobiology **14**, 4, 308–343 (2014).

Russell, M. J., R. M. Daniel, A. J. Hall and J. A. Sherringham, "A hydrothermally precipitated catalytic iron sulphide membrane as a first step toward life", Journal of Molecular Evolution **39**, 231–243 (1994).

Rutter, E. H. and K. H. Brodie, "Experimental "syntectonic" dehydration of serpentinite under conditions of controlled pore water pressure", Journal of Geophysical Research **93**, B5, 4907–4932 (1988).

Safronov, V. S., "The heating of the Earth during its formation", Icarus **33**, 1, 3–12 (1978).

Saito, M. A., E. M. Bertrand, S. Dutkiewicz, V. V. Bulygin, D. M. Moran, F. M. Monteiro, M. J. Follows, F. W. Valois and J. B. Waterbury, "Iron conservation by reduction of metalloenzyme inventories in the marine diazotroph *Crocosphaera watsonii*", Proceedings of the National Academy of Sciences **108**, 6, 2184–2189 (2011).

Saito, M. A., J. W. Moffett, S. W. Chisholm and J. B. Waterbury, "Cobalt limitation and uptake in *Prochlorococcus*", Limnology and Oceanography **47**, 6, 1629–1636 (2002).

Saito, M. A., J. W. Moffett and G. R. DiTullio, "Cobalt and nickel in the Peru upwelling region: A major flux of labile cobalt utilized as a micronutrient", Global Biogeochemical Cycles **18**, 4 (2004).

Saito, M. A., G. Rocap and J. W. Moffett, "Production of cobalt binding ligands in a *Synechococcus* feature at the Costa Rica upwelling dome", Limnology and Oceanography **50**, 1, 279–290 (2005).

Saito, M. A., D. M. Sigman and F. M. M. Morel, "The bioinorganic chemistry of the ancient ocean: the co-evolution of cyanobacterial metal requirements and biogeochemical cycles at the Archean–Proterozoic boundary?", Inorganica Chimica Acta **356**, 308–318 (2003).

Sammis, C. G. and M. F. Ashby, "The failure of brittle porous solids under compressive stress states", Acta Metallurgica **34**, 3, 511–526 (1986).

Sandford, S. A., J. Aléon, C. M. O. Alexander, T. Araki, S. Bajt, G. A. Baratta, J. Borg, J. P. Bradley, D. E. Brownlee, J. R. Brucato, M. J. Burchell, H. Busemann, A. Butterworth, S. J. Clemett, G. Cody, L. Colangeli, G. Cooper, L. D'Hendecourt,

Z. Djouadi, J. P. Dworkin, G. Ferrini, H. Fleckenstein, G. J. Flynn, I. A. Franchi, M. Fries, M. K. Gilles, D. P. Glavin, M. Gounelle, F. Grossemy, C. Jacobsen, L. P. Keller, A. L. D. Kilcoyne, J. Leitner, G. Matrajt, A. Meibom, V. Mennella, S. Mostefaoui, L. R. Nittler, M. E. Palumbo, D. A. Papanastassiou, F. Robert, A. Rotundi, C. J. Snead, M. K. Spencer, F. J. Stadermann, A. Steele, T. Stephan, P. Tsou, T. Tyliszczak, A. J. Westphal, S. Wirick, B. Wopenka, H. Yabuta, R. N. Zare and M. E. Zolensky, "Organics captured from comet 81P/Wild 2 by the Stardust spacecraft", Science **314**, 5806, 1720–1724 (2006).

Sassani, D. C. and E. L. Shock, "Solubility and transport of platinum-group elements in supercritical fluids: Summary and estimates of thermodynamic properties for ruthenium, rhodium, palladium, and platinum solids, aqueous ions, and complexes to 1000°C and 5 kbar", Geochimica et Cosmochimica Acta **62**, 15, 2643–2671 (1998).

Sauvé, V., S. Bruno, B. C. Berks and A. M. Hemmings, "The SoxYZ complex carries sulfur cycle intermediates on a peptide swinging arm", Journal of Biological Chemistry **282**, 32, 23194–23204 (2007).

Schaller, E. L. and M. E. Brown, "Volatile loss and retention on Kuiper belt objects", The Astrophysical Journal Letters **659**, 1, L61–L64 (2007).

Schenk, P. M., "Fluid volcanism on Miranda and Ariel: Flow morphology and composition", Journal of Geophysical Research: Solid Earth (1978–2012) **96**, B2, 1887–1906 (1991).

Schloss, P. D., S. L. Westcott, T. Ryabin, J. R. Hall, M. Hartmann, E. B. Hollister, R. A. Lesniewski, B. B. Oakley, D. H. Parks, C. J. Robinson, J. W. Sahl, B. Stres, G. G. Thallinger, D. J. Van Horn and C. F. Weber, "Introducing *mothur*: open-source, platform-independent, community-supported software for describing and comparing microbial communities", Applied and Environmental Microbiology **75**, 23, 7537–7541 (2009).

Schmidt, B. E., D. D. Blankenship, G. W. Patterson and P. M. Schenk, "Active formation of chaos terrain over shallow subsurface water on Europa", Nature **479**, 7374, 502–505 (2011).

Schorghofer, N., "Predictions of depth to ice on asteroid Ceres", in "46th Lunar and Planetary Science Conference Abstracts", p. 1091 (Lunar and Planetary Institute, 2015).

Schulte, M. D., D. Blake, T. Hoehler and T. McCollom, "Serpentinization and its implications for life on the early Earth and Mars", Astrobiology **6**, 2, 364–376 (2006).

Schulte, M. D., E. L. Shock and R. H. Wood, "The temperature dependence of the standard-state thermodynamic properties of aqueous nonelectrolytes", Geochimica et Cosmochimica Acta **65**, 21, 3919–3930 (2001).

Schulze-Makuch, D., J. M. Dohm, C. Fan, A. G. Fairén, J. A. P. Rodriguez, V. R. Baker and W. Fink, "Exploration of hydrothermal targets on Mars", Icarus **189**, 2, 308–324 (2007).

Schwenzer, S. P., O. Abramov, C. C. Allen, J. C. Bridges, S. M. Clifford, J. Filiberto, D. A. Kring, J. Lasue, P. J. McGovern, H. E. Newsom, A. H. Treiman, D. T. Vaniman, R. C. Wiens and A. Wittmann, "Gale crater: Formation and post-impact hydrous environments", Planetary and Space Science **70**, 1, 84–95 (2012a).

Schwenzer, S. P., O. Abramov, C. C. Allen, S. M. Clifford, C. S. Cockell, J. Filiberto, D. A. Kring, J. Lasue, P. J. McGovern, H. E. Newsom, A. H. Treiman, D. T. Vaniman and R. C. Wiens, "Puncturing Mars: How impact craters interact with the Martian cryosphere", Earth and Planetary Science Letters **335-336**, 0, 9–17 (2012b).

Schwenzer, S. P. and D. A. Kring, "Impact-generated hydrothermal systems capable of forming phyllosilicates on Noachian Mars", Geology **37**, 12, 1091–1094 (2009).

Scott, E. R. D. and A. N. Krot, "Chondritic meteorites and the high-temperature nebular origins of their components", in "Chondrites and the Protoplanetary Disk", vol. 341, pp. 15–53 (2005).

Segerer, A. H., S. Burggraf, G. Fiala, G. Huber, R. Huber, U. Pley and K. O. Stetter, "Life in hot springs and hydrothermal vents", Origins of Life and Evolution of Biospheres **23**, 1, 77–90 (1993).

Shaked, Y., Y. Xu, K. Leblanc and F. M. M. Morel, "Zinc availability and alkaline phosphatase activity in *Emiliania huxleyi*: Implications for Zn-P co-limitation in the ocean", Limnology and Oceanography **51**, 1, 299–309 (2006).

Sharp, Z. D. and D. S. Draper, "The chlorine abundance of Earth: Implications for a habitable planet", Earth and Planetary Science Letters **369**, 71–77 (2013).

Sherwood, B., "Strategic map for exploring the ocean-world Enceladus", in "66th International Astronautical Congress Abstracts", pp. IAC–15,A7,1,2,x30092 (2015).

Sherwood Lollar, B., S. K. Frape, S. M. Weise, P. Fritz, S. A. Macko and J. A. Welhan, "Abiogenic methanogenesis in crystalline rocks", Geochimica et Cosmochimica Acta **57**, 23, 5087–5097 (1993).

Shields, A., "Application of similarity principles and turbulence research to bed-load movement", Tech. rep., Soil Conservation Service (1936).

Shock, E. L., "Geochemical constraints on the origin of organic compounds in hydrothermal systems", Origins of Life and Evolution of the Biosphere **20**, 3-4, 331–367 (1990).

Shock, E. L., "Hydrothermal dehydration of aqueous organic compounds", Geochimica et Cosmochimica Acta **57**, 14, 3341–3349 (1993).

Shock, E. L., "Organic acids in hydrothermal solutions: Standard molal thermodynamic properties of carboxylic acids and estimates of dissociation constants at high temperatures and pressures", American Journal of Science **295**, 5, 496–580 (1995).

Shock, E. L., "High-temperature life without photosynthesis as a model for Mars", Journal of Geophysical Research **102**, E10, 23687–23694 (1997).

Shock, E. L. and H. C. Helgeson, "Calculation of the thermodynamic and transport properties of aqueous species at high pressures and temperatures: Correlation algorithms for ionic species and equation of state predictions to 5 kb and 1000°C", Geochimica et Cosmochimica Acta **52**, 8, 2009–2036 (1988a).

Shock, E. L. and H. C. Helgeson, "Calculation of the thermodynamic and transport properties of aqueous species at high pressures and temperatures: Correlation algorithms for ionic species and equation of state predictions to 5 kb and 1000°C", Geochimica et Cosmochimica Acta **52**, 8, 2009–2036 (1988b).

Shock, E. L. and H. C. Helgeson, "Calculation of the thermodynamic and transport properties of aqueous species at high pressures and temperatures: Standard partial molal properties of organic species", Geochimica et Cosmochimica Acta **54**, 4, 915–945 (1990).

Shock, E. L., H. C. Helgeson and D. A. Sverjensky, "Calculation of the thermodynamic and transport properties of aqueous species at high pressures and temperatures: Standard partial molal properties of inorganic neutral species", Geochimica et Cosmochimica Acta **53**, 9, 2157–2183 (1989).

Shock, E. L., M. Holland, J. P. Amend, G. R. Osburn and T. P. Fischer, "Quantifying inorganic sources of geochemical energy in hydrothermal ecosystems, Yellowstone National Park, USA", Geochimica et Cosmochimica Acta **74**, 14, 4005–4043 (2010).

Shock, E. L. and M. E. Holland, "Quantitative habitability", Astrobiology **7**, 6, 839–851 (2007).

Shock, E. L. and C. M. Koretsky, "Metal-organic complexes in geochemical processes: Calculation of standard partial molal thermodynamic properties of aqueous acetate complexes at high pressures and temperatures", Geochimica et Cosmochimica Acta **57**, 20, 4899–4922 (1993).

Shock, E. L. and W. B. McKinnon, "Hydrothermal processing of cometary volatiles – Applications to Triton", Icarus **106**, 2, 464–477 (1993).

Shock, E. L., D. C. Sassani and H. Betz, "Uranium in geologic fluids: Estimates of standard partial molal properties, oxidation potentials, and hydrolysis constants at high temperatures and pressures", Geochimica et Cosmochimica Acta **61**, 20, 4245–4266 (1997a).

Shock, E. L., D. C. Sassani, M. Willis and D. A. Sverjensky, "Inorganic species in geologic fluids: correlations among standard molal thermodynamic properties of aqueous ions and hydroxide complexes", Geochimica et Cosmochimica Acta **61**, 5, 907–950 (1997b).

Shoji, D. and K. Kurita, "Compositional diapirism as the origin of the low-albedo terrain and vaporization at midlatitude on Ceres", Journal of Geophysical Research: Planets **119**, 12, 2457–2470 (2014).

Shuter, B., "A model of physiological adaptation in unicellular algae", Journal of Theoretical Biology **78**, 4, 519–552 (1979).

Sicardy, B., T. Widemann, E. Lellouch, C. Veillet, J.-C. Cuillandre, F. Colas, F. Roques, W. Beisker, M. Kretlow, A.-M. Lagrange, E. Gendron, F. Lacombe, J. Lecacheux, C. Birnbaum, A. Fienga, C. Leyrat, A. Maury, E. Raynaud, S. Renner, M. Schultheis, K. Brooks, A. Delsanti, O. R. Hainaut, R. Gilmozzi, C. Lidman, J. Spyromilio, M. Rapaport, P. Rosenzweig, O. Naranjo, L. Porras, F. Diaz, H. Calderon, S. Carrillo, A. Carvajal, E. Recalde, L. G. Cavero, C. Montalvo, D. Barria, R. Campos, R. Duffard and H. Levato, "Large changes in Pluto's atmosphere as revealed by recent stellar occultations", Nature **424**, 6945, 168–170 (2003).

Sierks, H., H. Keller, R. Jaumann, H. Michalik, T. Behnke, F. Bubenhagen, I. Büttner, U. Carsenty, U. Christensen, R. Enge *et al.*, "The *Dawn* Framing Camera", Space Science Reviews **163**, 1-4, 263–327 (2011).

Skelton, A., R. Whitmarsh, F. Arghe, P. Crill and H. Koyi, "Constraining the rate and extent of mantle serpentinization from seismic and petrological data: implications for chemosynthesis and tectonic processes", Geofluids **5**, 3, 153–164 (2005).

Sleep, N. H., A. Meibom, T. Fridriksson, R. G. Coleman and D. K. Bird, "H_2-rich fluids from serpentinization: geochemical and biotic implications", Proceedings of the National Academy of Sciences **101**, 35, 12818–12823 (2004).

Smith, B. A., L. A. Soderblom, D. Banfield, C. Barnet, A. T. Basilevsky, R. F. Beebe, K. Bollinger, J. M. Boyce, A. Brahic, G. A. Briggs, R. H. Brown, C. Chyba, S. A. Collins, T. Colvin, A. F. Cook, D. Crisp, S. K. Croft, D. Cruikshank, J. N. Cuzzi, G. E. Danielson, M. E. Davies, E. De Jong, L. Dones, D. Godfrey, J. Goguen,

I. Grenier, V. R. Haemmerle, H. Hammel, C. J. Hansen, c. P. Helfenstein, C. Howell, G. E. Hunt, A. P. Ingersoll, T. V. Johnson, J. Kargel, R. Kirk, D. I. Kuehn, S. Limaye, H. Masursky, A. McEwen, D. Morrison, T. Owen, W. Owen, J. B. Pollack, C. C. Porco, K. Rages, P. Rogers, D. Rudy, C. Sagan, J. Schwartz, E. M. Shoemaker, M. Showalter, B. Sicardy, D. Simonelli, J. Spencer, L. A. Sromovsky, C. Stoker, R. G. Strom, V. E. Suomi, S. P. Synott, R. J. Terrile, P. Thomas, W. R. Thompson, A. Verbiscer and J. Veverka, "*Voyager 2* at Neptune: Imaging science results", Science **246**, 4936, 1422–1449 (1989).

Soderblom, L. A., R. H. Brown, J. M. Soderblom, J. W. Barnes, R. L. Kirk, C. Sotin, R. Jaumann, D. J. Mackinnon, D. W. Mackowski, K. H. Baines, B. J. Buratti, R. N. Clark and P. D. Nicholson, "The geology of Hotei Regio, Titan: correlation of *Cassini* VIMS and RADAR", Icarus **204**, 2, 610–618 (2009).

Soderblom, L. A., S. W. Kieffer, T. L. Becker, R. H. Brown, A. F. Cook, C. J. Hansen, T. V. Johnson, R. L. Kirk and E. M. Shoemaker, "Triton's geyser-like plumes: Discovery and basic characterization", Science **250**, 4979, 410–415 (1990).

Sohl, F., M. Choukroun, J. S. Kargel, J. Kimura, R. T. Pappalardo, S. Vance and M. Y. Zolotov, "Subsurface water oceans on icy satellites: Chemical composition and exchange processes", Space Science Reviews **153**, 1-4, 485–510 (2010).

Sotin, C., R. Jaumann, B. J. Buratti, R. H. Brown, R. N. Clark, L. A. Soderblom, K. H. Baines, G. Bellucci, J.-P. Bibring, F. Capaccioni, P. Cerroni, M. Combes, A. Coradini, D. P. Cruikshank, P. Drossart, V. Formisano, Y. Langevin, D. L. Matson, T. B. McCord, R. M. Nelson, P. D. Nicholson, B. Sicardy, S. LeMouélic, S. Rodriguez, K. Stephan and C. K. Scholz, "Release of volatiles from a possible cryovolcano from near-infrared imaging of Titan", Nature **435**, 7043, 786–789 (2005).

Sparks, R. S. J., "The dynamics of bubble formation and growth in magmas: a review and analysis", Journal of Volcanology and Geothermal Research **3**, 1, 1–37 (1978).

Speedy, R. J. and C. A. Angell, "Isothermal compressibility of supercooled water and evidence for a thermodynamic singularity at −45°C", The Journal of Chemical Physics **65**, 3, 851–858 (1976).

Spencer, J. R., J. A. Stansberry, L. M. Trafton, E. F. Young, R. P. Binzel and S. K. Croft, *Volatile transport, seasonal cycles, and atmospheric dynamics on Pluto*, pp. 435–474 (University of Arizona Press, 1997).

Spencer, R. J., N. Møller and J. H. Weare, "The prediction of mineral solubilities in natural waters: A chemical equilibrium model for the Na–K–Ca–Mg–Cl–SO_4–H_2O system at temperatures below 25°C", Geochimica et Cosmochimica Acta **54**, 3, 575–590 (1990).

Squyres, S. W., R. E. Arvidson, S. Ruff, R. Gellert, R. V. Morris, D. W. Ming, L. Crumpler, J. D. Farmer, D. J. Des Marais, A. Yen, S. M. McLennan, W. Calvin, J. F. Bell, B. C. Clark, A. Wang, T. J. McCoy, M. E. Schmidt and P. A. de Souza, "Detection of silica-rich deposits on Mars", Science **320**, 5879, 1063–1067 (2008).

Stec, B., K. M. Holtz and E. R. Kantrowitz, "A revised mechanism for the alkaline phosphatase reaction involving three metal ions", Journal of Molecular Biology **299**, 5, 1303–1311 (2000).

Steele-MacInnis, M., L. Han, R. P. Lowell, J. D. Rimstidt and R. J. Bodnar, "The role of fluid phase immiscibility in quartz dissolution and precipitation in sub-seafloor hydrothermal systems", Earth and Planetary Science Letters **321**, 139–151 (2012).

Steenbergh, A. K., P. L. E. Bodelier, M. Heldal, C. P. Slomp and H. J. Laanbroek, "Does microbial stoichiometry modulate eutrophication of aquatic ecosystems?", Environmental Microbiology **15**, 5, 1572–1579 (2013).

Stefánsson, A., "Dissolution of primary minerals of basalt in natural waters: I. Calculation of mineral solubilities from 0°C to 350°C", Chemical Geology **172**, 3, 225–250 (2001).

Stern, S. A., D. C. Slater, M. C. Festou, J. W. Parker, G. R. Gladstone, M. F. A'Hearn and E. Wilkinson, "The discovery of argon in comet C/1995 O1 (Hale-Bopp)", The Astrophysical Journal Letters **544**, 2, L169–L172 (2000).

Stern, S. A., D. C. Slater, J. Scherrer, J. Stone, G. Dirks, M. Versteeg, M. Davis, G. R. Gladstone, J. W. Parker, L. A. Young and O. H. W. Siegmund, "ALICE: The ultraviolet imaging spectrograph aboard the *New Horizons* Pluto–Kuiper belt mission", Space Science Reviews **140**, 1-4, 155–187 (2008).

Stern, S. A. and J. Spencer, "*New Horizons*: The first reconnaissance mission to bodies in the Kuiper belt", Earth, Moon, and Planets **92**, 1-4, 477–482 (2003).

Sterner, R. W. and J. J. Elser, *Ecological Stoichiometry: the Biology of Elements from Molecules to the Biosphere* (Princeton University Press, 2002).

Stevenson, D. J., "Volcanism and igneous processes in small icy satellites", Nature **298**, 142–144 (1982).

Storrie-Lombardi, M. and K. Nealson, "Multivariate analysis of elemental chemistry as a robust biosignature", in "EGS-AGU-EUG Joint Assembly Abstracts", p. 13600 (2003).

Summons, R. E., J. P. Amend, D. Bish, R. Buick, G. D. Cody, D. J. Des Marais, G. Dromart, J. L. Eigenbrode, A. H. Knoll and D. Y. Sumner, "Preservation of

Martian organic and environmental records: Final report of the Mars biosignature working group", Astrobiology **11**, 2, 157–181 (2011).

Sunda, W. G., "Trace metal interactions with marine phytoplankton", Biological Oceanography **6**, 5-6, 411–442 (1989).

Sunda, W. G. and S. A. Huntsmann, "Cobalt and zinc interreplacement in marine phytoplankton: Biological and geochemical implications", Limnology and Oceanography **40**, 8, 1404–1417 (1995).

Sverjensky, D. A., E. L. Shock and H. C. Helgeson, "Prediction of the thermodynamic properties of aqueous metal complexes to 1000°C and 5 kb", Geochimica et Cosmochimica Acta **61**, 7, 1359–1412 (1997).

Swan, B. K., M. Martinez-Garcia, C. M. Preston, A. Sczyrba, T. Woyke, D. Lamy, T. Reinthaler, N. J. Poulton, E. D. P. Masland, M. Lluesma Gomez, M. E. Sieracki, E. F. DeLong, G. J. Herndl and R. Stepanauskas, "Potential for chemolithoautotrophy among ubiquitous bacteria lineages in the dark ocean", Science **333**, 6047, 1296–1300 (2011).

Thomas, P. C., J. W. Parker, L. A. McFadden, C. T. Russell, S. A. Stern, M. V. Sykes and E. F. Young, "Differentiation of the asteroid Ceres as revealed by its shape", Nature **437**, 7056, 224–226 (2005).

Thomas, P. J., R. T. Reynolds, S. W. Squyres and P. M. Cassen, "The Viscosity of Miranda", in "18th Lunar and Planetary Institute Science Conference Abstracts", p. 1016 (Lunar and Planetary Institute, 1987).

Thomas, R. J., D. A. Rothery, S. J. Conway and M. Anand, "Explosive volcanism on Mercury and the Moon: Insights into the nature of sub-surface magma storage", in "46th Lunar and Planetary Science Conference Abstracts", p. 1347 (Lunar and Planetary Institute, 2015).

Thomassin, J. H., J. Goni, P. Baillif, J. C. Touray and M. C. Jaurand, "An XPS study of the dissolution kinetics of chrysotile in 0.1 N oxalic acid at different temperatures", Physics and Chemistry of Minerals **1**, 4, 385–398 (1977).

Titus, T. N., "Ceres: Predictions for near-surface water ice stability and implications for plume generating processes", Geophysical Research Letters **42**, 7, 2130–2136 (2015).

Tobie, G., J. I. Lunine and C. Sotin, "Episodic outgassing as the origin of atmospheric methane on Titan", Nature **440**, 7080, 61–64 (2006).

Tomeoka, K. and P. R. Buseck, "Matrix mineralogy of the Orgueil CI carbonaceous chondrite", Geochimica et Cosmochimica Acta **52**, 6, 1627–1640 (1988).

Tortell, P. D., M. T. Maldonado, J. Granger and N. M. Price, "Marine bacteria and biogeochemical cycling of iron in the oceans", FEMS Microbiology Ecology **29**, 1, 1–11 (1999).

Travis, B. J., P. A. Bland, W. C. Feldman and M. V. Sykes, "Unconsolidated Ceres model has a warm convecting rocky core and a convecting mud ocean", in "46th Lunar and Planetary Science Conference Abstracts", p. 2360 (2015).

Travis, B. J., J. Palguta and G. Schubert, "A whole-moon thermal history model of Europa: Impact of hydrothermal circulation and salt transport", Icarus **218**, 2, 1006–1019 (2012).

Travis, B. J., N. D. Rosenberg and J. N. Cuzzi, "On the role of widespread subsurface convection in bringing liquid water close to Mars' surface", Journal of Geophysical Research **108**, E4, 8040 (2003).

Tromans, D. and J. A. Meech, "Fracture toughness and surface energies of minerals: theoretical estimates for oxides, sulphides, silicates and halides", Minerals Engineering **15**, 12, 1027–1041 (2002).

Trump, J. E. V. and S. L. Miller, "Carbon monoxide on the primitive Earth", Earth and Planetary Science Letters **20**, 145–150 (1973).

Tsou, P., D. E. Brownlee, C. P. McKay, A. D. Anbar, H. Yano, K. Altwegg, L. W. Beegle, R. Dissly, N. J. Strange and I. Kanik, "LIFE: Life investigation for Enceladus, a sample return mission concept in search for evidence of life", Astrobiology **12**, 8, 730–742 (2012).

Turcotte, D. L. and G. Schubert, *Geodynamics* (Cambridge University Press, 2014).

Twining, B. S. and S. B. Baines, "The trace metal composition of marine phytoplankton", Annual Review of Marine Science **5**, 191–215 (2013).

Twining, B. S., S. B. Baines, J. B. Bozard, S. Vogt, E. A. Walker and D. M. Nelson, "Metal quotas of plankton in the equatorial Pacific Ocean", Deep Sea Research Part II: Topical Studies in Oceanography **58**, 3, 325–341 (2011).

Twining, B. S., S. B. Baines and N. S. Fisher, "Element stoichiometries of individual plankton cells collected during the Southern Ocean Iron Experiment (SOFeX)", Limnology and Oceanography **49**, 6, 2115–2128 (2004).

Tyburczy, J. A., T. S. Duffy, T. J. Ahrens and M. A. Lange, "Shock wave equation of state of serpentine to 150 GPa: Implications for the occurrence of water in the Earth's lower mantle", Journal of Geophysical Research: Solid Earth (1978–2012) **96**, B11, 18011–18027 (1991).

Tyler, G. L., I. R. Linscott, M. K. Bird, D. P. Hinson, D. F. Strobel, M. Pätzold, M. E. Summers and K. Sivaramakrishnan, "The *New Horizons* Radio Science Experiment (REX)", Space Science Reviews **140**, 1-4, 217–259 (2008).

Vaccaro, B. J., A. L. Menon, W. A. Lancaster and M. W. W. Adams, "Metallomics using inductively-coupled plasma mass spectrometry", Current Protocols in Chemical Biology **4**, 249–274 (2009).

Vance, S., J. Harnmeijer, J. Kimura, H. Hussmann, B. deMartin and J. M. Brown, "Hydrothermal systems in small ocean planets", Astrobiology **7**, 6, 987–1005 (2007).

Varnes, E. S., B. M. Jakosky and T. M. McCollom, "Biological potential of Martian hydrothermal systems", Astrobiology **3**, 2, 407–414 (2003).

Vernazza, P., T. Mothé-Diniz, M. A. Barucci, M. Birlan, J. Carvano, G. Strazzulla, M. Fulchignoni and A. Migliorini, "Analysis of near-IR spectra of 1 Ceres and 4 Vesta, targets of the *Dawn* mission", Astronomy & Astrophysics **436**, 3, 1113–1121 (2005).

Voss, C. I. and A. M. Provost, SUTRA - *A Model for Saturated-Unsaturated, Variable-Density Ground-Water Flow with Solute or Energy Transport* (USGS, 2010).

Wade, H. E., "Variation in the phosphorus content of *Escherichia coli* during cultivation", Journal of General Microbiology **7**, 1-2, 24–30 (1952).

Wadhwa, M., "Redox conditions on small bodies, the Moon and Mars", Reviews in Mineralogy and Geochemistry **68**, 1, 493–510 (2008).

Wagman, D. D., W. H. Evans, V. B. Parker, R. H. Schumm and I. Halow, "The NBS tables of chemical thermodynamic properties. selected values for inorganic and c_1 and c_2 organic substances in SI units", Tech. rep., DTIC (1982).

Wagner, W. and A. Prüß, "The IAPWS formulation 1995 for the thermodynamic properties of ordinary water substance for general and scientific use", Journal of Physical and Chemical Reference Data **31**, 2, 387–535 (2002).

Waite, J. H., W. S. Lewis, B. A. Magee, J. I. Lunine, W. B. McKinnon, C. R. Glein, O. Mousis, D. T. Young, T. Brockwell, J. Westlake, M.-J. Nguyen, B. D. Teolis, H. B. Niemann, R. L. McNutt Jr, M. Perry and W.-H. Ip, "Liquid water on Enceladus from observations of ammonia and ^{40}Ar in the plume", Nature **460**, 7254, 487–490 (2009).

Wakita, S. and M. Sekiya, "Thermal evolution of icy planetesimals in the solar nebula", Earth, Planets and Space **63**, 12, 1193–1206 (2011).

Wall, S. D., R. M. C. Lopes, E. R. Stofan, C. A. Wood, J. L. Radebaugh, S. M. Hörst, B. W. Stiles, R. M. Nelson, L. W. Kamp, M. A. Janssen, R. D. Lorenz, J. I. Lunine, T. G. Farr, G. Mitri, P. Paillou, F. Paganelli and K. L. Mitchell, "*Cassini* RADAR images at Hotei Arcus and western Xanadu, Titan: Evidence for geologically recent cryovolcanic activity", Geophysical Research Letters **36**, 4, L04203 (2009).

Walsh, J. B., "The effect of cracks on the compressibility of rock", Journal of Geophysical Research **70**, 2, 381–389 (1965).

Walter, M. R. and D. J. Des Marais, "Preservation of biological information in thermal spring deposits: developing a strategy for the search for fossil life on Mars", Icarus **101**, 1, 129–143 (1993).

Wang, D. and Z. Li, "Modeling solid–liquid equilibrium of NH_4Cl–$MgCl_2$–H_2O system and its application to recovery of NH_4Cl in MgO production", AIChE Journal **57**, 6, 1595–1606 (2011).

Wang, J.-J., J.-G. Zhu, C. F. Chiu and H. Zhang, "Experimental study on fracture toughness and tensile strength of a clay", Engineering Geology **94**, 1, 65–75 (2007).

Warner, N. H. and J. D. Farmer, "Subglacial hydrothermal alteration minerals in Jokulhlaup deposits of southern Iceland, with implications for detecting past or present habitable environments on Mars", Astrobiology **10**, 5, 523–547 (2010).

Wasson, J. T. and G. W. Kallemeyn, "Compositions of chondrites", Philosophical Transactions of the Royal Society of London A **325**, 1587, 535–544 (1988).

Watkins, G. H., *Ammonium aluminosilicates: the examination of a mechanism for the high temperature condensation of ammonia in circumplanetary subnebulae*, Master's thesis, Massachusetts Institute of Technology (1981).

Weber, T. S. and C. Deutsch, "Ocean nutrient ratios governed by plankton biogeography", Nature **467**, 7315, 550–554 (2010).

Weertman, J., S. White and A. H. Cook, "Creep laws for the mantle of the Earth [and discussion]", Philosophical Transactions of the Royal Society of London A **288**, 1350, 9–26 (1978).

Wiens, R. C., S. Maurice, B. Barraclough, M. Saccoccio, W. C. Barkley, J. F. Bell, S. Bender, J. Bernardin, D. Blaney, J. Blank, M. Bouyé, N. Bridges, N. Bultman, P. Caïs, R. C. Clanton, B. Clark, S. Clegg, A. Cousin, D. Cremers, A. Cros, L. DeFlores, D. Delapp, R. Dingler, C. D'Uston, M. Darby Dyar, T. Elliott, D. Enemark, C. Fabre, M. Flores, O. Forni, O. Gasnault, T. Hale, C. Hays, K. Herkenhoff, E. Kan, L. Kirkland, D. Kouach, D. Landis, Y. Langevin, N. Lanza, F. LaRocca, J. Lasue, J. Latino, D. Limonadi, C. Lindensmith, C. Little, N. Mangold, G. Manhes,

P. Mauchien, C. McKay, E. Miller, J. Mooney, R. V. Morris, L. Morrison, T. Nelson, H. Newsom, A. Ollila, M. Ott, L. Pares, R. Perez, F. Poitrasson, C. Provost, J. W. Reiter, T. Roberts, F. Romero, V. Sautter, S. Salazar, J. J. Simmonds, R. Stiglich, S. Storms, N. Striebig, J.-J. Thocaven, T. Trujillo, M. Ulibarri, D. Vaniman, N. Warner, R. Waterbury, R. Whitaker, J. Witt and B. Wong-Swanson, "The ChemCam instrument suite on the Mars Science Laboratory (MSL) rover: Body unit and combined system tests", Space Science Reviews pp. 1–61 (2012).

Williams, R. J. P., "Aluminium and biological systems: an introduction", Coordination Chemistry Reviews **149**, 1–9 (1996).

Williams, R. J. P. and J. J. R. Fraústo da Silva, "The distribution of elements in cells", Coordination Chemistry Reviews **200**, 247–348 (2000).

Windman, T., N. Zolotova, F. Schwandner and E. L. Shock, "Formate as an energy source for microbial metabolism in chemosynthetic zones of hydrothermal ecosystems", Astrobiology **7**, 6, 873–890 (2007).

Wolery, T. J., "*EQ3/6*: A software package for geochemical modeling of aqueous systems: package overview and installation guide (version 7.0)", Tech. rep., Lawrence Livermore National Laboratory (1992).

Wolfe-Simon, F., J. S. Blum, T. R. Kulp, G. W. Gordon, S. E. Hoeft, J. Pett-Ridge, J. F. Stolz, S. M. Webb, P. K. Weber, P. C. W. Davies, A. D. Anbar and R. S. Oremland, "A bacterium that can grow by using arsenic instead of phosphorus", Science **332**, 6034, 1163–1166 (2011).

Woods, H. A., W. Makino, J. B. Cotner, S. E. Hobbie, J. F. Harrison, K. Acharya and J. J. Elser, "Temperature and the chemical composition of poikilothermic organisms", Functional Ecology **17**, 2, 237–245 (2003).

Wunder, B., R. Wirth and M. Gottschalk, "Antigorite", European Journal of Mineralogy **13**, 3, 485–496 (2001).

Xu, T. and K. Pruess, "Modeling multiphase non-isothermal fluid flow and reactive geochemical transport in variably saturated fractured rocks: 1. Methodology", American Journal of Science **301**, 1, 16–33 (2001).

Xu, Y., D. Shi, L. Aristilde and F. M. M. Morel, "The effect of pH on the uptake of zinc and cadmium in marine phytoplankton: Possible role of weak complexes", Limnology and Oceanography **57**, 1, 293–304 (2012).

Xu, Y., D. Tang, Y. Shaked and F. M. M. Morel, "Zinc, cadmium, and cobalt interreplacement and relative use efficiencies in the coccolithophore *Emiliania huxleyi*", Limnology and Oceanography **52**, 5, 2294–2305 (2007).

Yatsenko, O. B. and I. G. Chudotvortsev, "Ice melting and crystallization in binary water–salt systems", Inorganic materials **38**, 9, 907–913 (2002).

Yee, D. and F. M. M. Morel, "*In vivo* substitution of zinc by cobalt in carbonic anhydrase of a marine diatom", Limnology and Oceanography **41**, 3, 573–577 (1996).

Yen, A. S., R. Gellert, C. Schröder, R. V. Morris, J. F. Bell, A. T. Knudson, B. C. Clark, D. W. Ming, J. A. Crisp, R. E. Arvidson, D. Blaney, J. Brückner, P. R. Christensen, D. J. DesMarais, P. A. de Souza, T. E. Economou, A. Ghosh, B. C. Hahn, K. E. Herkenhoff, L. A. Haskin, J. A. Hurowitz, B. L. Joliff, J. R. Johnson, G. Klingelhöfer, M. B. Madsen, S. M. McLennan, H. Y. McSween, L. Richter, R. Rieder, D. Rodionov, L. Soderblom, S. W. Squyres, N. J. Tosca, A. Wang, M. Wyatt and J. Zipfel, "An integrated view of the chemistry and mineralogy of martian soils", Nature **436**, 7047, 49–54 (2005).

Yomogida, K. and T. Matsui, "Physical properties of ordinary chondrites", Journal of Geophysical Research: Solid Earth (1978–2012) **88**, B11, 9513–9533 (1983).

Young, E. D., "The hydrology of carbonaceous chondrite parent bodies and the evolution of planet progenitors", Philosophical Transactions of the Royal Society of London A **359**, 1787, 2095–2110 (2001).

Young, E. D., K. K. Zhang and G. Schubert, "Conditions for pore water convection within carbonaceous chondrite parent bodies–Implications for planetesimal size and heat production", Earth and Planetary Science Letters **213**, 3, 249–259 (2003).

Young, P. A., S. J. Desch, A. D. Anbar, R. Barnes, N. R. Hinkel, R. Kopparapu, N. Madhusudhan, N. Monga, M. D. Pagano, M. A. Riner, S. Evan, S.-H. Shim and A. Truitt, "Astrobiological stoichiometry", Astrobiology **14**, 7, 603–626 (2014).

Yund, R. A. and R. H. McCallister, "Kinetics and mechanisms of exsolution", Chemical Geology **6**, 5–30 (1970).

Zar, J. H., *Biostatistical Analysis, 5th Edition*, pp. 130–138 (Prentice Hall, 2010).

Zerkle, A. L., C. H. House and S. L. Brantley, "Biogeochemical signatures through time as inferred from whole microbial genomes", American Journal of Science **305**, 6-8, 467–502 (2005).

Zerkle, A. L., C. H. House, R. P. Cox and D. E. Canfield, "Metal limitation of cyanobacterial N_2 fixation and implications for the Precambrian nitrogen cycle", Geobiology **4**, 4, 285–297 (2006).

Zhong, F., K. L. Mitchell, C. C. Hays, M. Choukroun, M. Barmatz and J. S. Kargel, "The rheology of cryovolcanic slurries: motivation and phenomenology of methanol-water slurries with implications for Titan", Icarus **202**, 2, 607–619 (2009).

Zimmerman, A. E., S. D. Allison and A. C. Martiny, "Phylogenetic constraints on elemental stoichiometry and resource allocation in heterotrophic marine bacteria", Environmental Microbiology **16**, 5, 1398–1410 (2014).

Zolensky, M., R. Barrett and L. Browning, "Mineralogy and composition of matrix and chondrule rims in carbonaceous chondrites", Geochimica et Cosmochimica Acta **57**, 13, 3123–3148 (1993).

Zolensky, M. E., R. J. Bodnar, E. K. Gibson, L. E. Nyquist, Y. Reese, C.-Y. Shih and H. Wiesmann, "Asteroidal water within fluid inclusion-bearing halite in an H5 chondrite, Monahans (1998)", Science **285**, 5432, 1377–1379 (1999).

Zolensky, M. E., W. L. Bourcier and J. L. Gooding, "Aqueous alteration on the hydrous asteroids: Results of *EQ3/6* computer simulations", Icarus **78**, 2, 411–425 (1989).

Zolotov, M. Y., "An oceanic composition on early and today's Enceladus", Geophysical Research Letters **34**, 23, L23203 (2007).

Zolotov, M. Y., "On the composition and differentiation of Ceres", Icarus **204**, 1, 183–193 (2009).

Zolotov, M. Y., "Aqueous fluid composition in CI chondritic materials: Chemical equilibrium assessments in closed systems", Icarus **220**, 713–729 (2012).

Zolotov, M. Y., "Formation of brucite and cronstedtite-bearing mineral assemblages on Ceres", Icarus **228**, 13–26 (2014).

Zolotov, M. Y. and J. S. Kargel, "On the chemical composition of Europa's icy shell, ocean, and underlying rocks", in "Europa", edited by R. T. Pappalardo, W. B. McKinnon and K. Khurana, pp. 431–458 (University of Arizona Press, 2009).

Zolotov, M. Y. and M. V. Mironenko, "Hydrogen chloride as a source of acid fluids in parent bodies of chondrites", in "38th Lunar and Planetary Science Conference Abstracts", p. 2340 (2007).

Zolotov, M. Y. and E. L. Shock, "Composition and stability of salts on the surface of Europa and their oceanic origin", Journal of Geophysical Research **106**, E12, 32815–32832 (2001).

Zolotov, M. Y., E. L. Shock, A. C. Barr and R. T. Pappalardo, "Brine pockets in the icy shell on Europa: Distribution, chemistry, and habitability", in "Workshop on Europa's Icy Shell: Past, Present, and Future", p. 7028 (2004).

APPENDIX A

ELEMENTAL ABUNDANCES IN SOLUTIONS, *E. COLI*, AND FIELD SAMPLES

Table 21: Elemental abundances (by mass relative to sample dry mass) in autoclaved solutions used in the separation procedure, unseparated and separated *E. coli* cells, and field samples

The sampling site names given in quotes are unofficial and correspond only to our own sampling program. For the solutions and *E. coli* samples, the uncertainties are 2x the standard error on the mean over replicates (about 95% confidence level). For the field samples, the uncertainties are the maximum between the standard deviation from the mean and 2x the standard error on separated *E. coli*. The latter uncertainty estimation is useful when a separation yielded enough sample to analyze only one replicate, but can lead to overestimates for elements which are scarce in *E. coli* but abundant in field samples. The %C and %N values of field samples were corrected to account for a 10% loss during separation. "BDL" indicates a measured value of less than either the lowest calibration standard (IRMS) or 3 times the analytical blank (ICP-MS). "BQL" indicates a measured value of less than 10 times the instrumental uncertainty on the analytical blank, considered a lower limit for quantification. "BSFD" indicates a measured net negative value after subtraction of the measurement on a sample-free digestion. [a] Uncertainty estimate based on that for *E. coli*. [b] Value above top ICP-MS calibration standard. [c] Wade (1952). [d] Data collected using atomic absorption spectrophotometry (Jones *et al.*, 1979). [e] The sediment sample was a hanging mat splashed by hot spring water; the temperature and pH refer to those measured in the spring.

Table 21: (Continued from previous page.)

	T_{spring} °C	pH (spring)	Photo-synthesis?	# replicates IRMS	C %	N %	δ^{13}C ‰	δ^{15}N ‰	# replicates ICP-MS	^{31}P-H_2 %	^{31}P %
Nycodenz				4	25.8 ± 0.6	5.1 ± 0.1	-30.3 ± 0.7	0.0 ± 0.4	4	BDL	$(3 \pm 4)10^{-4}$
Extraction buffer				2	16.3 ± 0.2	BDL	-26.4 ± 0.2	BDL	4	2.03 ± 0.08	1.83 ± 0.07
0.85% NaCl				4	BDL	BDL	BDL	BDL	4	BDL	$(1 \pm 1)10^{-4}$
E. coli, unseparated, NaCl-washed	37			4	44.1 ± 1.6	13.7 ± 0.6	-21.7 ± 0.2	4.3 ± 0.2	4	N/A	1.62 ± 0.08
E. coli, unseparated, buffer-washed	37			4	44.1 ± 1.6	13.7 ± 0.6	-21.7 ± 0.2	4.3 ± 0.2	4	N/A	1.63 ± 0.08
E. coli, separated	37			38	39.6 ± 0.3	12.3 ± 1.8	-21.8 ± 0.5	4.0 ± 0.4	4	N/A	1.40 ± 0.04
E. coli, seawater medium	20	7.5 to 7.8		N/A	N/A	N/A	N/A	N/A	N/A	N/A	2.3 ± 0.5[c]
'Bison Pool' outflow #4	66	8	Yes	N/A	N/A	N/A	N/A	N/A	1	0.12 ± 0.01	0.12 ± 0.01[a]
'Boulder spring', source	93	8	Yes[e]	3	33.7 ± 1.5	5.0 ± 0.7	-14.7 ± 0.8	-4.1 ± 0.4	3	0.12 ± 0.06	0.11 ± 0.04
'Boulder spring', outflow #3, red filaments	66	9	Yes	N/A	N/A	N/A	N/A	N/A	1	BQL	0.016 ± 0.001[a]
'Goldilocks spring', source	53	2	No	N/A	N/A	N/A	N/A	N/A	1	0.23 ± 0.04	0.19 ± 0.02[a]
'Goldilocks spring', black mat	41	3	Yes	7	41.5 ± 3.1	5.9 ± 0.5	-11.8 ± 0.6	-0.4 ± 0.5	7	0.34 ± 0.09	0.29 ± 0.06
'Goldilocks spring', green filaments	41	3	Yes	3	43.4 ± 0.6	9.0 ± 0.4	-20.9 ± 1.6	-5.4 ± 0.4	3	0.53 ± 0.08	0.44 ± 0.07
'Green Cheese'	57	6	Yes	3	34.7 ± 3.4	3.1 ± 0.4	-23.3 ± 1.2	-4.3 ± 2.8	1	0.12 ± 0.01[a]	0.11 ± 0.01[a]
'Mound spring', marsh	24	10	Yes	N/A	N/A	N/A	N/A	N/A	1	BQL	0.08 ± 0.01[a]
'Mound spring', outflow #1, West	88	8	No	N/A	N/A	N/A	N/A	N/A	1	BDL	0.09 ± 0.01
'Octopus spring', outflow #3	67	8	Yes	N/A	N/A	N/A	N/A	N/A	2	0.42 ± 0.10	0.34 ± 0.04[a]
'Spears'	26	3	Yes	N/A	N/A	N/A	N/A	N/A	1	0.12 ± 0.01[a]	0.11 ± 0.01[a]

Table 21: (Continued from previous page.)

	^{24}Mg ppm	^{27}Al ppm	^{39}K ppm	^{44}Ca ppm	^{48}Ti ppm	^{51}V ppm	^{52}Cr ppm	^{55}Mn-H_2 ppm	^{55}Mn ppm
Nycodenz	BQL	0.6 ± 1.4	BDL	BQL	0.8 ± 0.3	BDL	0.03 ± 0.09	BDL	BQL
Extraction	1.0 ± 0.2	1.9 ± 1.1	640 ± 20	BDL	2.1 ± 0.7	BQL	BSFD	BDL	BQL
0.85% NaCl	1.1 ± 0.6	0.9 ± 0.7	28 ± 6	BDL	0.3 ± 0.1	BDL	0.11 ± 0.10	BDL	BQL
E. coli, unseparated, NaCl-washed	829 ± 58	4.3 ± 1.9	240 ± 36^{b}	237 ± 19	1.71 ± 0.29	0.21 ± 0.07	0.08 ± 0.05	6.40 ± 0.64	5.53 ± 0.37
E. coli, unseparated, buffer-washed	391 ± 8	3.0 ± 0.8	389 ± 19^{b}	166 ± 12	1.51 ± 0.20	0.10 ± 0.02	0.09 ± 0.05	3.63 ± 0.36	3.12 ± 0.22
E. coli, separated	542 ± 32^{a}	5.4 ± 1.4	97 ± 3^{b}	327 ± 49	6.13 ± 2.79	0.20 ± 0.01	0.32 ± 0.05	5.86 ± 0.35^{a}	5.02 ± 0.30^{a}
E. coli, seawater medium	1351	N/A	1789	42	N/A	N/A	N/A	3	3
'Bison Pool' outflow #4	199 ± 36^{a}	1130 ± 600^{a}	59 ± 15^{a}	8800 ± 3300	10.1 ± 2.4^{a}	BDL	0.1 ± 0.2	34.8 ± 8.0^{a}	30.1 ± 6.9^{a}
'Boulder spring', source	300 ± 200	5000 ± 2400^{a}	290 ± 260^{a}	1070 ± 4000^{a}	19 ± 16	1.1 ± 1.1^{a}	1.1 ± 0.8^{a}	28.3 ± 18.1	23.1 ± 15.0
'Boulder spring', outflow #3, red filaments	390 ± 70^{a}	2200 ± 1100^{a}	300 ± 70^{a}	800 ± 300^{a}	25.5 ± 6.1^{a}	1.1 ± 1.1^{a}	1.5 ± 1.1^{a}	113 ± 26^{a}	99 ± 23^{a}
'Goldilocks spring', source	42.4 ± 7.6^{a}	360 ± 170^{a}	131 ± 33^{a}	1100 ± 400^{a}	55.1 ± 13.2^{a}	1.0 ± 1.0^{a}	1.8 ± 1.3^{a}	1.6 ± 0.5	1.4 ± 0.3^{a}
'Goldilocks spring', black mat	38.1 ± 14.7	850 ± 410^{a}	44.2 ± 15.4	BQL	86.1 ± 21.5	1.4 ± 1.4^{a}	2.6 ± 1.9^{a}	7.2 ± 2.0	6.1 ± 1.4^{a}
'Goldilocks spring', green filaments	237 ± 43^{a}	1440 ± 690^{a}	219 ± 55^{a}	110 ± 40^{a}	18.5 ± 11.7	0.5 ± 0.5^{a}	0.8 ± 0.6^{a}	28.8 ± 0.6^{a}	25.0 ± 5.8^{a}
'Green Cheese'	353 ± 64^{a}	6100 ± 2900^{a}	380 ± 95^{a}	6000 ± 2200^{a}	380 ± 90^{a}	22 ± 21^{a}	46 ± 33^{a}	44.4 ± 10.2^{a}	38.6 ± 8.9^{a}
'Mound spring', marsh	266 ± 48^{a}	490 ± 240^{a}	286 ± 71^{a}	5600 ± 2100^{a}	19.6 ± 4.7^{a}	3.1 ± 3.0^{a}	2.9 ± 2.1^{a}	13.6 ± 3.1^{a}	12.1 ± 2.7^{a}
'Mound spring', outflow #1, West	39 ± 7^{a}	1850 ± 890^{a}	BDL	BQL	10.0 ± 2.4^{a}	BDL	0.35 ± 0.26	8.5 ± 1.9^{a}	8.3 ± 1.9^{a}
'Octopus spring', outflow #3	572 ± 100^{a}	10500 ± 5100^{a}	551 ± 160	2000 ± 700^{a}	15.9 ± 3.9^{a}	1.8 ± 1.7^{a}	0.5 ± 0.4^{a}	91 ± 21^{a}	74 ± 17^{a}
'Spears'	94 ± 17^{a}	3300 ± 1600^{a}	337 ± 84^{a}	BQL	90 ± 22^{a}	9.0 ± 8.7^{a}	9.3 ± 6.7^{a}	4.2 ± 1.0^{a}	3.7 ± 0.9^{a}

Table 21: (Continued from previous page.)

	^{54}Fe ppm	^{56}Fe ppm	^{57}Fe ppm	^{59}Co ppm	^{58}Ni ppm	^{60}Ni ppm	^{63}Cu ppm	^{65}Cu ppm	^{66}Zn ppm	^{68}Zn ppm	^{95}Mo ppm
Nycodenz	BQL	BQL	BDL	0.2 ± 0.1	BQL	0.04 ± 0.01	2.8 ± 0.6	BQL	0.4 ± 0.2	0.3 ± 0.2	BSFD
Extraction buffer	BQL	0.7 ± 1.3	BDL	1.8 ± 1.5	BDL	BDL	20 ± 3	BQL	2.1 ± 0.4	1.8 ± 0.3	BSFD
0.85% NaCl	BQL	0.4 ± 0.5	BDL	0.2 ± 0.1	BQL	BQL	52 ± 8	0.7 ± 0.03	0.5 ± 0.2	0.5 ± 0.2	BSFD
E. coli, unseparated, NaCl-washed	208 ± 17	207 ± 17	209 ± 19	1.04 ± 0.85	2.17 ± 0.13	2.40 ± 0.17	3.34 ± 0.23	3.07 ± 0.21	44.8 ± 1.3^{b}	40.7 ± 1.2	3.47 ± 0.62
E. coli, unseparated, buffer-washed	203 ± 18	201 ± 18	203 ± 16	0.57 ± 0.09	2.20 ± 0.15	2.48 ± 0.17	3.37 ± 0.24	3.19 ± 0.22	42.9 ± 1.7	39.1 ± 1.6	3.63 ± 1.65
E. coli, separated	247 ± 32	203 ± 10	201 ± 19	5.74 ± 0.75^{a}	2.25 ± 0.13	2.35 ± 0.13	3.55 ± 0.31	3.20 ± 0.24	43.2 ± 1.0	38.8 ± 1.0	3.35 ± 0.13
E. coli, seawater medium	111	111	111	N/A	1	1	11	11	76	76	N/A
'Bison Pool' outflow #4	129 ± 22	128 ± 10^{a}	126 ± 19	127 ± 48^{a}	1.2 ± 0.3^{a}	1.4 ± 0.5^{a}	14.0 ± 3.4^{a}	10.5 ± 2.2^{a}	25.2 ± 4.3^{a}	23.2 ± 4.2^{a}	BSFD
'Boulder spring', source	720 ± 570	710 ± 570	710 ± 570	52 ± 53^{a}	4.4 ± 2.9	3.0 ± 1.1^{a}	14.4 ± 3.7	9.8 ± 2.5	29.0 ± 13.6	27.3 ± 12.5	BSFD
'Boulder spring', outflow #3, red filaments	1940 ± 250^{a}	1940 ± 160^{a}	1970 ± 180^{a}	45 ± 46^{a}	8.7 ± 2.3^{a}	0.9 ± 0.3^{a}	22.6 ± 5.4^{a}	17.6 ± 3.7^{a}	25.1 ± 4.3^{a}	22.8 ± 4.1^{a}	1.8 ± 0.2^{a}
'Goldilocks spring', source	110 ± 20	111 ± 9^{a}	100 ± 25	14 ± 14^{a}	2.1 ± 0.6^{a}	3.2 ± 1.2^{a}	50.1 ± 12.0^{a}	29.0 ± 6.0^{a}	16.2 ± 2.8^{a}	14.6 ± 2.6^{a}	80.5 ± 10.5^{a}
'Goldilocks spring', black mat	1180 ± 320	1180 ± 320	1180 ± 330	26 ± 27^{a}	7.6 ± 2.1^{a}	5.0 ± 1.9^{a}	11.6 ± 2.8^{a}	10.2 ± 2.1^{a}	32.8 ± 11.5	29.9 ± 10.8	5.3 ± 1.4
'Goldilocks spring', green filaments	550 ± 90	540 ± 90	550 ± 90	0.7 ± 0.7^{a}	6.8 ± 1.8^{a}	8.8 ± 3.3^{a}	1.8 ± 0.4^{a}	1.7 ± 0.4^{a}	25.4 ± 4.3^{a}	23.6 ± 4.2^{a}	6.0 ± 0.9^{a}
'Green Cheese'	3200 ± 420^{a}	3160 ± 250^{a}	3170 ± 290^{a}	59 ± 59^{a}	17.7 ± 4.8^{a}	8.1 ± 3.1^{a}	12.4 ± 3.0^{a}	10.8 ± 2.3^{a}	32.4 ± 5.5^{a}	32.4 ± 5.8^{a}	10.9 ± 1.4^{a}
'Mound spring', marsh	410 ± 50^{a}	400 ± 30^{a}	400 ± 50	80 ± 82^{a}	3.7 ± 1.0^{a}	4.2 ± 1.6^{a}	15.1 ± 3.6^{a}	8.1 ± 1.7^{a}	38.0 ± 6.5^{a}	34.7 ± 6.2^{a}	BSFD
'Mound spring', outflow #1, West	440 ± 60	420 ± 30^{a}	410 ± 80	30 ± 31^{a}	2.7 ± 0.7^{a}	BQL	BQL	BQL	20.6 ± 3.5^{a}	18.2 ± 3.3^{a}	BSFD
'Octopus spring', outflow #3	610 ± 130	610 ± 130	610 ± 120	14 ± 14^{a}	4.3 ± 1.2^{a}	3.5 ± 1.3^{a}	15.1 ± 3.6^{a}	10.7 ± 2.2^{a}	25.3 ± 4.3^{a}	23.2 ± 4.2^{a}	BSFD
'Spears'	2890 ± 380^{a}	2910 ± 230^{a}	2900 ± 260^{a}	37 ± 38^{a}	13.1 ± 3.5^{a}	1.0 ± 0.4^{a}	$9,2 \pm 2.2^{a}$	7.7 ± 1.6^{a}	12.0 ± 2.0^{a}	11.5 ± 2.1^{a}	7.4 ± 1.0^{a}

APPENDIX B

ELEMENTAL COMPOSITION OF CELL COMMUNITIES SEPARATED FROM YNP SEDIMENT

Table 22: Elemental composition of cell communities separated from YNP sediment

Sediment was sampled at the hot springs listed in Tables 3 and 4. Uncertainties are the maximum between the standard deviation from the mean over n biological replicates and 2x the standard error on separated *E. coli*. The latter uncertainty estimation is useful when a separation yielded enough sample to analyze only one replicate. The percentages in brackets are estimates of the level of sediment contamination for the element measured, assuming all Al in cells came from sediment (see text). Calculated values can be higher than 100% due to measurement uncertainties. "IRMS": Isotope Ratio Mass Spectrometry analysis; "ICP-MS": Inductively-Coupled Plasma Mass Spectrometry analysis; "N/A": not available; "BDL": below detection limit (3x the instrumental uncertainty on the blank, determined by averaging over 3 ICP-MS measurements of the same sample); "BQL": below quantification limit (10x the instrumental uncertainty on the blank); "BBV": below blank value. [a] These samples underwent DNA sequencing (Table 5). [b] For these samples, C and N abundances could not be obtained.

Table 22: (Continued from previous page.)

Sample ID	# biological replicates (n)	% C (by dry mass)	% N (by dry mass)	% P (by dry mass)	ppm Mg (by dry mass)	ppm Ca (by dry mass)	ppm Ti (by dry mass)	ppm V (by dry mass)
090725D1	4 IRMS / 2 ICP-MS	35 ± 1.4 [3.7%]	5.5 ± 0.1 [3.3%]	0.34 ± 0.04 [2.8%]	572 ± 100 [35%]	1970 ± 730 [66%]	16 ± 4 [1140%]	1.8 ± 1.7 [94%]
090730V1 (black mat)[a]	7 IRMS / 7 ICP-MS	38 ± 2.8 [1.0%]	5.4 ± 0.4 [0.6%]	0.29 ± 0.06 [0.5%]	38 ± 15 [25%]	N/A	86 ± 22 [43%]	1.4 ± 1.4 [9%]
090730V1 (green filaments)[a]	3 IRMS / 3 ICP-MS	39 ± 0.5 [3.7%]	8.1 ± 0.4 [3.2%]	0.44 ± 0.07 [1.6%]	237 ± 42 [22%]	106 ± 40 [45%]	18 ± 12 [332%]	0.5 ± 0.5 [49%]
090802W1[a]	3 IRMS / 1 ICP-MS	32 ± 3.1 [0.7%]	2.8 ± 0.4 [0.8%]	0.11 ± 0.01 [2.9%]	353 ± 62 [49%]	5960 ± 2220 [10%]	382 ± 93 [49%]	22 ± 21 [12%]
090726O1	4 IRMS / 4 ICP-MS	37 ± 1.5 [14%]	4.5 ± 0.1 [13%]	0.2 ± 0.2 [17%]	1430 ± 1450 [66%]	2030 ± 2290 [162%]	318 ± 320 [117%]	6.8 ± 6.9 [88%]
090804P1[a]	1 IRMS / 2 ICP-MS	31 ± 0.2 [1.6%]	5.1 ± 0.1 [1.2%]	0.06 ± 0.003 [8.8%]	579 ± 107 [94%]	480 ± 100 [213%]	64 ± 15 [268%]	0.7 ± 1.0 [308%]
090804J1	1 IRMS / 1 ICP-MS	32 ± 0.8 [5.0%]	5.5 ± 0.1 [3.8%]	0.04 ± 0.001 [17%]	362 ± 26 [97%]	858 ± 100 [137%]	78 ± 10 [403%]	3.0 ± 6.0 [106%]
090728A1[a]	3 IRMS / 3 ICP-MS	31 ± 1.4 [13%]	4.5 ± 0.6 [9.0%]	0.11 ± 0.04 [7.1%]	301 ± 203 [25%]	10700 ± 3970 [9%]	19 ± 16 [126%]	1.1 ± 1.1 [35%]
090729Q1[a]	4 IRMS / 1 ICP-MS	21 ± 0.9 [12%]	2.1 ± 0.1 [17%]	0.08 ± 0.003 [29%]	1249 ± 231 [87%]	1230 ± 170 [227%]	531 ± 103 [367%]	22 ± 0.4 [96%]
090730C1	1 IRMS / 1 ICP-MS	45 ± 0.8 [0.3%]	10.1 ± 0.1 [0.2%]	0.06 ± 0.001 [2.1%]	4.5 ± 0.3 [57%]	BBV	13 ± 2 [37%]	0.2 ± 0.3 [15%]
090723K	8 IRMS / 4 ICP-MS	37 ± 7.6 [4.5%]	1.9 ± 0.4 [8.1%]	0.23 ± 0.11 [4.3%]	977 ± 468 [114%]	3430 ± 1200 [92%]	1598 ± 1038 [76%]	97 ± 49 [22%]
090723F	2 IRMS / 4 ICP-MS	29 ± 0.8 [0.1%]	1.2 ± 0.3 [0.2%]	0.01 ± 0.02 [2.5%]	53 ± 49 [23%]	96 ± 95 [74%]	220 ± 136 [19%]	13.0 ± 6.9 [3%]
090730T1	2 IRMS / 4 ICP-MS	26 ± 1.9 [4.0%]	0.6 ± 0.1 [18%]	0.11 ± 0.09 [15%]	420 ± 462 [115%]	4760 ± 4480 [57%]	473 ± 560 [408%]	4.8 ± 6.4 [139%]
090723C	1 IRMS / 3 ICP-MS	21 ± 0.8 [3.0%]	2.2 ± 0.1 [3%]	0.04 ± 0.04 [12%]	882 ± 264 [89%]	277 ± 181 [916%]	804 ± 187 [104%]	56 ± 16 [22%]
090728D1[b]	1 ICP-MS	N/A	N/A	0.02 ± 0.002 [4.3%]	391 ± 69 [13%]	880 ± 330 [25%]	25 ± 6 [265%]	1.1 ± 1.0 [42%]
090724QA[b]	1 ICP-MS	N/A	N/A	0.08 ± 0.01 [1.3%]	266 ± 47 [17%]	5640 ± 2090 [6%]	20 ± 5 [80%]	3.1 ± 3.0 [11%]
090730U1[b]	1 ICP-MS	N/A	N/A	0.19 ± 0.02 [0.02%]	42 ± 7 [2%]	1120 ± 420 [1%]	55 ± 13 [29%]	1.0 ± 1.0 [3%]
090724OA[b]	1 ICP-MS	N/A	N/A	0.09 ± 0.01 [1.4%]	39 ± 7 [74%]	N/A	10 ± 2 [102%]	BBV
090728RA[b]	1 ICP-MS	N/A	N/A	0.01 ± 0.02 [5%]	29 ± 5 [16%]	N/A	47 ± 11 [387%]	BBV
090730UA[b]	2 ICP-MS	N/A	N/A	0.01 ± 0.002 [2.2%]	11 ± 3 [19%]	172 ± 91 [10%]	375 ± 337 [36%]	2.3 ± 4.1 [6%]
090725DA[b]	3 ICP-MS	N/A	N/A	0.12 ± 0.04 [6.0%]	1430 ± 490 [84%]	890 ± 230 [371%]	1320 ± 390 [93%]	68 ± 21 [32%]
090726N1[b]	2 ICP-MS	N/A	N/A	0.03 ± 0.003 [N/A]	2330 ± 640 [32%]	N/A	353 ± 125 [100%]	6.8 ± 2.7[66%]
090730XA [b]	2 ICP-MS	N/A	N/A	0.03 ± 0.01 [2.8%]	22 ± 5 [16%]	420 ± 147 [10%]	120 ± 23 [81%]	BBV
090730Z1[b]	1 ICP-MS	N/A	N/A	0.32 ± 0.02 [1.2%]	243 ± 17 [80%]	1170 ± 140 [32%]	928 ± 124 [83%]	2.8 ± 5.6 [38%]
090802NA[b]	1 ICP-MS	N/A	N/A	0.28 ± 0.01 [0.2%]	1127 ± 80 [91%]	1090 ± 130 [21%]	84 ± 11 [129%]	2.7 ± 5.4 [57%]
090802OA[b]	1 ICP-MS	N/A	N/A	0.04 ± 0.002 [3.4%]	71 ± 5 [89%]	393 ± 46 [81%]	15 ± 2 [121%]	0.6 ± 1.2 [64%]
090802PA[b]	1 ICP-MS	N/A	N/A	0.12 ± 0.003 [6.3%]	3330 ± 240 [35%]	1150 ± 130 [375%]	194 ± 26 [148%]	218 ± 430 [12%]
090802QA[b]	1 ICP-MS	N/A	N/A	0.4 ± 0.001 [61%]	2900 ± 200 [81%]	349 ± 41 [1500%]	358 ± 48 [271%]	173 ± 342 [27%]
R^2, Coefficient of determination (Fig. 1)	0.0006	0.0008	0.013	0.74	0.0002	0.47	0.76	

Table 22: (Continued from previous page.)

Sample ID	ppm Cr (by dry mass)	ppm Mn (by dry mass)	ppm Fe (by dry mass)	ppm Co (by dry mass)	ppm Ni (by dry mass)	ppm Cu (by dry mass)	ppm Zn	ppm Mo
090725D1	0.5 ± 0.4 [237%]	74 ± 17 [95%]	600 ± 130 [196%]	14 ± 13 [1.4%]	3.5 ± 1.3 [13%]	10.7 ± 2.2 [5.0%]	23 ± 4[36%]	BDL
090730V1 (black mat)[a]	2.6 ± 1.8 [5%]	6.1 ± 1.4 [15%]	1170 ± 320 [5%]	26 ± 25 [0.03%]	5.0 ± 1.9 [2%]	10.2 ± 2.1 [0.7%]	30 ± 11 [2.3%]	5.3 ± 1.4 [2.6%]
090730V1 (green filaments)[a]	0.8 ± 0.6 [25%]	25 ± 6 [13%]	540 ± 90 [30%]	0.7 ± 0.7 [2.0%]	8.8 ± 3.3 [4%]	1.7 ± 0.4 [9.8%]	24 ± 4 [7.5%]	6.0 ± 0.9 [9.6%]
090802W1[a]	46 ± 33 [11%]	39 ± 9 [54%]	3150 ± 250 [41%]	58 ± 54 [0.6%]	8.1 ± 3.0 [13%]	10.8 ± 2.3 [6.7%]	32 ± 6 [15%]	10.9 ± 1.4 [6.2%]
090726O1	16 ± 17 [123%]	360 ± 364 [65%]	6550 ± 6480 [51%]	9 ± 13 [9.4%]	14 ± 12 [43%]	4.4 ± 3.6 [83%]	31 ± 29 [73%]	3.6 ± 2.0 [40%]
090804P1[a]	3.9 ± 2.6 [98%]	59 ± 12 [111%]	1280 ± 150 [103%]	57 ± 37 [0.4%]	4.0 ± 1.6 [32%]	5.0 ± 1.8 [14%]	17 ± 2 [42%]	0.3 ± 0.1 [99%]
090804J1	3.6 ± 0.1 [55%]	116 ± 4 [69%]	2270 ± 90 [81%]	0.7 ± 0.1 [46%]	3.3 ± 0.2 [26%]	14.9 ± 1.7 [12%]	48 ± 4 [25%]	1.2 ± 0.1 [42%]
090728A1[a]	1.1 ± 0.8 [73%]	23 ± 15 [83%]	710 ± 560 [73%]	52 ± 49 [0.1%]	3.0 ± 1.1 [15%]	9.8 ± 2.5 [3.3%]	27 ± 13 [13%]	BDL
090729Q1[a]	13 ± 6 [88%]	260 ± 50 [67%]	24500 ± 2500 [51%]	5.7 ± 2.3 [26%]	9.7 ± 2.4 [36%]	7.8 ± 0.8 [45%]	84 ± 10 [95%]	46 ± 14 [51%]
090730C1	0.002 ± 0.003 [3100%]	0.4 ± 0.01 [49%]	48 ± 2 [12%]	0.1 ± 0.01 [2.7%]	BBV	6.1 ± 0.7 [0.4%]	20 ± 2 [0.5%]	106 ± 0.5 [0.4%]
090723K	141 ± 98 [22%]	147 ± 46 [51%]	15100 ± 5900 [39%]	3.8 ± 2.4 [45.3%]	11.4 ± 10.7 [51%]	67 ± 83 [9.1%]	96 ± 92 [24%]	124 ± 183 [8.6%]
090723F	16 ± 10 [5%]	4.2 ± 2.1 [89%]	760 ± 500 [25%]	2.0 ± 1.6 [2.0%]	1.4 ± 1.6 [12%]	36 ± 23 [0.7%]	7 ± 5 [17%]	269 ± 158 [0.3%]
090730T1	BBV	120 ± 101 [56%]	7700 ± 5600 [93%]	1.3 ± 0.6 [43%]	BBV	27 ± 24 [15%]	30 ± 23 [121%]	BBV
090723C	56 ± 21 [30%]	31 ± 10 [187%]	9060 ± 2780 [45%]	2.4 ± 0.6 [48%]	5.6 ± 5.1 [62%]	63 ± 9 [4.8%]	48 ± 21 [34%]	88 ± 11 [5.5%]
090728D1[b]	1.5 ± 1.1 [23%]	99 ± 23 [17%]	1930 ± 160 [27%]	45 ± 42 [0.1%]	0.9 ± 0.3 [9%]	18 ± 4 [0.6%]	23 ± 4 [12%]	1.8 ± 0.2 [15%]
090724QA[b]	2.9 ± 2.1 [10%]	12 ± 3 [37%]	402 ± 32 [31%]	81 ± 76 [0.1%]	4.2 ± 1.6 [4%]	8.1 ± 1.7 [12%]	35 ± 6 [11%]	BDL
090730U1[b]	1.8 ± 1.3 [2%]	1.4 ± 0.3 [30%]	110 ± 9 [20%]	150 ± 140 [0.002%]	3.2 ± 1.2 [0.2%]	29 ± 6 [0.1%]	15 ± 3 [2.3%]	81 ± 10 [0.1%]
090724OA[b]	0.4 ± 0.3 [51%]	8.3 ± 1.9 [59%]	422 ± 34 [23%]	30 ± 28 [0.1%]	BQL	BQL	18 ± 3 [5.2%]	BDL
090728RA[b]	3.7 ± 2.6 [34%]	2.3 ± 0.5 [18%]	670 ± 50 [27%]	200 ± 190 [0.3%]	BQL	BQL	43 ± 8 [0.3%]	BDL
090730UA[b]	1.7 ± 0.8 [13%]	0.3 ± 0.1 [268%]	159 ± 94 [524%]	18 ± 10 [0.4%]	1.0 ± 0.3 [33%]	5.2 ± 2.6 [6.1%]	19 ± 3 [5.8%]	4.8 ± 3.6 [7.6%]
090725DA[b]	74 ± 35 [39%]	44 ± 9 [176%]	10600 ± 3700 [45%]	20 ± 12 [9.1%]	11.0 ± 2.8 [49%]	59 ± 45 [9.2%]	51 ± 10 [48%]	51 ± 18 [13%]
090726N1[b]	7.9 ± 3.7 [40%]	890 ± 240 [22%]	7580 ± 1960 [36%]	12 ± 8 [4.3%]	4.9 ± 1.2 [25%]	4.0 ± 0.4 [23%]	49 ± 9 [43%]	0.8 ± 0.3 [70%]
090730XA[b]	1.9 ± 0.9 [18%]	2.1 ± 0.4 [83%]	910 ± 590 [92%]	4.2 ± 1.9 [2.0%]	0.7 ± 0.2 [19%]	4.1 ± 1.8 [8.8%]	20 ± 3 [5.3%]	7.8 ± 1.5 [14%]
090730Z1[b]	21 ± 3 [3%]	17 ± 1 [54%]	8790 ± 780 [133%]	6.5 ± 1.2 [21%]	11.9 ± 0.8 [11%]	23 ± 3 [19%]	122 ± 11 [15%]	14.4 ± 0.7 [41%]
090802NA[b]	215 ± 12 [1%]	115 ± 4 [56%]	2430 ± 120 [32%]	4.8 ± 0.9 [3.7%]	106 ± 7 [0.5%]	25 ± 3 [1.3%]	79 ± 7 [4.7%]	24 ± 1 [1.1%]
090802OA[b]	0.7 ± 0.3 [46%]	8.4 ± 0.4 [101%]	255 ± 26 [58%]	0.8 ± 0.1 [7.2%]	BBV	4.7 ± 0.5 [2.7%]	41 ± 4 [3.6%]	BBV
090802PA[b]	17 ± 3 [27%]	420 ± 10 [32%]	5070 ± 410 [50%]	3.2 ± 0.6 [23%]	1.9 ± 0.1 [93%]	22 ± 2.5 [20%]	81 ± 7 [55%]	BBV
090802QA[b]	29 ± 2 [54%]	110 ± 4 [130%]	162000 ± 740 [49%]	2.9 ± 0.5 [70%]	5.8 ± 0.4 [81%]	18 ± 2 [21%]	58 ± 5 [64%]	1.8 ± 0.1 [126%]
R^2, Coefficient of determination (Fig. 1)	0.21	0.62	0.79	0.05	0.0009	0.36	0.32	0.04

APPENDIX C

ADDED THERMODYNAMIC DATA FOR SOLIDS

Table 23: Thermodynamic data for solids in the expanded database

These data were added to the *llnl.dat* database to create the expanded *core5.dat* database. [a] Marion *et al.* (2009). [b] Wang and Li (2011). [c] Christov (2002a). [d] Marion (2002). [e] Marion *et al.* (2008). [f] Marion *et al.* (2003). [g] Marion (2001). [h] Christov (2002b). [i] Marion *et al.* (2010). [j] Spencer *et al.* (1990). [k] Marion *et al.* (2010). [l] Marion and Farren (1999). [m] Clegg *et al.* (1998b). [n] Clegg *et al.* (1998a). [o] Marion *et al.* (2012). [p] Also called buddingtonite. The molar volume is provided for the formula $NH_4AlSi_3O_8 \cdot 0.5\ H_2O$. [q] Thermodynamic data from Watkins (1981) for the NH_4-silicate, Shock and Helgeson (1988a) for H^+ and NH_4^+, Shock *et al.* (1989) for SiO_2(aq), Shock *et al.* (1997b) for Al^{3+}, and Wagner and Prüß (2002) for H_2O. [r] Richard and Helgeson (1998). [s] Helgeson *et al.* (2009). [t] Helgeson *et al.* (1998). [u] Richard (2001).

Table 23: (Continued from previous page.)

Species	From reaction	$\log K = a_1 + a_2 T + a_3/T + a_4 \log(T) + a_6 T^2$ (T in K) a_1	a_2 (K^{-1})	a_3 (K)	a_4	a_6 (K^{-2})	T range (K)	Molar volume (cm^3 mol^{-1})
Alum-Na[a]	$NaAl(SO_4)_2 \cdot 12H_2O = Na^+ + Al^{3+} + 2SO4^{2-} + 12H_2O$	-7.604	0.01127	0	0	0	273–298	264.9
Alunogen[a]	$Al_2(SO_4)_3 \cdot 17H_2O = 2Al^{3+} + 3SO4^{2-} + 17H_2O$	-0.02575	0.1266	0	0	-2.327×10^{-4}	261–298	379.19
Bischofite[b]	$MgCl_2 \cdot 6H_2O = Mg^{2+} + 2Cl^- + 6H_2O$	72.85	0.03544	-76.59	-31.79	0	273–400	129.57
Chloraluminite[a]	$AlCl_3 \cdot 6H_2O = Al^{3+} + 3Cl^- + 6H_2O$	-47.09	0.2932	0	0	-3.746×10^{-4}	218–303	144.57
$Cr_2(SO_4)_3 \cdot 16H_2O$[c]	$Cr_2(SO_4)_3 \cdot 16H_2O = 2Cr^{3+} + 3SO_4^{2-} + 16H_2O$	-9.9070	0	0	0	0	N/A	N/A
Darapskite[d]	$Na_2SO_4 \cdot NaNO_3 \cdot 2H_2O = 3Na^+ + SO_4^{2-} + NO_3^- + 2H_2O$	61.66	-0.4861	0	0	9.415×10^{-4}	N/A	119.57
$Fe_2(SO_4)_3 \cdot 2K_2SO_4 \cdot 14H_2O$[e]	$Fe_2(SO_4)_3 \cdot 2K_2SO_4 \cdot 14H_2O = 2Fe^{3+} + 4K^+ + 5SO_4^{2-} + 14H_2O$	-13.8473	0	0	0	0	273–298	406.95
$FeCl_2 \cdot 4H_2O$[e,f]	$FeCl_2 \cdot 4H_2O = Fe^{2+} + 2Cl^- + 4H_2O$	-1.995	0.06328	0	0	-1.503×10^{-4}	N/A	103.01
$FeCl_2 \cdot 6H_2O$[e,f]	$FeCl_2 \cdot 6H_2O = Fe^{2+} + 2Cl^- + 6H_2O$	289.33	-1.93	0	0	3.26×10^{-3}	N/A	133.65
$FeCl_3 \cdot 10H_2O$[e]	$FeCl_3 \cdot 10H_2O = Fe^{3+} + 3Cl^- + 10H_2O$	-33.51	0.1279	0	0	-3.333×10^{-5}	238–273	207.59
Ferricopiapite[e]	$Fe_5(SO_4)_6O(OH) \cdot 20H_2O + 3H^+ = 5Fe^{3+} + 6SO_4^{2-} + 22H_2O$	-63.27	0	11800	0	0	273–298	594.71
$FeSO_4 \cdot K_2SO_4 \cdot 6H_2O$[e]	$FeSO_4 \cdot K_2SO_4 \cdot 6H_2O = Fe^{2+} + 2K^+ + 2SO_4^{2-} + 6H_2O$	-15.82	0.03895	0	0	0	273–298	184.01
$FeSO_4 \cdot Na_2SO_4 \cdot 4H_2O$[e]	$FeSO_4 \cdot Na_2SO_4 \cdot 4H_2O = Fe^{2+} + 2Na^+ + 2SO_4^{2-} + 4H_2O$	-2.9188	0	0	0	0	292–298	162.23
$H_2SO_4 \cdot 4H_2O$[d]	$H_2SO_4 \cdot 4H_2O = 2H^+ + SO_4^{2-} + 4H_2O$	-30.84	0.2708	0	0	-5.556×10^{-4}	N/A	113.98
$H_2SO_4 \cdot 6.5H_2O$[d]	$H_2SO_4 \cdot 6.5H_2O = 2H^+ + SO_4^{2-} + 6.5H_2O$	-38.85	0.3217	0	0	-6.417×10^{-4}	N/A	154.86
Halotrichite[a]	$FeSO_4 \cdot Al_2(SO_4)_3 \cdot 22H_2O = Fe^{2+} + 2Al^{3+} + 4SO_4^{2-} + 22H_2O$	-8.5567	0	0	0	0	N/A	483.91
$HCl \cdot 3H_2O$[d]	$HCl \cdot 3H_2O = H^+ + Cl^- + 3H_2O$	2.233	7.078×10^{-3}	0	0	0	N/A	62.51
$HCl \cdot 6H_2O$[d]	$HCl \cdot 6H_2O = H^+ + Cl^- + 6H_2O$	1.896	1.579×10^{-3}	0	0	0	N/A	101.06
$HNO_3 \cdot 3H_2O$[d]	$HNO_3 \cdot 3H_2O = H^+ + NO_3^- + 3H_2O$	-5.515	0.03061	0	0	0	N/A	73.09
Hydrohalite[d]	$NaCl \cdot 2H_2O = Na^+ + Cl^- + 2H_2O$	-4.428	0.01678	0	0	0	N/A	57.96
Hydromolysite[e]	$FeCl_3 \cdot 6H_2O = Fe^{3+} + 3Cl^- + 6H_2O$	42.19	-0.4094	0	0	9.307×10^{-4}	273–298	146.9
Ikaite[g]	$CaCO_3 \cdot 6H_2O = Ca^{2+} + CO_3^{2-} + 6H_2O$	0.1598	0	-2011	0	0	N/A	117.54
Jarosite-H_3O[e]	$H_3OFe_3(SO_4)_2(OH)_6 + 5H^+ = 3Fe^{3+} + 2SO_4^{2-} + 7H_2O$	-45.86	0	11870	0	0	273–298	178.05
$K_2SO_4 \cdot Al_2(SO_4)_3 \cdot 24H_2O$[h]	$K_2SO_4 \cdot Al_2(SO_4)_3 \cdot 24H_2O = 2K^+ + 4SO_4^{2-} + 2Al^{3+} + 24H_2O$	-11.8975	0	0	0	0	N/A	N/A
$K_2SO_4 \cdot Cr_2(SO_4)_3 \cdot 24H_2O$[h]	$K_2SO_4 \cdot Cr_2(SO_4)_3 \cdot 24H_2O = 2K^+ + 4SO_4^{2-} + 2Cr^{3+} + 24H_2O$	-11.8541	0	0	0	0	N/A	N/A
$K_3H(SO_4)_2$[d]	$K_3H(SO_4)_2 = H^+ + 2SO_4^{2-} + 3K^+$	19.81	-0.1892	0	0	3.711×10^{-4}	N/A	N/A
$K_5H_3(SO_4)_4$[d]	$K_5H_3(SO_4)_4 = 3H^+ + 4SO_4^{2-} + 5K^+$	-15.43	0.02914	0	0	0	N/A	N/A
Kalicinite[g]	$KHCO_3 = HCO_3^- + K^+$	-2.822	5.650×10^{-3}	0	0	1.495×10^{-5}	273–343	46.14
Lansfordite[i]	$MgCO_3 \cdot 5H_2O = Mg^{2+} + CO_3^{2-} + 5H_2O$	26.90	-0.23	0	0	4.122×10^{-4}	271–293	100.8
$MgCl_2 \cdot 8H_2O$[j]	$MgCl_2 \cdot 8H_2O = Mg^{2+} + 2Cl^- + 8H_2O$	989.2	0.282	-27050	-395.4	0	N/A	159.08
$MgCl_2 \cdot 12H_2O$[j]	$MgCl_2 \cdot 12H_2O = Mg^{2+} + 2Cl^- + 12H_2O$	-45.7457	0.12	0	0	-9.47×10^{-5}	273–343	218.1
$Mg(ClO_4)_2 \cdot 6H_2O$[k]	$Mg(ClO_4)_2 \cdot 6H_2O = Mg^{2+} + 2ClO_4^- + 6H_2O$	-5.492	0.06257	0	0	-8.445×10^{-5}	273–366	167.28
$MgSO_4 \cdot 12H_2O$[l]	$MgSO_4 \cdot 12H_2O = Mg^{2+} + SO_4^{2-} + 12H_2O$	-12.84	0.03844	0	0	0	N/A	220.5
$Na_2SO_4 \cdot Al_2(SO_4)_3 \cdot 24H_2O$[c]	$Na_2SO_4 \cdot Al_2(SO_4)_3 \cdot 24H_2O = 2Na^+ + 4SO_4^{2-} + 2Al^{3+} + 24H_2O$	-8.6409	0	0	0	0	N/A	N/A
$Na_2SO_4 \cdot Cr_2(SO_4)_3 \cdot 24H_2O$[c]	$Na_2SO_4 \cdot Cr_2(SO_4)_3 \cdot 24H_2O = 2Na^+ + 4SO_4^{2-} + 2Cr^{3+} + 24H_2O$	-8.1459	0	0	0	0	N/A	N/A
$Na_2SO_4 \cdot (NH_4)_2SO_4 \cdot 4H_2O$[c]	$Na_2SO_4 \cdot (NH_4)_2SO_4 \cdot 4H_2O = 2Na^+ + 2SO_4^{2-} + 2NH_4^+ + 4H_2O$	-1.6761	0	0	0	0	N/A	N/A
$Na_2SO_4 \cdot NaNO_3 \cdot H_2O$[m,n]	$Na_2SO_4 \cdot NaNO_3 \cdot H_2O = 3Na^+ + SO_4^{2-} + NO_3^- + H_2O$	2.0945	0	0	0	0	N/A	N/A

Table 23: (Continued from previous page.)

Species	From reaction	$\log K = a_1 + a_2 T + a_3/T + a_4 \log(T) + a_6 T^2$ (T in K) a_1	a_2 (K^{-1})	a_3 (K)	a_4	a_6 (K^{-2})	T range (K)	Molar volume (cm^3 mol^{-1})
$Na_2SO_4 \cdot NiSO_4 \cdot 4H_2O$[c]	$Na_2SO_4 \cdot NiSO_4 \cdot 4H_2O = 2Na^+ + 2SO_4^{2-} + Ni^{2+} + 4H_2O$	-3.4199	0	0	0	0	N/A	N/A
$NaClO_4 \cdot H_2O$[k]	$NaClO_4 \cdot H_2O = Na^+ + ClO_4^- + H_2O$	0.01486	7.250×10^{-3}	0	0	0	273–323	69.53
$NaHSO_4$[m,n]	$NaHSO_4 = Na^+ + H^+ + SO_4^{2-}$	0.6087	0	0	0	0	N/A	43.82
$NaH_3(SO_4)_2 \cdot H_2O$[m,n]	$NaH_3(SO_4)_2 \cdot H_2O = Na^+ + 3H^+ + 2SO_4^{2-} + H_2O$	4.8127	0	0	0	0	N/A	N/A
Natroalunite[a]	$NaAl_3(SO_4)_2(OH)_6 + 6H^+ = Na^+ + 3Al^{3+} + 2SO_4^{2-} + 6H_2O$	-41.87	0	13420	0	0	273–298	144.77
$(NH_4)_2SO_4$[m]	$(NH_4)_2SO_4 = 2NH_4^+ + SO_4^{2-}$	-473.3	-0.1669	10390	197.3	0	254–380	74.74
$(NH_4)_2SO_4 \cdot Al_2(SO_4)_3 \cdot 24H_2O$[h]	$(NH_4)_2SO_4 \cdot Al_2(SO_4)_3 \cdot 24H_2O = 2NH_4^+ + 4SO_4^{2-} + 2Al^{3+} + 24H_2O$	-12.2666	0	0	0	0	N/A	N/A
$(NH_4)_2SO_4 \cdot Cr_2(SO_4)_3 \cdot 24H_2O$[h]	$(NH_4)_2SO_4 \cdot Cr_2(SO_4)_3 \cdot 24H_2O = 2NH_4^+ + 4SO_4^{2-} + 2Cr^{3+} + 24H_2O$	-11.3417	0	0	0	0	N/A	N/A
$(NH_4)_3H(SO_4)_2$[m,n]	$(NH_4)_3H(SO_4)_2 = 3NH_4^+ + H^+ + 2SO_4^{2-}$	-0.8408	0	0	0	0	N/A	N/A
NH_4Cl[o]	$NH_4Cl = NH_4^+ + Cl^-$	-3.078	0.0155	0	0	-3.451×10^{-6}	258–303	34.96
$NH_4Cl \cdot MgCl_2 \cdot 6H_2O$[b]	$NH_4Cl \cdot MgCl_2 \cdot 6H_2O = NH_4^+ + Mg^{2+} + 3Cl^- + 6H_2O$	2475	0.66	-67830	-986.1	0	273–400	N/A
NH_4ClO_4[o]	$NH_4ClO_4 = NH_4^+ + ClO_4^-$	-16.42	0.09132	0	0	-1.233×10^{-4}	270–307	60.25
NH_4-feldspar[p,q]	$NH_4AlSi_3O_8 + 4H^+ = NH_4^+ + Al^{3+} + 3SiO_2 + 2H_2O$	-74.34	0.3080	0	0	-2.270×10^{-4}	298–600	114.78
NH_4HCO_3[o]	$NH_4HCO_3 = NH_4^+ + HCO_3^-$	-15.87	0.09703	0	0	-1.472×10^{-4}	269–313	50.04
NH_4HSO_4[m,n]	$NH_4HSO_4 = NH_4^+ + H^+ + SO_4^{2-}$	0.27	0	0	0	0	N/A	N/A
$NH_4HSO_4 \cdot NH_4NO_3$[m,n]	$NH_4HSO_4 \cdot NH_4NO_3 = 2NH_4^+ + H^+ + SO_4^{2-} + NO_3^-$	1.1274	0	0	0	0	N/A	N/A
$(NH_4)_2SO_4 \cdot 2NH_4NO_3$[m,n]	$(NH_4)_2SO_4 \cdot 2NH_4NO_3 = 4NH_4^+ + SO_4^{2-} + 2NO_3^-$	1.9326	0	0	0	0	N/A	N/A
$(NH_4)_2SO_4 \cdot 3NH_4NO_3$[m,n]	$(NH_4)_2SO_4 \cdot 3NH_4NO_3 = 5NH_4^+ + SO_4^{2-} + 3NO_3^-$	2.9463	0	0	0	0	N/A	N/A
NH_4-muscovite[q]	$NH_4Al_3Si_3O_{10}(OH)_2 + 10H^+ = NH_4^+ + 3Al^{3+} + 3SiO_2 + 6H_2O$	-66.38	0.3170	0	0	-2.386×10^{-4}	298–600	N/A
NH_4NO_3[o]	$NH_4NO_3 = NH_4^+ + NO_3^-$	-8.998	0.05692	0	0	-7.966×10^{-5}	N/A	48.20
Pickeringite[a]	$MgSO_4 \cdot Al_2(SO_4)_3 \cdot 22H_2O = Mg^{2+} + 2Al^{3+} + 4SO_4^{2-} + 22H_2O$	-8.0131	0	0	0	0	N/A	471.9
Rhomboclase[e]	$Fe(SO_4)_3 \cdot H_2SO_4 \cdot 8H_2O = 2Fe^{3+} + 2H^+ + 4SO_4^{2-} + 8H_2O$	-28.50	0	8304	0	0	273–298	295.61
Römerite[e]	$Fe_3(SO_4)_4 \cdot 14H_2O = Fe^{2+} + 2Fe^{3+} + 4SO_4^{2-} + 14H_2O$	-29.16	0	5186	0	0	273–298	373.96
Rozenite[e]	$FeSO_4 \cdot 4H_2O = Fe^{2+} + SO_4^{2-} + 4H_2O$	-2.795	4.203×10^{-3}	0	0	0	273–298	138.84
Schwertmannite[e]	$FeO(OH)_{0.75}(SO_4)_{0.125} + 2.75H^+ = Fe^{3+} + 0.125SO_4^{2-} + 1.75H_2O$	-11.66	0	3823	0	0	273–298	24.9
Soda-niter[d]	$NaNO_3 = Na^+ + NO_3^-$	92.2125	-0.6628	0	0	1.197×10^{-3}	273–343	37.6
Szomolnokite[e,f]	$FeSO_4 \cdot H_2O = Fe^{2+} + SO_4^{2-} + H_2O$	2.746	-0.01212	0	0	0	N/A	57.21
Trona[g]	$NaHCO_3 \cdot Na_2CO_3 \cdot 2H_2O = 3Na^+ + HCO_3^- + CO_3^{2-} + 2H_2O$	-4.336	-0.01113	0	0	0	N/A	107.2
Vaterite[g]	$CaCO_3 = Ca^{2+} + CO_3^{2-}$	-172.1	-0.07798	3074	71.60	0	N/A	37.72
Voltaite[e]	$K_2Fe_9(SO_4)_{12} \cdot 18H_2O = 2K^+ + 4Fe^{3+} + 5Fe^{2+} + 12SO_4^{2-} + 18H_2O$	-101.0	0	18560	0	0	273–298	762.15
"KerogenC515"[r,s]	$C_{515}H_{596}O_{72} + 628O_2 = 515CO_2 + 298H_2O$	104660.55	-244.27	0	0	0.183	273–623	6989.3
"KerogenC292"[r,s]	$C_{292}H_{288}O_{12} + 358O_2 = 292CO_2 + 144H_2O$	59184.26	-138.37	0	0	0.10	273–623	3398.2
"KerogenC128"[r,s]	$C_{128}H_{68}O_7 + 141.5O_2 = 128CO_2 + 34H_2O$	23405.37	-54.726	0	0	0.041	273–623	1320.7
Pyridine[t]	$C_5H_5N + 6.25O_2 = 5CO_2 + 2.5H_2O + 0.5N_2$	1071.04	-2.50773	0	0	0.00188	273–623	64.4
"(6)(CB)(CB)S"[u]	$S + O_2 = SO_2$	137.16	-0.320465	0	0	2.41×10^{-4}	273–623	16.5
"(aro)-O-(aro)"[r]	$O = 0.5O_2$	-46.6	0.111	0	0	-7.99×10^{-5}	273–623	-2.4